The Dissertation Committee for Wei Yu Certifies that this is the approved version of the following dissertation:

Developments in Modeling and Optimization of Production in Unconventional Oil and Gas Reservoirs

Committee:

Kamy Sepehrnoori, Supervisor

Lee Chin

Mojdeh Delshad

Kishore K. Mohanty

Tadeusz W. Patzek

Developments in Modeling and Optimization of Production in Unconventional Oil and Gas Reservoirs

by

Wei Yu, B.S.; M.E.

Dissertation

Presented to the Faculty of the Graduate School of

The University of Texas at Austin

in Partial Fulfillment

of the Requirements

for the Degree of

Doctor of Philosophy

The University of Texas at Austin

May 2015

Dedication

To my parents, Ruie Sun and Zhongzhao Yu,

To my wife, Kan Wu,

for their endless love, support and encouragement.

Acknowledgements

Thank you to my supervisor Dr. Kamy Sepehrnoori. During my PhD study at The University of Texas at Austin, Sepehrnoori has been tirelessly helped me to improve myself in all aspects over the years. I deeply appreciate his excellent guidance, patience, support, and encouragement. No words can fully express my gratitude to him. His professional guidance will benefit me in my future career development. I would also like to thank my committee members: Dr. Lee Chin, Dr. Mojdeh Delshad, Dr. Kishore Mohanty, and Dr. Tad Patzek for their valuable comments, feedback, and guidance through my research.

Special thanks go to Dr. Abdoljalil Varavei. He spent a lot of time discussion with me and resolving my technical questions. Thank you to Dr. Chowdhury Mamun for his review and comments of my dissertation. Thank you to Dr. Roger Terzian, Tim Guinn, Frankie Hart, John Cassibry, Joanna Castillo, and Glen Baum for their computer technical and administrative help. Also, I would like to thank for the time and help from the rest of the PGE department staff and faculties.

Thank you to Hilcorp Energy Company and Chief Oil and Gas LLC for providing financial support to make this dissertation work possible. I want to acknowledge Computer Modeling Group (CMG) and Schlumberger for providing software used in this work.

Thank you to my great officemates for their help and support Hamidreza Lashgari, Aboulghasem Kazemi Nia Korrani, Emad Al-Shalabi, Shayan Tavassoli, Reza Ganjdenesh, Walter Fair, Mahmoud Shakiba, Ali Abouie, Jose Sergio, Yifei Xu, Wensi

Fu, Xianchao Chen, and Wenda Wang. Many thanks also extend to all of my friends for the good times and conversations.

Finally, thank you to my parents for their endless love, understanding, and support: my mother Ruie Sun and my father Zhongzhao Yu. I would like to thank my beloved wife Dr. Kan Wu for her love, support and encouragement. She makes it all worthwhile.

Developments in Modeling and Optimization of Production in Unconventional Oil and Gas Reservoirs

Wei Yu, Ph.D.

The University of Texas at Austin, 2015

Supervisor: Kamy Sepehrnoori

The development of unconventional resources such as shale gas and tight oil exploded in recent years due to two key enabling technologies of horizontal drilling and multi-stage fracturing. In reality, complex hydraulic fracture geometry is often generated. However, an efficient model to simulate shale gas or tight oil production from complex non-planar fractures with varying fracture width along fracture length is still lacking in the petroleum industry. In addition, the pore size distributions for shale gas reservoirs and conventional gas reservoirs are quite different. The diffusivity equation of conventional gas reservoirs is not adequate to describe gas flow in shale reservoirs. Hence, a new diffusivity equation including the important transport mechanisms such as gas slippage, gas diffusion, and gas desorption is required to model gas flow in shale reservoirs.

Furthermore, there are high cost and large uncertainty in the development of shale gas and tight oil reservoirs because of many uncertain reservoir properties and fracture parameters. Therefore, an efficient and practical approach to perform sensitivity studies, history matching, and economic optimization for the development of shale gas and tight oil reservoirs is clearly desirable. For tight oil reservoirs, the primary oil recovery factor is very low and substantial volumes of oil still remain in place. Hence, it is important to

investigate the potential of CO_2 injection for enhanced oil recovery, which is a new subject and not well understood in tight oil reservoirs.

In this research, an efficient semi-analytical model was developed by dividing fractures into several segments to approximately represent the complex non-planar fractures. It combines an analytical solution for the diffusivity equation about fluid flow in shale and a numerical solution for fluid flow in fractures. For shale gas reservoirs, the diffusivity equation of conventional gas reservoirs was modified to consider the important flow mechanisms such as gas slippage, gas diffusion, and gas desorption. The key effects of non-Darcy flow and stress-dependent fracture conductivity were included in the model. We verified this model against a numerical reservoir simulator for both rectangular fractures and planar fracture with varying width. The well performance and transient flow regime analysis between single rectangular fracture, single planar fracture with varying width, and single curving non-planar fracture were compared and investigated. A well from Marcellus shale was analyzed by combining non-planar fractures, which were generated from a three-dimensional fracture propagation model developed by Wu and Olson (2014a), and the semi-analytical model. Contributions to gas recovery from each gas flow mechanism were analyzed. The key finding is that modeling gas flow from non-planar fractures as well as modeling the important flow mechanisms in shale gas reservoirs is significant. This work, for the first time, combines the complex non-planar fracture geometry with varying width and all the important gas flow mechanisms to efficiently analyze field production data from Marcellus shale.

We analyzed several core measurements for methane adsorption from some area in Marcellus shale and found that the gas desorption behaviors of this case study deviate from the Langmuir isotherm, but obey the BET (Brunauer, Emmett and Teller) isotherm. To the best of our knowledge, such behavior has not been presented in the literature for

shale gas reservoirs to behave like multilayer adsorption. The effect of different gas desorption models on calculation of original gas in place and gas recovery prediction was compared and analyzed.

We developed an integrated reservoir simulation framework to perform sensitivity analysis, history matching, and economic optimization for shale gas and tight oil reservoirs by integrating several numerical reservoir simulators, the semi-analytical model, an economic model, two statistical methods, namely, Design of Experiment and Response Surface Methodology. Furthermore, an integrated simulation platform for unconventional reservoirs (ISPUR) was developed to generate multiple input files and choose a simulator to run the files more easily and more efficiently. The fracture cost was analyzed based on four different fracture designs in Marcellus shale. The applications of this framework to optimize fracture treatment design in Marcellus shale and optimize multiple well placement in Bakken tight oil reservoir were performed. This framework is effective and efficient for hydraulic fracture treatment design and production scheme optimization for single well and multiple wells in shale gas and tight oil reservoirs.

We built a numerical reservoir model to simulate CO_2 injection using a huff-n-puff process with typical reservoir and fluid properties from the Bakken formation by considering the effect of CO_2 molecular diffusion. The simulation results show that the CO_2 molecular diffusion is an important physical mechanism for improving oil recovery in tight oil reservoirs. In addition, the tight oil reservoirs with lower permeability, longer fracture half-length, and more heterogeneity are more favorable for the CO_2 huff-n-puff process. This work can provide a better understanding of the key parameters affecting the effectiveness of CO_2 huff-n-puff in the tight oil reservoirs.

Table of Contents

List of Tables

List of Figures

CHAPTER 1: General Introduction

In this dissertation, several new developments for simulation of unconventional oil and gas reservoirs are presented to facilitate production from such reservoirs. A semi-analytical model was developed to simulate shale gas and tight oil production from ideal rectangular hydraulic fractures with constant fracture width and more realistic non-planar hydraulic fractures with varying fracture width along fracture length. For simulation of shale gas production, the semi-analytical model considers the important gas transport mechanisms including gas slippage, gas diffusion, and gas desorption. In addition, an integrated reservoir simulation framework was developed to optimize hydraulic fracture treatment design for the economic development of shale gas and tight oil reservoirs. The framework integrates several numerical reservoir simulators, the semi-analytical model, an economic model, Design of Experiment (DOE), and Response Surface Methodology (RSM). Furthermore, an integrated simulation platform for unconventional resources (ISPUR) was developed and implemented in the framework to generate multiple input files for reservoir simulators more easily and more efficiently. Finally, due to low oil recovery factor in tight oil reservoirs, CO_2 injection for enhanced oil recovery by considering CO_2 molecular diffusion was investigated.

This chapter first introduces the background related to shale gas and tight oil reservoirs and hydraulic fracturing. Then, statement of the problem and the objectives of this research are presented. Finally, the organization of the dissertation is described.

1.1 BACKGROUND

Unconventional resources, such as shale gas and tight oil, are making a major contribution to the world energy. U.S. Energy Information Administration (EIA, 2013a) reported that the technically recoverable world shale oil resources are 345 billion barrels and world shale gas resources are 7,299 trillion cubic feet (TCF). Figure 1.1 shows the top reserve holders of shale gas resources throughout the world. As shown, the United States has 24.4 trillion cubic meters gas estimation, China has 36.1 trillion cubic meters gas estimation, and Argentina has 21.9 trillion cubic meters gas estimation. Figure 1.2 shows the major shale gas basins distribution in the United States. It is predicted that shale gas production will increase from 40% of total U.S. dry gas production in 2012 to 53% in 2040 (EIA, 2014a). Figure 1.3 shows the top ten holders of tight oil resources throughout the world. Based on the early release overview of U.S. Energy Information Administration in 2013, onshore tight oil production will increase from 33% of total lower 48 onshore oil production to 51% in 2040 (EIA, 2013b).

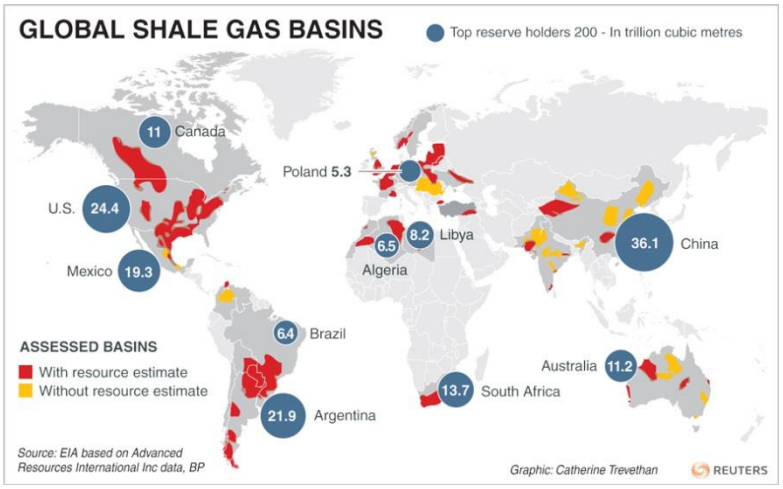

Figure 1.1: Global shale gas basins distribution in the world (U.S. Energy Information Administration, 2012). http://blog.thomsonreuters.com/index.php/global-shale-gas-basins-graphic-of-the-day.

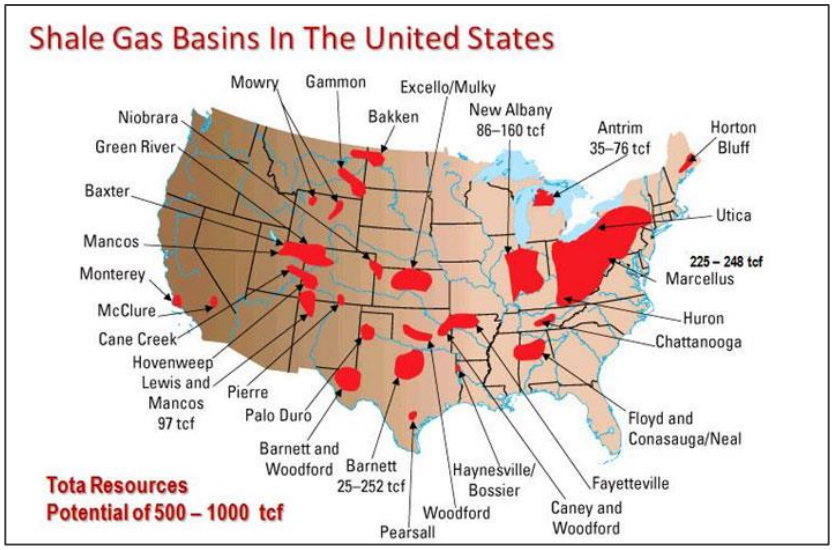

Figure 1.2: Major shale gas basins distribution in the United States. http://naturalgas resourcecenter.com/tag/shale-gas-basins.

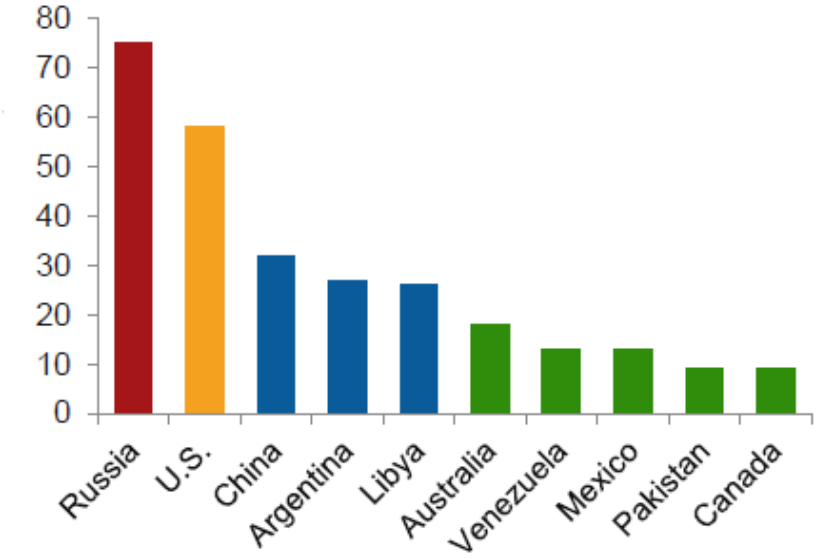

Figure 1.3: Top ten countries for technically recoverable tight oil resources (billion barrels). http://www.eia.gov/conference/2014/pdf/presentations/webster.pdf.

Gas shales are typically characterized by ultra-low permeability and low porosity and have a significant amount of total organic content (TOC). The permeability in shale

gas reservoirs is around nano-Darcy, as shown in Figure 1.4. Figure 1.5 presents one core sample from Barnett shale.

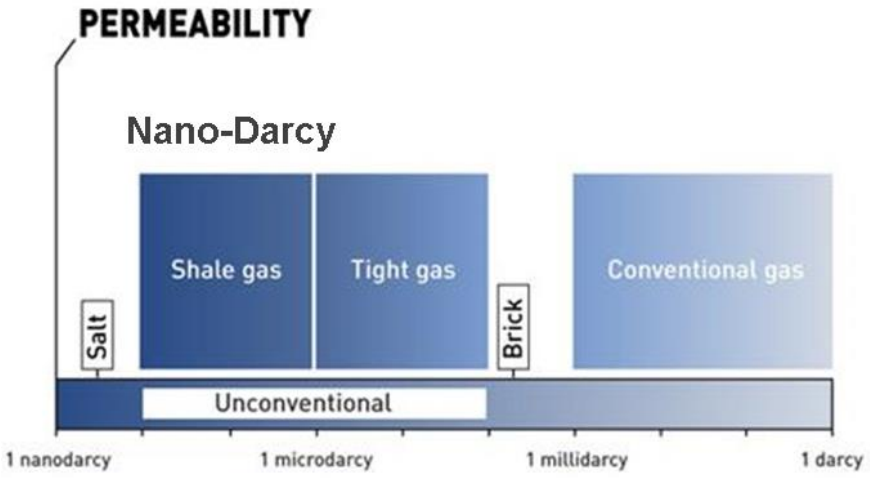

Figure 1.4: Permeability of nano-Darcy for shale gas reservoirs (modified from Total). http://www.total.com/en/energies-expertise/oil-gas/exploration-production/strategic-sectors/unconventional-gas/presentation/three-main-sources-unconventional-gas?%FFbw=kludge1%FF.

Figure 1.5: One core sample from Barnett shale (Bowker, 2013).

In order to economically develop shale gas and tight oil reservoirs, two key technologies such as horizontal drilling and multi-stage fracturing are required, as shown in Figure 1.6. The actual fracture stimulation process involves pumping large volume of

fluids, which can create the complex fractures, and large amount of proppants, which can prevent the fractures closure. During hydraulic fracturing treatments, complex fracture networks are often generated and the interaction of hydraulic and natural fractures significantly impacts the complexity (Daniels et al., 2007; Maxwell, et al., 2013). The complex fracture networks can create a huge contact area between the formation and horizontal wellbore (Cipolla and Wallace, 2014). The effectiveness of fracturing stimulation treatment plays an important role in economic production of the unconventional reservoirs (Weng, 2014). Three to six perforation clusters per fracturing stage are typically used in most horizontal wells (Cipolla et al., 2010). U.S. Energy Information Administration (EIA, 2015) reported that four countries including the United States, Canada, China, and Argentina are currently producing commercial volumes of shale gas and tight oil and the United States is the dominant producer (see Figure 1.7).

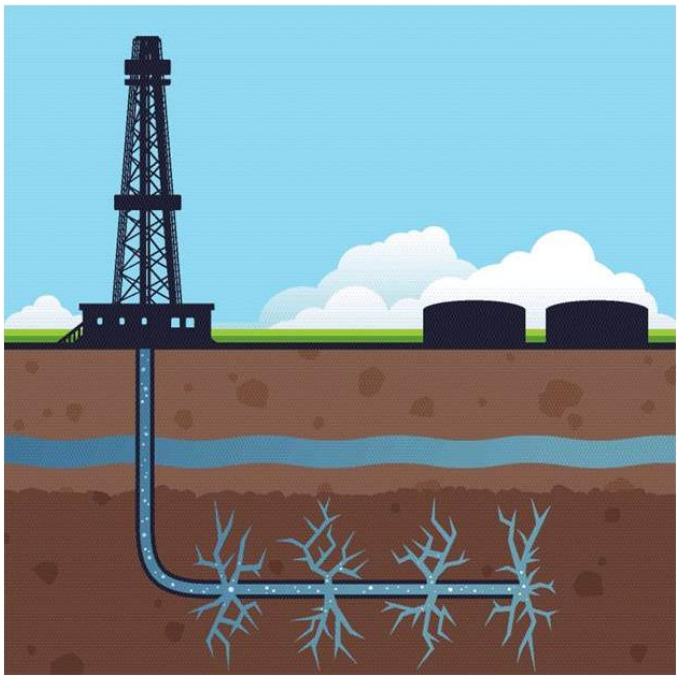

Figure 1.6: Horizontal drilling and multi-stage hydraulic fracturing (after Nikiforuk, 2011). http://thetyee.ca/News/2011/12/19/Fracking-Contamination/.

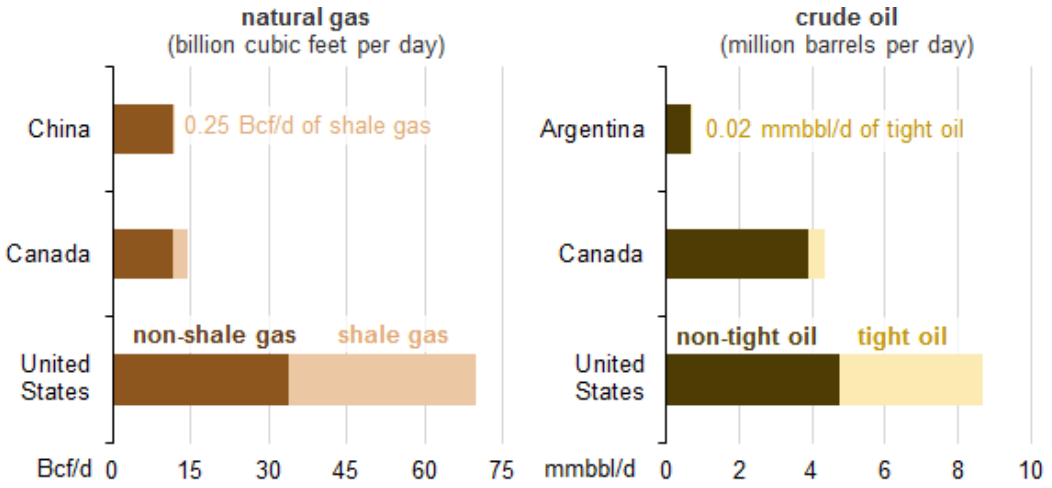

Figure 1.7: Four countries producing commercial volumes of shale gas and tight oil (EIA, 2015). http://www.eia.gov/todayinenergy/detail.cfm?id=19991.

1.2 STATEMENT OF THE PROBLEM

The actual hydraulic fracturing process often generates complex non-planar hydraulic fractures. The fracture width and fracture permeability are changing along fracture length. In general, some ideal fracture geometries such as bi-wing fractures and orthogonal fracture networks are used to represent the complex non-planar fractures. Although there are numerical models to handle the complex fracture geometry, most of them are computationally more expensive. Also, there is a big challenge of gridding issue for modeling fractures. More importantly, the effects of varying fracture width and permeability along the fracture length are not considered by the current models. Hence, an efficient model to simulate production from the complex non-planar fractures is still lacking in the petroleum industry. In addition, there are very few work that have combined the realistic fracture geometry modeling as well as production simulation using such fracture geometries to analyze field well performance. Accordingly, it is significant to combine them together to evaluate well performance from unconventional oil and gas reservoirs.

For shale gas reservoirs, the gas transport mechanisms are quite different from conventional gas reservoirs, which include not only gas advection, but also gas slippage, gas diffusion, and gas desorption. This is because the pore size distributions for shale gas reservoirs and conventional gas reservoirs are different. There are more nanopores in shale gas reservoirs compared with conventional gas reservoirs (Javadpour et al., 2007; Civan et al., 2010; Sakhaee-Pour and Bryant, 2012; Shi et al., 2013; Rezaveisi et al., 2014; Wu et al., 2014; Wu et al., 2015a, 2015b). The diffusivity equation of conventional gas reservoir is not adequate to describe gas flow in shale. In addition, gas flow velocity in hydraulic fractures is so high that non-Darcy flow effect should be considered. Furthermore, multiple long hydraulic fractures with uniform proppant distribution and sufficient fracture conductivity play an important role in achieving effective well stimulation and economic production of shale gas reservoirs (Gu and Mohanty, 2014; Gu et al., 2014, 2015); however, it is very challenging to maintain such conductivity due to proppant settlement, proppant fines generation and migration in the fracture, proppant diagenesis, proppant embedment in softer rock, and proppant crushing in harder rock (Darin and Huitt, 1960; Pope et al., 2009; LaFollette and Carman, 2010; Fan et al., 2010). The effect of stress-dependent fracture conductivity should be taken into account. Consequently, a comprehensive model by considering the important mechanisms for gas flow in shale and the effects of non-planar fractures, non-Darcy flow and stress-dependent fracture conductivity is highly required.

There is a high uncertainty in reservoir properties, which has a significant effect on shale gas and tight oil production. In reality, the order of magnitude of permeability for shale gas reservoirs is nano-Darcy and for tight oil reservoirs is micro-Darcy. Typical shale gas reservoirs exhibit a net thickness of 50 to 600 ft, porosity of 2-8%, TOC of 1-14% and are found at depths ranging from 1,000 to 13,000 ft (Cipolla et al., 2010). In

addition, many fracture parameters are also uncertain and significantly affect the well performance such as fracture spacing, fracture half-length, fracture height, and fracture conductivity. Moreover, the cost of hydraulic fracturing is expensive, although it can make shale gas and tight oil produced economically. The optimization of hydraulic fracture treatment design is important to obtain the most economical production scenario. Therefore, the development of a framework to perform sensitivity analysis and optimize shale gas and tight oil production in an efficient and effective way is clearly desirable.

With the development of unconventional resources, there is a considerable number of wells required for performing history matching and forecasting using reservoir simulation approach. Generally, we use local grid refinement to model fractures and the size of matrix grids gradually becomes small when moving to the fracture grid. This results in a very complex gridding issue. In addition, when performing sensitivity studies and history matching, a large number of simulation cases are required and each case might have different fracture length and fracture number. It will be very time-consuming to generate the input files for these simulation cases manually. Therefore, a user-friendly and efficient platform to generate multiple input files for reservoir simulators more easily and more efficiently is important.

Although tight oil production has been boosted by the combination of horizontal drilling and multi-stage fracturing, the primary oil recovery factor is very low so that substantial volumes of oil still remain in place. Although CO_2 injection for enhanced oil recovery (EOR) is widely used in conventional oil reservoirs, it is a new subject for tight oil reservoirs with extremely low permeability. The physical mechanisms behind CO_2-EOR in tight oil reservoirs have not been clearly understood. Hence, a better understanding of the physical mechanisms and key parameters affecting the effectiveness of CO_2-EOR in tight oil reservoirs using reservoir simulation approach is necessary.

1.3 RESEARCH OBJECTIVES

The general objectives of this dissertation are to develop various simulation tools for production of oil and gas from unconventional reservoirs. Hence, we address developments of a semi-analytical model to simulate shale gas and tight oil production with the complex non-planar hydraulic fractures and an integrated reservoir simulation framework and platform to optimize hydraulic fracture treatment design for unconventional oil and gas reservoirs; build a simulation model to investigate CO_2-EOR in tight oil reservoirs. The specific objectives of this dissertation are:

- Develop an efficient semi-analytical model to simulate shale gas production from multiple non-planar hydraulic fractures with varying fracture width and fracture permeability by considering the important physical mechanisms such as gas slippage, gas diffusion, and gas desorption, and the effects of non-Darcy flow and stress-dependent fracture conductivity.
- Extend the semi-analytical model to simulate tight oil production from multiple non-planar hydraulic fractures by considering the stress-dependent fracture conductivity effect.
- Develop an integrated reservoir simulation framework for performing sensitivity studies, history matching, and economic optimization for shale gas and tight oil reservoirs using Design of Experiment and Response Surface Methodology.
- Develop an integrated simulation platform for unconventional reservoirs (ISPUR) to generate a large number of input files for reservoir simulators (CMG, ECLIPSE, and UTCOMP) and the semi-analytical model easily and more efficiently.

- Analyze field well performance from Marcellus shale by combining the fracturing propagation modeling and production simulation modeling together; investigate the effects of gas slippage, gas diffusion, gas desorption, non-Darcy flow, geomechanics, and non-planar fractures on well performance in shale gas reservoirs.
- Analyze the core measurements of gas adsorption from Marcellus shale using different gas adsorption models such as Langmuir isotherm and BET (Brunauer, Emmett and Teller) isotherm.
- Investigate the effects of stress-dependent fracture conductivity and non-planar fractures on well performance in tight oil reservoirs.
- Apply the framework and ISPUR to perform sensitivity analysis, history matching and economic optimization of hydraulic fracture treatment design for single well in Marcellus shale gas reservoirs.
- Apply the framework and ISPUR to perform sensitivity analysis, history matching, and economic optimization of hydraulic fracture treatment design for multiple well placement in Bakken tight oil reservoirs.
- Build a simulation model for CO_2 huff-n-puff in Bakken tight oil reservoirs, understand the effect of CO_2 molecular diffusion on the CO_2 huff-n-puff process, and quantify the key parameters controlling this process.

1.4 ORGANIZATION OF THE DISSERTATION

The dissertation is divided into eight chapters. Following this chapter, Chapter 2 presents a semi-analytical model to simulate gas and oil flow from non-planar hydraulic fractures by dividing fractures into several segments. The stress-dependent fracture conductivity is considered. For shale gas reservoirs, the diffusivity equation of

conventional gas reservoirs is modified by including the important transport mechanisms such as gas slippage, gas diffusion, and gas desorption. Non-Darcy flow effect is also considered. In addition, the analytical model is verified against a numerical reservoir simulator for single rectangular fracture, single planar fracture with varying width, and multiple rectangular fractures. After verification, we combine the fracture propagation model and production simulation using the semi-analytical model to analyze a well performance from Marcellus shale. Also, we perform a series of cases studies for tight oil reservoirs and analyze the transient flow regime to characterize single rectangular fracture, single planar fracture with varying width, and single curving non-planar fracture.

In Chapter 3, several experimental measurements of methane adsorption from Marcellus shale core samples are analyzed using Langmuir isotherm and BET isotherm. Original gas in place is calculated and discussed using the two adsorption models. In addition, we perform history matching and production forecasting using a well from Marcellus shale by comparing the contributions of gas desorption to gas recovery using the two adsorption models.

Chapter 4 introduces an integrated reservoir simulation framework for shale reservoirs by integrating several numerical reservoir simulators, the semi-analytical model, an economic model, DOE, and RSM with a global optimization search engine. Also, an integrated simulation platform for unconventional reservoirs (ISPUR) is developed to generate multiple input files for reservoir simulators (CMG, ECLISPE, and UTCOMP) and the semi-analytical model more easily and more efficiently.

In Chapter 5, the framework developed in Chapter 4 is applied to perform sensitivity analysis and economic optimization of fracture treatment design for single well in Marcellus shale. Six uncertain parameters such as fracture height, fracture

conductivity, fracture half-length, cluster spacing, permeability, and initial reservoir pressure are studied. Each parameter is given a reasonable range. Based on the sensitivity analysis, we perform history matching and production forecasting with a well from Marcellus shale. Finally, we perform economic optimization based on the important design parameters to quantify the best economic production scenario in Marcellus shale.

In Chapter 6, the framework developed in Chapter 4 is used to perform sensitivity analysis and optimization of multiple well placement in Bakken tight oil reservoirs. First, six uncertain parameters including fracture spacing, fracture half-length, fracture conductivity, permeability, porosity, and initial water saturation are investigated for single well. Based on the sensitivity analysis, we perform history matching and production forecasting with a well from the Bakken formation. Finally, we perform economic optimization based on the significant design variables of single well in combination of a new variable of number of well to obtain the best economic scenario for multiple well placement in the Bakken formation.

Chapter 7 presents a numerical reservoir model to simulate CO_2 injection using a huff-n-puff process with typical reservoir and fracture properties from the Bakken formation. Effects of CO_2 molecular diffusion, number of cycle, fracture half-length, permeability and reservoir heterogeneity on the effectiveness of CO_2 huff-n-puff are examined in detail.

Chapter 8 presents the conclusions of this dissertation and provides some recommendations for future research.

CHAPTER 2: A Semi-Analytical Model for Simulation of Production in Shale Reservoirs

In reality, complex non-planar hydraulic fractures with varying fracture width and permeability are often created during the hydraulic fracturing process. However, it is challenging to simulate well performance with the complex fracture geometry. For the sake of simplicity, the complex fracture geometry is often represented by two ideal fracture geometries such as bi-wing fractures and orthogonal fracture networks. However, such ideal geometries are not adequate to capture the physics of the transient flow behavior. Although significant efforts have been made in recent years to numerically model well performance from the complex fracture geometry, these approaches are still challenging to apply efficiently due to a very complicated gridding issue and an expensive computational cost presented in the literature. In addition, the effect of varying fracture width along fracture length is not considered in the models. Hence, an efficient model to handle the complex fracture geometry is still lacking in the industry. In this study, we developed an efficient semi-analytical model to fill this gap by dividing fractures into several segments to describe the complex fracture geometry. The stress-dependent fracture conductivity effect was also considered. For shale gas reservoirs, the diffusivity equation of conventional gas reservoirs was modified by considering the important gas transport mechanisms such as gas slippage, gas diffusion, and gas desorption. We verified this model against a numerical reservoir simulator for both rectangular fractures and non-planar fractures. Furthermore, we performed a series of case studies to simulate production from shale gas and tight oil reservoirs. This work can provide significant insights into optimization of fracture treatment design for shale gas and tight oil reservoirs.

2.1 INTRODUCTION

In the last decade, the technical advancements in horizontal drilling and multi-stage fracturing have led to a boom in the development of unconventional resources such as shale gas and tight oil in the United States and abroad. The effectiveness of fracturing stimulation treatment plays an important role in economic production of these unconventional reservoirs (Weng, 2014). Microseismic monitoring of hydraulic fracture treatments plays a significant role in understanding the stimulation effectiveness and fracture geometry (Cipolla et al., 2012). Microseismic measurements indicate that the stimulation treatments often create complex fracture geometry, especially in the brittle shale reservoirs (Maxwell et al., 2002; Fisher et al., 2002; Warpinski et al., 2005; Cipolla and Wallace, 2014). Figure 2.1 shows one example indicating the complex fracture geometry created in a vertical well. The complex fracture geometry is strongly affected by in-situ stresses and pre-existing natural fractures (Zhou et al., 2013; Weng, 2014). Although many attempts have been focused on developing hydraulic fracture propagation models to predict the complex non-planar fracture geometry (Wu et al., 2012; Xu and Wong, 2013; Wu and Olson, 2013, 2014a, 2014b; Wu, 2014), it is still challenging to measure the complex fracture geometry completely and exactly.

Figure 2.1: Complex fracture geometry in a vertical well (Fisher et al., 2004).

For the sake of simplicity, two ideal fracture geometries such as bi-wing fractures and orthogonal fracture networks are widely used to represent the complex geometry for simulation of well performance in unconventional reservoirs (Yu and Sepehrnoori, 2013a, 2013b, 2013c; Tavassoli et al., 2013a, 2013b; Aybar et al., 2015), as shown in Figure 2.2. In addition, such ideal fracture geometries can be easily handled by analytical solutions, semi-analytical solutions and numerical solutions (Gringarten et al., 1972; Gringarten and Rameny, 1973; Cinco-Ley and Samaniego, 1981; Guppy et al., 1982; Blasingame and Poe, 1993; Chen and Raghavan, 1997; Khan et al., 2011; Yu et al., 2014a; Shakiba, 2014). In general, local grid refinement (LGR) is employed by using numerical solutions to model hydraulic fracture explicitly with a small and constant fracture width but a larger permeability, which can effectively capture the transient flow behavior in fractured shale reservoirs (Rubin, 2010; Yu et al., 2014b, 2014c, 2014d; Yu and Sepehrnoori, 2014a, 2014b, 2014c; Yu et al., 2015a, 2015b).

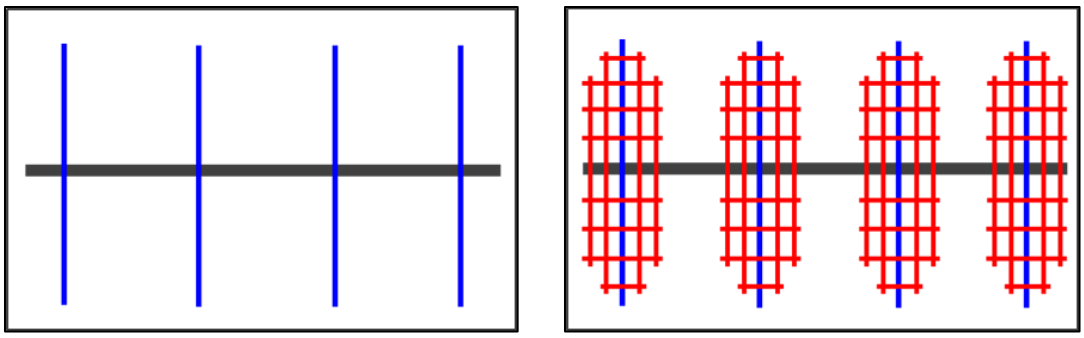

(a) (b)

Figure 2.2: Two ideal fracture geometries used for simulation of well production in shale reservoirs. (a) Bi-wing fractures. (b) Orthogonal fracture networks.

In recent years, significant efforts have been made to model well performance from the complex fracture geometry. Xu et al. (2010) developed a wire-mesh model to simulate the elliptical fracture network. However, the wire-mesh model is difficult to simulate non-orthogonal fracture network. Weng et al. (2011) developed an unconventional fracture model (UFM) to predict the complex fracture geometry, which can be integrated with a numerical reservoir simulator using the automatic generation of unstructured grids to properly simulate production from the complex fracture geometry (Cipolla et al., 2011; Mirzaei and Cipolla, 2012). However, this approach has some practical challenging issues such as the difficulties of model set-up and long turnaround time (Zhou et al., 2013). Olorode et al. (2013) proposed a 3D Voronoi mesh-generation application to generate the non-ideal fracture geometry for simulator to investigate the effect of irregular fracture geometry on well performance of unconventional gas reservoirs. Moinfar et al. (2013) developed an embedded discrete fracture model (EDFM) based on the algorithm presented by Li and Lee (2008) to simulate fluid flow from unstructured fracture geometry. However, the above numerical approaches are still challenging to use efficiently due to a very complicated gridding issue or an expensive computational cost or complexities in development of computational codes. In order to

overcome these challenges, Zhou et al. (2013) proposed a semi-analytical model to handle the complex fracture geometry efficiently. However, the semi-analytical model did not consider the effects of gas slippage, gas diffusion, gas desorption, stress-dependent fracture conductivity, and non-planar fractures. In reality, the complex non-planar fracture geometry with varying fracture width and fracture permeability is often generated, especially in the deviated wells (Olson, 1995; Olson and Wu, 2012), as shown in Figures 2.3 and 2.4. However, most production simulation models only assume hydraulic fractures with constant width. Furthermore, gas transport mechanisms such as gas slippage, gas diffusion, and gas desorption in shale reservoirs are still poorly understood. Hence, an efficient model to simulate production from the complex non-planar fractures by considering the flow mechanisms stated above is still lacking in the petroleum industry. Hence, significant efforts are still required to develop an efficient model to fill this gap and evaluate the well performance of unconventional reservoirs with the complex non-planar fractures.

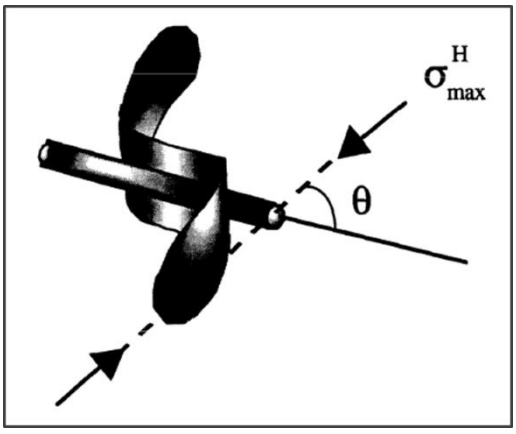

Figure 2.3: A single curving non-planar hydraulic fracture (after Olson, 1995).

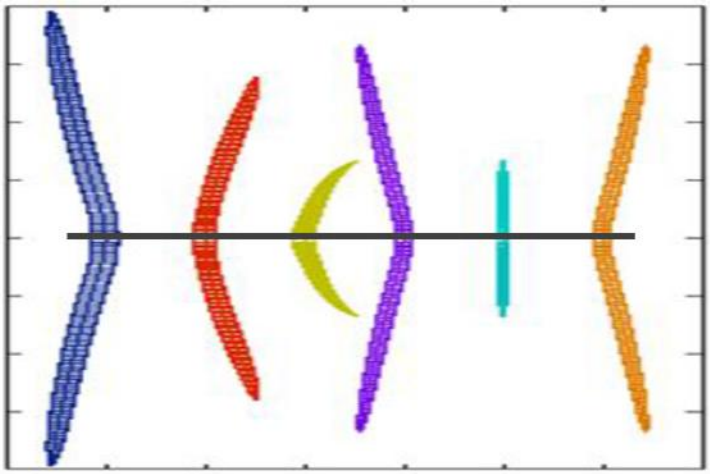

Figure 2.4: Multiple curving non-planar hydraulic fractures (after Wu, 2014).

In this study, we extended the semi-analytical model proposed by Zhou et al. (2013) to simulate production from multiple non-planar fractures. Also, the effects of important gas transport mechanisms, non-Darcy flow and stress-dependent fracture conductivity are considered. More importantly, the diffusivity equation of conventional gas reservoirs was modified to model gas flow in shale reservoirs and fully implemented in the semi-analytical model. We verified the semi-analytical model against a numerical reservoir simulator of CMG-GEM (CMG-GEM, 2012) for rectangular fractures and planar fracture with varying width. We performed a series of case studies for simulation of production from shale gas and tight oil reservoirs. This work provides an efficient production simulation model to simulate fluid flow from unconventional reservoirs with the complex non-planar hydraulic fractures, which can provide critical insights into understanding the stimulation effectiveness for the field development of unconventional reservoirs.

2.2 MODEL ASSUMPTIONS AND FRACTURE DISCRETIZATION

Some assumptions are made for the semi-analytical model development: 1. the well is intercepted by a fully penetrating fracture; 2. the reservoir is bounded by an upper and a lower impermeable layer; 3. the reservoir is isotropic and homogeneous with a constant height, porosity, and permeability; 4. the initial reservoir pressure is uniform; 5. for tight oil reservoirs, the reservoir contains a slightly compressible fluid with constant oil density, viscosity, and compressibility; 6. fluid flow takes place only through fractures; 7. there is no pressure loss along the wellbore; 8. pressure gradients are so small that the gravity effect is negligible. Under these assumptions, the diffusivity equation can be used to describe the flow behavior (Matthews and Russell, 1967).

The semi-analytical model mainly consists of two parts describing fluid flow from reservoir to the wellbore. The first is fluid flow from shale to fractures. The second is fluid flow from fractures to wellbore, as shown in Figure 2.5. More details about these two parts will be introduced and discussed in detail in the following sections.

In order to capture the complex non-planar fracture geometry, the hydraulic fracture in this model will be discretized into several small fracture segments (N_f) and the associated nodes (N_v) connecting these segments. Figure 2.6 presents one example for the fracture discretization. For this example, three non-planar hydraulic fractures are divided into 18 small fracture segments with 19 nodes. It is convenient to set up each fracture segment with different fracture properties such as fracture width and fracture permeability. In addition, each fracture segment can be oriented in any direction.

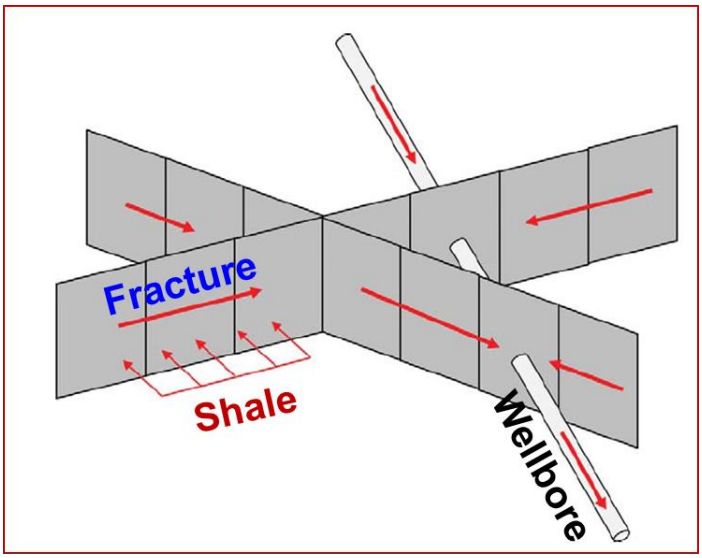

Figure 2.5: Fluid flow from shale to fracture, then from fracture to wellbore, finally from wellbore to surface (modified from Zhou et al., 2013).

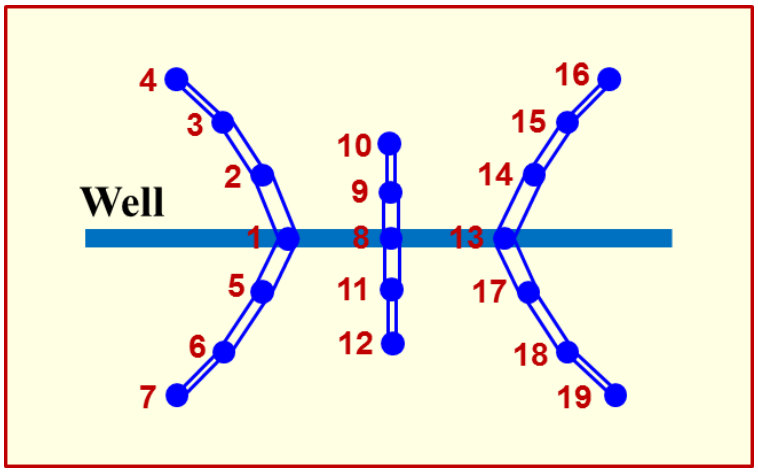

Figure 2.6: An example for fracture discretization with 18 small segments and 19 nodes.

2.3 MODEL DEVELOPMENT FOR SHALE GAS SIMULATION

Gas transport through shale formation with a large amount of nanopores and extremely low permeability is quite different from conventional gas reservoirs, where the laminar flow is dominant. It is generally agreed that the main flow mechanisms involved in shale gas reservoirs include not only gas advection, but also gas slippage, gas

diffusion, and gas desorption. Hence, the diffusivity equation for conventional gas reservoirs should be modified by taking into account all these important flow mechanisms. In addition, gas velocity along the fracture is so high that non-Darcy flow effect should be considered. Also, the geomechanics effect, which is mainly focused on stress-dependent fracture conductivity in this work, should be taken into account in the model. More details about the modification of the diffusivity equation, non-Darcy flow effect, and geomechanics effect will be discussed in the following sections.

2.3.1 Continuity equation for conventional gas reservoirs

The well-known diffusivity equation is widely used in the petroleum industry to describe the conventional gas flow in porous media under the isotherm condition (Dake, 1978). It can be expressed below if neglecting the gas gravity effect and the source terms:

$$\frac{\partial\left(\rho_g \phi\right)}{\partial t} - \nabla \cdot \left(\frac{\rho_g k}{\mu_g} \nabla p \right) = 0 , \tag{2.1}$$

where ρ_g is gas density, ϕ is rock porosity, k is reservoir permeability, and μ_g is gas viscosity.

Al-Hussainy et al. (1966) introduced the concept of real gas pseudopressure to simplify the non-linear diffusivity equation, which is defined by

$$m(p) = 2\int_{p^*}^{p} \frac{p}{\mu_g(p) Z_g(p)} dp , \tag{2.2}$$

where p^* is the reference pressure.

The final continuity equation is obtained as follows:

$$\frac{\partial^2 m(p)}{\partial x^2} + \frac{\partial^2 m(p)}{\partial y^2} + \frac{\partial^2 m(p)}{\partial z^2} = \frac{\phi c_g \mu_g}{k} \frac{\partial m(p)}{\partial t} . \tag{2.3}$$

This equation in combination with different initial and boundary conditions can be solved using exact numerical solution or approximate analytical solution. However, it is still inadequate to describe gas flow in shale reservoirs over the entire timescale of

production due to many physical mechanisms such as gas diffusion, gas slippage, and gas desorption are ignored (Xu, 2014).

2.3.2 Continuity equation for shale gas reservoirs

In recent years, increased consideration has been given to modify the continuity for conventional gas transport to accurately model gas flow in shale reservoirs, which should fully couple the different gas transport mechanisms.

2.3.2.1 Molecular diffusion

Molecular diffusion occurs due to the molecules concentration difference, which is defined as "the process by which matter is transported from one part of a system to another as a result of random molecular motions" (Crank, 1975). Figure 2.7 demonstrates the Darcian flow due to pressure gradient and Fickian flow due to concentration gradient. The green circles display the gas molecules. The big arrow represents the Darcian flow direction while the small arrows indicate the random flow. As shown in Figure 2.7(a), the difference of pressure is the driving force for the Darcian flow and there is a zero net effect for the Fickian flow due to the equal densities. However, as illustrated in Figure 2.7(b), the difference of density is the driving force for the Fickian flow.

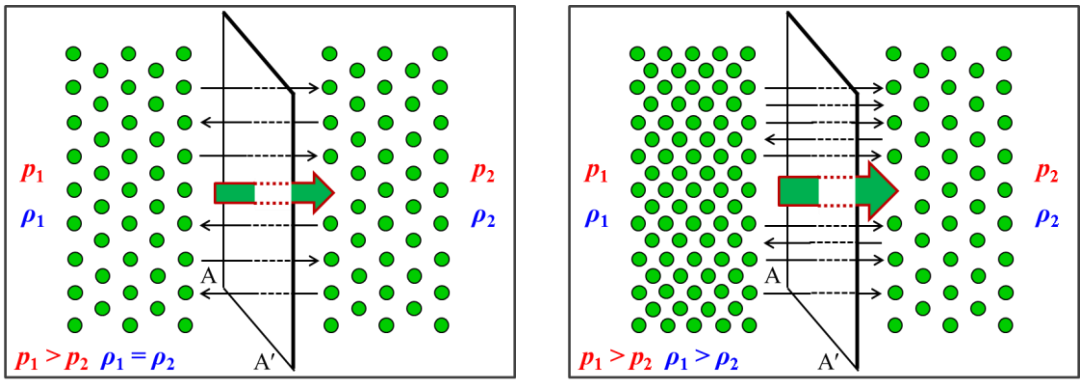

(a) (b)

Figure 2.7: Schematic representation of Darcian flow due to pressure gradient and Fickian flow due to concentration gradient (modified from Ertekin et al., 1986). (a) Darcian flow. (b) Darcian flow and Fickian flow.

The molecule diffusion process is governed by Fick's law below (Ertekin et al., 1986; Bird et al., 2007):

$$J = -D\nabla C, \tag{2.4}$$

where J is diffusion flux, C is molar concentration, and D is diffusivity coefficient, which is a property of the transported substance and the medium. In a saturated porous medium, the Fick's law can be written as follows:

$$J = -D_{eff}\nabla C, \tag{2.5}$$

where D_{eff} is the effective diffusivity coefficient, which is related to the free-solution diffusion coefficient as (Xu, 2014):

$$D_{eff} = \frac{\delta}{\tau}\phi D_0, \tag{2.6}$$

where D_0 is bulk diffusivity in free solution, δ is a dimensionless constrictivity factor (≤ 1), which accounts for variation of the pore size along its length caused by small pores, and τ is a dimensionless tortuosity factor (≥ 1), accounting for the elongated diffusion path compared to the straight path (Carman, 1956). There are two classes to define the dimensionless tortuosity as follows (Dullien, 1979; McDuff and Ellis, 1979):

$$\tau = \frac{L_e}{L}, \tag{2.7}$$

or

$$\tau = \left(\frac{L_e}{L}\right)^2, \tag{2.8}$$

where L_e is the effective diffusion length and L is geometrical length of the medium. The tortuosity for the gas flow in porous medium can be estimated from porosity and gas saturation by (Dullien, 1979)

$$\tau = \frac{1}{\phi^{1/3} S_g^{7/3}}. \tag{2.9}$$

The dimensionless constrictivity factor, which depends on the ratio of molecule diameter to the pore diameter, is quantified by the empirical equation developed by Satterfield et al. (1983).

$$\delta = \left(1 - \frac{d_{\text{gas}}}{d_{\text{pore}}}\right)^2, \tag{2.10}$$

where d_{gas} is gas molecule diameter and d_{pore} is the pore diameter.

For a real gas, gas density is given by

$$\rho_g = \frac{pM}{Z(p)RT}, \tag{2.11}$$

where, p is pressure in kPa, M is the molecule weight of the gas ($M = \gamma_g M_{air}$, where γ_g is gas specific gravity and M_{air} is air molecular weight and equals 29 kg/kmoles), R is the ideal gas constant with 8.3145 kPa·m^3/(kmoles·K), and T is absolute temperature (K). $Z(p)$ is the gas compressibility factor.

The gas molar concentration can be obtained as follows:

$$C = \frac{\rho_g}{M}. \tag{2.12}$$

The actual molecular diffusion process is very complex, which might be the combination of three distinct mechanisms acting individually or simultaneously: bulk

diffusion (molecule/molecule collisions dominate the gas transport), Knudsen diffusion (molecule-pore wall collisions dominate the gas transport), and surface diffusion (transport of adsorbed molecule layer) (Smith and Williams, 1984), as shown in Figure 2.8.

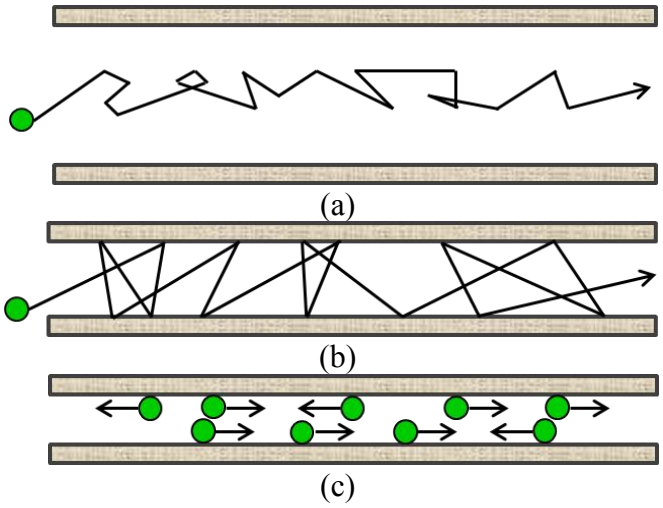

Figure 2.8: Three distinct types of molecular diffusion (modified from Albo et al., 2006). (a) Bulk diffusion. (b) Knudsen diffusion. (c) Surface diffusion.

The gas transport equation will be expressed below by considering the molecular diffusion effect:

$$\frac{\partial\left(\rho_g\phi\right)}{\partial t}-\nabla\cdot\left(\frac{\rho_g k}{\mu_g}\nabla p+\frac{\delta}{\tau}\phi D_g\nabla\rho_g\right)=0\,, \tag{2.13}$$

where D_g is Fickian diffusivity of gas component through the pore.

2.3.2.2 Gas slippage

Gas slippage is often described by the Klinkenberg effect, as shown in Figure 2.9. In this study, the continuity equation will be expressed by the following expression by considering the Klinkenberg effect (Xu, 2014):

$$u_g = -\frac{k\left(1+8\alpha K_n\right)}{\mu_g}\nabla p\,, \tag{2.14}$$

where α is a constant and close to 1, K_n is Knudsen number, which is defined by (Bird, 1994)

$$K_n = \frac{\lambda}{d}\,, \tag{2.15}$$

where d is the pore diameter, λ is the mean free path of gas molecules, which is defined by (Heidemann et al., 2006)

$$\lambda = \frac{k_B T}{\sqrt{2}\pi\sigma^2 p}\,, \tag{2.16}$$

where k_B is the Boltzmann constant (1.3805×10^{-23} J/K), T is temperature in K, p is pressure in Pa, and σ is diameter of gas molecules.

The gas transport equation will be altered below by considering the molecular diffusion and Klinkenberg effects:

$$\frac{\partial\left(\rho_g\phi\right)}{\partial t} - \nabla\cdot\left[\frac{\rho_g k\left(1+8\alpha K_n\right)}{\mu_g}\nabla p + \frac{\delta}{\tau}\phi D_g \nabla\rho_g\right] = 0\,. \tag{2.17}$$

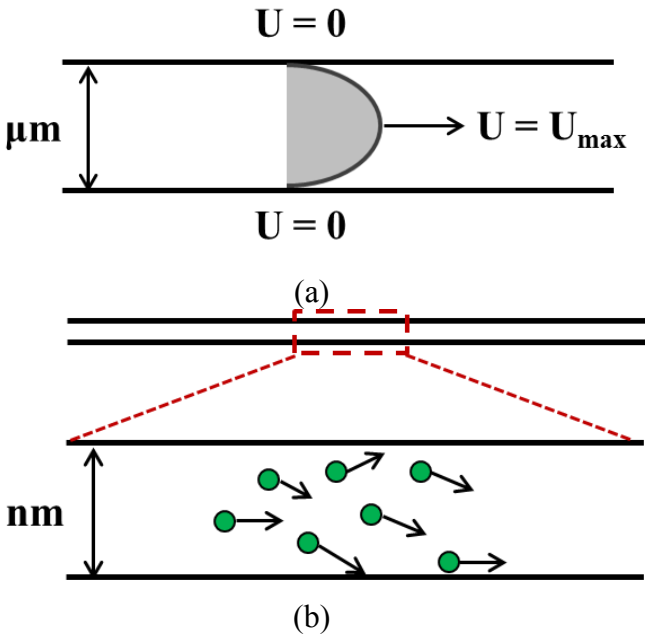

Figure 2.9: Comparison of gas flow in micropores and nanapores (modified from Javdpour et al., 2007). (a) Darcy flow in micropores. (b) Slip flow in nanopores.

2.3.2.3 Gas desorption

The continuity equation to describe gas transport in shale reservoirs by considering the gas desorption effect is given below:

$$\frac{\partial\left[\rho_g\phi+(1-\phi)\rho_a\right]}{\partial t}-\nabla\cdot\left[(1-V_a)\frac{\rho_g k(1+8\alpha K_n)}{\mu_g}\nabla p+(1-V_a)\frac{\delta}{\tau}\phi D_g\nabla\rho_g\right]=0, \quad (2.18)$$

where ρ_a is adsorbed gas mass per unit shale sample volume, V_a is pore volume fraction of adsorbed gas.

The relationship between gas density gradient and pressure gradient is given by

$$\nabla\rho_g=\rho_g c_g\nabla p, \quad (2.19)$$

where c_g is the isothermal gas compressibility factor, which can be determined as

$$c_g=\frac{1}{\rho_g}\left(\frac{\partial\rho_g}{\partial p}\right)_T. \quad (2.20)$$

Mahmoud (2014) developed a new correlation for calculating the real gas compressibility as follows:

$$c_g = \frac{c_{pr}}{p_c}, \tag{2.21}$$

$$c_{pr} = \frac{1}{p_{pr}} - \frac{1}{Z(p)}\left[\left(1.404e^{-2.5T_{pr}}\right)p_{pr} - \left(5.524e^{-2.5T_{pr}}\right)\right], \tag{2.22}$$

$$p_{pr} = \frac{p}{p_c}, \tag{2.23}$$

$$T_{pr} = \frac{T}{T_c}, \tag{2.24}$$

where p_c is the gas critical pressure, c_{pr} is the reduced gas compressibility, p_{pr} is the reduced pressure, and T_{pr} is the reduced temperature.

Expansion of the left-side term of the Eq. 2.18 results in the following expression:

$$\frac{\partial\left[\rho_g\phi + (1-\phi)\rho_a\right]}{\partial t} \approx \phi\frac{\partial\rho_g}{\partial p}\frac{\partial p}{\partial t} + (1-\phi)K_a\frac{\partial\rho_g}{\partial p}\frac{\partial p}{\partial t}, \tag{2.25}$$

where K_a is the differential equilibrium portioning coefficient of gas at a constant temperature, which is function of pressure and temperature and defined as (Cui et al., 2009; Patzek et al., 2013):

$$K_a = \left(\frac{\partial\rho_a}{\partial\rho_g}\right)_T. \tag{2.26}$$

Substituting Eqs. 2.25 and 2.26 into Eq. 2.18, the general nonlinear equation of transient gas flow in shale gas reservoirs is obtained below:

$$\begin{aligned}&\nabla\cdot\left\{(1-V_a)\left[\frac{\rho_g k(1+8\alpha K_n)}{\mu_g} + \frac{\delta}{\tau}\phi D_g\rho_g c_g\right]\nabla p\right\}\\ &= \left[\phi + (1-\phi)K_a\right]c_g\rho_g\frac{\partial p}{\partial t}.\end{aligned} \tag{2.27}$$

For the gas desorption effect, the mass balance of adsorbed gas in one unit bulk volume is described by

$$\rho_a V_b (1-\phi) = \rho_g (p_{ST},\ T_{ST})\, \rho_b V_b v, \tag{2.28}$$

where ρ_b is bulk density of shale, V_b is unit volume of bulk rock, v is the specific volume of gas adsorbed per unit mass of bulk rock (SCF/ton), which is measured at the reservoir pressure and temperature and then transferred to standard condition, $\rho_g (p_{ST},\ T_{ST})$ is the stock tank gas density. The adsorbed gas density at the standard condition can be calculated as follows:

$$\rho_a = \frac{\rho_g (p_{ST},\ T_{ST})\, \rho_b v}{1-\phi}. \tag{2.29}$$

The differential equilibrium partitioning coefficient of gas can be expressed by

$$K_a = \left(\frac{\partial \rho_a}{\partial \rho_g} \right)_T = \frac{\rho_g (p_{ST},\ T_{ST})\, \rho_b}{1-\phi} \frac{\partial v}{\partial p} \frac{\partial p}{\partial \rho_g}. \tag{2.30}$$

Substituting Eq. 2.20 into Eq. 2.30 yields

$$K_a = \left(\frac{\partial \rho_a}{\partial \rho_g} \right)_T = \frac{\rho_g (p_{ST},\ T_{ST})\, \rho_b}{(1-\phi)\, \rho_g c_g} \frac{\partial v}{\partial p}. \tag{2.31}$$

The most commonly applied gas adsorption/desorption model for shale gas reservoirs is the classic Langmuir isotherm (Langmuir, 1918), which is based on the assumption that there is a dynamic equilibrium at constant temperature and pressure between adsorbed and non-adsorbed gas. Also, it is assumed that there is only a single layer of molecules covering the solid surface, as shown in Figure 2.10(a). The Langmuir isotherm is defined by

$$v = \frac{p v_L}{p + p_L}, \tag{2.32}$$

where v_L is the Langmuir volume, referred to as the maximum gas volume of adsorption at the infinite pressure, and p_L is the Langmuir pressure, which is the pressure corresponding to one-half Langmuir volume. Instantaneous equilibrium of the sorbing surface and the storage in the pore space is assumed to be established for the Langmuir

isotherm (Freeman et al., 2012). Gao et al. (1994) demonstrated that the instantaneous equilibrium is a reasonable assumption because the ultra-low permeability in shale leads to very low gas flow rate through the kerogen component of shale.

Yu et al. (2014) found the measured methane adsorption in four samples from some area of the lower Marcellus shale is better described by the BET isotherm, rather than by the Langmuir isotherm. In 1938, Stephen Brunauer, Paul Hugh Emmett, and Edward Teller (BET) published their theory in the Journal of the American Chemical Society (Brunauer et al., 1938). The BET isotherm is a generalization of the Langmuir isotherm to multiple adsorbed layers, as shown in Figure 2.10(b). The expression is shown as follows:

$$v(p) = \frac{v_m C p}{(p_o - p)\left[1 + (C-1)\, p / p_o\right]}, \tag{2.33}$$

where p_o is the saturation pressure of the gas, v_m is the maximum adsorption gas volume when the entire adsorbent surface is being covered with a complete monomolecular layer, and C is a constant related to the net heat of adsorption, which is defined as below:

$$C = \exp\left(\frac{E_1 - E_L}{RT}\right), \tag{2.34}$$

where E_1 is the heat of adsorption for the first layer, and E_L is that for the second and higher layers and is equal to the heat of liquefaction. The assumptions in the BET model include homogeneous surface, no lateral interaction between molecules, and the uppermost layer is in equilibrium with gas phase.

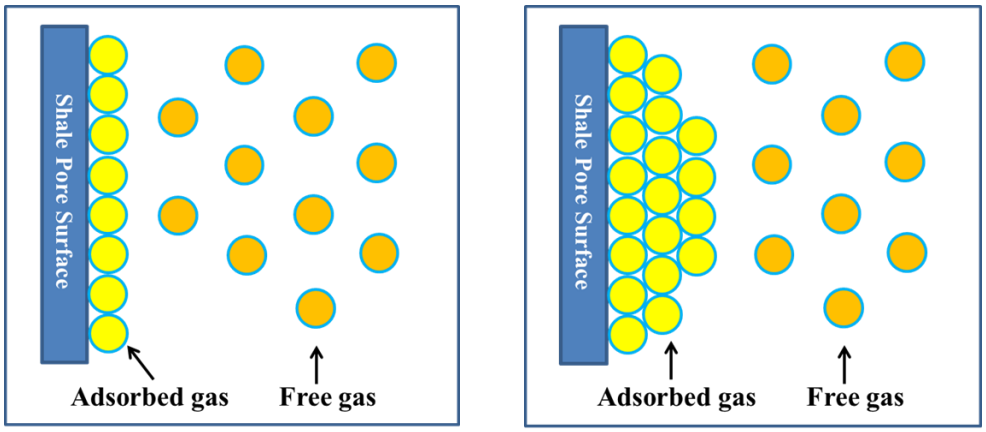

Figure 2.10: Schematic plot of monolayer and multilayer gas adsorption (Yu et al., 2014e). (a) Monolayer Langmuir adsorption. (b) Multilayer BET adsorption.

Consequently, for the Langmuir isotherm equation, the differential equilibrium partitioning coefficient of gas can be expressed as follows:

$$K_a = \left(\frac{\partial \rho_a}{\partial \rho_g}\right)_T = \frac{\rho_g\left(p_{ST},\, T_{ST}\right)\rho_b}{(1-\phi)c_g\rho_g}\frac{v_L p_L}{\left(p_L+p\right)^2} = \frac{\rho_g\left(p_{ST},\, T_{ST}\right)\rho_b}{(1-\phi)c_g\rho_g}\frac{v^2 p_L}{v_L p^2}. \tag{2.35}$$

For the BET isotherm, the differential equilibrium partitioning coefficient of gas can be expressed as

$$K_a = \left(\frac{\partial \rho_a}{\partial \rho_g}\right)_T = \frac{\rho_g\left(p_{ST},\, T_{ST}\right)\rho_b}{(1-\phi)c_g\rho_g}\frac{v^2}{Cv_m p_o}\left(\frac{p_o^{\,2}}{p^2}+C-1\right). \tag{2.36}$$

2.3.3 Continuity equation for two-phase flow in shale gas reservoirs

For two-phase flow, the gas molar concentration is defined by

$$C = \frac{S_g\rho_g}{M}. \tag{2.37}$$

The general nonlinear equation of transient gas flow in shale gas reservoirs is given by

$$\nabla\cdot\left\{\left(1-V_a\right)\left[\frac{\rho_g k_{rg} k\left(1+8\alpha K_n\right)}{\mu_g}+\frac{\delta}{\tau}\phi D_g \rho_g c_g S_g\right]\nabla p\right\}$$
$$=\left[S_g\phi+\left(1-\phi\right)K_a\right]c_g\rho_g\frac{\partial p}{\partial t}. \tag{2.38}$$

where k_{rg} is gas relative permeability.

2.3.4 Gas flow in fracture

There are two scenarios for fluid flow from fracture to the wellbore based upon the fracture conductivity value, which is defined as the product of fracture width and fracture permeability in this work. For the infinite fracture conductivity, it is often assumed that there is no pressure drop along the fracture (Gringarten et al., 1975). For the finite fracture conductivity, the pressure drop caused by fluid flow along the fracture can be modeled as one dimension for the sake of simplicity, as shown in Figure 2.11.

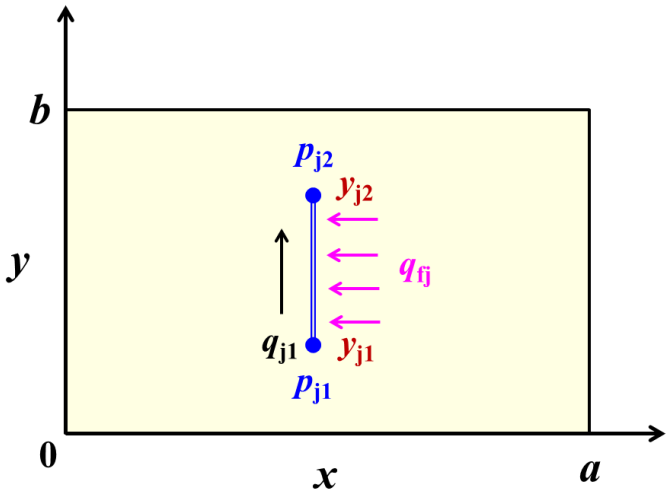

Figure 2.11: Fluid flow along single fracture for the finite fracture conductivity case.

Zhou et al. (2013) provided the expressions for calculation of pressure drop along the fracture by considering both Darcy flow and non-Darcy flow behaviors. For the

Darcy flow behavior, the pressure drop along the fracture is proportional to the fluid velocity and can be calculated by

$$p_{j1} - p_{j2} = \int_{y_{j1}}^{y_{j2}} \left(\mu \Big/ \rho k_f b_f d \right)_j \left[q_{j1} + q_{fj} \left(y - y_{j1} \right) \right] dy \,, \tag{2.39}$$

where k_f is fracture permeability, b_f is fracture width, q_{fj} is fracture flux, q_{j1} is fluid flow rate inside the fracture at one side.

For the non-Darcy flow behavior, an additional pressure drop should be taken into account due to the inertial forces as given below:

$$\begin{aligned} p_{j1} - p_{j2} &= \int_{y_{j1}}^{y_{j2}} \left(\mu \Big/ \rho k_f b_f d \right)_j \left[q_{j1} + q_{fj} \left(y - y_{j1} \right) \right] dy \\ &+ \rho\beta \int_{y_{j1}}^{y_{j2}} \left\{ \frac{\left[q_{j1} + q_{fj} \left(y - y_{j1} \right) \right]^2}{\left(\rho b_f d \right)_j^{\,2}} \right\} dy. \end{aligned} \tag{2.40}$$

where β is the non-Darcy Forchheimer coefficient, which can be determined using the correlation proposed by Evans and Civan (1994) as given below:

$$\beta = \frac{1.485 \times 10^9}{k_f^{\,1.021}}, \tag{2.41}$$

where the unit of fracture permeability k_f is md and the unit of β is ft^{-1}. This correlation was obtained based on over 180 data points including those for propped fractures and can match the data very well with the correlation coefficient of 0.974 (Rubin 2010). This correlation is implemented into the semi-analytical model to account for the non-Darcy flow behavior occurrence in hydraulic fractures.

2.3.5 Fracture width and fracture permeability calculations

When the fracture direction is parallel to the maximum horizontal stress direction, planar fracture geometry with varying fracture width will be generated, as shown in Figure 2.12. Sneddon (1951) provided an analytical solution to calculate the

corresponding fracture width distribution for the single planar fracture geometry as follows:

$$w(x)=\frac{4(1-\nu^2)\,p}{E}\left(x_f{}^2-x^2\right), \tag{2.42}$$

where w is fracture width, ν is Possion ratio, E is Young's modulus, p is the constant net pressure, and x_f is fracture half-length.

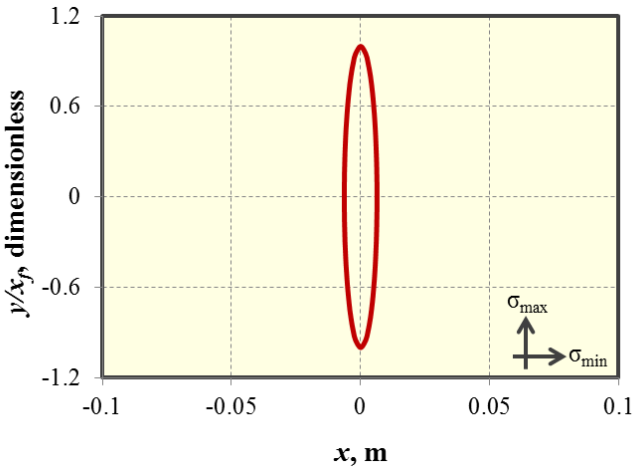

Figure 2.12: Single planar fracture geometry with varying fracture width along the fracture length.

If the fracture direction or the well orientation does not coincide with the maximum horizontal stress direction, a curving non-planar fracture with fracture width restriction near the wellbore will be generated, as shown in Figure 2.13. The corresponding fracture width distribution is calculated using the complex fracture propagation model, which is developed by Wu (2014). However, the complex fracture propagation model is beyond the scope of this study. More details can be found by the work of Wu (2014).

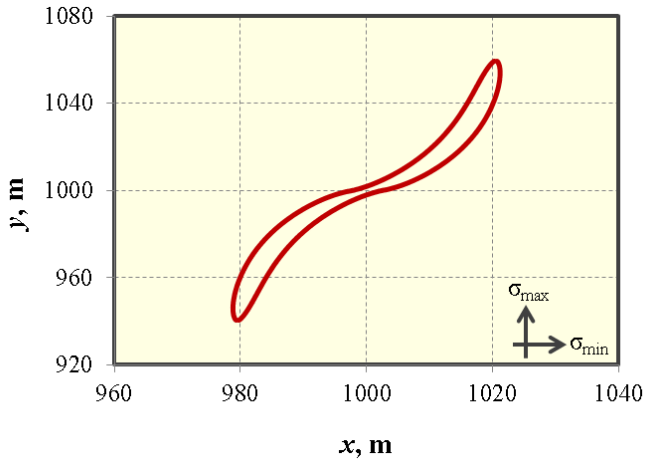

Figure 2.13: Single curving non-planar fracture with fracture width restriction near the wellbore.

Fracture permeability corresponding to fracture width without considering the proppant effect can be calculated by the following expression (Witherspon et al., 1980):

$$k_f = \frac{w_f^{\,2}}{12}, \tag{2.43}$$

where the unit of fracture permeability k_f is cm^2 and the unit of fracture width w_f is cm. In order to consider the effect of proppant inside the fracture, a coefficient multiplied by the Eq. 2.43 is used in this study.

2.3.6 Geomechanics effect

In this study, the geomechanics effect is primarily focused on stress-dependent fracture conductivity, meaning that fracture conductivity is not a constant value, but decreases with the increasing closure pressure due to proppant embedment (see Figure 2.14). Alramahi and Sundberg (2012) presented the laboratory measurement data about the relationship between normalized fracture conductivity and closure pressure due to proppant embedment for different shale samples from stiff shale to soft shale, as shown in Figure 2.15. Through fitting the laboratory measurement data, the expressions between

normalized fracture conductivity and closure pressure are obtained below (Yu and Sepehrnoori, 2014d):

$$\text{Stiff Shale:}\quad \log(FC) = -0.0001\times\sigma - 0.1082, R^2 = 0.954, \tag{2.44}$$

$$\text{Medium Shale:}\quad \log(FC) = -0.0004\times\sigma + 0.2191, R^2 = 0.998, \tag{2.45}$$

$$\text{Soft Shale:}\quad \log(FC) = -0.0006\times\sigma - 0.4256, R^2 = 0.987, \tag{2.46}$$

where FC is fracture conductivity (fracture permeability multiplied by fracture width, md-ft), and σ is closure pressure (psi). It should be noted that these expressions are only suitable for planar hydraulic fractures. As shown in Figure 2.15, the magnitude of normalized fracture conductivity loss at the highest closure stress (10,000 psi) is about 1, 3.5, and 6 for the still shale, medium shale, and soft shale, respectively.

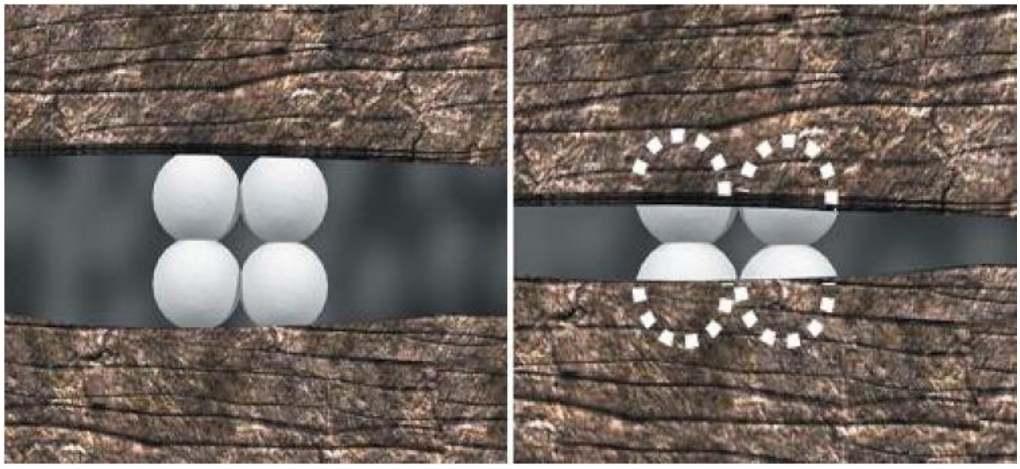

Figure 2.14: Proppant embedment into the fracture faces resulting in a decrease of fracture width and conductivity (after Terracina et al., 2010).

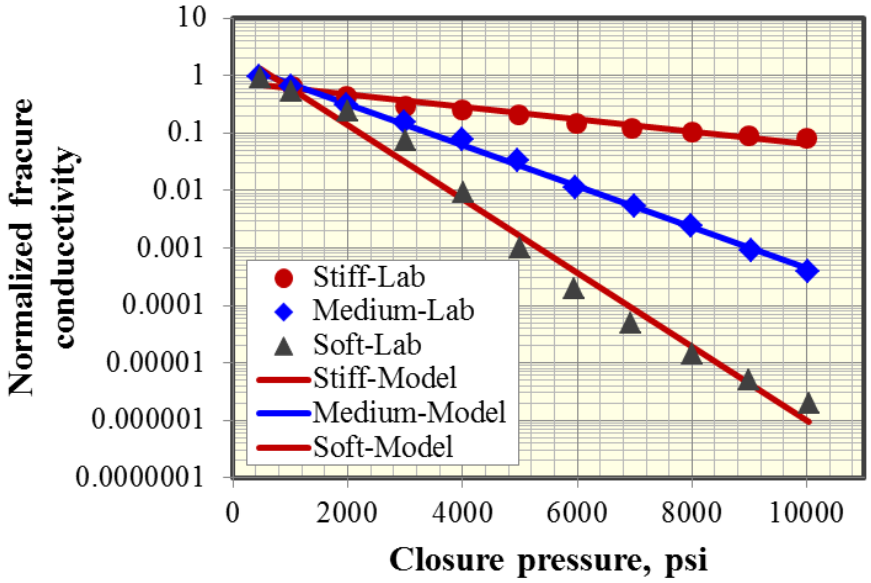

Figure 2.15: The relationship between normalized fracture conductivity and closure pressure for different shale samples.

2.4 MODEL DEVELOPMENT FOR TIGHT OIL SIMULATION

In comparison with the model development in shale gas simulation, the flow mechanisms such as gas slippage, diffusion, and desorption are not considered for the model development in tight oil simulation. The unsteady-state oil flow from tight formation to fracture can be described by the diffusivity equation without considering the source terms below (Thambynayagam, 2011):

$$\eta_x \frac{\partial^2 p}{\partial x^2} + \eta_y \frac{\partial^2 p}{\partial y^2} + \eta_z \frac{\partial^2 p}{\partial z^2} = \frac{\partial p}{\partial t}, \tag{2.47}$$

where p is pressure, η is the hydraulic diffusivity coefficient, which is defined as:

$$\eta_j = \frac{k}{\phi c_t \mu}, \tag{2.48}$$

where k is permeability, ϕ is porosity, c_t is total compressibility of the system, and μ is viscosity.

For oil flow in fracture, the pressure drop along the fracture satisfies the Darcy flow behavior, which can be calculated using Eq. 2.39.

2.5 MODEL UNKNOWNS AND GOVERNING EQUATIONS

Two well simulation constraints including constant flow rate and constant bottom hole pressure (BHP) are considered in the semi-analytical model. For the constant flow rate constraint, all unknown variables with assumptions of N_f fracture segments and N_v nodes ($N_v = N_f + 1$) are listed below (Zhou et al., 2013):

(1) N_f fluid flow rate inside the fracture at one side, $q_{j1}, j = 1 \cdots N_f$.

(2) N_f flux of fracture segment, $q_{fj}, j = 1 \cdots N_f$.

(3) N_v pressure at each node, $p_j, j = 1 \cdots N_v$.

These unknown variables can be represented by the following vector form:

$$x^T = \left[q_{11}, q_{21} \cdots q_{Nf1},\ q_{f1}, q_{f2} \cdots q_{fNf},\ p_1, p_2 \cdots p_{Nv} \right]. \tag{2.49}$$

For the constant BHP constraint, all unknown variables are listed in the following:

(1) N_v fluid flow rate including N_f flow rate inside the fracture at one side, $q_{j1}, j = 1 \cdots N_v$.

(2) N_f flux of fracture segment, $q_{fj}, j = 1 \cdots N_f$.

(3) N_f pressure at each node with known pressure of the well node, $p_j, j = 1 \cdots N_f$.

These unknown variables can be represented by the following vector form:

$$x^T = \left[q_{11}, q_{21} \cdots q_{Nv1},\ q_{f1}, q_{f2} \cdots q_{fNf},\ p_1, p_2 \cdots p_{Nf} \right]. \tag{2.50}$$

Hence, the total number of unknowns is $2N_f + N_v$ for both well simulation constraints. The associated number of governing equations also includes $2N_f + N_v$, which are described below:

(1) N_v mass balance equations at each node. Actually, the mass balance is satisfied for each intersection point of fracture segments. It is convenient to assume that fluid flow

is under steady-state inside the fracture and there is no flow storage effect so that the inflow is equal to outflow for each intersection node of fracture segments (Zhou et al., 2013). It can be expressed as follows:

$$\left(q_i\right)_{\text{inflow}} = \left(q_i\right)_{\text{outflow}}, \; i = 1 \cdots N_v. \tag{2.51}$$

(2) N_f pressure drop equations for each fracture segment (Eq. 2.39 for Darcy flow effect or Eq. 2.40 for non-Darcy flow effect).

(3) N_f pressure solutions at the center of each fracture segment, which combines fluid flow in shale and fluid flow in fracture, as shown in Figure 2.16. The integral transform technique or Green's function method can be used to solve the unsteady-state diffusivity equations analytically with the assumptions of homogeneous reservoir and slightly compressible fluid (Gringarten et al., 1972; Gringarten and Rameny, 1973). Thambynayagam (2011) provides many analytical solutions of this unsteady-state diffusivity equation for different initial and boundary conditions. Additionally, Zhou et al. (2013) presented a plane-source solution for describing fluid flow into single fracture segment with an inclination angle of θ (see Figure 2.17). The corrected version of the original solution is shown as follows:

$$p\left(x,y,z,t\right) = \frac{U\left(t-t_0\right)}{4\phi c_t ab}\int_0^t q_j\left(t-t_0-\tau\right)G_j\left(x,y,z,\tau\right)\,d\tau\,, \tag{2.52}$$

where q_j is the flux of fracture segment, $U\left(t-t_0\right) = \begin{cases} 0, & t < t_0 \\ 1, & t > t_0 \end{cases}$ is the Heaviside's unit step function, $G_j\left(x,y,z,\tau\right)$ is the instantaneous plane source solution of the j^{th} fracture segment, which can be described below:

$$
\begin{aligned}
&G_j(x,y,z,\tau)= \\
&\int_0^{x_{j2}-x_{j1}}\left[\Theta_3\left\{\frac{\pi\left[x-\left(x_{j1}+\bar{x}\right)\right]}{2a},e^{-\left(\frac{\pi}{a}\right)^2\eta_x\tau}\right\}+\Theta_3\left\{\frac{\pi\left[x+\left(x_{j1}+\bar{x}\right)\right]}{2a},e^{-\left(\frac{\pi}{a}\right)^2\eta_x\tau}\right\}\right] \\
&\times\left[\Theta_3\left\{\frac{\pi\left[y+\left(y_{j1}+\bar{x}\tan\theta_j\right)\right]}{2b},e^{-\left(\frac{\pi}{b}\right)^2\eta_y\tau}\right\}+\Theta_3\left\{\frac{\pi\left[y-\left(y_{j1}+\bar{x}\tan\theta_j\right)\right]}{2b},e^{-\left(\frac{\pi}{b}\right)^2\eta_y\tau}\right\}\right] \\
&\times\left[2\Theta_3^{\int}\left\{\frac{\pi z}{2d},e^{-\left(\frac{\pi}{d}\right)^2\eta_z\tau}\right\}+\Theta_3^{\int}\left\{\frac{\pi[z-d]}{2d},e^{-\left(\frac{\pi}{d}\right)^2\eta_z\tau}\right\}+\Theta_3^{\int}\left\{\frac{\pi[z+d]}{2d},e^{-\left(\frac{\pi}{d}\right)^2\eta_z\tau}\right\}\right]d\bar{x},
\end{aligned}
\tag{2.53}
$$

where a, b, and d represent reservoir length, width, and height, respectively, $\bar{x}$ is the integration variable, η_x, η_y, η_z are hydraulic diffusivities in x, y, z direction, respectively, which are defined as $\eta_i = k_i / \phi\mu c_t$, $i = x, y, z$, Θ_3 is the elliptic theta function of the third kind and $\Theta_3^{\int}$ is the integral of the elliptic theta function of the third kind, which are defined below. More details can be found elsewhere (Bellman, 1961; Thambynayagam, 2011).

$$
\begin{aligned}
&\Theta_3\left(\pi X, e^{-2\pi^2 T}\right) \\
&=\begin{cases}
1+2\sum_{n=1}^{\infty}e^{-n^2\pi^2 T}\cos(2n\pi X), & e^{-2\pi^2 T}<\dfrac{1}{\pi} \\
\dfrac{1}{\sqrt{\pi T}}\sum_{n=-\infty}^{+\infty}e^{-\frac{(X+n)^2}{T}}, & e^{-2\pi^2 T}\geq\dfrac{1}{\pi}
\end{cases},
\end{aligned}
\tag{2.54}
$$

$$
\begin{aligned}
&\Theta_3^{\int}\left(\pi X, e^{-2\pi^2 T}\right)=\int_0^X\Theta_3\left(\pi X', e^{-2\pi^2 T}\right)dX' \\
&=\begin{cases}
X+\dfrac{1}{\pi}\sum_{n=1}^{\infty}\dfrac{e^{-n^2\pi^2 T}}{n}\sin(2n\pi X), & e^{-2\pi^2 T}<\dfrac{1}{\pi} \\
\dfrac{1}{2}\sum_{n=-\infty}^{+\infty}\left[erf\left(\dfrac{X+n}{\sqrt{T}}\right)-erf\left(\dfrac{n}{\sqrt{T}}\right)\right], & e^{-2\pi^2 T}\geq\dfrac{1}{\pi}
\end{cases},
\end{aligned}
\tag{2.55}
$$

where the error function is defined by

$$
erf(X)=\frac{2}{\sqrt{\pi}}\int_0^X e^{-X'^2}dX'. \tag{2.56}
$$

According to the superposition principle, the pressure change at any location in the system can be calculated by adding the contributions from all N_f fracture segments as follows (Zhou et al., 2013):

$$p(x,y,z,t)=\frac{U(t-t_0)}{4\phi c_t ab}\sum_{j=1}^{N_f}\int_0^t q_j(t-t_0-\tau)G_j(x,y,z,\tau)\,d\tau\,. \tag{2.57}$$

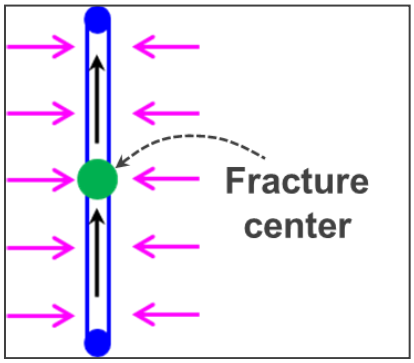

Figure 2.16: Fracture center for each segment, which combines fluid flow in shale and fluid flow in fracture.

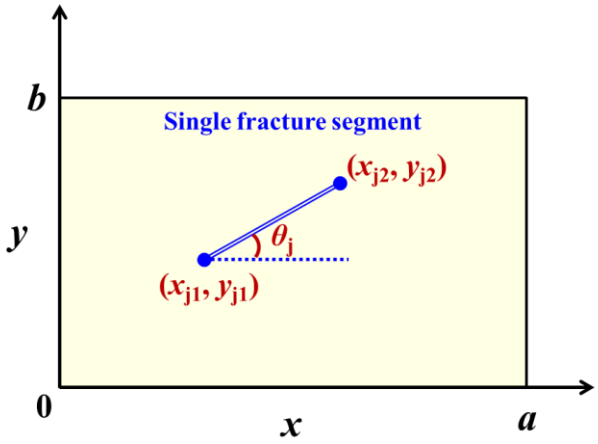

Figure 2.17: Single fracture segment with an inclination angle of θ.

The pressure solution at the center of each segment for fluid flow in shale can be calculated using the following expression:

$$p_{jc} = \frac{U(t-t_0)}{4\phi c_t ab} \sum_{j=1}^{N_f} \int_0^t q_j(t-t_0-\tau) G_j(x,y,z,\tau)\, d\tau \,. \tag{2.58}$$

The pressure solution at the center of each segment for fluid flow in fracture can be calculated using the following expression under the condition of Darcy flow behavior:

$$p_{jc} = p_{j1} - \int_{y_{j1}}^{y_{j2}} \left(\mu \Big/ \rho k_f b_f d \right)_j \left[q_{j1} + q_{fj}(y - y_{j1}) \right] dy \,. \tag{2.59}$$

Under the condition of non-Darcy flow behavior, the expression is below:

$$\begin{aligned} p_{jc} &= p_{j1} - \int_{y_{j1}}^{y_{j2}} \left(\mu \Big/ \rho k_f b_f d \right)_j \times \left[q_{j1} + q_{fj}(y - y_{j1}) \right] dy \\ &+ \rho\beta \int_{y_{j1}}^{y_{j2}} \left\{ \frac{\left[q_{j1} + q_{fj}(y - y_{j1}) \right]^2}{\left(\rho b_f d \right)_j^2} \right\} dy. \end{aligned} \tag{2.60}$$

Finally, the pressure solution at center of each segment can be obtained by combining Eq. 2.58 with Eq. 2.59 for Darcy flow effect and combining Eq. 2.58 with Eq. 2.60 for non-Darcy flow effect. Due to the non-Darcy flow effect, the final system of equations is non-linear.

2.6 MODEL SOLUTION

This semi-analytical model is capable of simulating not only oil flow but also gas flow in shale formation. In case of gas flow, the non-Darcy effect is significant, leading to the nonlinearity of the transport equation. Hence, the Newton-Raphson iterative method is employed to solve the above system of equations. This method can effectively and efficiently solve the non-linear problems if a good initial guess is given. In this study, the solution by considering Darcy flow behavior is used for the initial guess. The expression for this method is given by

$$Jdx = -F(x)\,, \tag{2.61}$$

$$x_{k+1} = x_k + dx\,, \tag{2.62}$$

where x_k is the solution at the k iteration, x_{k+1} is the solution at the k+1 iteration, dx is the incremental solution, $F(x)$ is the residual term, which consists of Eqs. 2.39, 2.40, 2.51, 2.58, 2.59, and 2.60, J is the Jacobian matrix, which is defined as follows:

$$J = \frac{\partial F(x_k)}{\partial x}. \tag{2.63}$$

Figure 2.18 shows the flowchart for the detailed calculation procedure based on the Newton-Raphson iteration method.

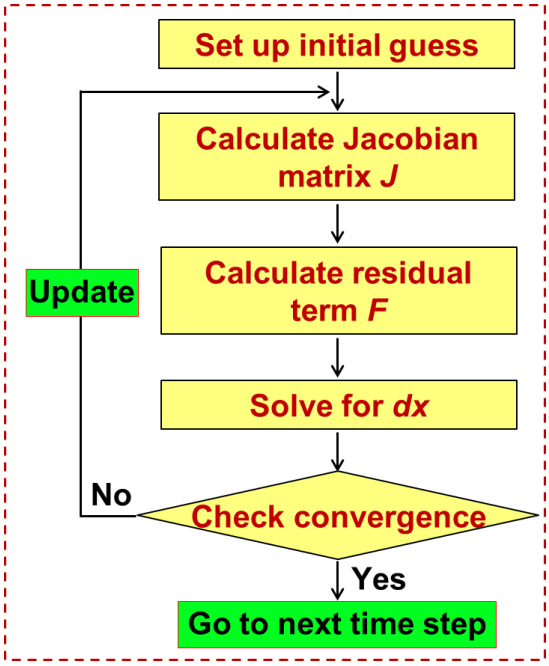

Figure 2.18: Flowchart for the calculation procedure.

2.7 MODEL VERIFICATION FOR SHALE GAS RESERVOIRS

2.7.1 Single rectangular fracture

A case study with single rectangular fracture was performed with the purpose of validating this semi-analytical model with a numerical reservoir simulator of CMG-GEM (CMG-GEM, 2012). Local grid refinement (LGR) method was utilized to model gas flow from matrix to fracture. The basic reservoir and fracture parameters used for the

simulations are summarized in Table 2.1. The reservoir is assumed to be homogeneous with only gas flow under the condition of residual water saturation. The value for BHP was held at 2,000 psi for all simulations. Fracture height is assumed to be equal to the formation thickness. The fracture width is fixed at 0.01 ft. The single fracture is divided into 20 segments with 35 ft for each segment, as shown in Figure 2.19. The gas properties for the input of the semi-analytical model are provided in Table 2.2, which is also used in the following simulation studies with the semi-analytical model.

Parameter	Value	Unit
Initial reservoir pressure	4,300	psi
Reservoir temperature	130	^{o}F
Reservoir permeability	800	nD
Reservoir porosity	12%	
Initial gas saturation	90%	
Gas gravity	0.58	
Total compressibility	10^{-6}	psi^{-1}
Fracture half-length	350	ft
Fracture conductivity	100	md-ft
Fracture height	100	ft

Table 2.1: Basic reservoir and fracture parameters used for the simulations.

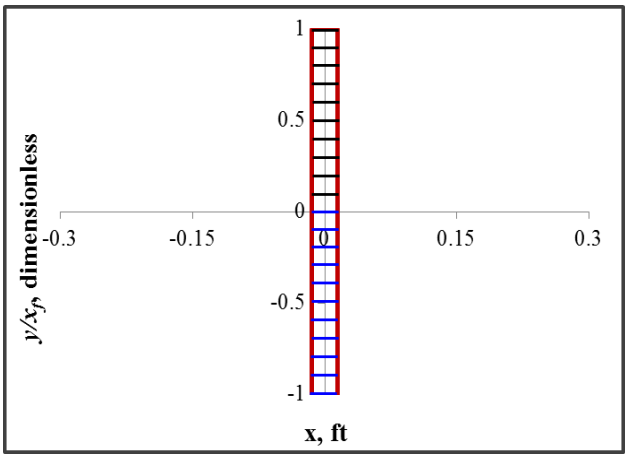

Figure 2.19: Single rectangular fracture geometry with 20 fracture segments.

Pressure, psi	Z-factor	Viscosity, cp	Density, g/cm^3
400	0.9599122	0.012790382	0.017741927
800	0.923723002	0.013324169	0.036874024
1200	0.893348224	0.014037685	0.05719167
1600	0.870786442	0.01492097	0.078231315
2000	0.857501402	0.015953252	0.099304165
2400	0.853847447	0.017098835	0.119674953
2800	0.859037099	0.018315144	0.138777296
3200	0.871632523	0.019563124	0.156310755
3600	0.89009075	0.020812726	0.172202924
4000	0.913065374	0.022043338	0.186522156
4400	0.939486444	0.023242019	0.199404276
4800	0.968535448	0.02440143	0.211007565
5000	0.98384549	0.024965214	0.216379152

Table 2.2: Gas properties for the input of the semi-analytical model.

2.7.2.1 Non-Darcy flow effect

The coefficient defined by Eq. 2.41 is used to describe the non-Darcy flow effect. The fracture width is fixed at 0.0001 ft. The comparison of gas flow rate between this model and numerical model is shown in Figure 2.20, illustrating that an extremely good match is obtained. Figure 2.21 shows the comparison of cumulative gas production between Darcy flow effect and non-Darcy flow effect. As shown, the gas recovery with the non-Darcy flow effect at 1,000 days of production declines by 6% compared to that with the Darcy flow effect.

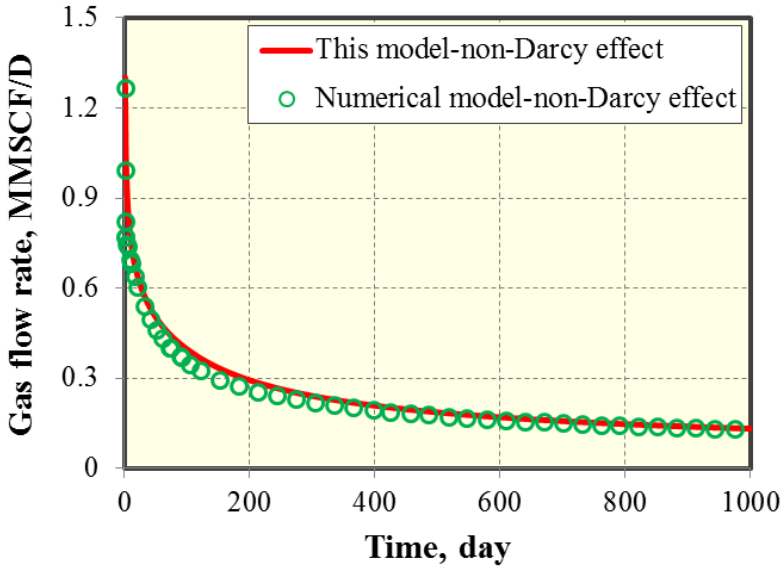

Figure 2.20: Comparison of gas flow rate by considering the non-Darcy flow effect between this model and numerical model.

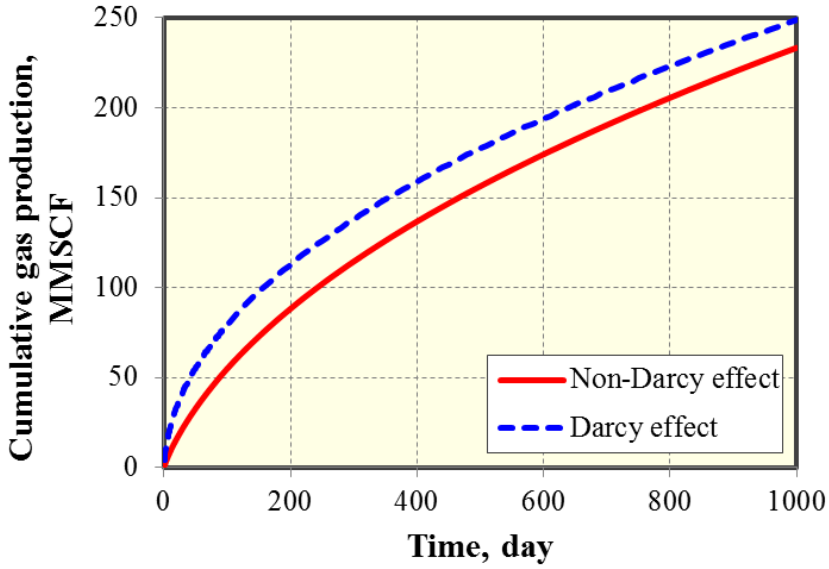

Figure 2.21: Comparison of cumulative gas production between Darcy flow effect and non-Darcy flow effect.

2.7.2.2 Gas desorption effect

The Langmuir desorption model with Langmuir pressure of 535 psi, Langmuir volume of 196.4 scf/ton, and bulk density of 2.52 g/cm^3 is used for verification. The comparison of gas flow rate between this model and numerical model by considering the gas desorption effect is shown in Figure 2.22, illustrating that an excellent match is obtained. Figure 2.23 shows the effect of gas desorption on cumulative gas production. As shown, the gas desorption effect contributes to around 5% increase of gas recovery at end of production (1,000 days).

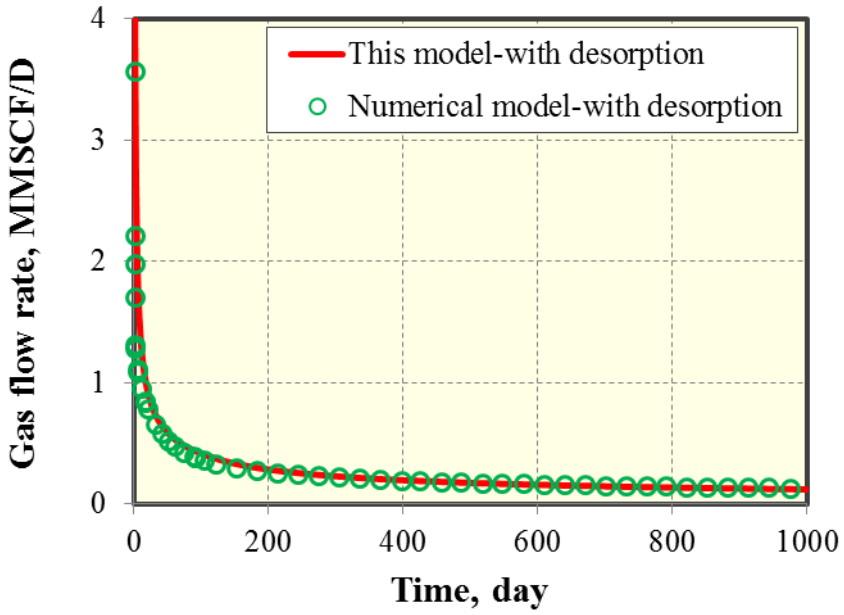

Figure 2.22: Comparison of gas flow rate by considering the gas desorption effect between this model and numerical model.

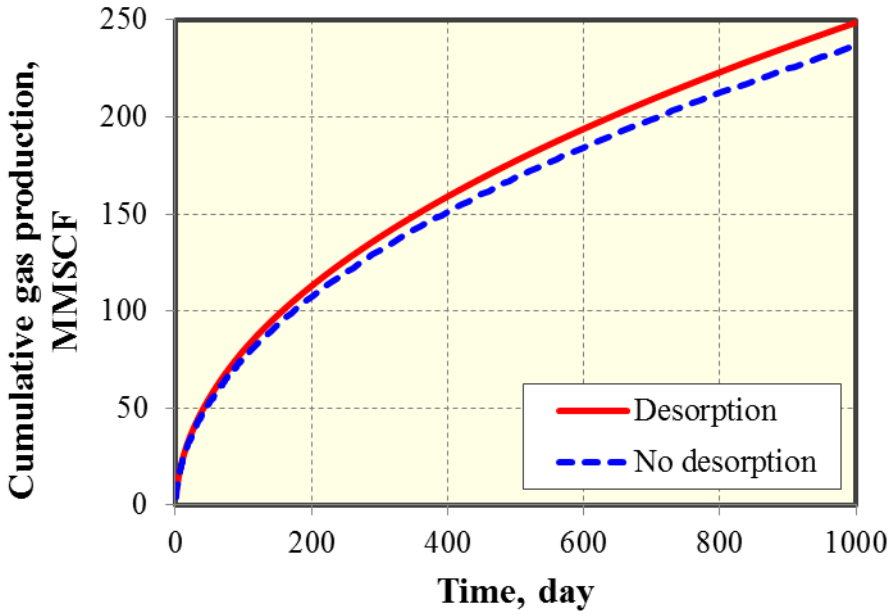

Figure 2.23: Effect of gas desorption on cumulative gas production.

2.7.2.3 Geomechanics effect

In this case study, the stiff shale case was selected to investigate the impact of geomechanics on well performance. Using Eq. 2.44 and assuming the minimum horizontal stress of 5,473 psi, the stress-dependent fracture conductivity curve was generated, as shown in Figure 2.24. It illustrates that the final fracture conductivity will reduce to 46% of initial fracture conductivity corresponding to the BHP of 2,000 psi.

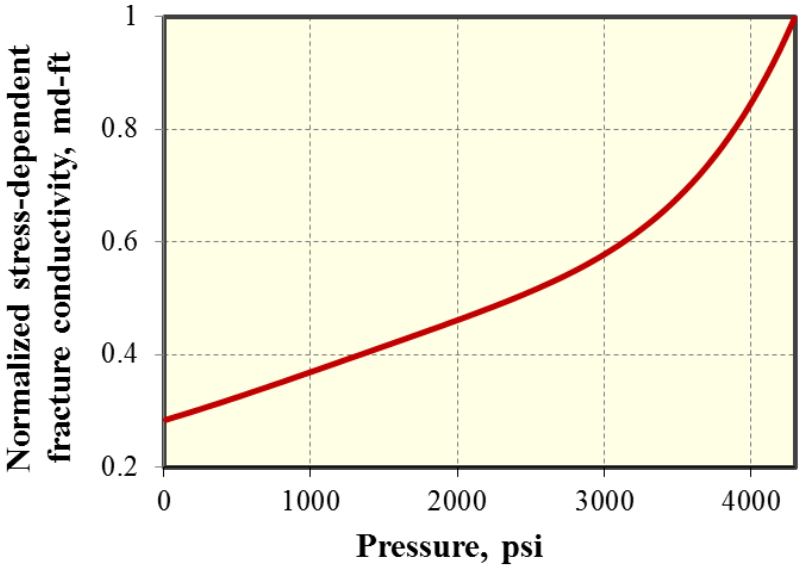

Figure 2.24: Stress-dependent fracture conductivity curve used for this case study.

The comparison of gas flow rate between this model and numerical model by considering the geomechanics effect is shown in Figure 2.25, illustrating that a good match is obtained. Figures 2.26 and 2.27 show the effect of geomechanics on cumulative gas production with initial fracture conductivity of 100 md-ft and 5 md-ft, respectively. As shown, the geomechanics effect reduces the gas recovery at end of production (1,000 days) by 0.5% for the initial fracture conductivity of 100 md-ft, while 13% for the initial fracture conductivity of 5 md-ft. It suggests that the geomechanics effect is important when the fracture conductivity is small.

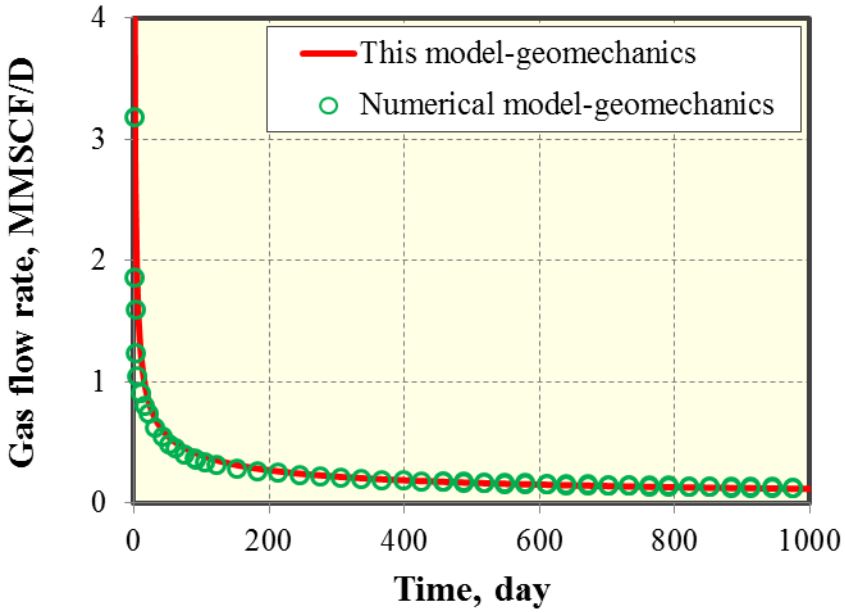

Figure 2.25: Comparison of gas flow rate by considering the geomechanics effect between this model and numerical model.

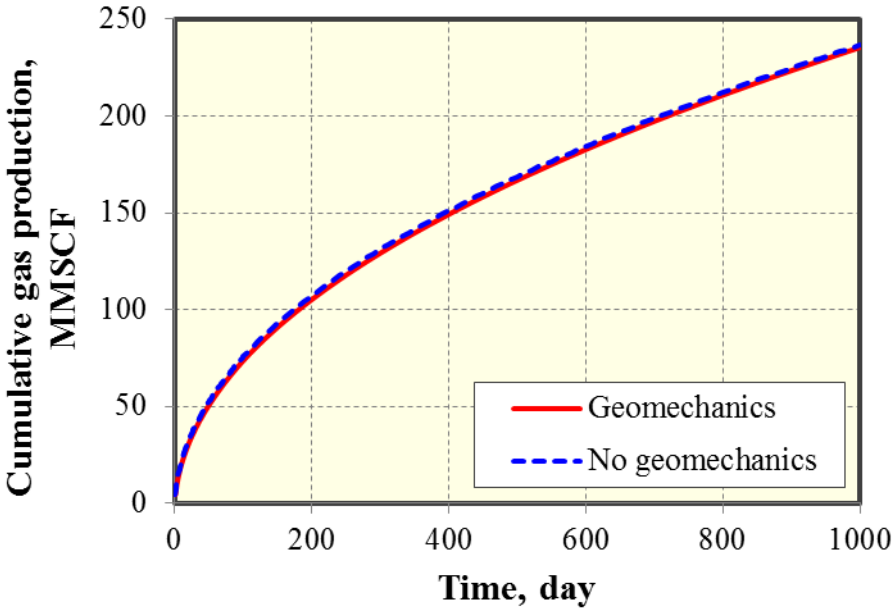

Figure 2.26: Effect of geomechanics on cumulative gas production with initial fracture conductivity of 100 md-ft.

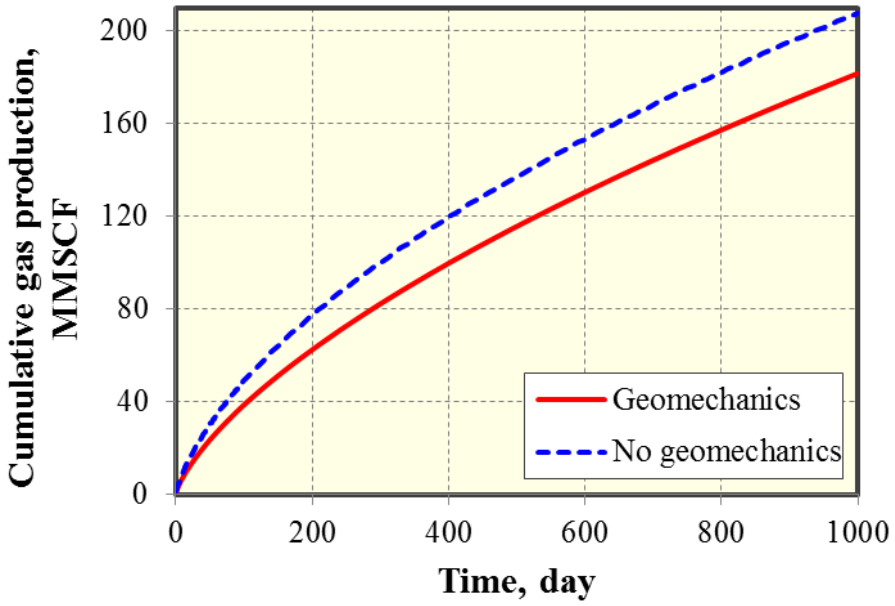

Figure 2.27: Effect of geomechanics on cumulative gas production with initial fracture conductivity of 5 md-ft.

2.7.2.4 Effect of fracture conductivity

The effect of fracture conductivity on cumulative gas production was studied and shown in Figure 2.28, illustrating that the trend of increase in gas recovery with time decreases with the increasing fracture conductivity. In addition, the gas recovery of the fracture conductivity of 100 md-ft approaches that of 500 md-ft. Hence, it can be suggested that the 100 md-ft is very close to the infinite fracture conductivity in this case study.

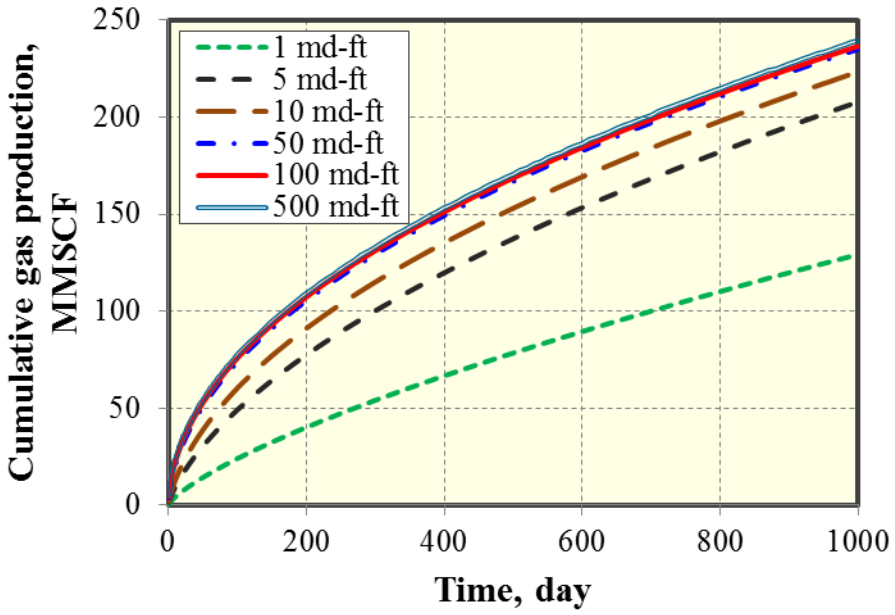

Figure 2.28: Effect of fracture conductivity on cumulative gas production.

2.7.2.5 Effect of number of fracture segment

If the fracture is divided into more segments, the simulation results will be more accurate. However, the computation will be more time-consuming. Hence, there is a tradeoff between them. In this case study, the effect of number of fracture segments on cumulative gas production was studied and shown in Figure 2.29, illustrating that 14 fracture segments with 50 ft for each one is very close to the real solution. Also, the computational time for this case with 14 fracture segments is about 5 minutes. It suggests that the length for each fracture segment, which is less than 50 ft, is good enough to obtain accurate results.

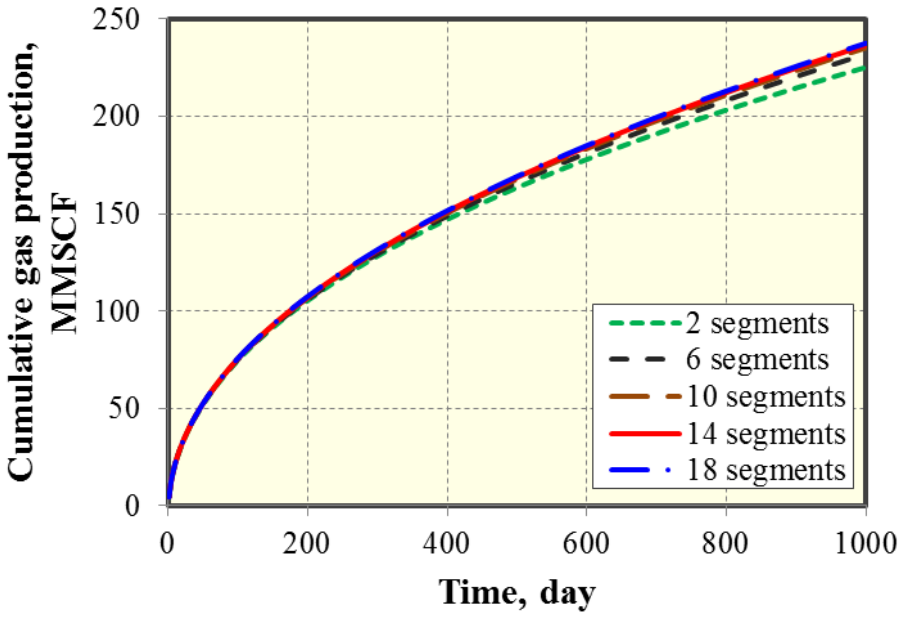

Figure 2.29: Effect of number of fracture segment on cumulative gas production.

2.7.2 Single planar fracture with varying width

For a single planar fracture with varying fracture width, as shown in Figure 2.30, Eq. 2.42 is used to calculate fracture width distribution by assuming the maximum fracture width of 0.0416 ft (0.5 inch) at center of the fracture and fracture half-length of 350 ft. The average fracture width is calculated as 0.03 ft based on the same fracture area in the x-y coordinate plane. For the constant fracture width case, the fracture permeability is 71 md and the fracture conductivity is 2.2 md-ft, which is far away from the infinite fracture conductivity. For the planar fracture with varying width, the fracture was also divided equally into 20 segments to approximately represent the real elliptical fracture shape in the x-y coordinate plane. In the numerical model, each segment with different fracture width was modeled explicitly using LGR approach and the corresponding fracture grids are set up with different fracture permeabilities. Hence, the actual length for each fracture segment is 35 ft, which is adequate to guarantee the simulation

accuracy. The fracture width and fracture permeability distribution along the fracture half-length in one wing is shown in Figure 2.31. Comparison of gas flow rate between this model and numerical model by considering non-Darcy flow effect is shown in Figure 2.32. As shown, an excellent agreement between this model and numerical model is obtained, illustrating that this model can have a capability to simulate production from the planar fracture geometry with varying fracture width and fracture permeability. Figure 2.33 presents the pressure distribution at end of production, clearly showing the drainage area.

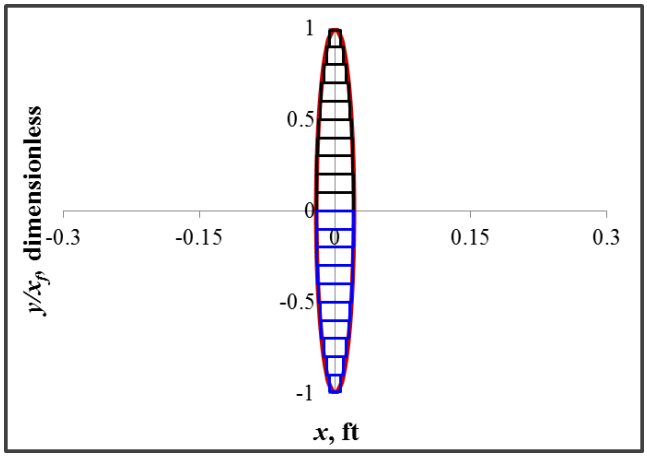

Figure 2.30: Single planar fracture geometry with varying fracture width.

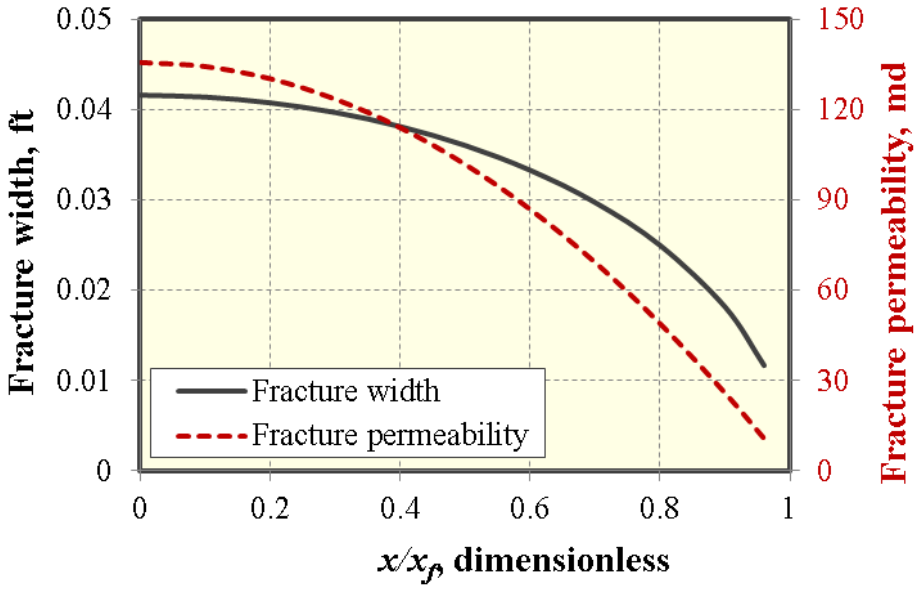

Figure 2.31: Fracture width and fracture permeability distribution along fracture half-length.

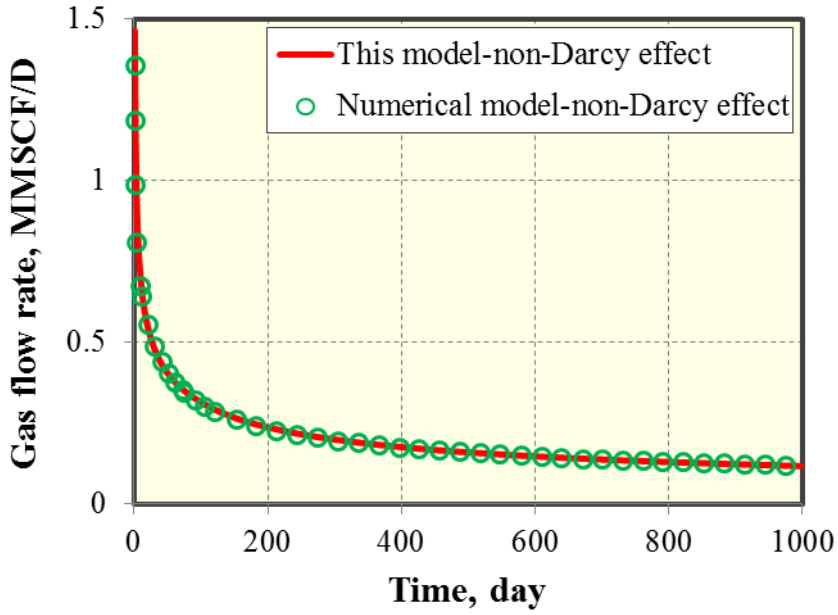

Figure 2.32: Comparison of cumulative gas production by considering non-Darcy flow effect between this model and numerical model.

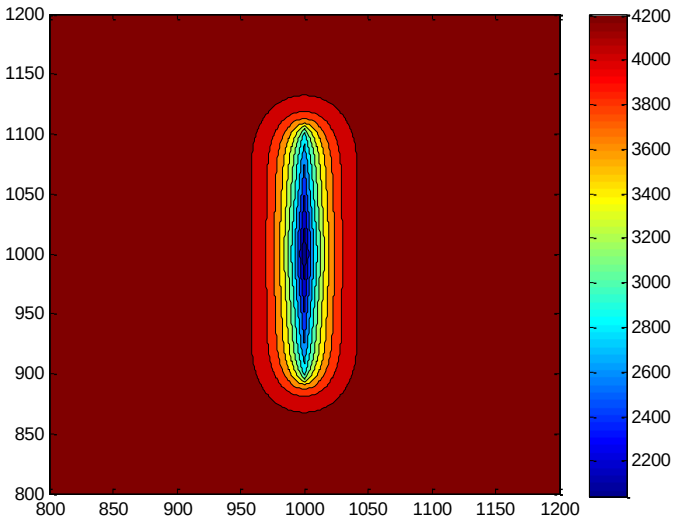

Figure 2.33: Pressure distribution at end of production for single planar fracture with varying width (pressure unit: psi).

Figure 2.34 shows the comparison of cumulative gas production between single rectangular fracture and single planar fracture with varying width. It can be seen that the planar fracture with varying width can produce more than 16% of gas recovery compared to that of single rectangular fracture.

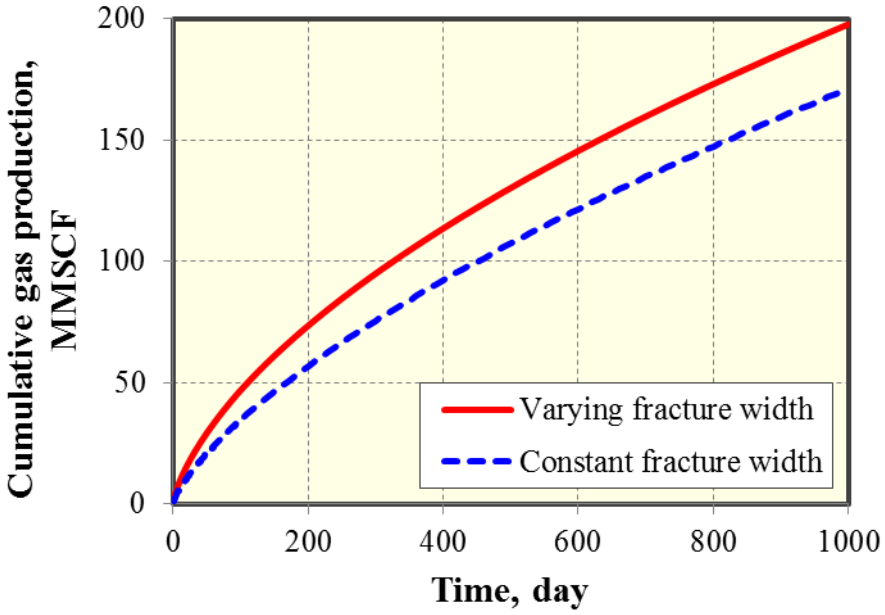

Figure 2.34: Comparison of cumulative gas production between single rectangular fracture and single planar fracture with varying width.

In addition, the fracture permeability was increased for both fracture geometries, as shown in Figure 2.35. For the rectangular fracture, the fracture conductivity is 100 md-ft, which is close to the infinite fracture conductivity. The comparison of gas recovery between these two fracture geometries under high fracture permeability is shown in Figure 2.36, illustrating that these is no big difference between them. Hence, it can be concluded that the difference between the rectangular fracture geometry and the planar fracture geometry with varying width decreases with the increasing fracture conductivity and will become negligible at the infinite fracture conductivity.

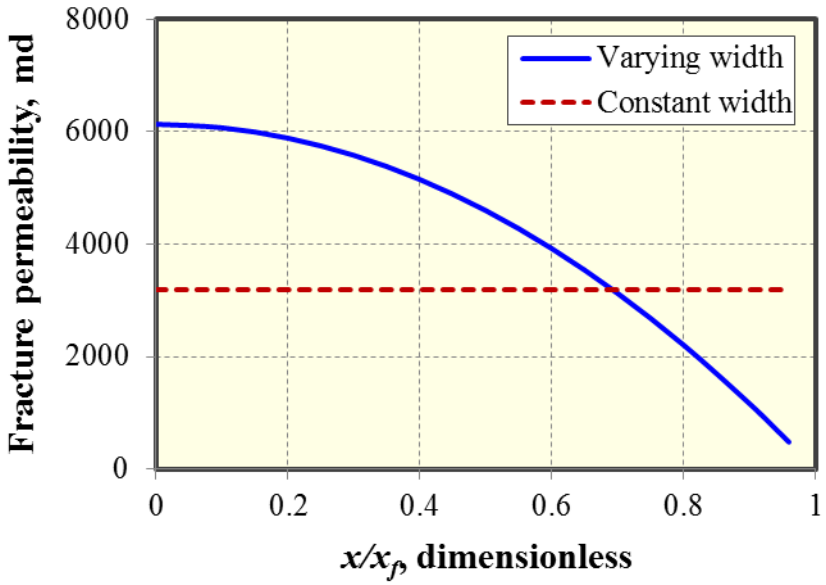

Figure 2.35: Fracture permeability distribution for single rectangular fracture and planar fracture with varying width under high fracture permeability.

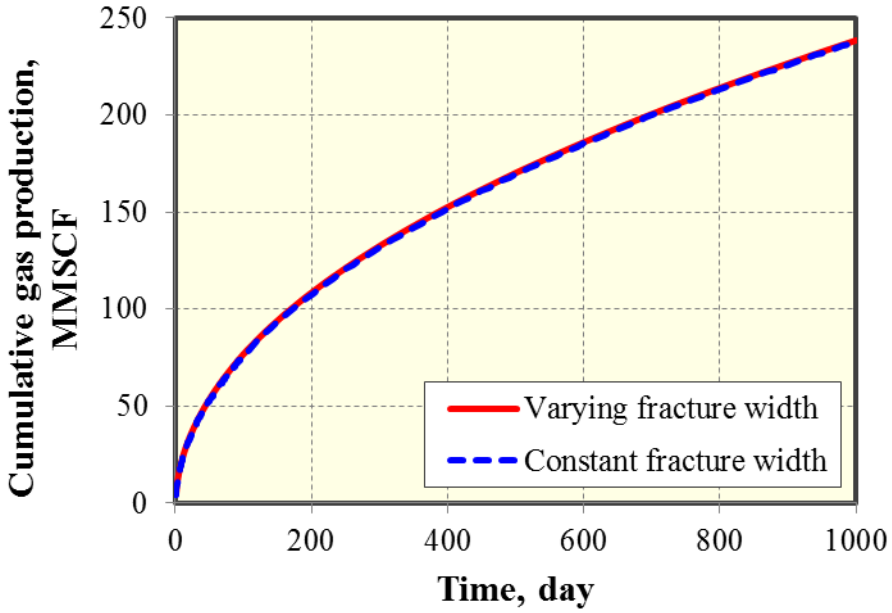

Figure 2.36: Comparison of cumulative gas production between single rectangular fracture and single planar fracture with varying width under high fracture permeability.

2.7.3 Multiple rectangular fractures

In addition to verification of the single hydraulic fracture, we also compared multiple hydraulic fractures results with the results generated using CMG-GEM by considering fracture interference during gas production. In this case study, three hydraulic fractures with an even fracture spacing of 100 ft were simulated. Fracture half-length of two outer fractures is 350 ft and fracture half-length of inner fracture is 250 ft. Fracture conductivity is 100 md-ft. The other parameters used in the simulations are the same as those in Table 2.1. The comparison of well performance between this model and numerical model is shown in Figure 2.37, illustrating that a good agreement is obtained. It is implied that the production interference between multiple fractures is well considered in the semi-analytical model. Figure 2.38 shows the pressure distribution at 1,000 days of production. The drainage area is clearly demonstrated.

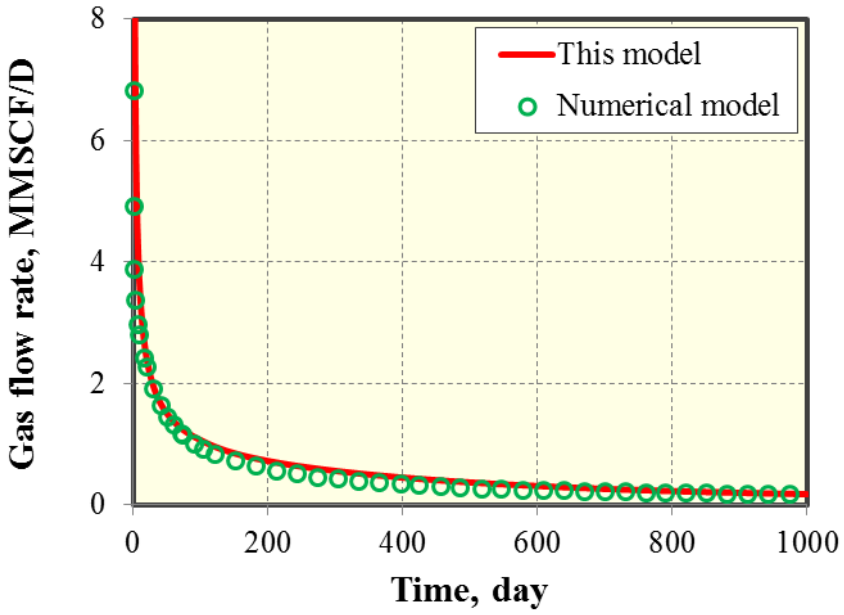

Figure 2.37: Comparison of cumulative gas production between this model and numerical model.

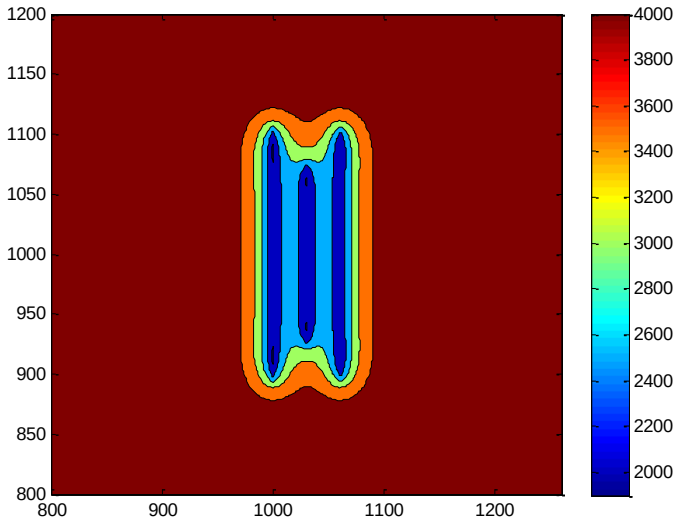

Figure 2.38: Pressure distribution at end of production (pressure unit: psi).

2.8 MODEL VERIFICATION FOR TIGHT OIL RESERVOIRS

2.8.1 Single rectangular fracture

We verified this semi-analytical model against the work by Zhou et al. (2013) for single rectangular fracture geometry and the numerical reservoir simulator under the assumptions of single phase flow and constant flow rate. The LGR approach was utilized in the numerical reservoir simulator of CMG-IMEX (CMG-IMEX, 2012) to model fluid flow from matrix to fracture. Table 2.3 summarizes the reservoir and fracture properties used for simulation. In this case study, fracture conductivity is 420 md-ft. The dimensionless fracture conductivity is defined below:

$$F_{cd} = \frac{k_f w_f}{k_m x_f}, \tag{2.64}$$

where k_f is fracture permeability, w_f is fracture width, k_m is matrix permeability, and x_f is fracture half-length. Hence, the dimensionless fracture conductivity is 20 corresponding to 420 md-ft.

Parameter	Value	Unit
Initial reservoir pressure	4,200	psi
Reservoir permeability	0.1	mD
Reservoir porosity	10%	
Reservoir thickness	50	ft
Total compressibility	3×10^{-6}	psi^{-1}
Fracture conductivity	420	md-ft
Fracture width	0.01	ft
Fracture half-length	210	ft
Oil viscosity	0.6	cp
Formation volume factor	1.273	bbl/STB
Oil flow rate	25	STB/D
Production time	1,000	day

Table 2.3: Basic reservoir and fracture parameters used for the simulations.

Figure 2.39 presents the comparison of BHP between this semi-analytical model, Zhou et al. (2013) model and numerical model. It can be seen that an extremely good match is obtained. In this case study, 14 equal fracture segments are used. Based on the fracture half-length of 210 ft, each fracture segment length is 30 ft. The impact of number of fracture segment on the BHP is investigated and shown in Figure 2.40. The fracture segment is assumed to be the same for each case. As shown, the BHP of 8 fracture segments approaches that of 14 fracture segments. The length of each fracture segment corresponding to 8 segments is 52.5 ft. Hence, in the following simulation studies, the length of fracture segment is set up at most for 52.5 ft in order to maintain the accuracy of simulation results.

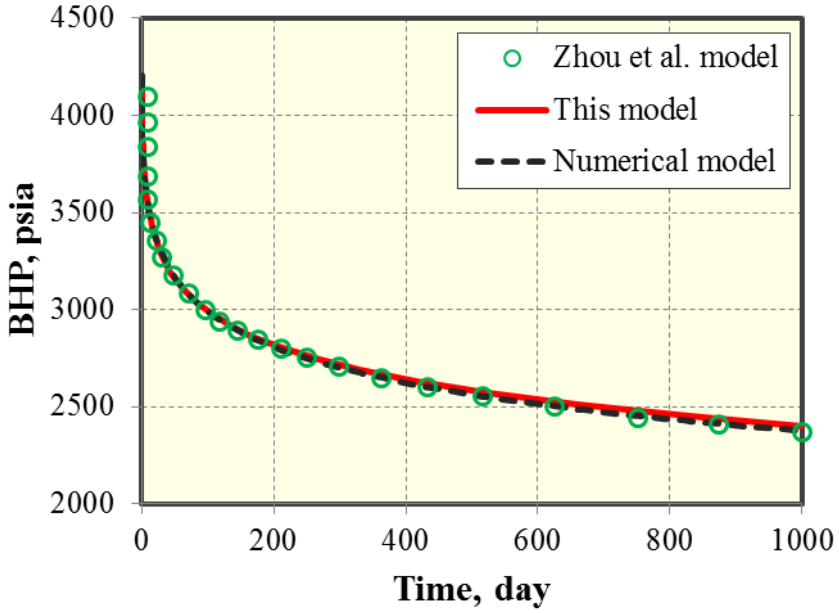

Figure 2.39: Comparison of BHP between three models for single rectangular fracture geometry.

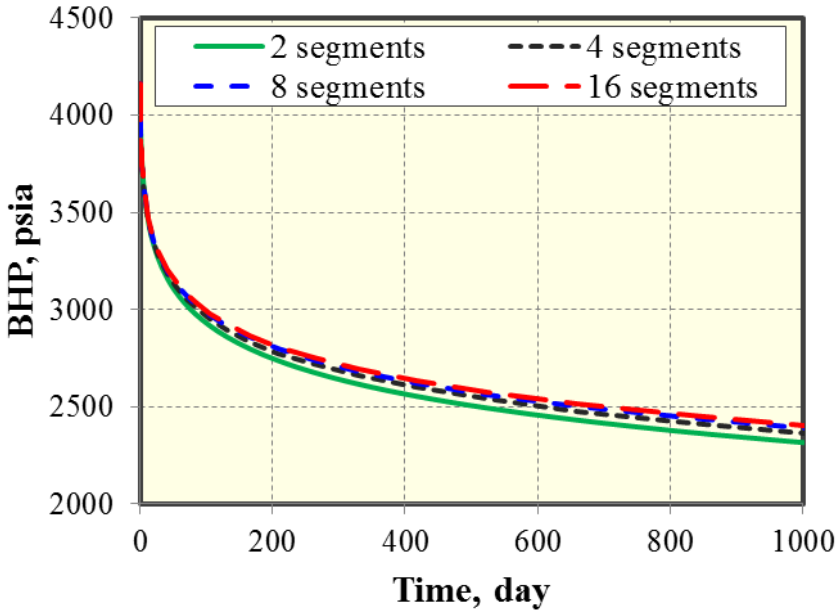

Figure 2.40: Effect of number of fracture segment on BHP.

2.8.1.1 Effect of fracture conductivity

The effect of fracture conductivity on BHP was also studied and shown in Figure 2.41, illustrating that the trend of decrease in BHP with time decreases with the increasing fracture conductivity. In addition, the BHP of the fracture conductivity of 200 md-ft approaches that of 1,000 md-ft. Hence, it can be suggested that the 200 md-ft is very close to the infinite fracture conductivity in this case study and the corresponding dimensionless fracture conductivity is calculated as 9.5.

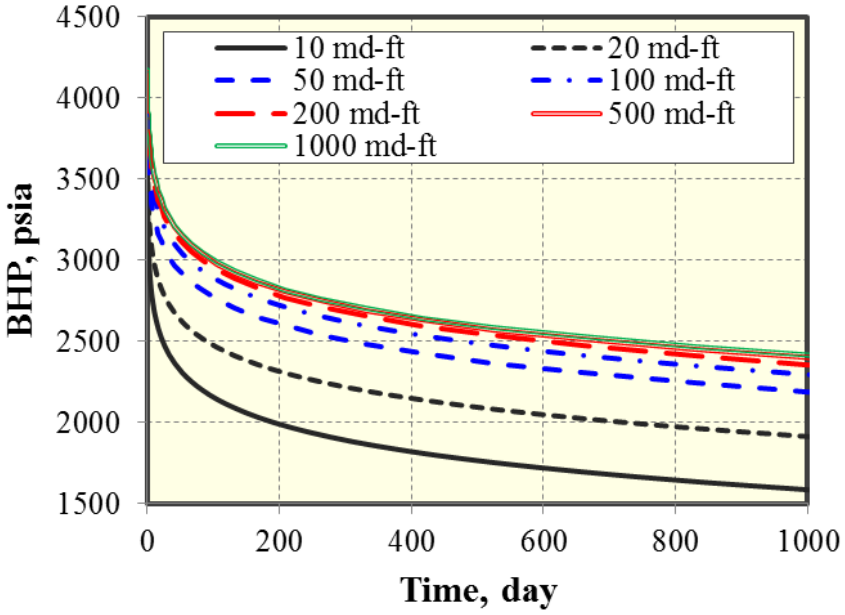

Figure 2.41: Effect of fracture conductivity on BHP.

2.8.1.2 Constant bottom hole pressure

For the constant BHP constraint, comparison of oil flow rate between this model and the numerical model is shown in Figure 2.42, illustration that a very good match is achieved. The constant BHP of 2,000 psi is used in this case study.

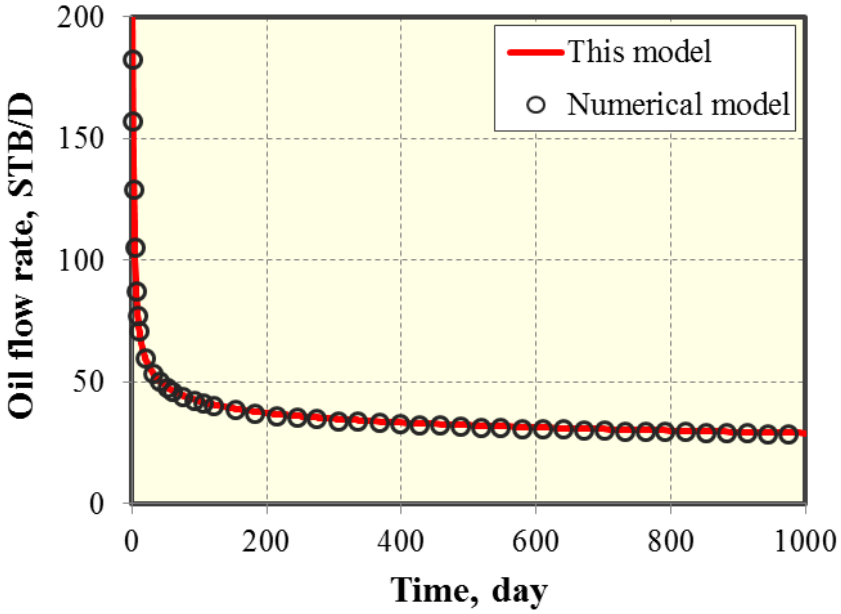

Figure 2.42: Comparison of oil flow rate between this model and the numerical model.

2.8.1.3 Geomechanics effect

For the geomechanics effect, the curve as shown in Figure 2.43 is used for simulation. Figure 2.44 presents the comparison of oil flow rate by considering the geomechanics effect under the constant BHP of 2,000 psi in the simulation. It can be seen that a good agreement between this model and the numerical model is obtained. Hence, it can be concluded that this semi-analytical model can effectively simulate the effect of geomechanics on well performance of tight oil reservoirs. Additionally, Figure 2.45 compares cumulative oil production with and without considering the geomechanics effect. As shown, the geomechanics effect makes the cumulative oil production at 1,000 days decrease by around 6% for this case study.

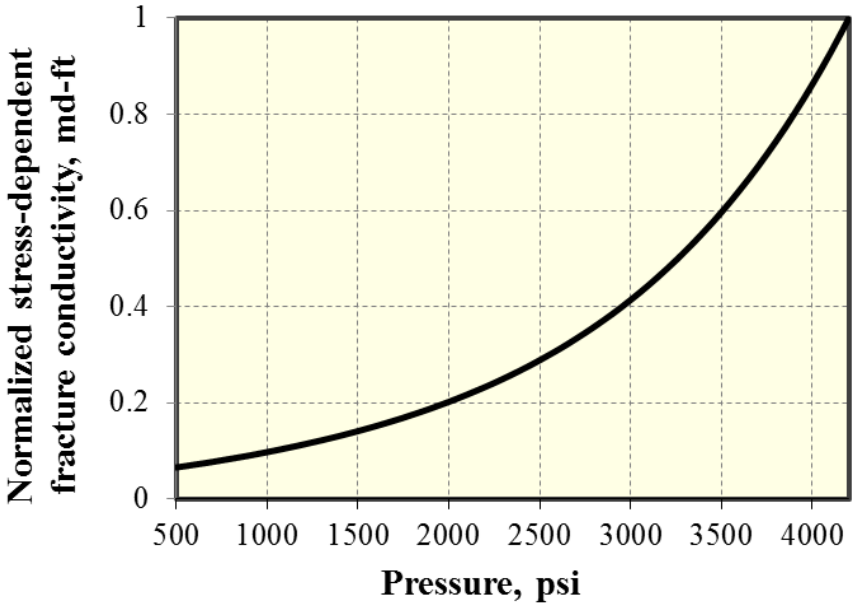

Figure 2.43: Relationship between the normalized fracture conductivity and pressure.

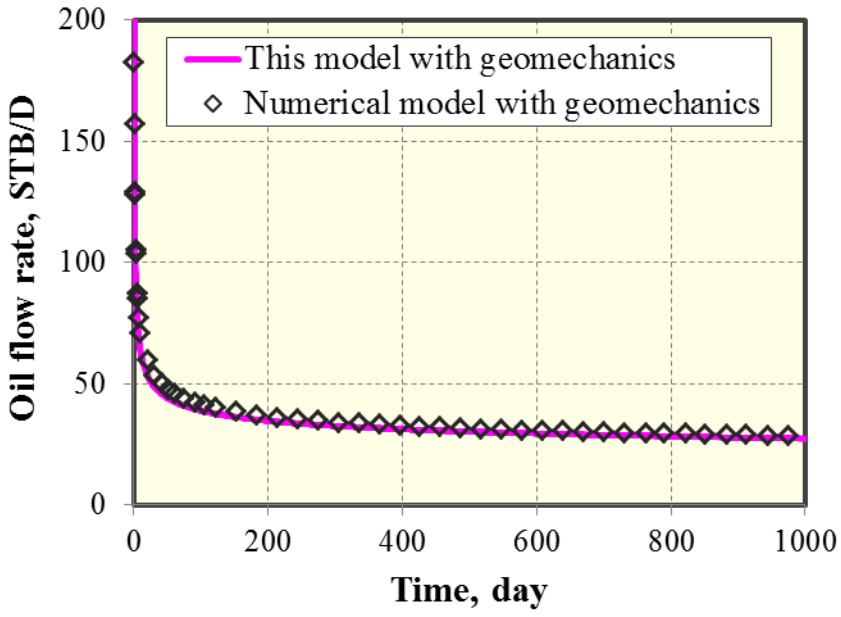

Figure 2.44: Comparison of oil flow rate by considering the geomechanics effect.

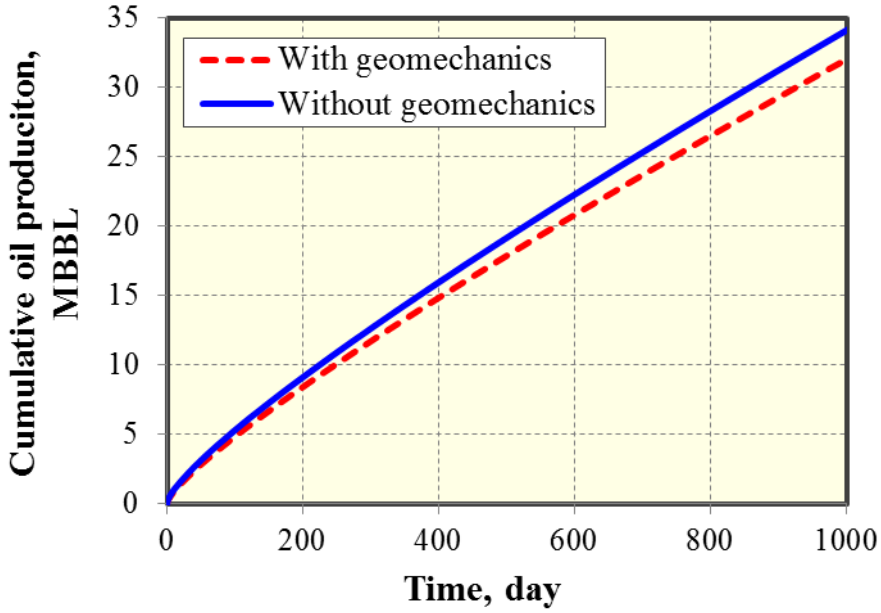

Figure 2.45: Comparison of cumulative oil production with and without considering the geomechanics effect.

2.8.2 Single planar fracture with varying width

A single planar fracture with varying width and the maximum fracture width of 0.0416 ft at center of the fracture and fracture half-length of 210 ft was studied. The fracture width and fracture permeability distribution is shown in Figure 2.46. The average fracture width is calculated as 0.03 ft based on the same fracture area in the x-y coordinate plane. The fracture is divided equally into 20 segments. Hence, the actual length for each fracture segment is 21 ft, which is adequate to guarantee the simulation accuracy. For the constant fracture width case, the fracture permeability is 773 md and the fracture conductivity is 23 md-ft, which is far away from the infinite fracture conductivity.

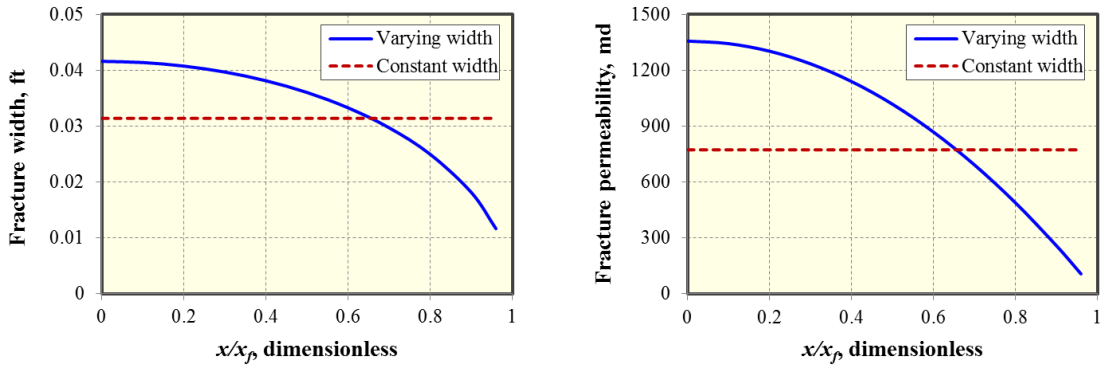

(a) (b)

Figure 2.46: Fracture width and fracture permeability distributions for both fracture geometries. (a) Fracture width distribution. (b) Fracture permeability distribution.

For the constant flow rate constraint, comparison of BHP between this model and numerical model for both fracture geometries is shown in Figure 2.47. As shown, an excellent agreement is obtained. In addition, it can be seen that BHP of the constant fracture width case has a larger pressure drop than that of the varying fracture width.

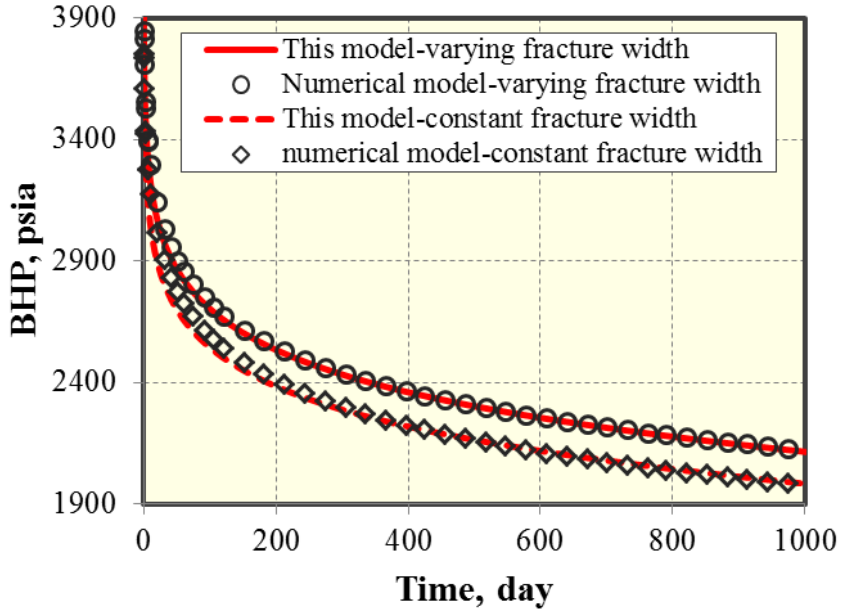

Figure 2.47: Comparison of BHP between this model and the numerical model.

Due to the fracture discretization in this model, it is convenient to investigate flux distribution along the fracture half-length. Figures 2.48 and 2.49 show the flux distribution of 10 fracture segments along the fracture half-length at time of 0.1 hour and 10 days for the constant fracture width case and varying fracture width case, respectively. As shown, for the rectangular fracture geometry at time of 0.1 hour, fluid entering the fracture is primarily from the fracture segments near the wellbore from 1 to 5; the first segment has the largest flux, which is around 0.6 bbl/day/ft. When the time increases to 10 days, the flux of fracture segment closest to the fracture tip becomes more productive; however, it is still less than that of the fracture segment near the wellbore. This is because the fracture conductivity is finite. A similar behavior was also found by Guppy et al. (1982). For the planar fracture geometry with varying width at time of 0.1 hour, the flux of the first segment decreases to around 0.45 bbl/day/ft while more fracture segments near the wellbore from 1 to 7 are productive; at time of 10 days, the segments away the wellbore are more pronounced while the flux of the last fracture segment closest to the fracture tip is less than that of the other fracture segments. This is because the fracture conductivity in this segment is much smaller than the other segments.

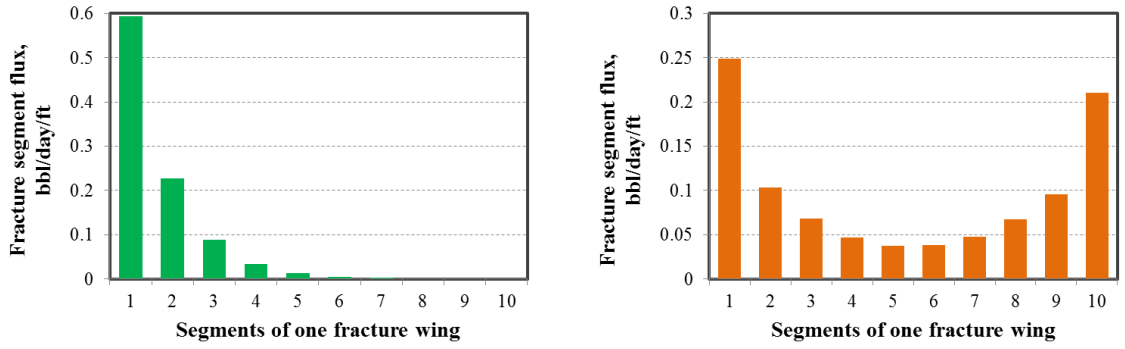

(a) (b)

Figure 2.48: Flux distribution of fracture segments along the fracture half-length for the rectangular fracture geometry. (a) At time = 0.1 hour. (b) At time = 10 days.

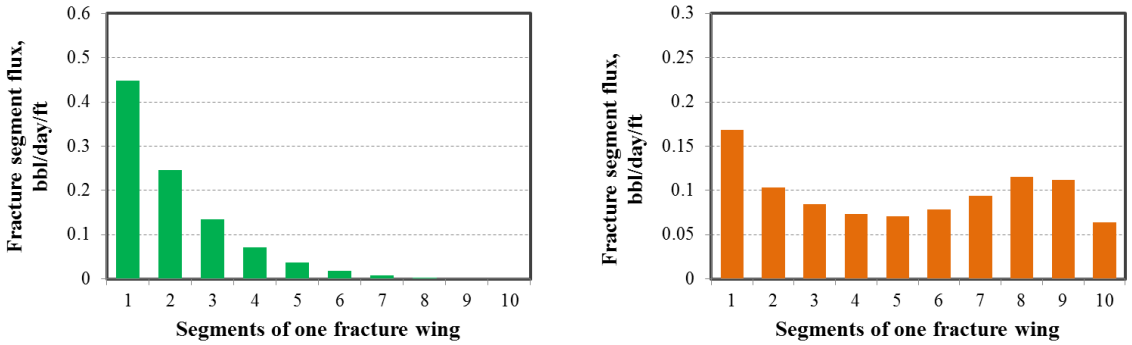

(a) (b)

Figure 2.49: Flux distribution of fracture segments along the fracture half-length for the planar fracture geometry with varying width. (a) At time = 0.1 hour. (b) At time = 10 days.

Figure 2.50 shows comparison of pressure distribution of these two fracture geometries at early time of 0.1 hour. As shown, more fracture segments of the planar fracture geometry with varying width are productive than that of the rectangular fracture geometry.

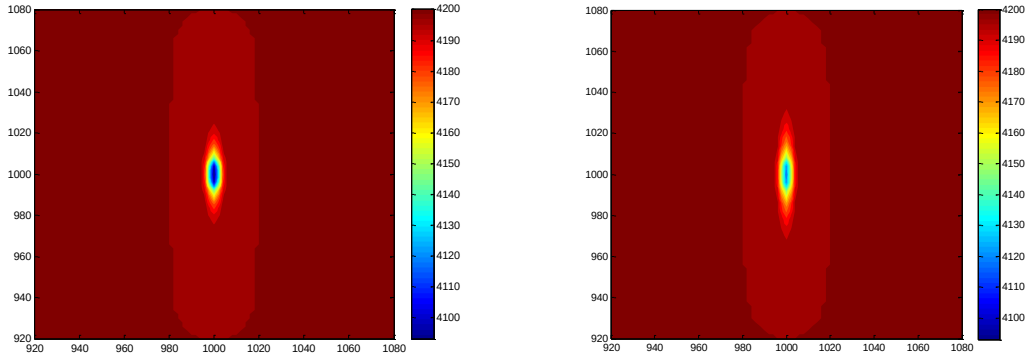

(a) (b)

Figure 2.50: Comparison of pressure distribution at time of 0.1 hour for both fracture geometries (pressure unit: psi). (a) Rectangular fracture geometry. (b) Planar fracture geometry with varying width.

We also compared BHP of these two fracture geometries under high fracture conductivity, as shown in Figure 2.51. The fracture conductivity for the constant fracture width case is 200 md-ft, which is very close to the infinite fracture conductivity. Figure 2.52 shows the comparison of the BHP for these two fracture geometries. As shown, there is no big difference of the BHP change with time.

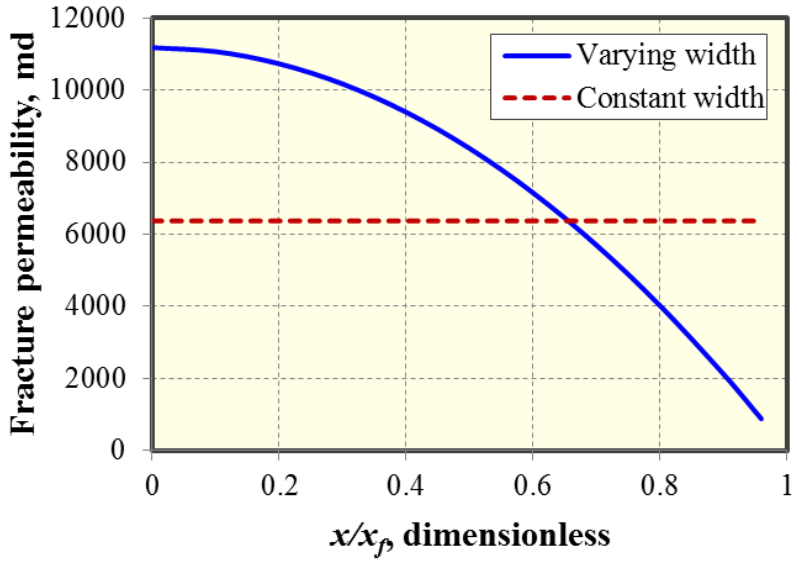

Figure 2.51: Fracture permeability distribution for both fracture geometries.

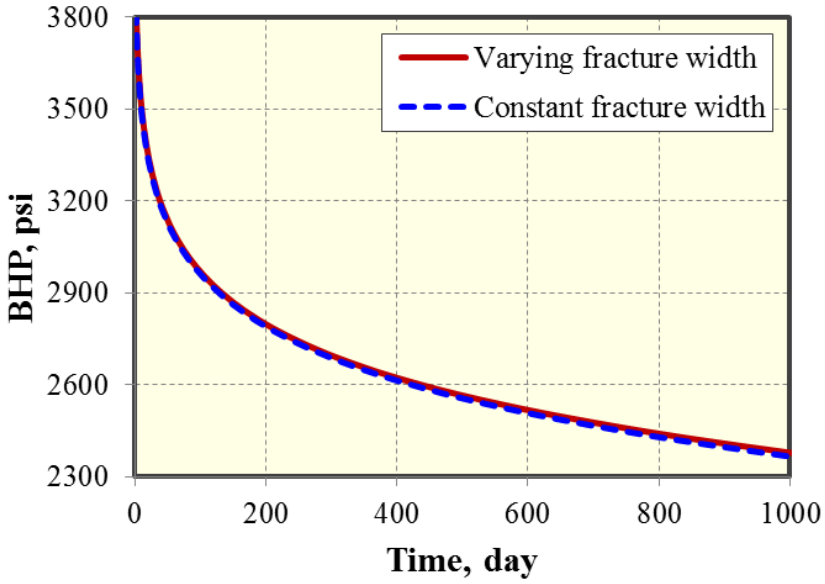

Figure 2.52: Comparison of BHP for both fracture geometries at high fracture conductivity.

Figures 2.53 and 2.54 show the flux distribution of fracture segments under the high fracture conductivity at different times for the rectangular fracture geometry and the planar fracture geometry with varying width, respectively. For the rectangular fracture geometry, the similar phenomenon is observed compared to the case at low fracture conductivity; however, more fracture segments contribute to the production at time of 0.1 hour. At time of 10 days, the flux of the fracture panel closest to the fracture tip will become more productive and it is the largest contribution than the other fracture segments. The similar phenomenon was found for the planar fracture geometry with varying width.

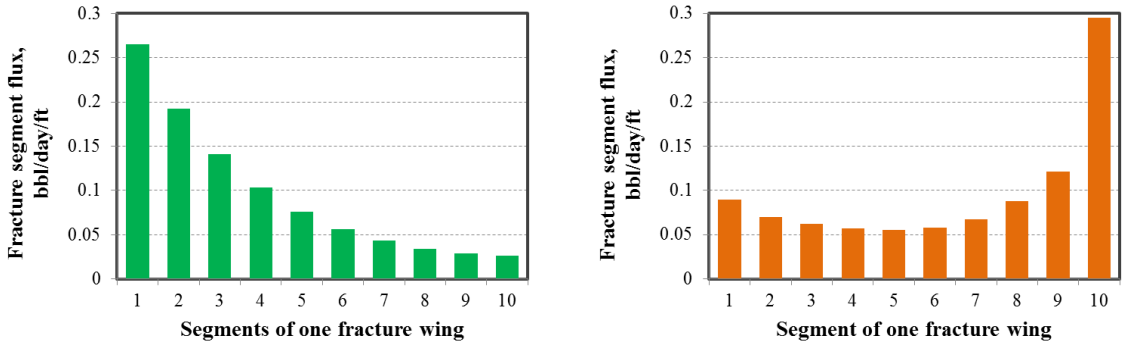

(a) (b)

Figure 2.53: Flux distribution of fracture segments along the fracture half-length at different times for the rectangular fracture geometry under high fracture conductivity. (a) At time = 0.1 hour. (b) At time = 10 days.

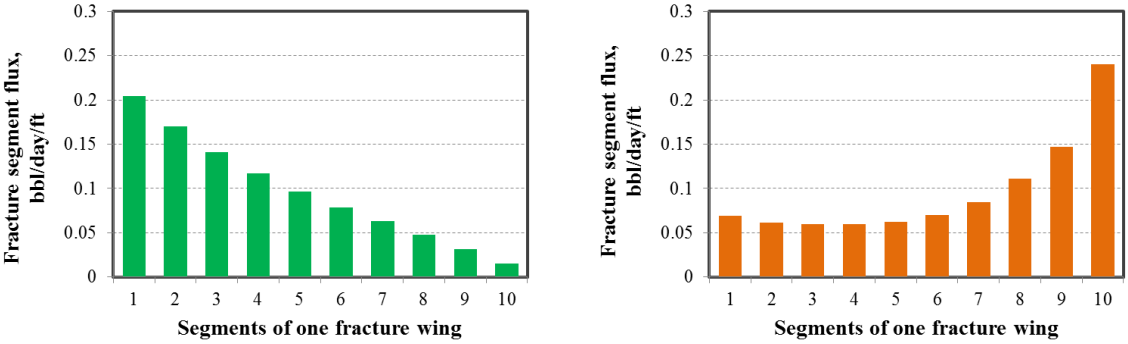

(a) (b)

Figure 2.54: Flux distribution of fracture segments along the fracture half-length at different times for the planar fracture geometry with varying width under high fracture conductivity. (a) At time = 0.1 hour. (b) At time = 10 days.

We also compared oil flow rate of this model with numerical model under the constant BHP constraint, as shown in Figure 2.55. It can be seen that a good agreement is obtained. Additionally, the oil flow rate of the varying fracture width case is larger than that of the constant fracture width case. Figure 2.56 compares cumulative oil production for these two cases. As shown, the relative difference between them at 1,000 days of production is around 9%. Hence, the effect of non-planar fracture geometry with varying

width on the well performance should be taken into account for production forecasting of unconventional oil reservoirs.

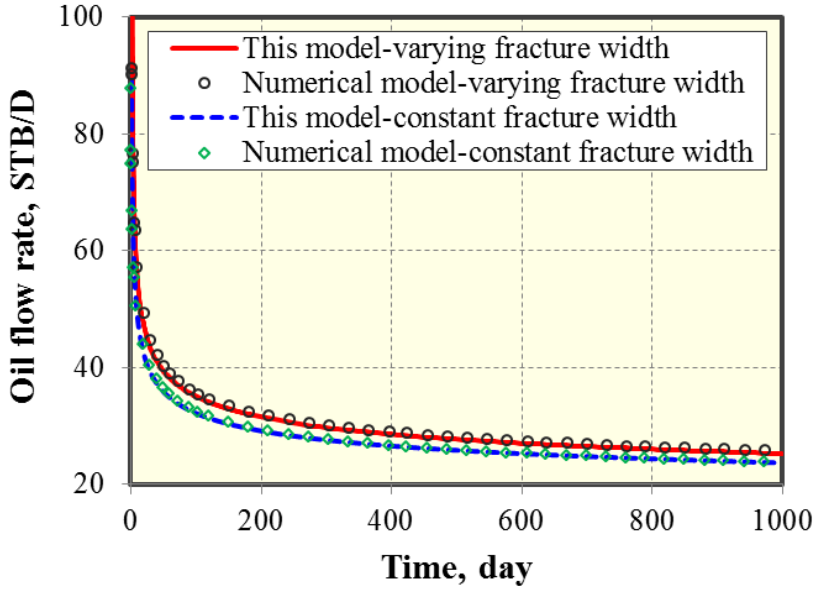

Figure 2.55: Comparison of oil flow rate between this model and the numerical model.

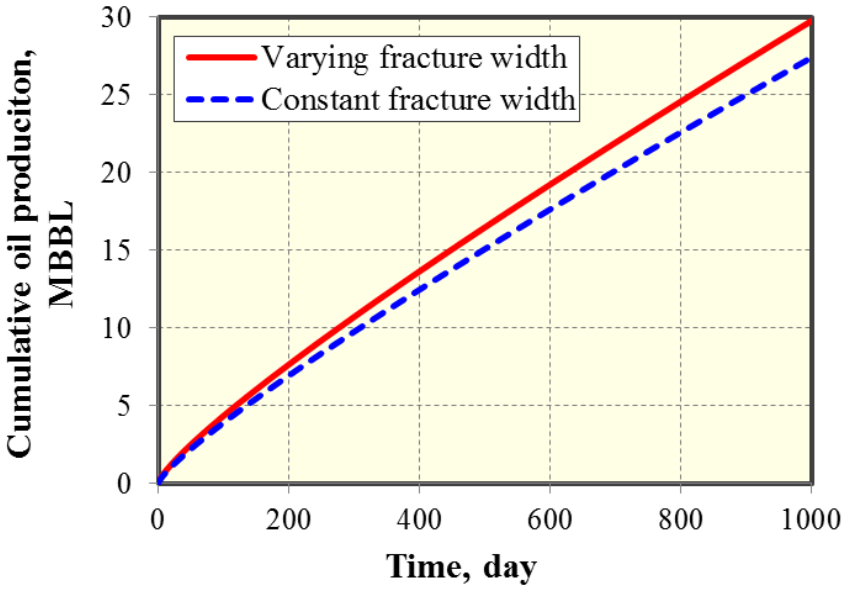

Figure 2.56: Comparison of cumulative oil production between the constant fracture width case and the varying fracture width case.

2.9 MODEL APPLICATION IN SHALE GAS RESERVOIRS

One horizontal well from the Marcellus shale reservoir was selected to perform history matching and production forecasting using the semi-analytical model. The production data was provided by Chief Oil and Gas LLC. This well was completed using a lateral length of 1,904 ft, seven fracturing stages, three perforation clusters per stage, and the cluster spacing is 68 ft. Almost 150 days of production data were available to perform history matching and evaluate the well performance. Table 2.4 summarizes the detailed reservoir and fracture properties of the well required for simulation.

Parameter	Value	Unit
Initial reservoir pressure	4,300	psi
Reservoir temperature	130	^{o}F
Reservoir porosity	12%	
Reservoir thickness	100	ft
Initial water saturation	10%	
Total compressibility	1×10^{-6}	psi^{-1}
Horizontal well length	1,904	ft
Number of stages	7	
Cluster spacing	68	ft
Total number of fractures	21	
Gas specific gravity	0.58	

Table 2.4: Reservoir and fracture parameters for one well in Marcellus shale.

Slick water was used for hydraulic fracturing. The injection rate is 20 bbl/min and the injection time is 500 seconds. Poisson ratio is 0.23. Young's modulus is 3×10^{6} psi. The maximum horizontal stress is 8,200 psi and the minimum horizontal stress is 8,000 psi. The leak-off coefficient is 5×10^{-6} ft/min$^{0.5}$. Based on these parameters, realistic non-

planar fracture geometry for one perforation stage was generated using the fracture propagation model developed by Wu and Olson (2014a), as shown in Figure 2.57. As shown, the middle fracture is shorter and narrower than the outer fractures. This is because stress shadow effects and uneven fluid rate distribution among different clusters. The non-planar fracture geometry is used for performing history matching and production forecasting. Flowing bottom hole pressure in Figure 2.58 is used to constrain the simulation and gas flow rate is the history-matching variable. Fracture half-length, fracture conductivity, and permeability were mainly tuned to perform history matching. The effects of flowback water and wettability of the formation are not considered in the simulation. Gas desorption is considered in the simulation based on the core measurements from Marcellus shale, which was provided by Chief Oil and Gas LLC, as shown in Figure 2.59. The BET isotherm is used to model the gas desorption measurements with p_o of 9833.4 psi, v_m of 134.07 scf/ton, and C of 39.14.

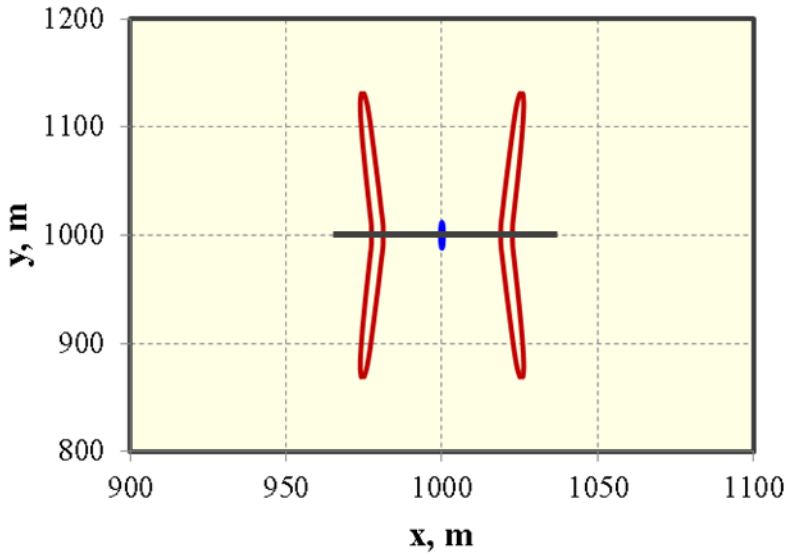

Figure 2.57: Fracture geometry prediction for one stage with three clusters using the fracture propagation model.

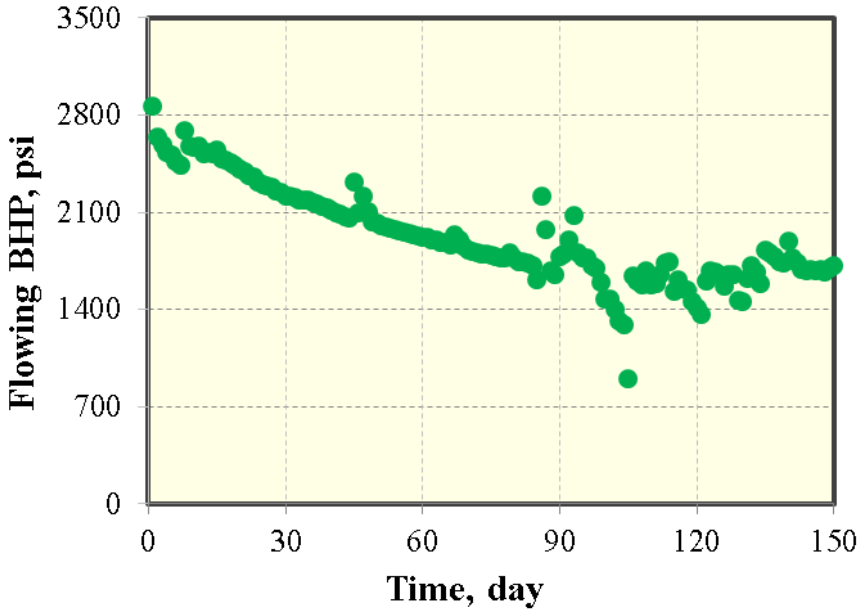

Figure 2.58: Flowing bottom hole pressure of the well in Marcellus shale.

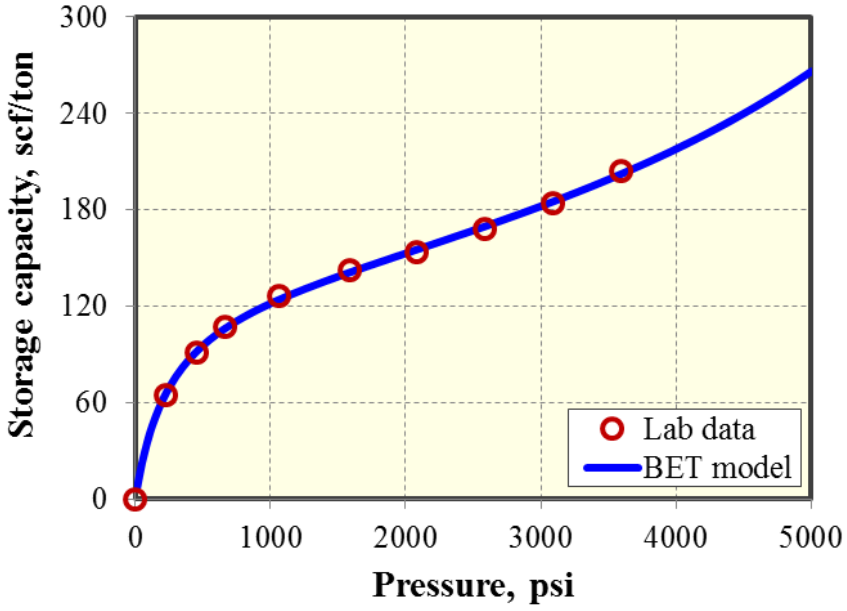

Figure 2.59: Gas desorption measurements from Marcellus shale.

The history matching results for gas flow rate is shown in Figure 2.60, illustrating that a good match between simulation results and field data is obtained with fracture half-

length of 430 ft for outer fractures per stage, fracture half-length of 38 ft for inner fracture per stage, and permeability of 800 nD. The fracture conductivity for outer fractures and inner fracture per stage was also quantified, as shown in Figure 2.61. The coefficient used to correct the fracture permeability defined by Eq. 2.43 was determined as 8.1×10^{-6} in this study. The pressure distribution at end of field production is shown in Figure 2.62, clearly showing the effective drainage area of this well. As shown, the middle fracture per stage contributes very little on gas recovery. It implies that in future fracture treatment design, the number of cluster per stage should be optimized in order to get a better economics.

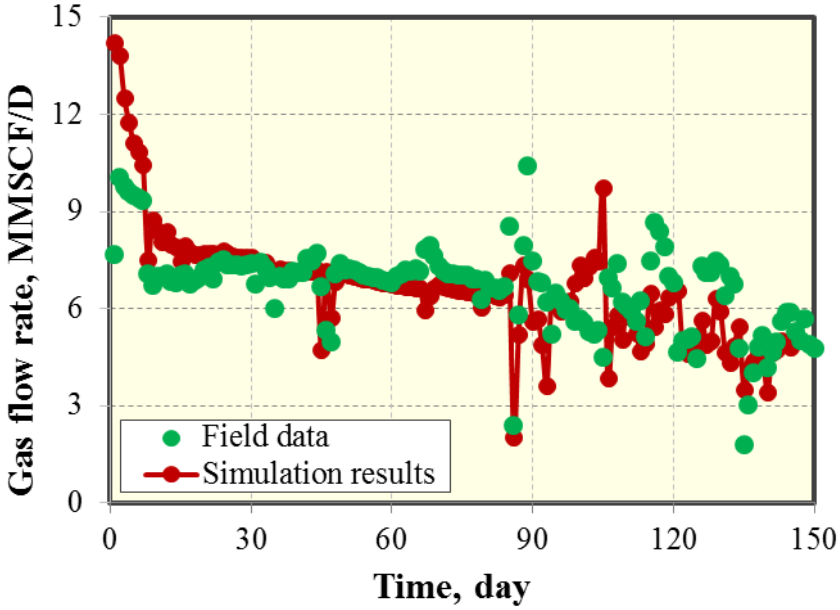

Figure 2.60: History matching results for gas flow rate.

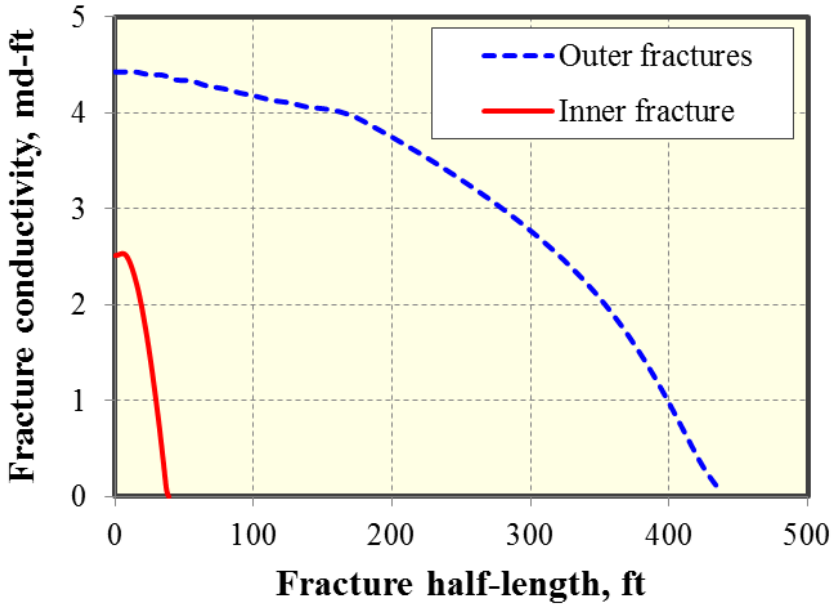

Figure 2.61: Fracture conductivity for outer fractures and inner fracture per stage.

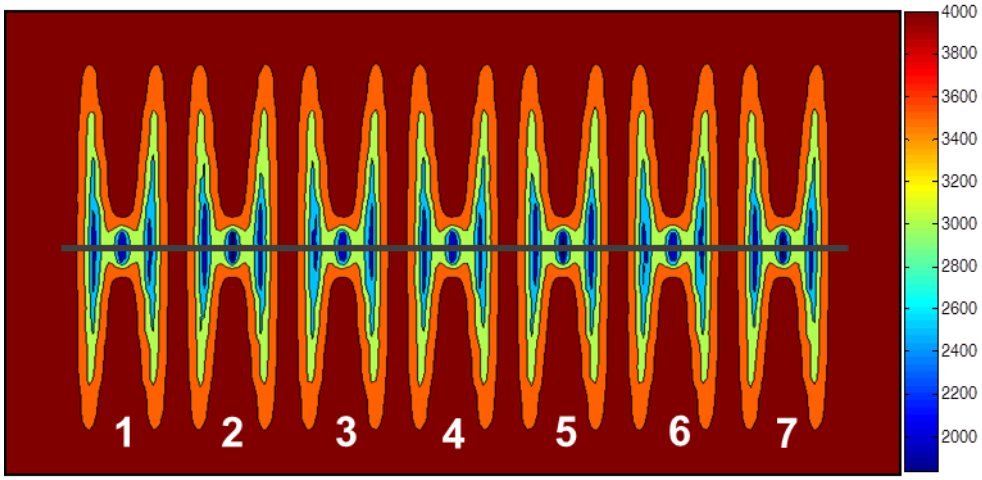

Figure 2.62: Pressure distribution at end of field production (pressure unit: psi).

After history matching, we performed a production forecasting for 30 years. After history matching period, bottom hole pressure of 1,000 psi remained constant until 30 years of production. Figure 2.63 shows the gas recovery at 30 years of production by considering the non-planar fractures, the rectangular fractures, and the important flow

mechanisms. The average pore diameter of 10 nm and the average diffusion coefficient of 10^{-5} m^2/s are used in this case study. The non-planar fractures and the rectangular fractures have the same total fracture length and fracture area. It can be seen that the difference of cumulative gas production between the realistic non-planar fractures and ideal rectangular fractures is 20% at 30 years of production. In addition, the contribution of flow mechanisms such as gas slippage, gas diffusion, and gas desorption to gas recovery at 30 years of production compared to that without considering them is 13%, 17%, and 22%, respectively. Totally, the contribution of all these important mechanisms is about 52%. Hence, the key finding of this case study was that modeling of gas production from the realistic non-planar fractures as well as modeling the important gas flow mechanisms in shale gas reservoirs is significant.

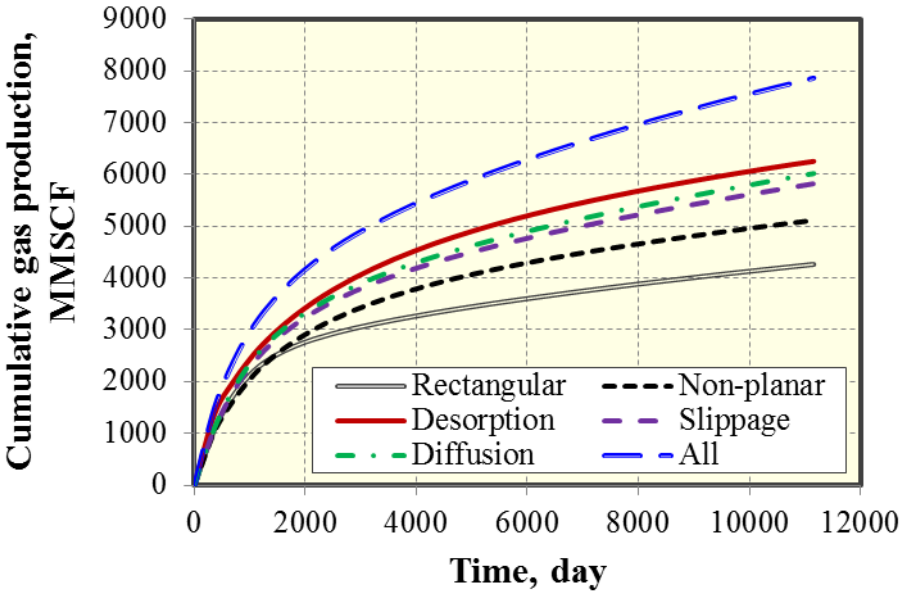

Figure 2.63: Production forecasting at 30-year period by considering non-planar fractures and rectangular fractures and the important gas flow mechanisms.

2.10 MODEL APPLICATION IN TIGHT OIL RESERVOIRS

Three scenarios with different fracture geometries were investigated in this case study, as shown in Figure 2.64. Scenario 1 is a single planar fracture with varying width. Scenario 2 is a single rectangular fracture, and the total fracture area in the x-y coordinate plane is the same as the scenario 1. Scenario 3 is a single curving non-planar fracture, and there is a severe fracture width restriction around the wellbore.

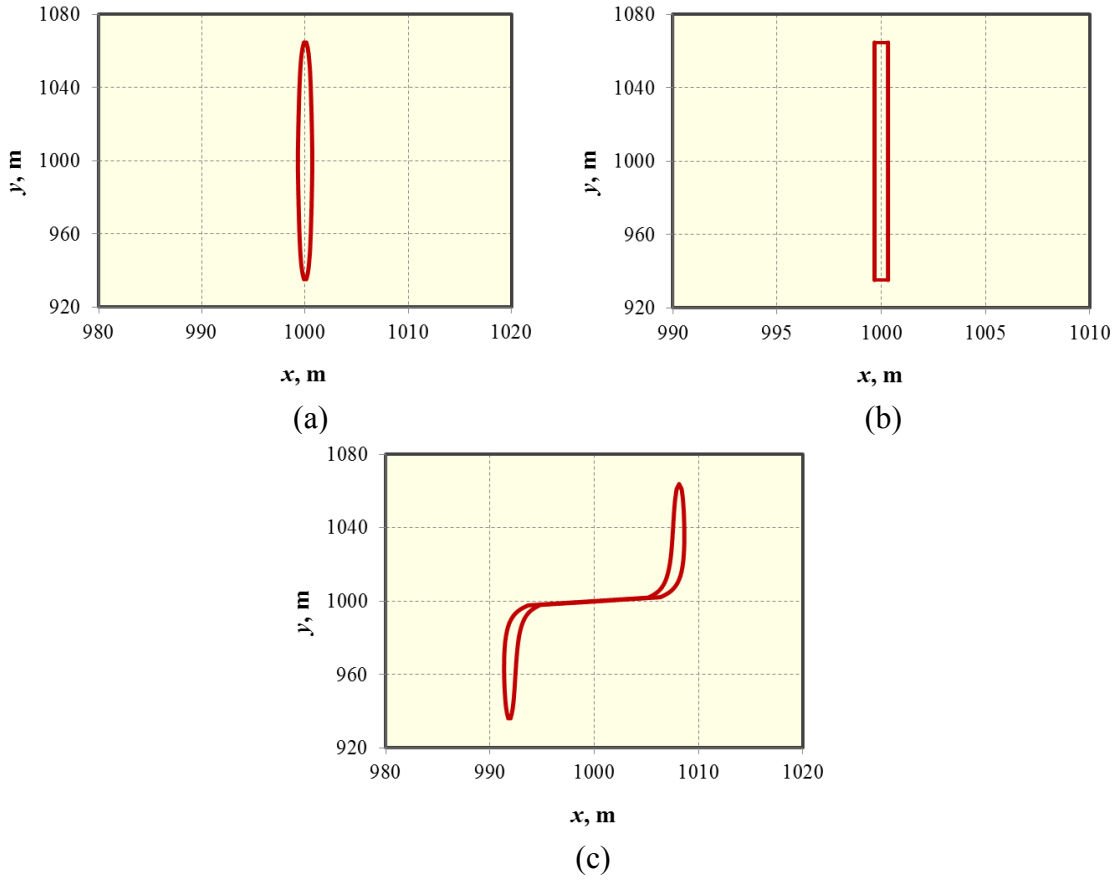

Figure 2.64: Three scenarios with different fracture geometries. (a) Scenario 1: a single planar fracture with varying width. (b) Scenario 2: a single rectangular fracture. (c) Scenario 3: a single curving non-planar fracture.

The fracture geometry of scenarios 1 and 3 were generated using the fracture propagation model by Wu and Olson (2014a). The fracture width and fracture

permeability distribution of these three scenarios along fracture half-length are shown in Figure 2.65. The fracture width of the scenario 2 is calculated as 0.0354 ft and the associated fracture conductivity is 28 md-ft, which is far away from the infinite fracture conductivity.

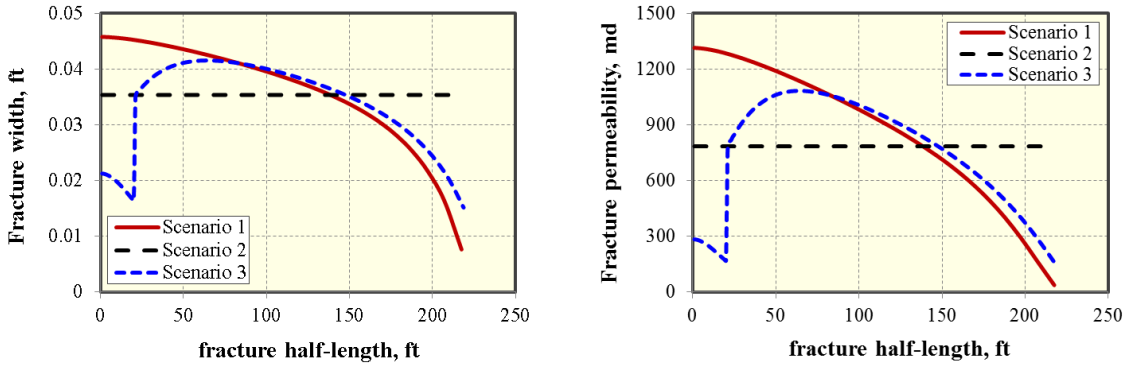

(a) (b)

Figure 2.65: Comparison of fracture width and the associated fracture permeability of the three scenarios along fracture half-length. (a) Fracture width distribution. (b) Fracture permeability distribution.

Comparison of BHP variation with time of these three scenarios is shown in Figure 2.66. As shown, the scenario 3 has the largest pressure drop, followed by the scenario 2 and scenario 1. This is because there is a severe fracture width restriction around the wellbore for the scenario 3, resulting in the largest pressure drop.

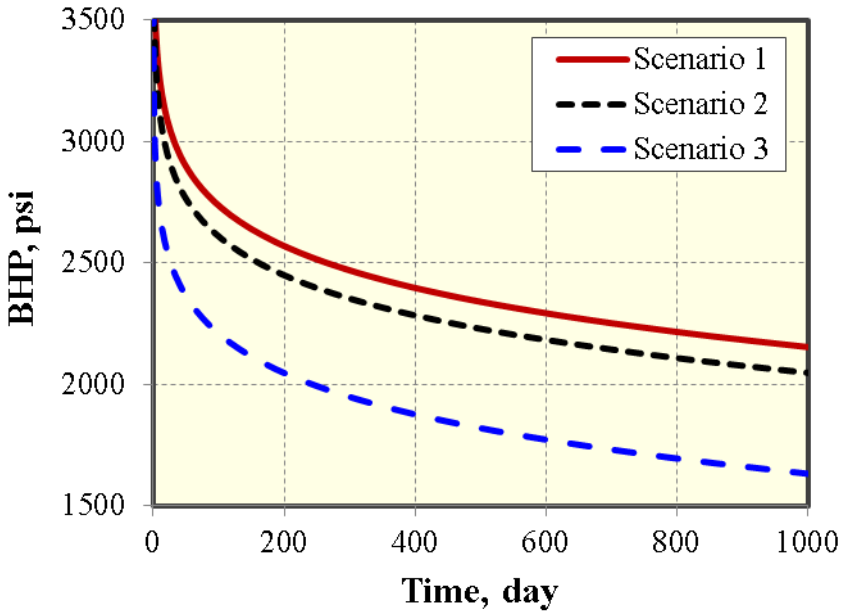

Figure 2.66: Comparison of BHP variation with time of the three scenarios.

Figure 2.67 presents the comparison of pressure distribution at time of 0.1 hour, illustrating that there is a larger pressure drop near the wellbore for scenario 3 than the other two scenarios. It can be concluded that the curving non-planar fracture geometry plays a significant negative effect on well performance, which should be avoided in the field operation.

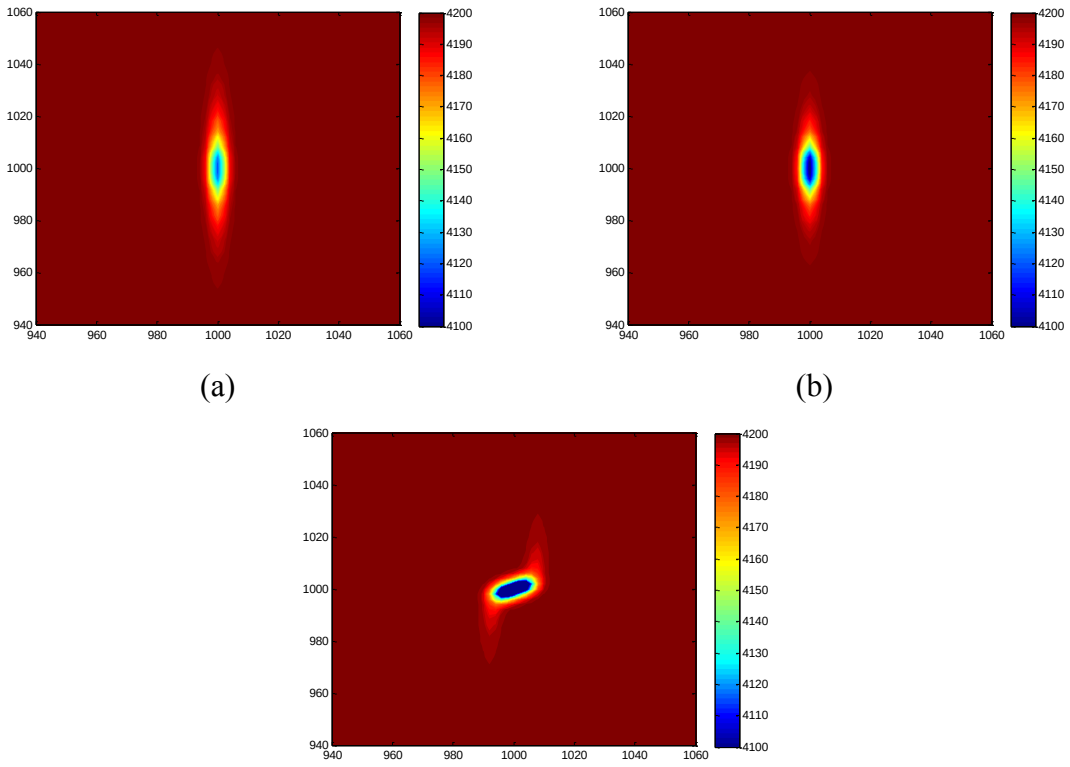

Figure 2.67: Pressure distribution of the three scenarios at time of 0.1 hour (pressure unit: psi). (a) Scenario 1: a single planar fracture with varying width. (b) Scenario 2: a single rectangular fracture. (c) Scenario 3: a single curving non-planar fracture.

The transient flow regime analysis for these three scenarios with finite fracture conductivity was also investigated. Cinco-Ley and Samaniego-V (1981) proposed four flow periods with production for a vertically fractured well, which can be characterized based on different slop in the log-log graph with the dimensionless time (t_{Dx_f}) and pressure drop (p_{wD}). The dimensionless variables can be represented by

$$P_{wD} = \frac{kh\left(P_i - P_{wf}\right)}{141.2qB\mu}, \tag{2.65}$$

$$t_{Dx_f} = \frac{0.0002637kt}{\phi\mu c_t x_f^2}, \tag{2.66}$$

where the units used are k in md, h in ft, P in psi, q in STB/D, B in bbl/STB, μ in cp, t in day, c_t in psi^{-1}, x_f in ft.

Figure 2.68 presents the four periods with time: (a) fracture linear flow with a 1/2 slope straight line; (b) bilinear flow with a 1/4 slope straight line; (c) formation linear flow with a 1/2 slope straight line; (d) pseudoradial flow, which stabilizes at 0.5 line in the pressure derivative log-log plot (Bourdet et al., 1983). Cinco-Ley and Samaniego-V (1981) reported that the formation linear flow only occurs in the fracture with the large dimensionless conductivity such as 300.

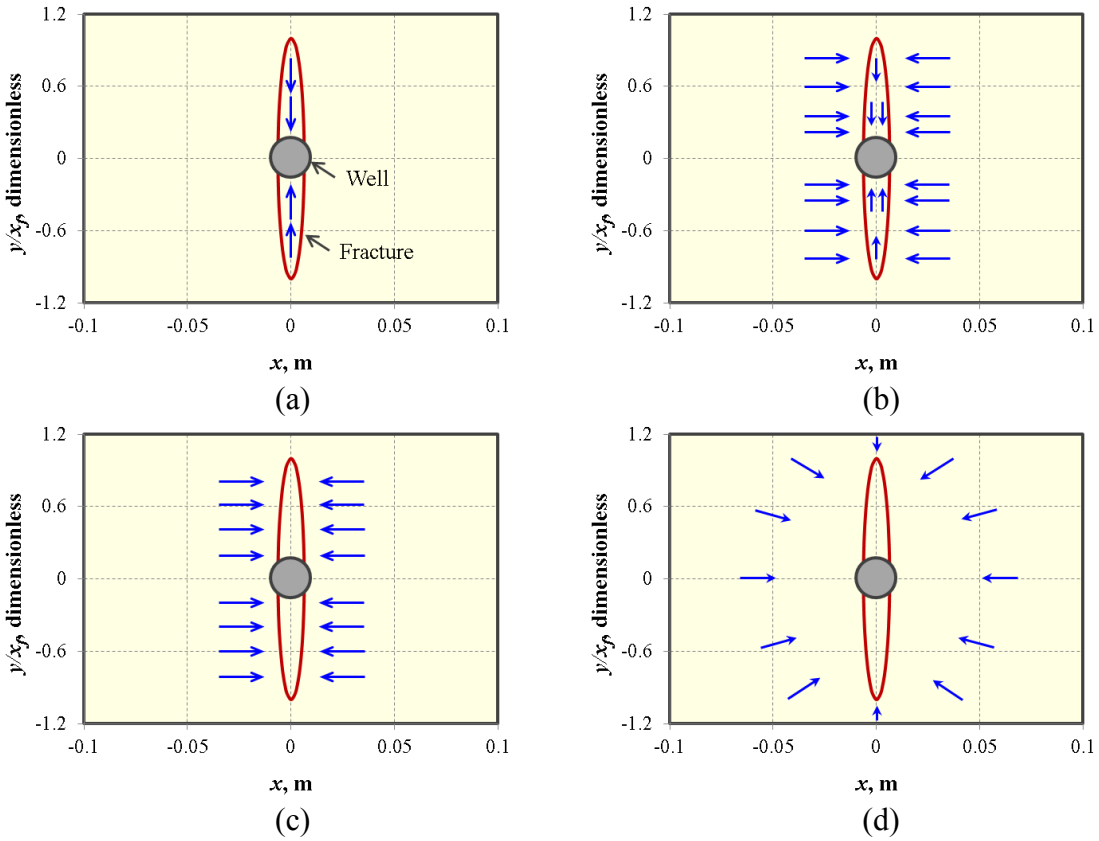

Figure 2.68: Four flow periods for a vertically fractured well (modified from Cinco-Ley and Samaniego-V, 1981). (a) Fracture linear flow. (b) Bilinear flow. (c) Formation linear flow. (d) Pseudoradial flow.

Comparison of transient flow behavior of these three scenarios is shown in Figure 2.69. As shown, the bilinear flow and the pseudoradial flow exhibit for both scenarios 1 and 2. However, the scenario 3 only shows the pseduradial flow and the slope at early times is less than 1/4, which might be applied in the field analysis to identify whether or not there is a severe fracture width restriction around the wellbore.

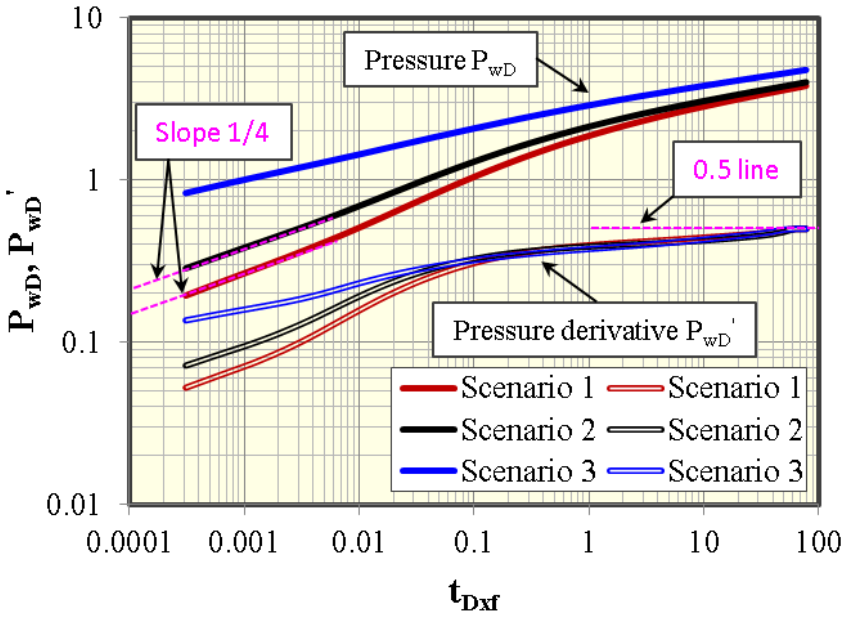

Figure 2.69: Comparison of flow regime characterization of the three scenarios.

Figure 2.70 compares the oil flow rate and cumulate oil production for these three scenarios under the constant BHP of 2,000 psi. As shown, the scenario 1 has the largest oil production, followed by the scenarios 2 and 3. There is a larger oil production drop for the scenario 3 because of the fracture width restriction. The oil production at 1,000 day for the scenarios 2 and 3 decreases by 6% and 24%, respectively, compared to the scenario 1. Hence, the curving non-planar fracture geometry jeopardizes the well performance compared to the other two geometries, which should be examined carefully in production forecasting of unconventional oil reservoirs.

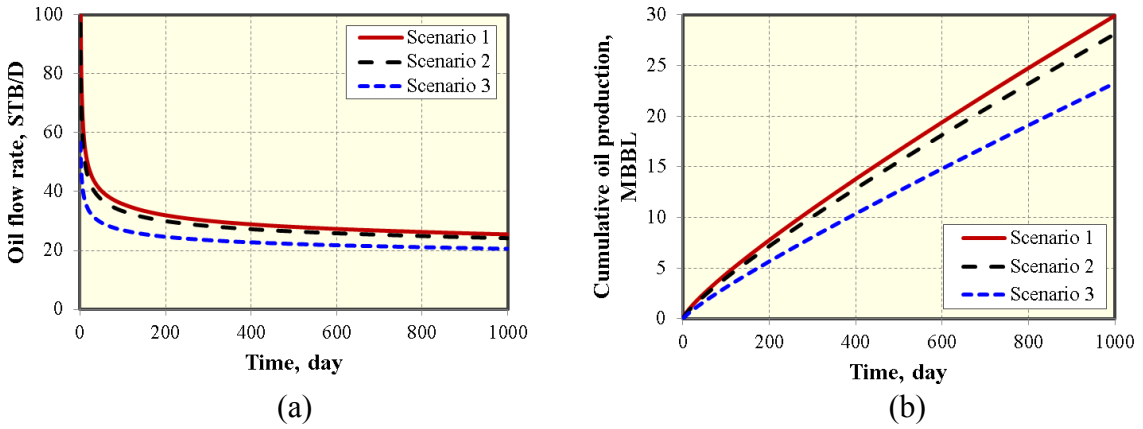

(a) (b)

Figure 2.70: Comparison of well performance of the three scenarios. (a) Oil flow rate. (b) Cumulative oil production.

2.11 CONCLUSIONS

We developed an efficient semi-analytical model for production simulation from non-planar hydraulic fractures in shale gas and tight oil reservoirs. We verified this model against a numerical reservoir simulator for single rectangular fracture, single planar fracture with varying width, and multiple rectangular fractures. For shale gas reservoirs, we applied this model to perform a field well performance and analyze the contributions of the important transport mechanisms to gas recovery. For tight oil reservoirs, flux distribution along the fracture for the rectangular fracture geometry and planar fracture geometry with varying width was compared under low and high fracture conductivity. Also, we simulated the well performance from three different fracture geometries including single rectangular fracture, single planar fracture with varying width, and single curving non-planar fracture. The following conclusions can be drawn from this work:

(1) A good agreement between the semi-analytical model and the numerical model was obtained for single rectangular fracture, single planar fracture with varying width, and multiple rectangular fractures by considering the effects of non-Darcy flow, gas desorption, and geomechanics for shale gas reservoirs.

(2) A good agreement between the semi-analytical model and the numerical model was also obtained for single rectangular fracture and single planar fracture with varying width by considering the effect of geomechanics for tight oil reservoirs.

(3) This work, for the first time, combined the fracture propagation model with production simulation using the semi-analytical model to analyze the field well performance in Marcellus shale.

(4) There is a big difference of cumulative gas production between the realistic non-planar fractures and ideal rectangular fractures under condition of low fracture conductivity.

(5) Modeling of production from the realistic non-planar fractures as well as modeling the important gas flow mechanisms in shale gas reservoirs is important.

(6) The flux distribution of planar fracture geometry with varying width is different from that of rectangular fracture geometry at low fracture conductivity. The difference between these two fracture geometries decreases with an increase in fracture conductivity and becomes negligible at the infinite fracture conductivity.

(8) The curving non-planar fracture geometry plays a significant negative effect on the well performance because of the fracture width restriction around the wellbore. Flow regime analysis might be used to identify the fracture width restriction for the curving non-planar fracture geometry.

CHAPTER 3: Evaluation of Gas Desorption in Marcellus Shale

Production from shale gas reservoirs plays an important role in natural gas supply in the United States. It is believed that gas in shale reservoirs is mainly composed of free gas within fractures and pores and adsorbed gas in organic matter (kerogen). It is generally assumed in the literature that the monolayer Langmuir isotherm describes gas adsorption behavior in shale gas reservoirs. However, in this study, we analyzed several experimental measurements of methane adsorption from some area in Marcellus shale and found that the gas desorption behavior deviates from the Langmuir isotherm, but obey the BET (Brunauer, Emmett and Teller) isotherm (Brunauer et al., 1938). To the best of our knowledge, such behavior has not been presented in the literature for shale gas reservoirs to behave like multilayer adsorption. Consequently, investigation of this specific gas desorption behavior is important for accurate evaluation of well performance and completion effectiveness in shale gas reservoirs. The difference in calculating original gas in place based on both isotherms was discussed. We also performed history matching with one horizontal well from Marcellus shale and evaluated the contribution of gas desorption to the well's performance. History matching shows that gas adsorption obeying the BET isotherm contributes more to overall gas recovery than gas adsorption obeying Langmuir isotherm, especially at early time of production. This work provides a better understanding of gas desorption in shale gas reservoirs and updates our current analytical and numerical models for simulation of shale gas production.

3.1 INTRODUCTION

In recent years, the boom of shale gas production was fueled by the improvements in horizontal drilling and multi-stage hydraulic fracturing technologies. As a result, shale gas has become an increasingly important source of natural gas supply in North America and around the world. In nature, gas shales are characterized by extremely small grain size, extremely low permeability on the order of nano-Darcy (10^{-6} md), small porosity, and high total organic carbon (TOC). Shale can serve as both source and reservoir rock. The amount of gas in place in shale is strongly affected by the TOC, clays, and the adsorption ability of methane on the internal surface of solid (Martin et al., 2010). In general, complex fracture networks that are generated connect the shale formation and the horizontal well. Shale matrix has strong gas storage capacity but cannot transport the gas for long distance because it is very tight; a fracture network can transport the gas efficiently due to large hydraulic conductivity but has limited storage capacity (Lane et al., 1989; Carlson and Mercer, 1991). Since a portion of gas in shale reservoirs is adsorbed, investigation of gas adsorption can provide critical insights into evaluation of well performance, shale characterization, and optimization of fracture design in shale gas reservoirs.

Generally, natural gas in shale reservoirs is stored as free gas in both organic matter (kerogen) and larger mineral pores and natural fractures, as well as adsorbed gas within organic matter (Leahy-Dios et al., 2011), as shown in Figure 3.1. The adsorbed gas has a higher density than the surrounding free gas. Clarkson and Haghshenas (2013) presented five mechanisms for methane existence in shale gas reservoirs: (1) adsorption on internal surface area; (2) conventional (compressed gas) storage in natural and hydraulic (induced) fractures; (3) conventional storage in matrix porosity (organic and inorganic); (4) solution in formation water; (5) absorption (solution) in organic matter.

The organic matter is nanoporous material primarily consisting of micropores (pore length less than 2 nm) and mesopores (pore length between 2 and 50 nm) (Kang et al., 2011). The organic matter occupies only a part of the bulk rock as connected clusters embedded in the rock or dispersion among mineral grains (Silin and Kneafsey, 2012). In the Appalachian Basin, the well performance from darker zones within Devonian shale with higher organic content is better than that from organic-poor gray zones (Schmoker, 1980). Lu et al. (1995) showed that the relationship between gas adsorption capacity and TOC is approximately linear when the TOC is high; while for a very low TOC, illite plays an important role in gas storage in Devonian shale. The adsorption process in shale gas reservoirs is mainly physical adsorption, which means that the adsorption is fully reversible, allowing gas molecules to completely adsorb and desorb, and the interaction force between the solid surface and the adsorbed gas molecules is controlled by the weak van der Waals force. The specific surface area, defined as surface area per gram of solid, plays an important role in controlling the adsorption capacity. The rougher solid surface and the smaller pore sizes can contribute a larger specific surface area (Solar et al., 2010). The specific surface area can be calculated using the BET method (Brunauer et al., 1938). A rough solid surface with many nanometer-scale cavities can adsorb gas more strongly than an ideally polished surface (Rouquerol et al., 1999; Solar et al., 2010).

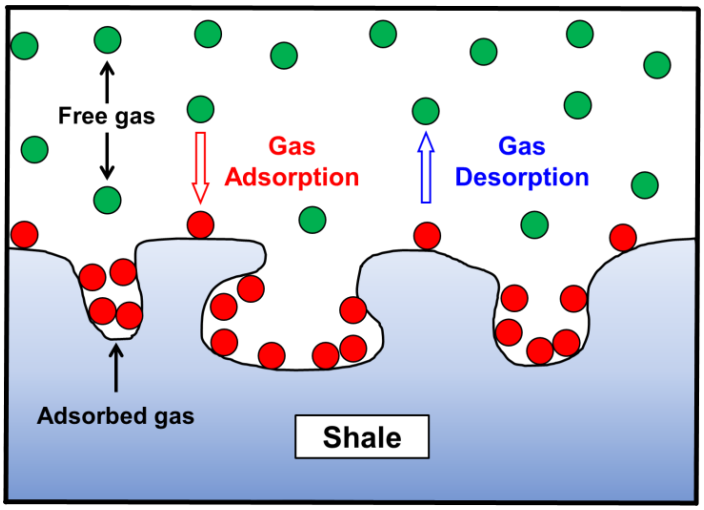

Figure 3.1: Free gas and adsorbed gas in shale gas reservoirs.

A recent study conducted by the Energy Information Administration (EIA, 2014b) concludes that the Marcellus Shale is one of six key tight oil and shale gas regions, which account for 95% of domestic oil production growth and all domestic natural gas production growth during 2011-2013. The Marcellus shale covers a total area of more than 100,000 square miles, and the depth is in the range of 4,000-8,500 ft with an average thickness of 50 ft to 200 ft (U.S. Department of Energy, 2013). The average estimated ultimate recovery (EUR) is about 2.325 billion cubic feet (BCF) per well and the average porosity is 8% and TOC is 12 wt% (EIA, 2011). The Marcellus shale has 1,500 trillion cubic feet (TCF) of original gas in place (OGIP) with 141 TCF of technically recoverable gas (U.S. Department of Energy, 2013). Reservoir temperature in the Marcellus shale is observed to be around 140 ^{o}F and bottom hole pressure is up to 6,000 psi (Williams et al., 2011).

Most publications to date have used the Langmuir isotherm to describe gas desorption in shale gas reservoirs. In this work, we observed that the gas desorption in some areas of the Marcellus shale follows the BET isotherm based on laboratory

measurements. The Langmuir and BET isotherms were compared with experimental data. In addition, through history matching with one production well in the Marcellus shale, we evaluated the effect of gas adsorption on well performance at short and long production times.

3.2 ADSORPTION MODEL FOR SHALE GAS RESERVOIRS

Adsorption at the gas/solid interface is referred to as the enrichment of one or more components in an interfacial layer (Sing et al., 1985). The organic matter in shale has a strong adsorption potential due to the large surface area and affinity to methane. In order to simulate gas production in shale gas reservoirs, an accurate model of gas adsorption is very important. According to the International Union of Pure and Applied Chemistry (IUPAC) standard classification system (Sing et al., 1985), there are six different types of adsorption, as shown in Figure. 3.2. The shape of the adsorption isotherm is closely related to the properties of adsorbate and solid adsorbent, and on the pore-space geometry (Silin and Kneafsey, 2012). The detailed description of the six isotherm classifications can be found in Sing et al. (1985).

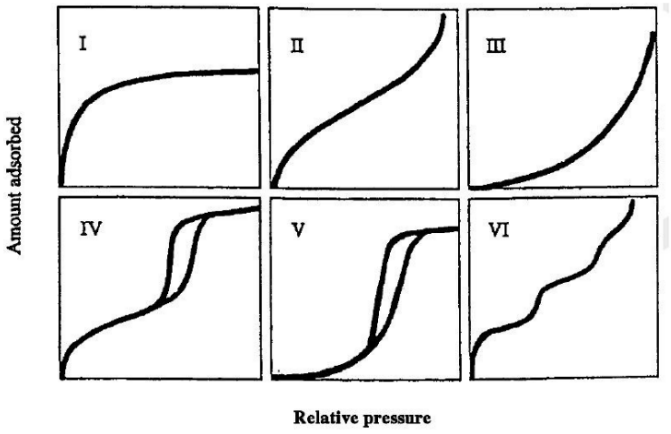

Figure 3.2: Six types of physical sorption isotherms according to the IUPAC classification (Sing et al., 1985).

The most commonly applied adsorption model for shale gas reservoirs is the classic Langmuir isotherm (Type I) (Langmuir, 1918), which is based on the assumption that there is a dynamic equilibrium at constant temperature and pressure between adsorbed and non-adsorbed gas. Also, it is assumed that there is only a single layer of molecules covering the solid surface

At high reservoir pressures, one might expect that natural gas sorbed on the organic carbon surfaces forms multi-molecular layers. Also, a similar gas adsorption behavior behaving like multi-molecular layers might be due to a severe surface roughness on the pore walls, resulting in a large specific surface area. In other words, the Langmuir isotherm may not be a good approximation of the amount of gas sorbed on organic carbon-rich mudrocks. Instead, multilayer sorption of natural gas should be expected on organic carbon surfaces, and the gas adsorption isotherm of Type II should be a better choice. Type II isotherm often occurs in a non-porous or a macroporous material (Kuila and Prasad, 2013). In 1938, Stephen Brunauer, Paul Hugh Emmett, and Edward Teller (BET) published their theory in the Journal of the American Chemical Society (Brunauer et al., 1938). The BET isotherm is a generalization of the Langmuir isotherm to multiple adsorbed layers. The assumptions in the BET theory include homogeneous surface, no lateral interaction between molecules, and the uppermost layer is in equilibrium with gas phase.

A more convenient form of the BET adsorption isotherm equation is as follows:

$$\frac{p}{v\left(p_o - p\right)} = \frac{1}{v_m C} + \frac{C-1}{v_m C} \times \frac{p}{p_o}. \tag{3.1}$$

A plot of $p/v(p_o\text{-}p)$ against p/p_o should give a straight line with intercept of $1/v_m C$ and slope of $(C\text{-}1)/v_m C$. Based on v_m, the specific surface area can be calculated using the following expression:

$$S = \frac{v_m Na}{22400}, \tag{3.2}$$

where S is the specific surface area in m^2/g, N is Avogadro constant (number of molecules in one mole, 6.023×10^{23}), a is the effective cross-sectional area of one gas molecule in m^2, 22,400 is the volume occupied by one mole of the adsorbed gas at standard temperature and pressure in mL.

The standard BET isotherm assumes that the number of adsorption layers is infinite. But, in the case of n adsorption layers in some finite number, then a general form of BET isotherm is given below:

$$v(p) = \frac{v_m C \dfrac{p}{p_o}}{1-\dfrac{p}{p_o}} \left[\frac{1-(n+1)\left(\dfrac{p}{p_o}\right)^n + n\left(\dfrac{p}{p_o}\right)^{n+1}}{1+(C-1)\dfrac{p}{p_o} - C\left(\dfrac{p}{p_o}\right)^{n+1}} \right]. \tag{3.3}$$

When n = 1, Eq. (3.3) will reduce to the Langmuir isotherm. When $n = \infty$, Eq. (3.3) will reduce to Eq. (3.1).

Here $v(p)$ is the specific volume of gas adsorbed at the reservoir pressure and temperature per unit mass of bulk rock, reference to a standard pressure and temperature (stock tank condition (ST) in the oil industry). The customary cubic fields are the standard cubic feet of sorbed gas per ton of bulk rock (scf/ton), or the standard cubic centimeters of gas per gram of rock. The conversion factor is

$$1\frac{\text{scf}}{\text{ton of bulk rock}} = \frac{1}{32}\frac{\text{standard cm}^3}{\text{g of bulk rock}}. \tag{3.4}$$

Figure 3.3 compares shapes of the Langmuir and BET isotherms: gas desorption along the BET isotherm contributes more significantly at early time of production than that with the Langmuir isotherm curve. This is because the slope of the BET isotherm curve at high pressure is larger than that of the Langmuir isotherm curve, resulting in more adsorbed gas releasing at early production times. In addition, under the same

pressure drop from the initial reservoir pressure to the bottom hole pressure (BHP), the amount of released adsorbed gas with the BET isotherm curve is larger than that with the Langmuir isotherm curve.

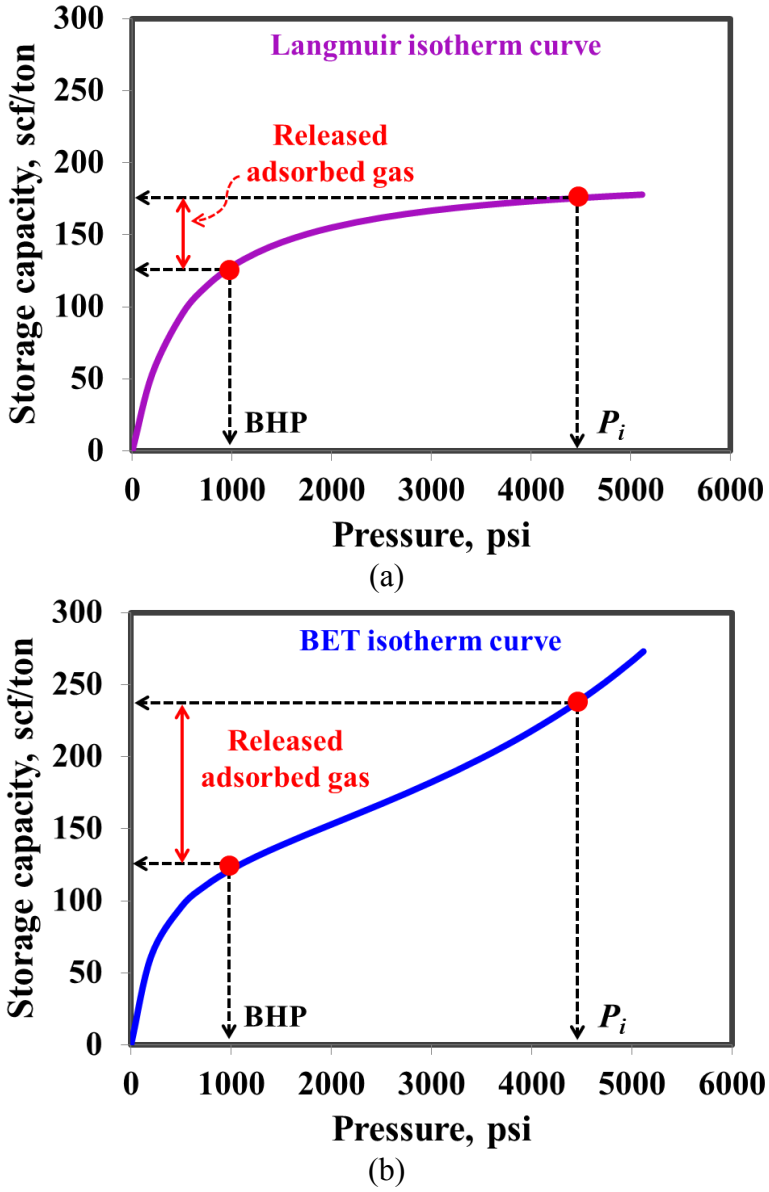

Figure 3.3: Comparison of the Langmuir and BET isotherms. (a) Langmuir isotherm. (b) BET isotherm.

3.3 GAS FLOW IN SHALE CONSIDERING GAS DESORPTION EFFECT

An equation to describe mass balance of gas flow in shale gas reservoirs by only considering the gas desorption effect can be obtained by simplifying the Eq. 2.38 as follows:

$$\nabla \cdot \left\{ \left(1-V_a\right) \frac{\rho_g k_{rg} k}{\mu_g} \nabla p \right\} = \left[S_g \phi + \left(1-\phi\right) K_a \right] c_g \rho_g \frac{\partial p}{\partial t}. \tag{3.5}$$

where V_a is pore volume fraction of adsorbed gas, S_g is initial gas saturation, ρ_g is the free gas density, k is reservoir permeability, c_g is the isothermal gas compressibility factor, K_a is the differential equilibrium partitioning coefficient of gas at a given temperature.

3.4 GAS ADSORPTION MEASUREMENTS IN MARCELLUS SHALE

In this work, we analyzed gas adsorption laboratory measurements on four samples from the lower Marcellus shale, which were provided by Chief Oil and Gas LLC, as shown in Figure 3.4. It can be seen that the adsorption measurements do not obey the Langmuir isotherm but obey the BET isotherm. We employed both the Langmuir and BET isotherms to fit the experimental measurements, as shown in Figure 3.5. The fitting parameters of Langmuir and BET isotherms are listed in Tables 1 and 2, respectively. The coefficient of determination, also known as R^2, is used to evaluate goodness of fit. The measurements are better approximated by the BET isotherm than by the Langmuir isotherm.

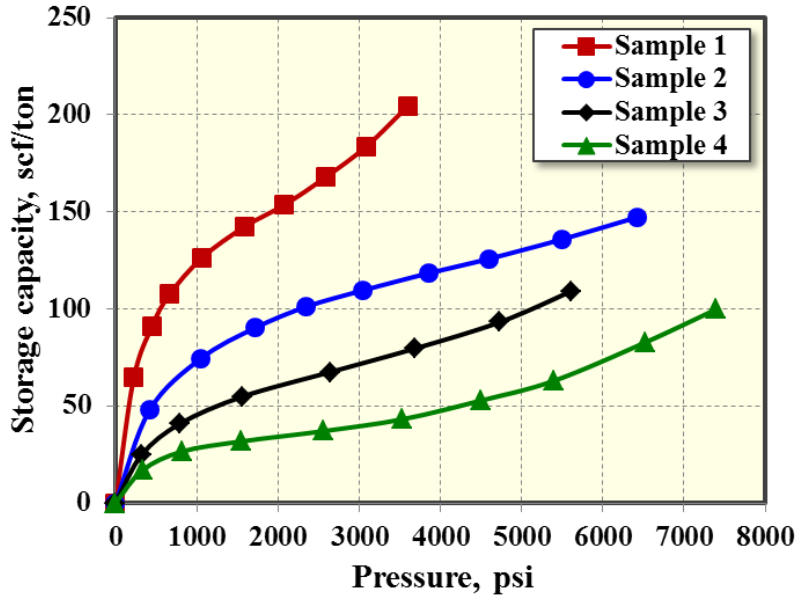

Figure 3.4: Experimental measurements of gas adsorption from the lower Marcellus shale.

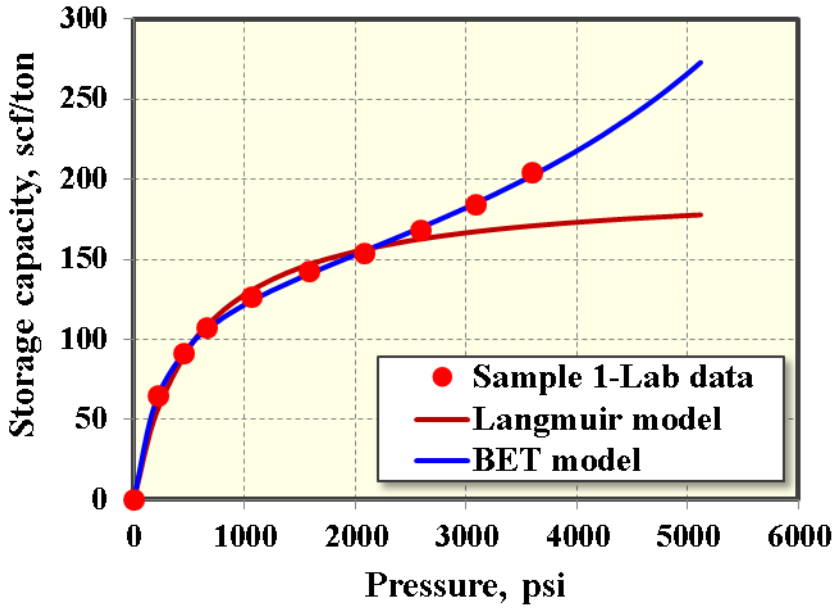

(a)

For Figure 3.5(b) and (c), see next page

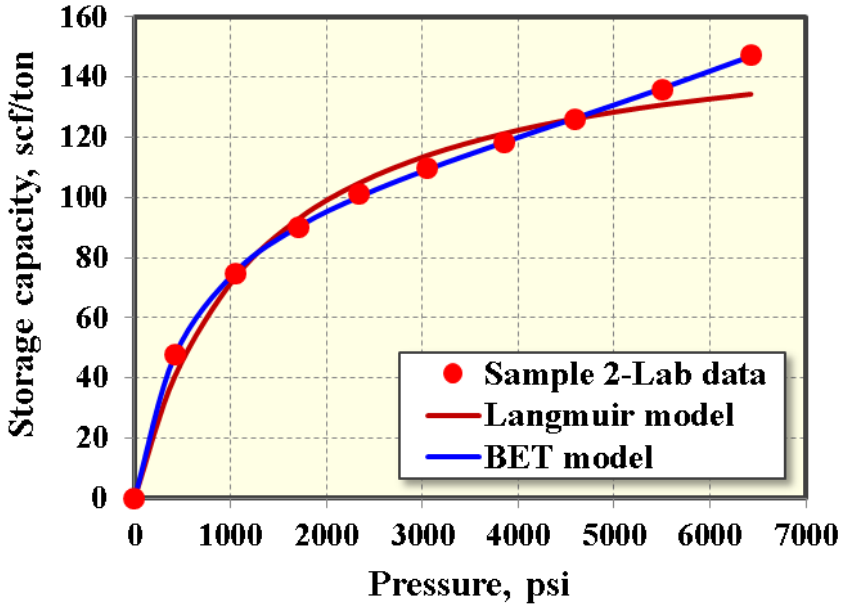

(b)

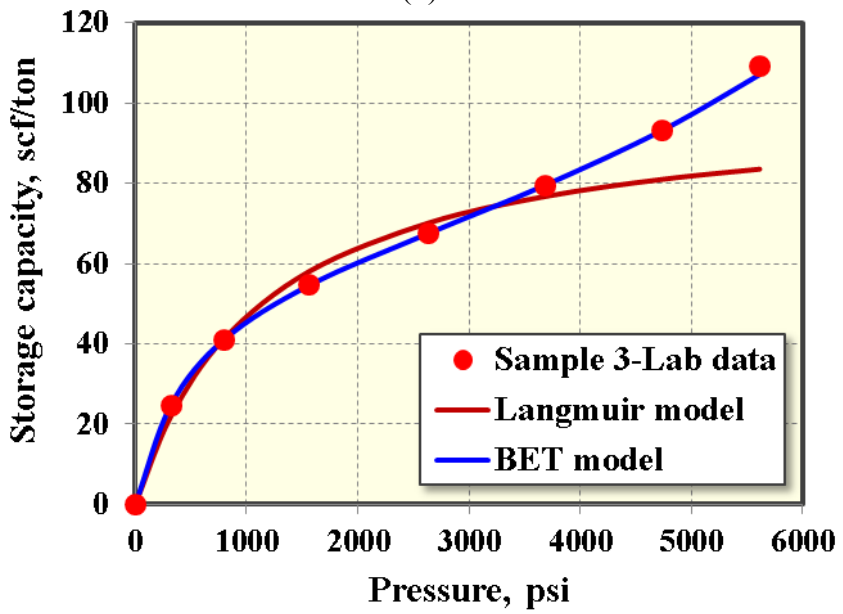

(c)

For Figure 3.5(d), see next page

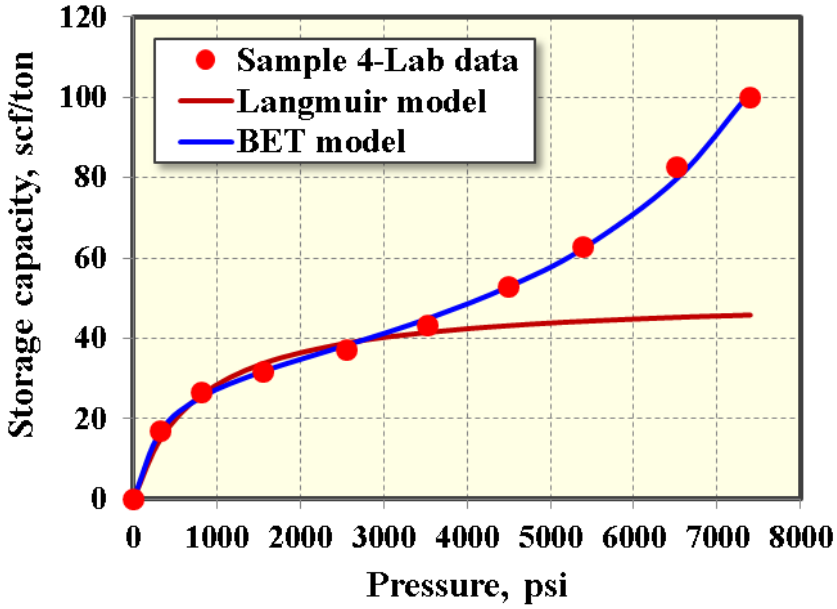

(d)

Figure 3.5: Comparison of fitting results using the Langmuir and BET isotherms. (a) Sample 1. (b) Sample 2. (c) Sample 3. (d) Sample 4.

Langmuir parameters	Sample 1	Sample 2	Sample 3	Sample 4
p_L, psi	535	1240	1144	776.4
v_L, scf/ton	196.4	160.3	100.6	50.7
R^2	0.908	0.961	0.84	0.195

Table 3.1: Langmuir isotherm parameters used for fitting the measurements.

BET parameters	Sample 1	Sample 2	Sample 3	Sample 4
p_o, psi	9833.4	21030.5	12292.8	10748.2
v_m, scf/ton	134.07	108.34	61.05	32.03
C	39.14	36.88	24.43	33.46
R^2	0.999	1.00	1.00	0.997

Table 3.2: BET isotherm parameters used for fitting the measurements.

The relationship between the TOC and gas storage capacity at the reference pressure of 5,000 psi is shown in Figure 3.6, illustrating that a good linear relationship is obtained. Based on Eq. 3.2, the specific surface area for the four samples is calculated by assuming the diameter of methane to be 0.4 nm, as shown in Figure 3.7. The range of specific surface area for the Marcellus shale is 3.38-14.16 m^2/g.

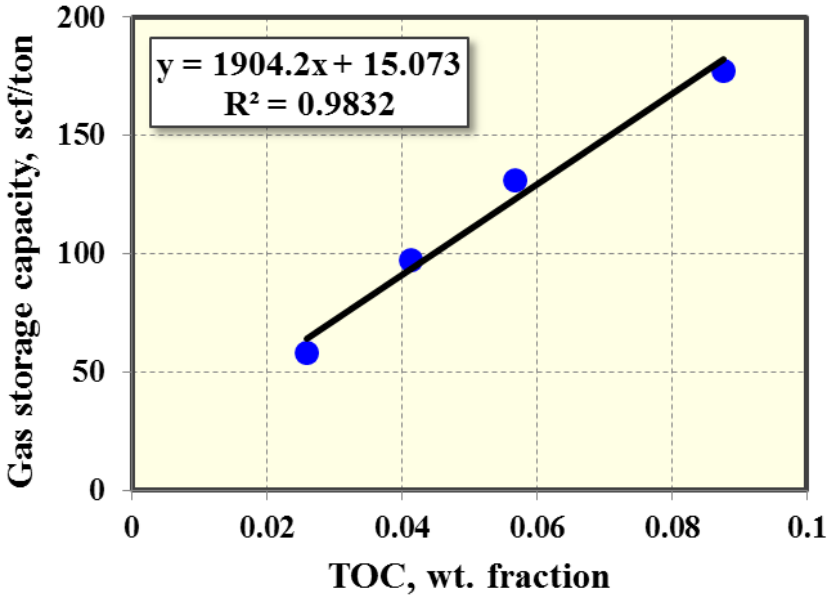

Figure 3.6: Relationship between gas storage capacity and the TOC.

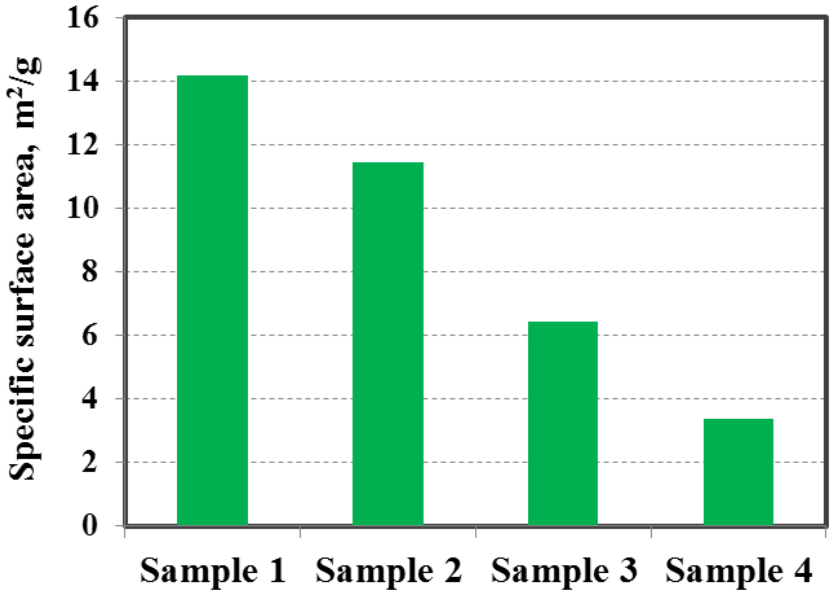

Figure 3.7: Specific surface area of four samples.

3.5 COMPARISON OF FREE GAS AND ADSORBED GAS

It can be seen from Eq. 3.5 that $(1-\phi)Ka$ and ϕS_g represent the contributions of adsorbed gas and free gas in shale. The actual reservoir properties of Marcellus shale are used. Porosity of 0.142 and initial gas saturation of 90% are employed for calculation. We calculated the $(1-\phi)Ka$ of four samples using Eq. 2.35 for the Langmuir isotherm and Eq. 2.36 for BET isotherm, respectively, as shown in Figure 3.8. For the Langmuir isotherm, Figure 3.8(a) shows that gas desorption is comparable to free gas at low reservoir pressure, while gas desorption is less important at high reservoir pressure. However, for the BET isotherm, Figure 3.8(b) illustrates that gas desorption is significant at both high and low reservoir pressure.

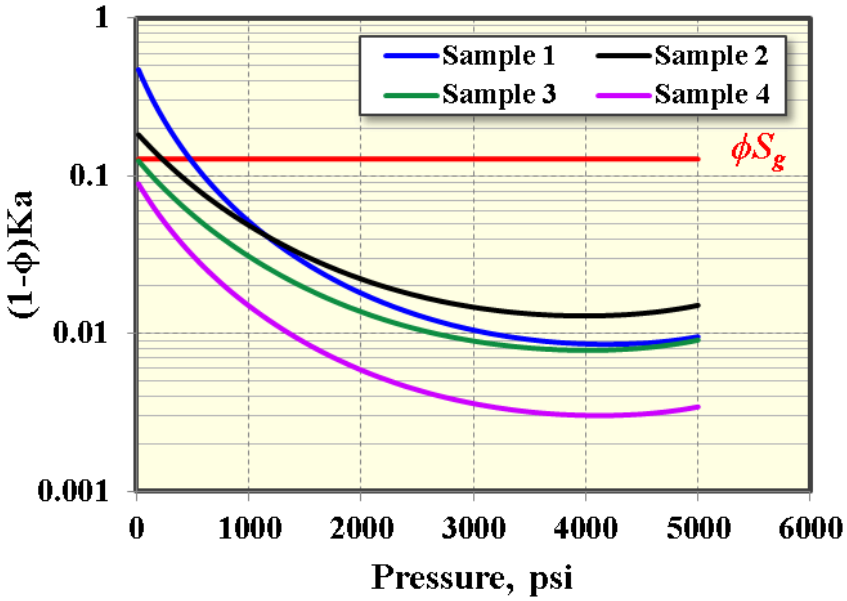

(a)

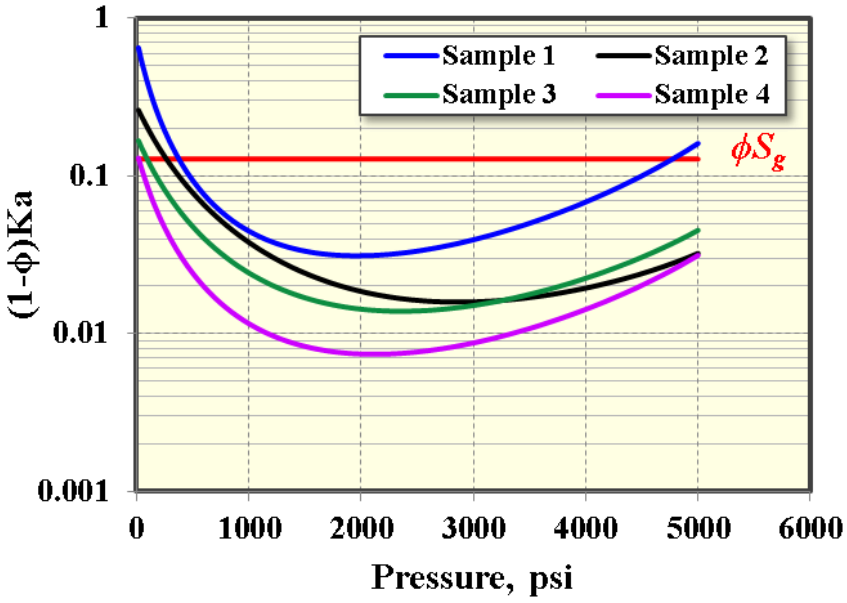

(b)

Figure 3.8: Comparison of free gas and adsorbed gas with different isotherms. (a) Langmuir isotherm used for calculation. (b) BET isotherm used for calculation.

3.6 CALCULATION OF ORIGINAL GAS IN PLACE

The traditional method for calculating the original gas in place (OGIP) for free gas is expressed below (Ambrose et al., 2010):

$$v_f = 32.0368 \times \frac{\phi S_{gi}}{\rho_b B_g}, \tag{3.6}$$

where v_f is the free gas volume in scf/ton, ϕ is reservoir porosity, S_{gi} is the initial gas saturation, ρ_b is the bulk rock density, g/cm^3, and B_g is the gas formation volume factor in reservoir volume/surface volume.

Ambrose et al. (2010) proposed a new method to calculate the free gas volume by considering the volume occupied by the adsorbed gas on the surface based on the Langmuir isotherm equation. The porosity occupied by adsorbed gas based on the Langmuir isotherm is

$$\phi_{a\_Langmuir} = 1.318 \times 10^{-6} M \frac{\rho_b}{\rho_s} \times \left(\frac{v_L p}{p + p_L} \right). \tag{3.7}$$

The final governing expression is shown below:

$$v_{f\_Langmuir} = \frac{32.0368}{B_g} \left[\frac{\phi(1 - S_w)}{\rho_b} - \frac{1.318 \times 10^{-6} M}{\rho_s} \times \left(\frac{v_L p}{p + p_L} \right) \right], \tag{3.8}$$

where S_w is the initial water saturation; ρ_s is the adsorbed gas density, g/cm^3; and M molecular weight of natural gas, lbm/lbmole.

The total original gas in place can be obtained by summation of free gas volume and adsorbed gas volume:

$$v_{t\_Langmuir} = v_{f\_Langmuir} + v_{a\_Langmuir}, \tag{3.9}$$

where $v_{f\_Langmuir}$ is the free gas volume based on the Langmuir isotherm, scf/ton, $v_{a\_Langmuir}$ is the adsorbed gas volume based on the Langmuir isotherm, scf/ton, and $v_{t\_Langmuir}$ is the total gas volume based on the Langmuir isotherm, scf/ton.

In this work, we modified the model for calculating original gas in place proposed by Ambrose et al. (2010) by considering the BET isotherm. The porosity occupied by adsorbed is modified as follows for the BET isotherm:

$$\phi_{a\_BET} = 1.318\times10^{-6} M \frac{\rho_b}{\rho_s} \times \left\{ \frac{v_m C p}{(p_o - p)\left[1+(C-1)\,p/p_o\right]} \right\}. \tag{3.10}$$

The governing equation is obtained below:

$$v_{f\_BET} = \frac{32.0368}{B_g} \left\{ \frac{\phi(1-S_w)}{\rho_b} - \frac{1.318\times10^{-6} M}{\rho_s} \times \left\{ \frac{v_m C p}{(p_o - p)\left[1+(C-1)\,p/p_o\right]} \right\} \right\}. \tag{3.11}$$

The total original gas in place can be obtained by summation of free gas volume and adsorbed gas volume:

$$v_{t\_BET} = v_{f\_BET} + v_{a\_BET}, \tag{3.12}$$

where v_{f_BET} is the free gas volume based on the BET isotherm in scf/ton, v_{a_BET} is the adsorbed gas volume based on the BET isotherm in scf/ton, and v_{t_BET} is the total gas volume based on the BET isotherm in scf/ton.

The actual reservoir properties of Marcellus shale are used for the calculation of original gas in place, as shown in Table 2.3. Using Eqs. 3.6-3.12, the porosities of gas adsorption, free gas in place, adsorbed gas in place, and the total original gas in place are calculated, as summarized in Tables 2.4 and 2.5. As shown, the average total original gas in place is 519 scf/ton, calculated using the BET isotherm, which is larger than the 507 scf/ton calculated using the Langmuir isotherm. Hence, characterizing the gas adsorption isotherm is important for quantifying the total original gas in place and evaluating the economic potential of gas shales.

Parameter	Value	Unit
Initial reservoir pressure	5,000	psi
Reservoir temperature	130	°F
Reservoir porosity	14%	
Initial water saturation	10%	
B_g	0.0033	
M	20	lb/lb-mol
ρ_b	2.63	g/cm^3
ρ_s	0.42	g/cm^3

Table 3.3: Parameters used for calculation in the Marcellus shale.

Sample	ϕ_{a_BET}	v_{a_BET}, scf/ton	v_{f_BET}, scf/ton	v_{t_BET}, scf/ton
1	0.044	266.18	302.92	569.10
2	0.022	130.77	385.43	516.19
3	0.016	97.11	405.93	503.05
4	0.010	57.90	429.83	487.72

Table 3.4: Original gas in place calculation based on the BET isotherm.

Sample	$\phi_{a\_Langmuir}$	$v_{a\_Langmuir}$, scf/ton	$v_{f\_Langmuir}$, scf/ton	$v_{t\_Langmuir}$, scf/ton
1	0.029	177.44	356.99	534.43
2	0.021	128.42	386.86	515.28
3	0.014	81.87	415.22	497.09
4	0.007	43.85	438.38	482.24

Table 3.5: Original gas in place calculation based on the Langmuir isotherm.

3.7 NUMERICAL SIMULATION MODEL

In this work, a compositional simulator of CMG-GEM (CMG-GEM, 2012) is used to model multiple hydraulic fractures and gas flow in Marcellus shale reservoirs. In our simulation model, local grid refinement (LGR) with logarithmic cell spacing is used to accurately model gas flow from shale matrix to hydraulic fractures. Non-Darcy flow is considered for which the non-Darcy Beta factor, used in the Forchheimer number, is determined using a correlation proposed by Evans and Civan (1994). In the simulation model, the Langmuir isotherm is used to model gas desorption. Also, the adsorption data obeying the BET isotherm can be entered as a table form. Increase in gas recovery is used to assess the contribution of gas desorption in this work, and it is defined by

$$\text{Increase in gas recovery} = \frac{Q_{GasDesorption} - Q_i}{Q_{GasDesorption}}, \tag{3.13}$$

where $Q_{GasDesorption}$ is cumulative gas production with gas desorption effect, whereas Q_i is cumulative gas production without gas desorption effect.

3.8 BASIC RESERVOIR MODEL

A Marcellus shale area of about 207 acres was simulated by setting up a basic 3D reservoir model with dimensions of 6,000 ft × 1,500 ft × 130 ft, which corresponds to length, width, and thickness, respectively, as shown in Figure 3.9. The reservoir has two shale layers. Porosity of bottom and upper layers is around 14.2% and 7.1%, respectively. The horizontal well are stimulated in the bottom layer with 16 fracturing stages and four perforation clusters per stage with cluster spacing of 50 ft. The total well length is 3,921 ft. The production data was provided by Chief Oil and Gas LLC. There are almost 190 days of production data available for performing history matching and evaluating the effect of gas desorption on well performance.

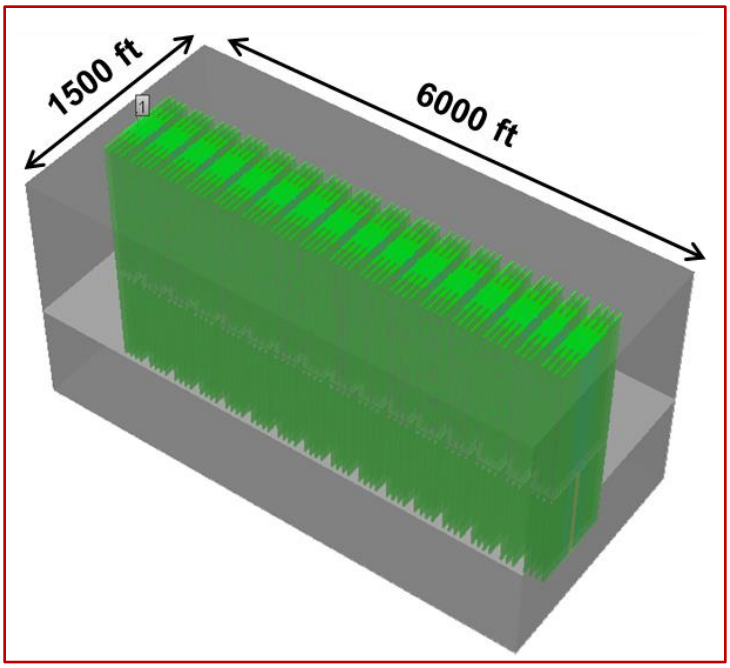

Figure 3.9: A basic 3D reservoir model for the Marcellus shale.

Table 3.6 summarizes the detailed reservoir and fracture properties of this well. The reservoir is assumed to be homogeneous and the fractures are evenly spaced, with stress-independent porosity and permeability. The flowing bottom hole pressure in Figure 3.10 is used to constrain the simulation and cumulative gas production is the history-matching variable. Table 3.7 lists reservoir permeability and fracture properties with a good history match without considering the gas desorption effect, as shown in Figure 3.11.

Parameter	Value	Unit
Initial reservoir pressure	5,100	psi
Reservoir temperature	130	^{o}F
Reservoir permeability	800	nD
Reservoir porosity (upper layer)	7.1%	
Reservoir porosity (bottom layer)	14.2%	
Initial water saturation	10%	
Total compressibility	3×10^{-6}	psi^{-1}
Horizontal well length	3,921	ft
Number of stages	16	
Cluster spacing	50	ft
Fracture half-length	400	ft
Fracture conductivity	3.5	md-ft
Fracture height	95	ft
Total number of fractures	64	
Gas specific gravity	0.58	

Table 3.6: Reservoir and fracture parameters for the Marcellus shale well.

Parameter	Value	Unit
Reservoir permeability	800	nD
Fracture half-length	400	ft
Fracture conductivity	3.5	md-ft
Fracture height	95	ft

Table 3.7: Reservoir and fracture parameters used for a good history match.

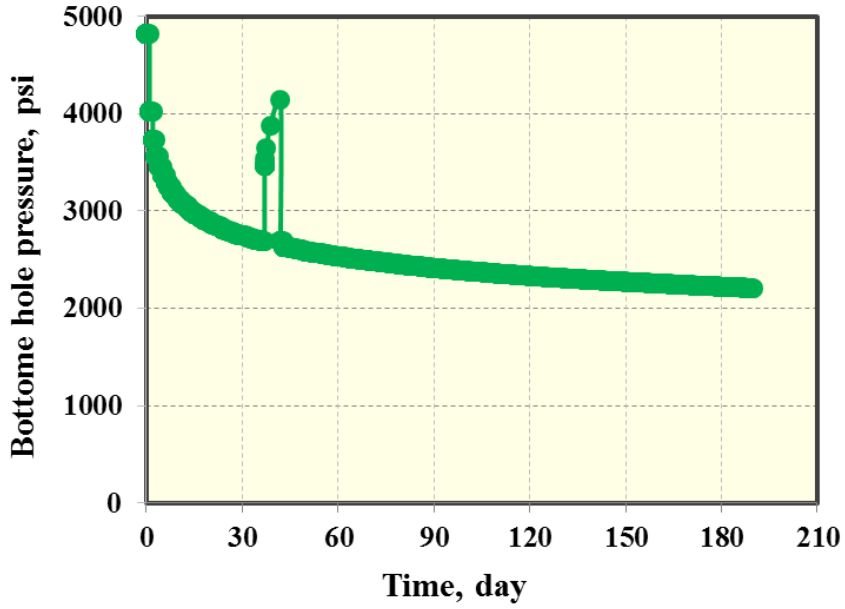

Figure 3.10: Flowing bottom hole pressure of the Marcellus shale well.

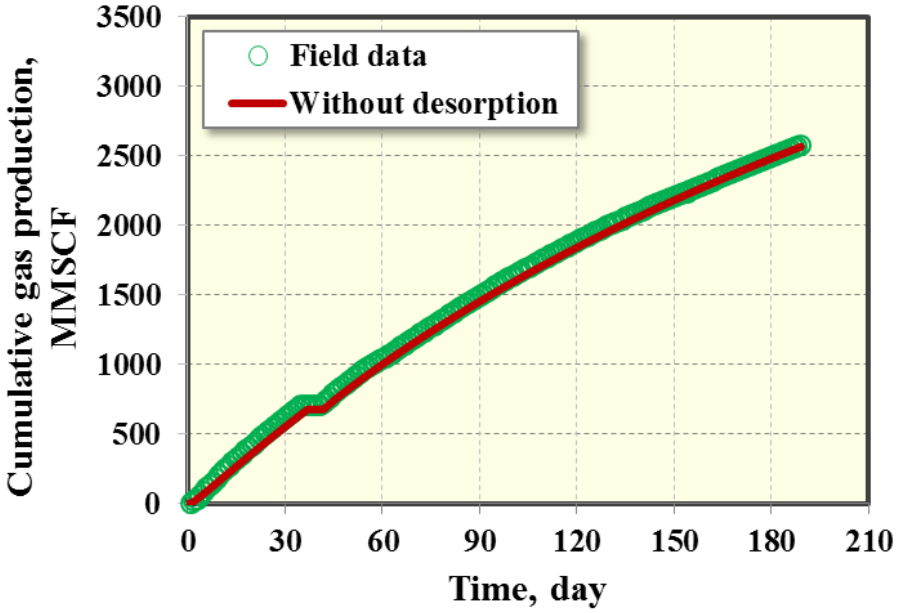

Figure 3.11: Comparison between simulation data and the field data of the Marcellus shale well.

In the subsequent simulation studies, we performed history matching by considering gas desorption from the four shale samples and production forecasting for a 30-year period by gradually dropping the bottom hole pressure at 190 days to 2,000 psi within one month and then maintaining 2,000 psi until 30 years. The comparisons of gas desorption effect between the Langmuir and the BET isotherms for the four shale samples are shown in Figures 3.12 through 3.15. It can be seen that gas desorption with the BET isotherm contributes more significantly to gas recovery than that with the Langmuir isotherm at the early time of production (190 days). The range of increase in gas recovery after 190 days of production with the BET isotherm is 6.3%-26%, while the range with the Langmuir isotherm is 1.1%-4.7%. At 30 years of production, the range of increase in gas recovery with the BET isotherm is 8.1%-36.5%, while the range with the Langmuir isotherm is 4.3%-15.1%. Hence, it can be concluded that the gas desorption effect with the BET isotherm plays an important role in performing history matching at early time of production and predicting the ultimate gas recovery.

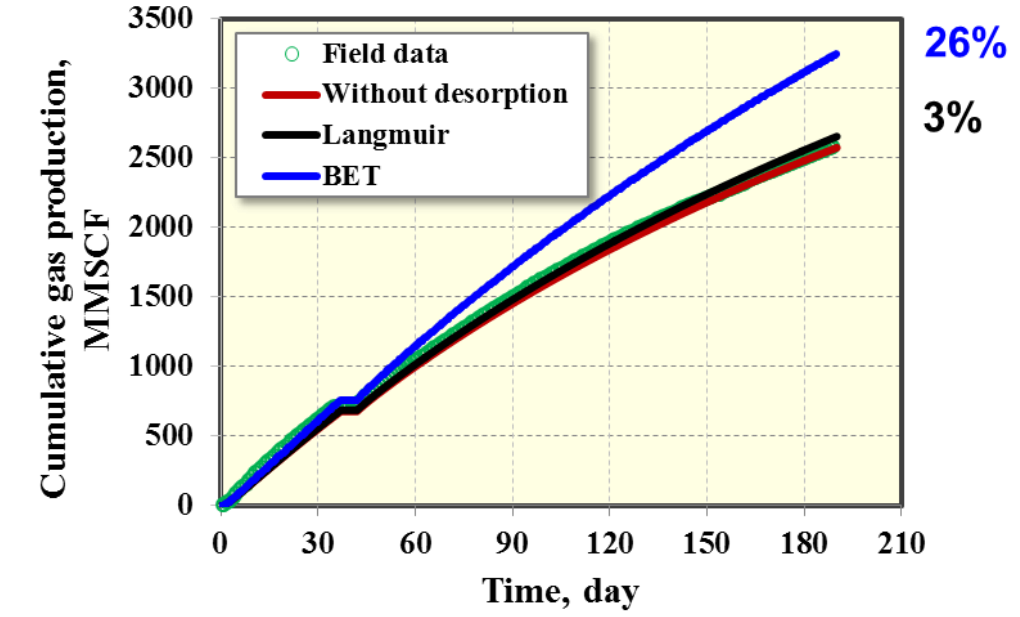

(a)

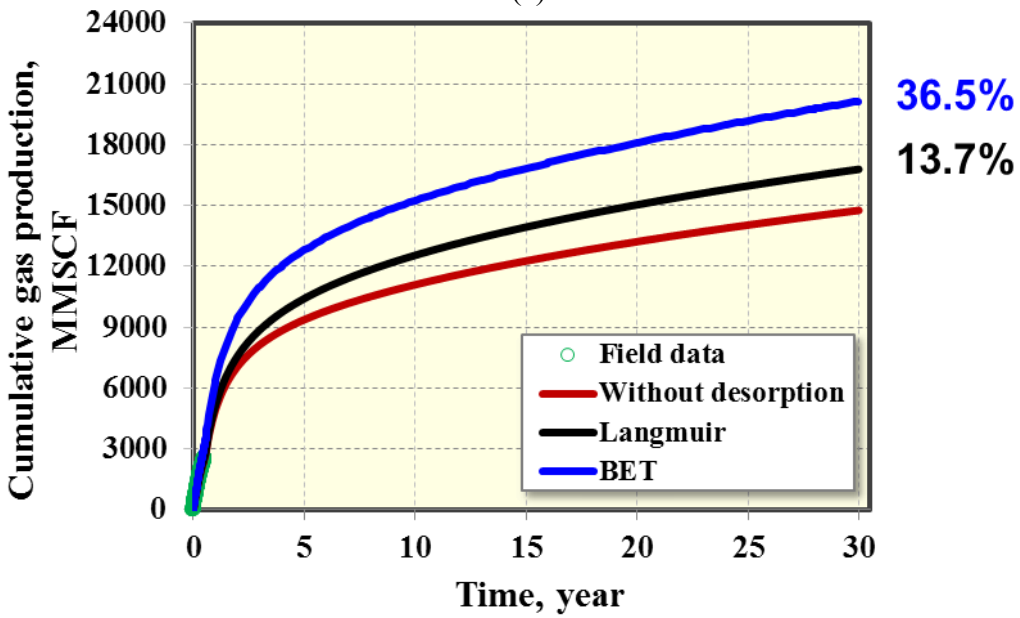

(b)

Figure 3.12: Comparison of gas desorption with the Langmuir and BET isotherms for sample 1. (a) History matching. (b) Production forecasting.

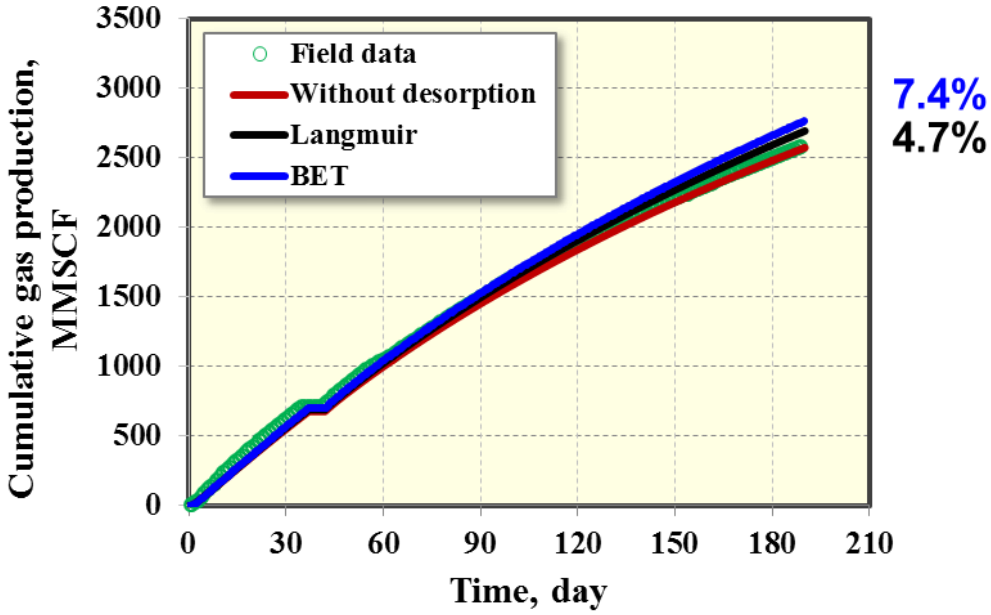

(a)

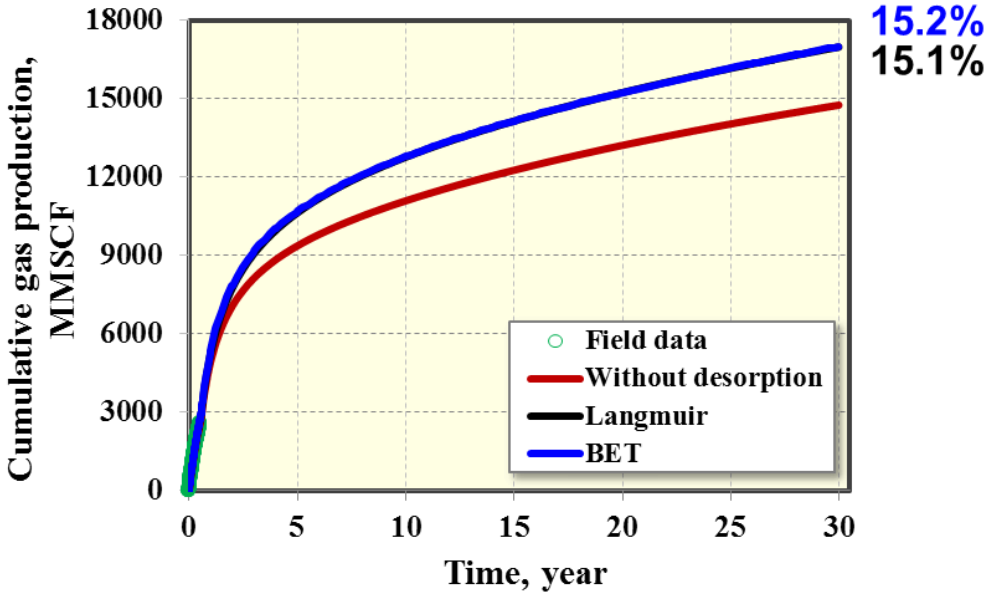

(b)

Figure 3.13: Comparison of gas desorption with the Langmuir and BET isotherms for sample 2. (a) History matching. (b) Production forecasting.

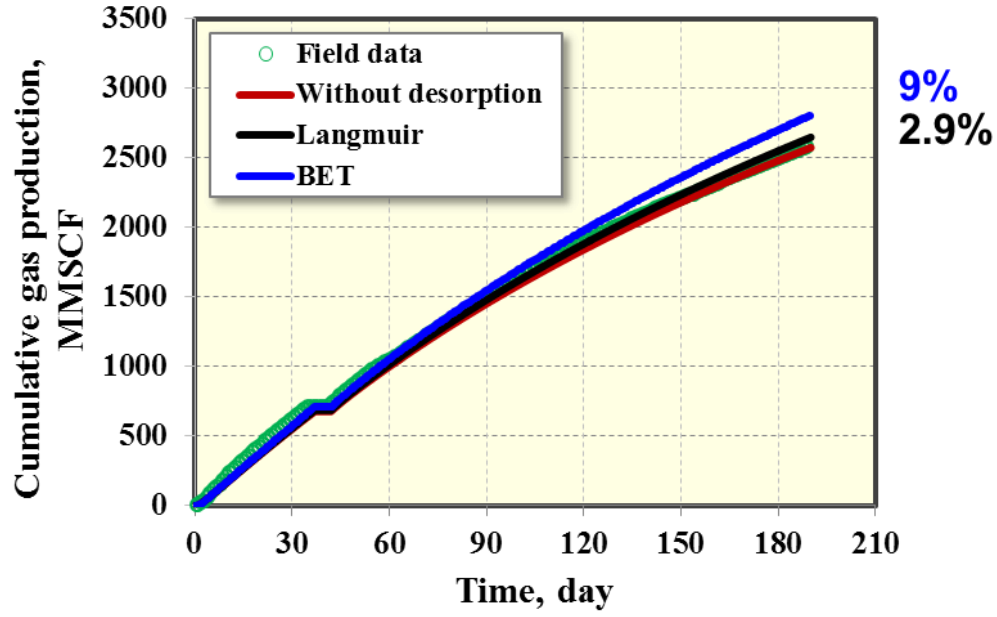

(a)

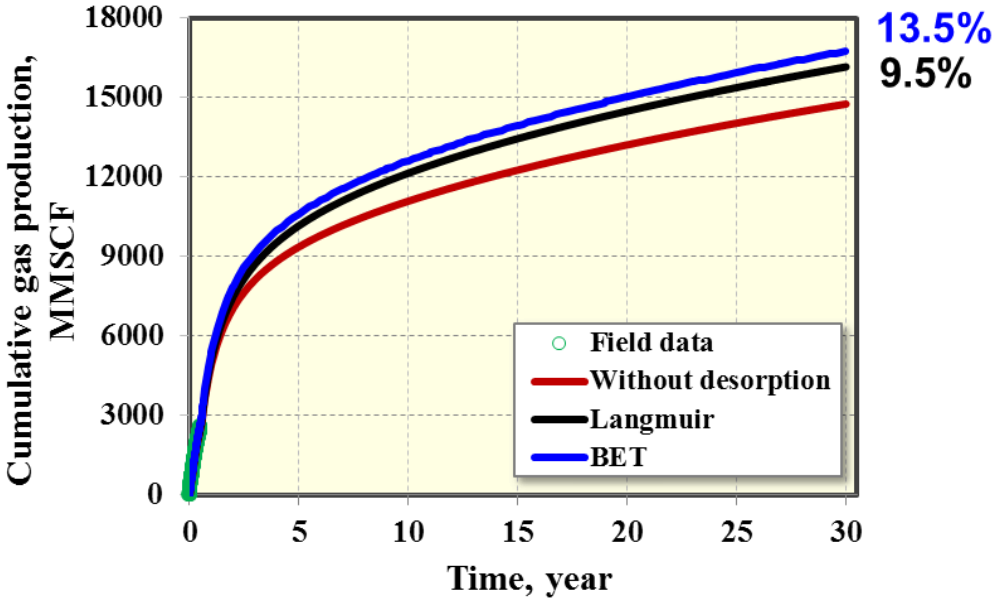

(b)

Figure 3.14: Comparison of gas desorption with the Langmuir and BET isotherms for sample 3. (a) History matching. (b) Production forecasting.

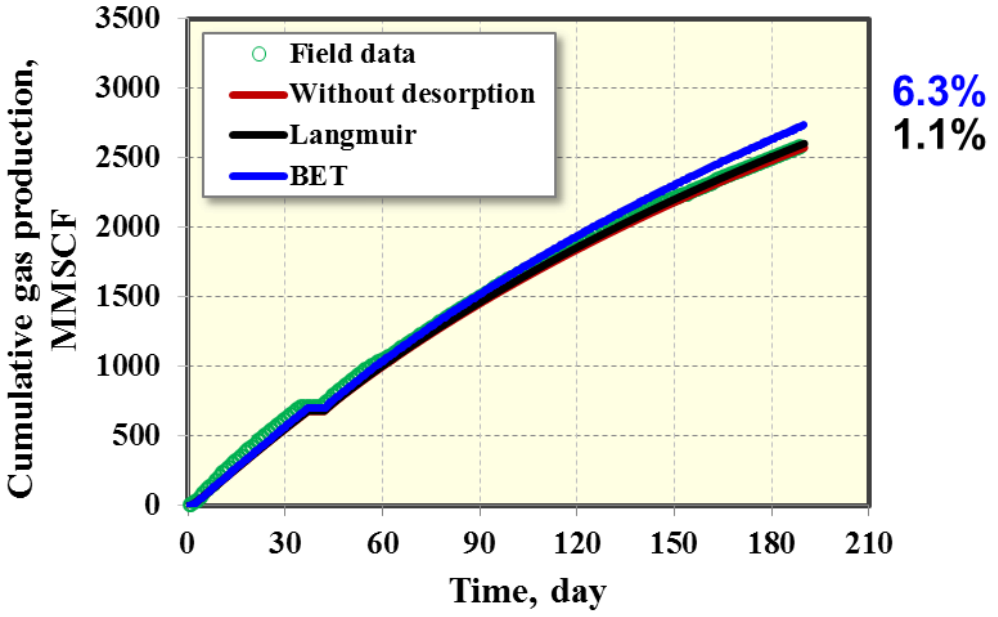

(a)

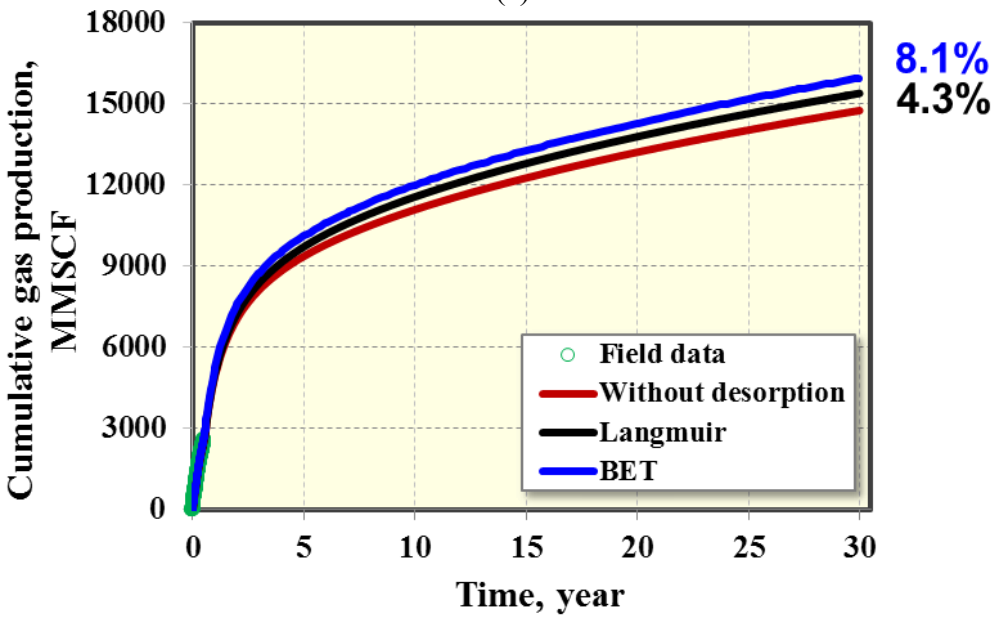

(b)

Figure 3.15: Comparison of gas desorption with the Langmuir and BET isotherms for sample 4. (a) History matching. (b) Production forecasting.

3.9 CONCLUSIONS

We analyzed the laboratory measurements of methane adsorption from four shale samples in some area of the Marcellus shale using the Langmuir and BET isotherms. The effect of gas adsorption on calculation of original gas in place and well performance has been investigated. The following conclusions can be drawn from this study:

(1) The measured gas adsorption in four samples from the lower Marcellus shale is better described by the BET isotherm, rather than by the Langmuir isotherm in this case study.

(2) A good linear relationship between gas storage capacity and TOC is obtained.

(3) The range of specific surface areas for the Marcellus shale is 3.38-14.16 m^2/g.

(4) Adsorbed gas with the gas desorption behavior obeying the BET isotherm is comparable to the free gas at both low and high reservoir pressure.

(5) The average total original gas in place is 519 scf/ton when calculated using the BET isotherm, and 507 scf/ton calculated using the Langmuir isotherm for the Marcellus shale in this study.

(6) For the horizontal well investigated in this study, the range of increase in gas recovery at 190 days of production with the BET isotherm is 6.3%-26%, while the range with the Langmuir isotherm is 1.1%-4.7%. After 30 years of production, the range of increase in gas recovery with the BET isotherm is 8.1%-36.5%, while the range with the Langmuir isotherm is 4.3%-15.1%.

CHAPTER 4: An Integrated Reservoir Simulation Framework for Shale Reservoirs

In the development of unconventional resources, there are high cost and considerable uncertainties because of many inestimable and uncertain parameters (e.g., reservoir permeability, porosity, number of fracture, fracture spacing, fracture half-length, fracture conductivity, gas desorption, geomechanics, and well spacing). Therefore, the development of an approach for sensitivity analysis, history matching, and optimization of fracture treatment design for the economic development of unconventional resources in an efficient and practical manner is clearly desirable. In this chapter, we present an integrated reservoir simulation framework to perform sensitivity analysis, history matching and economic optimization for shale gas and tight oil reservoirs by integrating numerical reservoir simulators, the semi-analytical model developed in Chapter 2, an economic model, two statistical methods including Design of Experiment (DOE) and Response Surface Methodology (RSM) with an efficient platform of ISPUR (Integrated Simulation Platform for Unconventional Reservoirs). Specifically, we first use DOE to determine the rank of influential parameters and screen insignificant ones; then, we perform history matching based on the rank of important parameters; subsequently, we use RSM to design models using design factors to fit a response surface; finally, we identify the most economical production scenario under conditions of uncertainty. This framework is effective and efficient for hydraulic fracture treatment design and production scheme optimization for single well and multiple wells in shale gas and tight oil reservoirs. It can contribute to providing guidance for engineers to modify the design of a hydraulic fracture treatment before the actual fracture treatment.

4.1 INTRODUCTION

The combination of horizontal drilling and multistage fracturing technology has made possible the current flourishing gas and oil production from shale reservoirs in the United States, as well as the global fast growing investment in shale gas and tight oil exploration and development. However, there are high uncertainties in reservoir and fracture properties, which have significant effects on well performance and economics. In reality, the ultralow permeability of shale ranges from 10 to 100 nano-Darcy. The operation cost of drilling and multistage fracturing is high, although it can make production from shale reservoirs that were previously recognized as caprock feasible economically. The optimization of hydraulic fracture parameters (e.g., number of fracture, fracture spacing, fracture half-length, and fracture conductivity) and well spacing is important to obtain the most economical scenario. In addition, with the development of unconventional resources, a large number of wells have been drilled and need to be evaluated efficiently. Therefore, the development of a method to quantify uncertainties, perform history matching and optimize production in an efficient and practical manner is clearly desirable.

There have been a significant number of attempts in recent years to optimize the design of transverse fractures of horizontal wells for shale gas reservoirs (Britt and Smith, 2009; Marongiu-Porcu et al., 2009; Zhang et al., 2009; Bagherian et al., 2010; Meyer et al., 2010; Bhattacharya and Nikolaou, 2011; Gorucu and Ertekin, 2011). In most of the reviewed works, the optimum fracture design is identified by local sensitivity analysis and one variable is usually varied while keeping all the other variables fixed. These optimization methods do not provide sufficient insights for screening insignificant parameters and considering parameter interactions to obtain the optimal design. Additionally, most reservoir modelling work in the literature has ignored the combined

impact of gas desorption and geomechanics on ultimate gas and oil recovery. If factors playing an important role in shale gas and tight oil production are unknown, it is obviously important to perform a screening design to identify which factors are significant. Different approaches such as Design of Experiment (DOE) and Response Surface Methodology (RSM) have been used to address the uncertainties (Damsleth et al., 1992; Dejean and Blanc, 1999). RSM is an efficient statistical method for evaluation and optimization of complex processes. Therefore, in this study, we developed an integrated reservoir simulation framework by combining numerical reservoir simulators, the semi-analytical model developed in Chapter 2, an economic model, DOE and RSM with an efficient platform of ISPUR (Integrated Simulation Platform for Unconventional Reservoirs) to perform a large number of reservoir simulation scenarios in order to optimize fracture design and multiple well placement for the economic development of shale gas and tight oil reservoirs.

4.2 DESIGN OF EXPERIMENT

DOE is a systematic method used to determine the relationship between uncertain factors affecting a process and the response of that process. It can be used to evaluate statistically the significance of different factors at the lowest experimental costs (Zhang et al., 2007).

Factorial designs are widely used in DOE to study several uncertain factors with the purpose of identifying both main effects and interactions. Two-level factorial design is a special case of factorial designs in which each factor is only given two values to determine the range: the minimum value and the maximum value. The design for k factors requires 2^k experimental runs. Therefore, it is called 2^k factorial design (Myers et al., 2008). It can investigate not only the effect from a single parameter but also the effect

from the interaction of parameters, compared with the traditional sensitivity analysis method such as changing one variable at a time.

When there are many factors involved, the full factorial design is not applicable in practice because an extensive number of factor combinations are required to be investigated. For example, 10 factors require 2^{10} (1,024) combinations to be investigated. However, this problem can be solved by using the two-level fractional factorial design, which can offer fewer numbers of scenarios. For example, one-half fractional factorial design, called 2^{k-1} fractional factorial design, would reduce by half the total number of cases required for the 2^k design. The selection of two-level fractional factorial design with a minimum number of cases is primarily based on the smallest effect from aliasing (Peng and Gupta, 2003) and the highest possible resolution (Myers et al., 2008).

4.3 RESPONSE SURFACE METHODOLOGY

RSM is a group of statistical and mathematical techniques, which is used to optimize processes. It can generate an empirical model from observed data of the system to approximately represent the true response surface of the objective function over a region of interest specified by the range of variability of input factors. Net present value (NPV) is often used as the objective function to perform economic analysis of shale gas and tight oil wells. The generated empirical model can be represented in a form of the linear regression model as follows:

$$y = \beta_o + \beta_1 x_1 + \beta_2 x_2 + \cdots\cdots + \beta_k x_k + \varepsilon \,, \tag{4.1}$$

where y is the objective function, x_i, i = 1, 2, ……, k, are uncertain variables, β_i, i = 0, 1, 2, ……, k, are regression coefficients, k is the number of uncertain variables investigated and optimized in the study, and ε is the error term. This equation is called a multiple linear

regression model with *k* repressors. It can also be modified by adding an interaction term as shown below:

$$y = \beta_o + \beta_1 x_1 + \beta_2 x_2 + \cdots\cdots + \beta_k x_k + \sum_{i<j}^{k} \sum_{=2} \beta_{ij} x_i x_j + \varepsilon \,. \tag{4.2}$$

Or it can be modified to form the second-degree polynomial equation as follows:

$$y = \beta_o + \beta_1 x_1 + \beta_2 x_2 + \cdots\cdots + \beta_k x_k + \sum_{i<j}^{k} \sum_{=2} \beta_{ij} x_i x_j + \sum_{i=1}^{k} \beta_{ii} x_i^{\,2} + \varepsilon \,. \tag{4.3}$$

Two popular designs, central composite design (CCD) and D-optimal design, are often used to fit the second-degree surface model. More detailed mathematical and statistical theories of CCD and D-optimal design can be found in the work by Myers et al. (2008).

4.4 ECONOMIC ANALYSIS

NPV is one of the most common methods used to evaluate the economic viability of investing in a project. The NPVs of shale gas and tight oil wells are calculated by use of the following expression:

$$NPV = \sum_{j=1}^{n} \frac{\left(V_F\right)_j}{\left(1+i\right)^j} - \sum_{j=1}^{n} \frac{\left(V_O\right)_j}{\left(1+i\right)^j} - \left[FC + \sum_{k=1}^{N} (C_{well} + C_{fracture}) \right], \tag{4.4}$$

where V_F is future value of production revenue for a fractured shale reservoir, V_o is future value of production revenue for an unfractured shale reservoir, FC is the total fixed cost, C_{well} is the cost of a single horizontal well, $C_{fracture}$ is the cost of hydraulic fracturing in a single horizontal well, N is the number of horizontal wells, i is the interest rate, and n is the number of periods.

4.5 INTEGRATED RESERVOIR SIMULATION FRAMEWORK

We present an integrated reservoir simulation framework for optimization of shale gas and tight oil production, as shown in Figure 4.1. The framework combines numerical reservoir simulators, the semi-analytical model, an economic model, DOE, and RSM to optimize hydraulic fracture treatment design for the economic development of shale gas and tight oil reservoirs. An efficient platform of ISPUR is developed to make this framework perform sensitivity studies, history matching, and economic optimization more effectively and more efficiently. In addition, this framework can be applied to investigate gas injection for enhanced oil recovery (EOR) in tight oil reservoirs and enhanced gas recovery (EGR) in shale gas reservoirs.

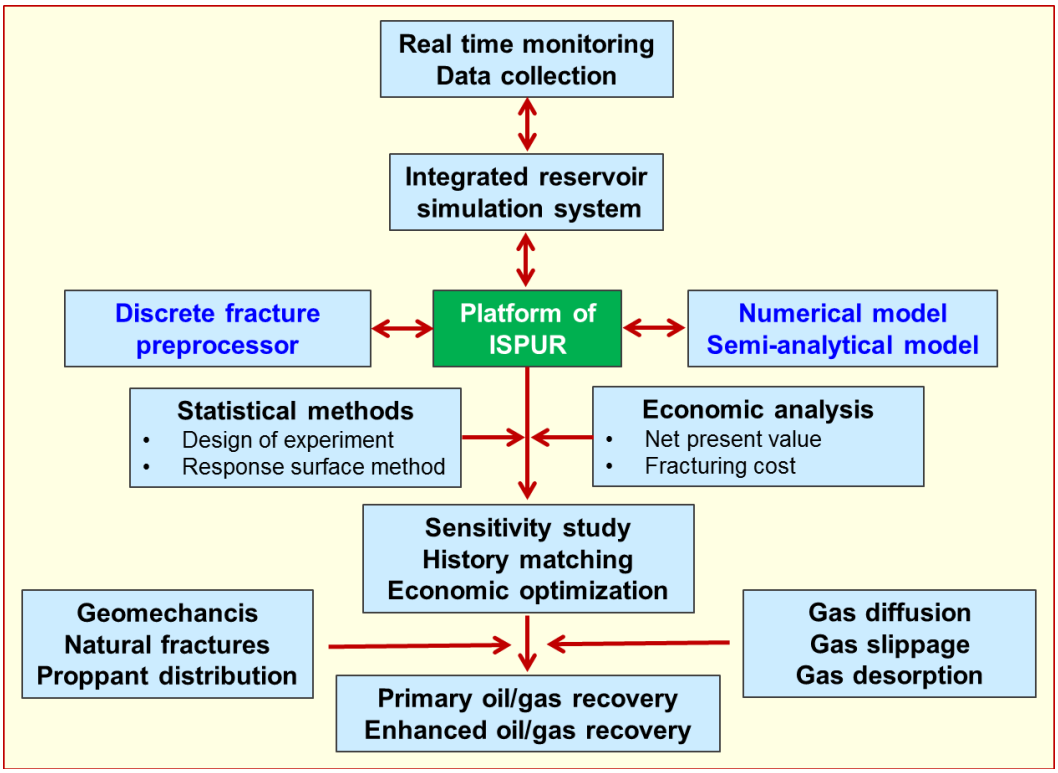

Figure 4.1: An integrated simulation framework for the economic development of shale gas and tight oil reservoirs.

4.5.1 Reservoir modeling including multiple fractures

In this framework, four fracture geometries can be handled during building a reservoir model for shale gas and tight oil reservoirs. They are bi-wing fractures, orthogonal fracture networks, unstructured fracture networks, and non-planar fractures. In addition, a three-dimensional fracture propagation model developed by Wu and Olson (2014a), which fully couples elastic deformation of the rock and fluid flow to simulate complex hydraulic fracture propagation, is used to predict the more-realistic non-planar fractures, which are input into the reservoir models to simulate production from such fractures. Three numerical reservoir simulators including CMG (Computer Modeling Group Ltd., 2012), ECLIPSE (Schlumberger, 2012) and UTCOMP (The University of Texas at Austin, 2014), and the semi-analytical model developed in the Chapter 2 are used to build reservoir model including multiple hydraulic fractures.

For shale gas simulation, the important gas transport mechanisms such as gas slippage, gas diffusion, and gas desorption can be simulated using the semi-analytical model. In addition, for gas flow in the fracture, the key effects of non-Darcy flow and geomechanics (stress-dependent fracture conductivity) can be taken into account.

4.5.2 Sensitivity study and optimization

A commercial software package of Design-Expert (Stat-Ease Incorporated, 2014) has been integrated in the framework to prepare multiple combinations based on investigated uncertain parameters, which are required by DOE and RSM. Also, it can be used for further results manipulation and graphical presentations. For sensitivity studies, the rank of important parameters and non-significant parameters can be quantified. For optimization, a response surface model describing the relationship between the objective function and important design variables can be obtained. Finally, the best case based on the response surface model can be determined.

4.5.3 Economic analysis

A package based on Microsoft Excel is designed and has been implemented in this framework to calculate NPV using the Eq. 4.4. The inputs mainly include gas price, oil price, well cost, well number, fracture cost, total fixed cost, interest rate, tax, cumulative gas production, and cumulative oil production. The fracture cost is related to fracture number, fracture area, and fracture conductivity. Fracture area is linked to liquid volume pumped and fracture conductivity is linked to proppant amount usage.

4.6 INTEGRATED SIMULATION PLATFORM FOR UNCONVENTIONAL RESERVOIRS

The approach of local grid refinement is often used to model hydraulic fractures and fracture networks, resulting in a complex gridding issue to prepare input files for reservoir simulators. In addition, a large number of simulation cases are required based on two statistical methods of DOE and RSE to perform sensitivity studies, history matching, and economic optimization. If these input files are prepared manually, it will be very time-consuming. Hence, an automated platform for simulation of unconventional reservoirs is necessary. In 2005, Zhang developed an integrated reservoir simulation platform (UT_IRSP) to prepare multiple reservoir simulation studies using different methodologies for the design and optimization of chemical flooding processes (Zhang, 2015). However, UT_IRSP is not designed for unconventional reservoirs with multiple hydraulic fractures. Consequently, in this work, we developed a new platform by borrowing the design principle of UT_IRSP, which is an integrated simulation platform for unconventional reservoirs (ISPUR), to generate a large number of input files for reservoir simulators more easily and more efficiently, as shown in Figure 4.2. ISPUR is designed and developed using MATLAB software package.

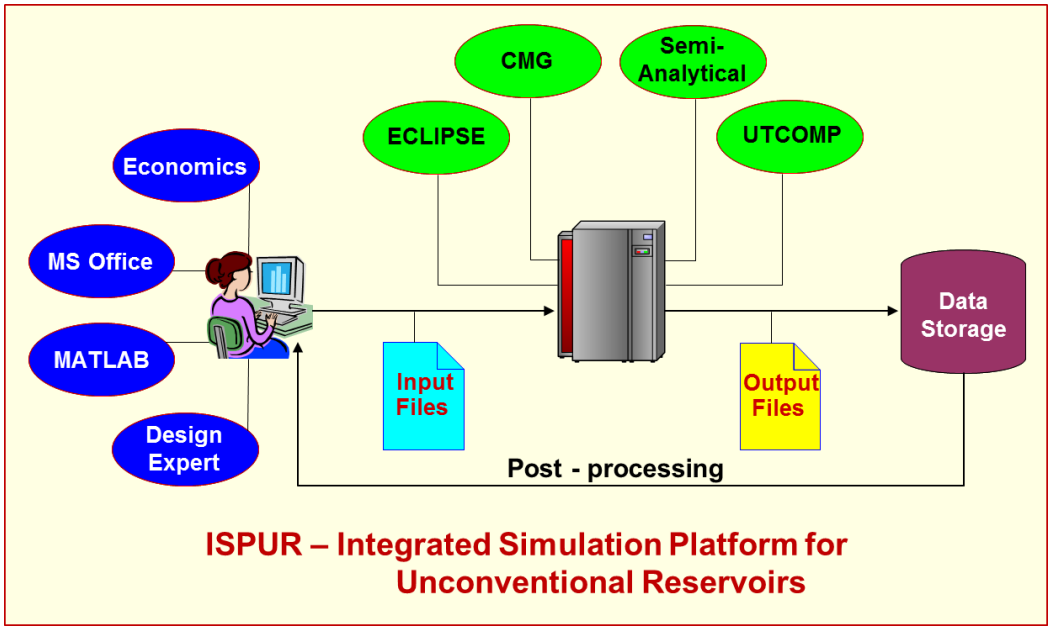

Figure 4.2: An integrated simulation platform for unconventional reservoirs (ISPUR) (modified from Zhang, 2005).

Before launching ISPUR, the main program requires the user to provide the name of reservoir simulator, the name of excel file for multiple cases, the number of uncertain parameters, the name of uncertain parameters, and the base case. After providing these requirements, the ISPUR will generate multiple cases automatically. Subsequently, ISPUR will call the executable files of different simulators to run these simulation cases automatically in a sequential mode (one simulation at a time) or a distributed mode (multiple simulations at a time). After finishing all simulation cases, the output files will be saved in different folders, which are named based on the simulation case number. Figure 4.3 shows one example of illustrating the workflow of using ISPUR to prepare and run 100 different simulation cases.

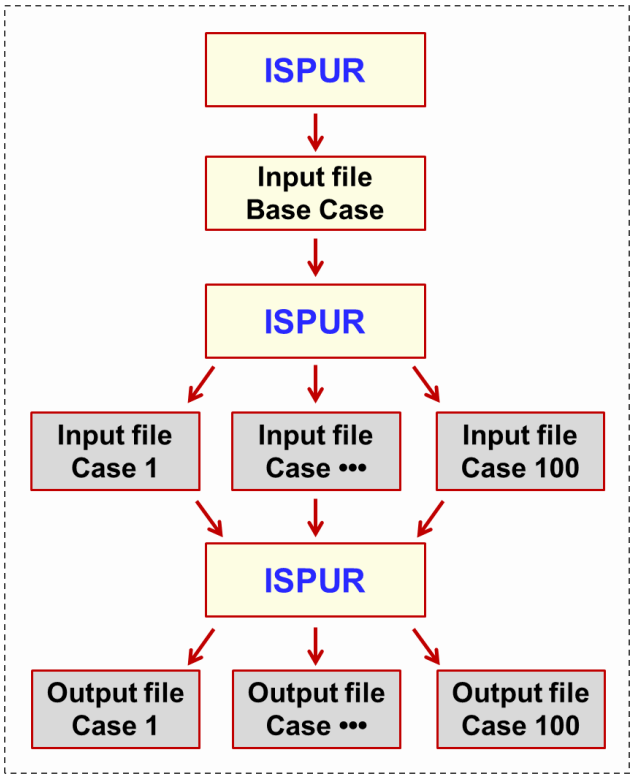

Figure 4.3: One example of illustrating the workflow of using ISPUR to prepare and run 100 different simulation cases.

4.6.1 Integration of reservoir simulators

In this platform, three numerical reservoir simulators including CMG (Computer Modeling Group Ltd., 2012), ECLIPSE (Schlumberger, 2012) and UTCOMP (The University of Texas at Austin, 2014), and the semi-analytical model developed in Chapter 2 have been integrated in the system. Specifically, for CMG software, CMG-IMEX (a black-oil simulator) and CMG-GEM (a compositional simulator) are included. For ECLIPSE, E100 (a black-oil simulator) and E300 (a compositional simulator) are included. UTCOMP is an in-house compositional simulator, which can simulate tight oil production with complex fracture networks using Embedded Discrete Fracture Model (EDFM) (Moinfar, 2013; Shakiba, 2014; Cavalcante Filho et al., 2015). The semi-

analytical model can be used to simulate shale gas and tight oil production from complex non-planar hydraulic fractures.

4.6.2 Base case

For preparing the input files of base case for different reservoir simulators, we develop pre-processing programs to generate these input files in order to simulate shale gas and tight oil production. Gas desorption and geomechanics effects are also included in the pre-processing programs. The main inputs include reservoir, fracture and well properties. After providing these properties, the programs will generate the input files of base case for different reservoir simulators automatically.

4.6.3 Multiple cases

The number of multiple cases is dependent on the number of uncertain parameters investigated. The package of Design-Expert (Stat-Ease Incorporated, 2014) is used to generate the required multiple combinations of the uncertain parameters. Subsequently, all the combinations will be stored as an Excel file, as shown in Figure 4.4. In combination with input file for the base case, ISPUR automatically reads this Excel file and modifies the input file to generate multiple input files for reservoir simulators such as CMG, ECILIPSE, UTCOMP, and the semi-analytical model. Specifically, using the keyword matching method compared with the input file for the base case, ISPUR finds the keywords corresponding to the uncertain parameters and changes the values according to the Excel file automatically. The other keywords in the input file of the base case where no change is required will be just copied to the new input files.

	A	B	C	D	E	F
1	Fracture height, ft	Fracture half-length, ft	Fracture conductivity, md-ft	Cluster spacing, ft	Permeability, nD	Reservoir pressure, psi
2	40	300	1	90	1000	4000
3	40	500	100	90	100	5000
4	40	300	100	90	1000	5000
5	135	500	100	40	100	5000
6	40	500	100	40	100	4000
7	40	500	1	40	100	5000
8	40	300	1	40	1000	5000
9	40	300	100	40	100	5000
10	135	300	100	40	100	4000
11	40	500	1	90	1000	5000
12	135	300	1	40	100	5000
13	40	500	100	40	1000	5000
14	135	500	1	40	1000	5000
15	135	500	1	90	100	5000
16	135	300	1	90	1000	5000
17	40	300	100	40	1000	4000
18	135	500	1	90	1000	4000
19	135	500	100	90	100	4000
20	135	300	1	90	100	4000
21	135	300	1	40	1000	4000
22	40	500	100	90	1000	4000
23	40	500	1	90	100	4000
24	135	500	100	40	1000	4000
25	135	300	100	40	1000	5000
26	40	300	1	90	100	5000
27	135	500	1	40	100	4000
28	40	300	100	90	100	4000
29	135	300	100	90	100	5000
30	135	300	100	90	1000	4000
31	40	300	1	40	100	4000
32	40	500	1	40	1000	4000
33	135	500	100	90	1000	5000

Figure 4.4: An example of an Excel file containing 32 different combinations with six uncertain parameters for sensitivity studies in a shale gas reservoir.

4.6.4 Simulation running mode

After generating multiple input files for reservoir simulators, ISPUR will call the executable file of the reservoir simulator of interest to run these simulation cases automatically. Two running modes have been integrated in the ISPUR: one is in sequential mode, meaning that only one simulation case at a time; another is in distributed model, meaning that multiple simulation cases at the same time. After finishing all simulation running, the simulation results for each case will be saved in different folders automatically in order to perform further data analysis and graphic presentations.

4.6.5 Post-processing

The simulation results such as cumulative gas production or cumulative oil production are input into the package of Design-Expert to perform sensitivity studies with the purpose of quantifying the rank of important parameters and screening non-significant ones. In addition, the simulation results can be input into the package of Microsoft Excel designed for economic analysis to calculate the NPVs for each case. Then, the NPVs will be input into the package of Design-Expert to perform optimization with purpose of quantifying the relationship between the NPV and uncertain parameters and determining the best economic production scenario.

4.6.6 Flowchart for sensitivity studies and economic optimization

The flowchart shown in Figure 4.5 summarizes how to perform sensitivity studies and optimization using the DOE and RSM. The main steps are listed as follows:

(1) Determine the objective function, and identify the reasonable range for each uncertain factor based on the field data or published work.

(2) Select DOE to prepare multiple combinations and use ISPUR to generate multiple input files and run all simulations by use of a reservoir simulator or the semi-analytical model.

(3) Export simulation results such as gas recovery and oil recovery and perform statistical analysis for obtaining the influence order of all factors and screening of insignificant factors.

(4) Select RSM to prepare multiple combinations again with the remaining significant factors and use ISPUR to generate multiple input files and run all simulations by use of a reservoir simulator or the semi-analytical model.

(5) Export simulation results for calculating the NPVs, and perform statistical analysis for obtaining the response surface model.

(6) Perform further optimization to obtain the best economic production scenario.

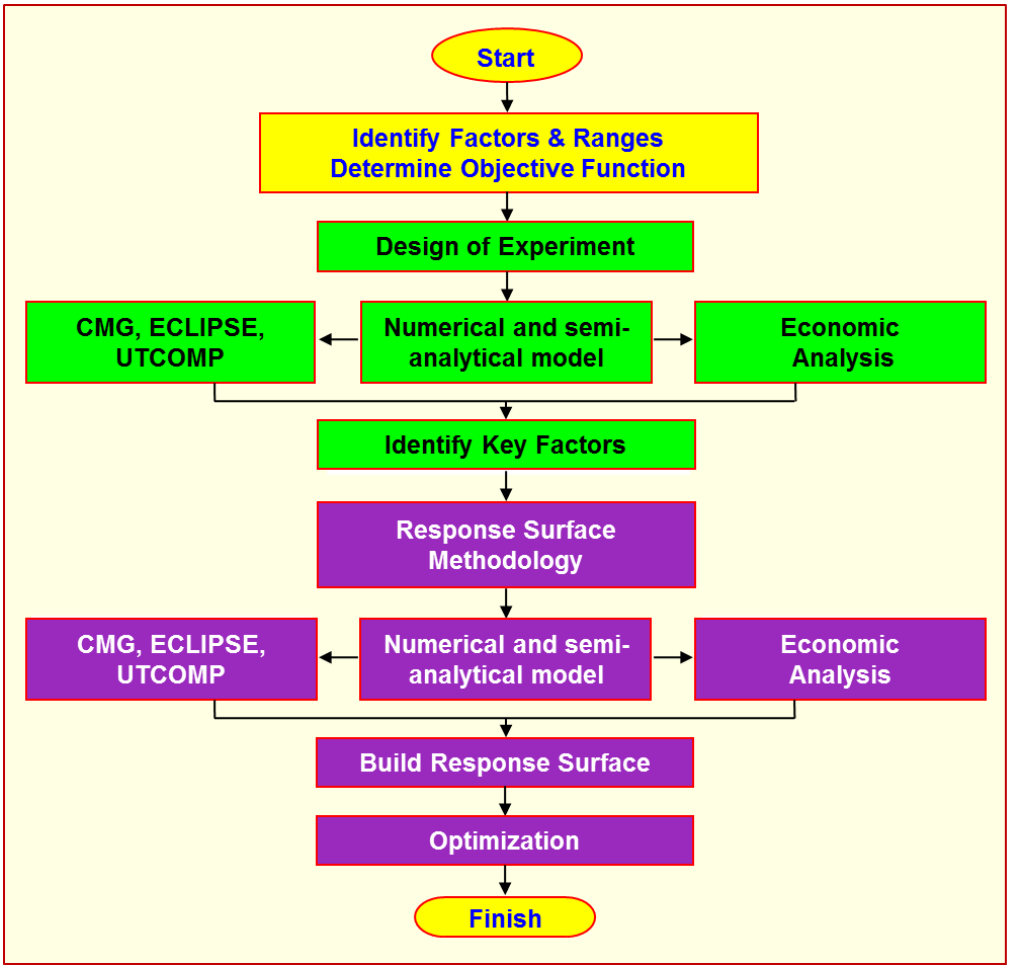

Figure 4.5: Flowchart for sensitivity studies and optimization for the development of unconventional oil and gas reservoirs.

4.7 CONCLUSIONS

An integrated reservoir simulation framework has been developed to optimize hydraulic fracture treatment design for the economic development of unconventional resources such as shale gas and tight oil. In this framework, two statistical methods, namely, DOE and RSM, are used to perform sensitivity studies and economic optimization. A package of Microsoft Excel has been implemented in this framework for

economic analysis with calculation of NPV. A platform of ISPUR has been developed using the MATLAB software package to generate a large number of input files required for reservoir simulators more easily and more efficiently. This framework can be used to optimize fracture treatment design in shale gas and tight oil reservoirs.

CHAPTER 5: Optimization of Fracture Treatment Design for Shale Gas Reservoirs

The framework developed in Chapter 4 is used to quantify the high uncertainties and perform optimization of fracture treatment design for the development of Marcellus shale. Six uncertain parameters including fracture height, fracture conductivity, fracture half-length, cluster spacing, permeability, and initial reservoir pressure were studied. We first used DOE to investigate the order of influence of each parameter and parameter interactions, and quantify which parameter significantly impacts the gas recovery and eliminate the variables that have little impact on the gas recovery. According to the rank of significant parameters, we performed history matching with one field production well. Additionally, a 30-year production forecasting was performed and its corresponding estimated ultimate recovery was quantified. Finally, we used RSM to build a response surface model in terms of net present value on the basis of the significant design variables to obtain the best economic production scenario. The proposed framework can provide a quantitative assessment of optimal horizontal well stimulations for shale gas production.

5.1 INTRODUCTION

According to a recent report released by Energy Information Administration (EIA, 2014b), Marcellus shale is one of six key tight oil and shale gas regions, as shown in Figure 5.1. The Marcellus shale is located in the Appalachian basin across six states, including Pennsylvania, New York, West Virginia, Ohio, Virginia, and Maryland. Although there are many horizontal wells drilled along with multi-stage hydraulic fracturing in the Marcellus shale, the completion effectiveness is not completely understood and a lot of research is required to evaluate well performance and perform optimization of completion strategy.

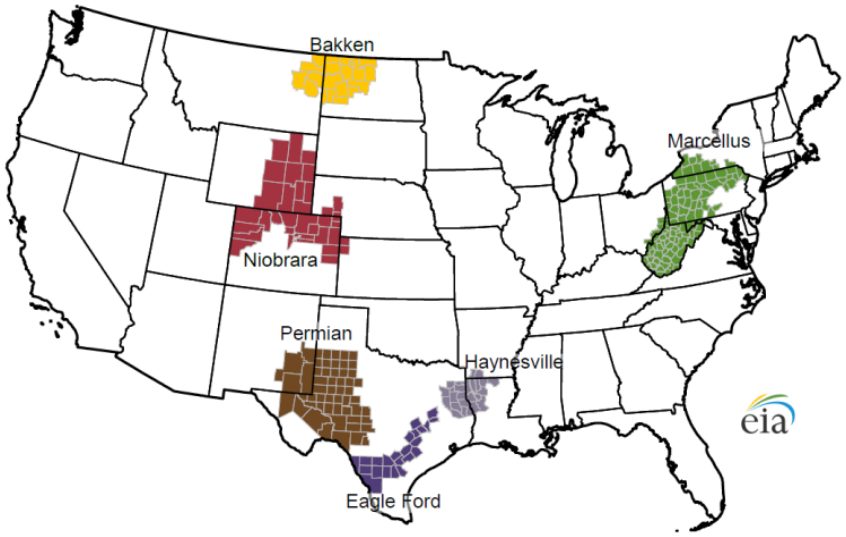

Figure 5.1: Six key U.S. shale gas and shale oil regions.

The well performance is strongly related to permeability-thickness product (k·h), initial reservoir pressure, total hydraulic fracture area and the distribution of fracture conductivity (Cipolla et al., 2008; Mayerhofer et al., 2008). However, it is very challenging to exactly characterize the actual fracture geometry and the distribution of fracture conductivity, even with microseismic images, since microseismic images do not

provide details about hydraulic fracture structure, total fracture area, and proppant distribution (Cipolla et al., 2012). Several authors stated that microseismic measurements represent only a small portion of the complete hydraulic fracture deformation (Maxwell, et al., 2013; Cipolla and Wallace, 2014). History matching with field production data may provide an effective way to predict fracture properties. During hydraulic fracturing treatments, complex fracture networks are actually often generated and the interaction of hydraulic fractures and natural fractures significantly impacts the complexity, which is an important contributor to ultimate gas recovery (Daniels et al., 2007; Maxwell, et al., 2013). The cost of hydraulic fracturing is expensive. The optimization of hydraulic fracture parameters, such as cluster spacing, fracture half-length, and fracture conductivity is important to obtain the most economical scenario. In addition, high uncertainties in shale gas reservoirs have resulted in the optimization of fracture design more challenging. Accordingly, the objective of this study is to use the framework to quantify the high uncertainties and investigate fracture properties through history matching with field production data. Six uncertain parameters including fracture height, fracture conductivity, fracture half-length, cluster spacing, permeability, and initial reservoir pressure were studied. Finally, the optimal fracture design can be determined in combination with economic analysis through this framework. The focus of this chapter is to guide completion evaluation and optimization of fracture design in the Marcellus shale, which can also be easily extended to the other shale gas reservoirs such as Barnet shale and Eagle Ford shale.

5.2 SENSITIVITY STUDY

In this case study, six uncertainty parameters were investigated including fracture height, fracture half-length, fracture conductivity, cluster spacing, permeability, and

initial reservoir pressure. Each parameter was given a reasonable range with the actual maximum and minimum values or coded symbol of "+1" and "–1" based on the actual field data of the Marcellus shale, as listed in Table 5.1. The other reservoir and fracture properties are listed in Table 5.2.

A basic 3D numerical reservoir model using the numerical reservoir simulator of CMG-GEM (a compositional simulator) was built with dimensions of 5,000 ft × 1,500 ft × 135 ft, which corresponds to length, width, and thickness, respectively. The reservoir was divided into two layers. The top layer is with thickness of 95 ft and porosity of 9%. The bottom layer is with thickness of 40 ft and porosity of 13%. The horizontal well with length of 4,500 ft was located in the bottom layer. Four clusters per stage are considered and each cluster is assumed to produce an effective hydraulic fracture. The number of stage corresponding to cluster spacing of 40 ft and 90 ft is 20 and 12, respectively. Constant flowing BHP of 200 psi is used for 30 years. In the simulation studies, single-phase gas flow was assumed and the effects of non-Darcy flow, gas desorption, and stress-dependent fracture conductivity were considered. The non-Darcy Forchheimer coefficient, as shown in Eq. 2.41, is used. The gas adsorption isotherm curve, as shown in Figure 3.4(a) is used. The stress-dependent fracture conductivity curves corresponding to different initial reservoir pressure in this study are shown in Figure 5.2. As shown, the fracture conductivity corresponding to the flowing BHP of 200 psi reduces to approximately 26%-32% of the original fracture conductivity.

Parameter	Coded symbol	Minimum (-1)	Maximum (+1)	Unit
Fracture height	A	40	135	ft
Fracture half-length	B	300	500	ft
Fracture conductivity	C	1	100	md-ft
Cluster spacing	D	40	90	ft
Permeability	E	100	1000	nD
Reservoir pressure	F	4000	5000	psi

Table 5.1: Six uncertainty parameters used for sensitivity study in the Marcellus shale.

Parameter	Value	Unit
Reservoir temperature	130	^{o}F
Reservoir porosity (top layer)	9%	
Reservoir porosity (bottom layer)	13%	
Reservoir thickness (top layer)	95	ft
Reservoir thickness (bottom layer)	45	ft
Initial water saturation	10%	
Total compressibility	3×10^{-6}	psi^{-1}
Horizontal well length	4,500	ft
Gas specific gravity	0.58	

Table 5.2: Parameters used for simulations in the Marcellus shale.

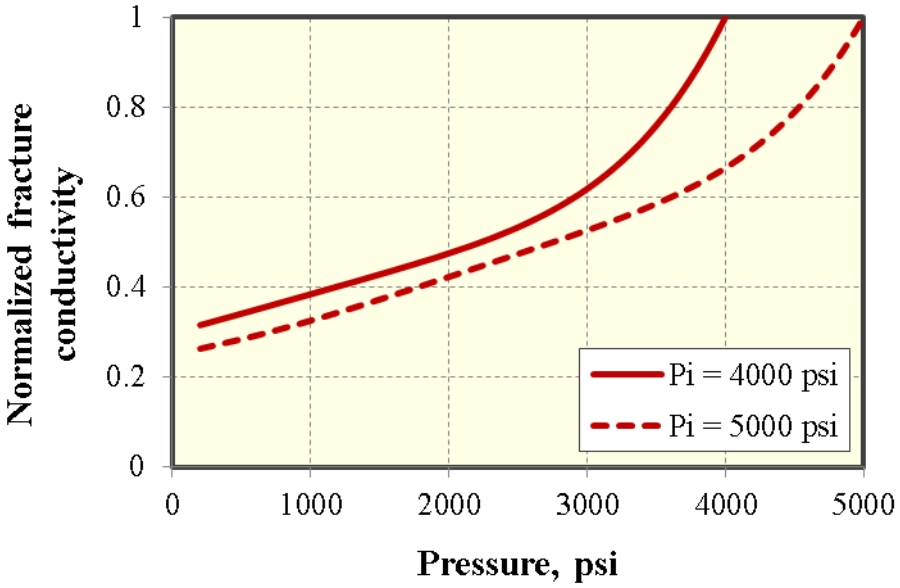

Figure 5.2: Stress-dependent fracture conductivity curves corresponding to initial reservoir pressure of 4,000 psi and 5,000 psi.

In accordance to six variables, 32 simulation cases need to be prepared on the basis of two-level fractional factorial design, which can be generated automatically and efficiently using the ISPUR, as shown in Table 5.3.

Run	A	B	C	D	E	F
1	40	300	1	90	1000	4000
2	40	500	100	90	100	5000
3	40	300	100	90	1000	5000
4	135	500	100	40	100	5000
5	40	500	100	40	100	4000
6	40	500	1	40	100	5000
7	40	300	1	40	1000	5000

Table 5.3 continued on next page

8	40	300	100	40	100	5000
9	135	300	100	40	100	4000
10	40	500	1	90	1000	5000
11	135	300	1	40	100	5000
12	40	500	100	40	1000	5000
13	135	500	1	40	1000	5000
14	135	500	1	90	100	5000
15	135	300	1	90	1000	5000
16	40	300	100	40	1000	4000
17	135	500	1	90	1000	4000
18	135	500	100	90	100	4000
19	135	300	1	90	100	4000
20	135	300	1	40	1000	4000
21	40	500	100	90	1000	4000
22	40	500	1	90	100	4000
23	135	500	100	40	1000	4000
24	135	300	100	40	1000	5000
25	40	300	1	90	100	5000
26	135	500	1	40	100	4000
27	40	300	100	90	100	4000
28	135	300	100	90	100	5000
29	135	300	100	90	1000	4000
30	40	300	1	40	100	4000
31	40	500	1	40	1000	4000
32	135	500	100	90	1000	5000

Table 5.3: 32 simulation cases based on half fractional factorial design for six uncertain parameters in Marcellus shale.

After numerical simulation of each case, cumulative gas production was obtained and shown in Figure 5.3. The figure clearly shows that there is a wide range of cumulative gas production ranging from 6.53 BCF to 30.61 BCF at 30 years of production.

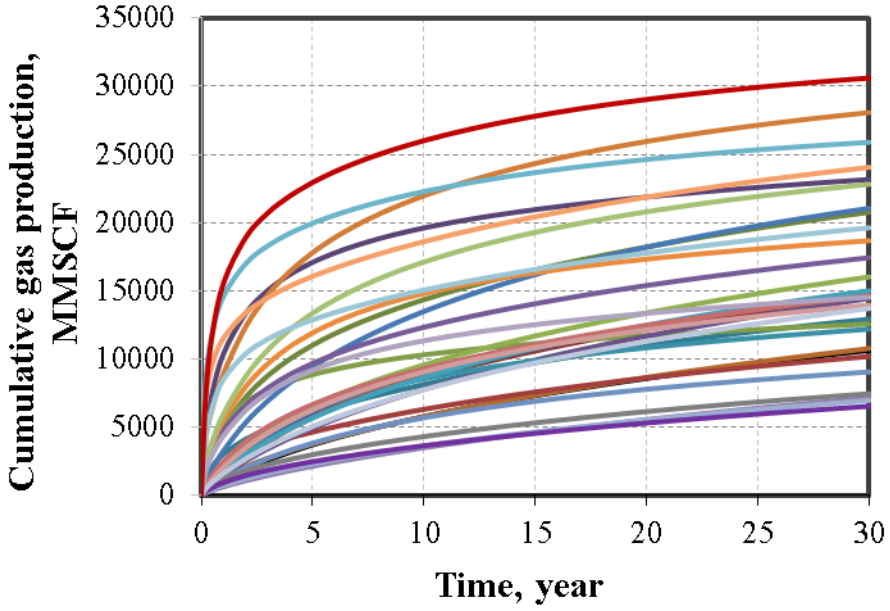

Figure 5.3: Cumulative gas production of 32 cases for the Marcellus shale.

Results from Figure 5.3 are then used to construct the half-normal plot, Pareto chart (Myers et al., 2008), and the analysis-of-variance (ANOVA) (Myers et al., 2008) table to identify the ranking of significant factors affecting the objective function of cumulative gas production. The half-normal plot and the corresponding Pareto chart at different period of production are presented in Figures 5.4 through 5.7. Any parameters or two-parameter interaction highly deviating from the straight line are recognized as the parameters that affect the cumulative gas production significantly. At early time of production (5 years), as shown in Figures 5.4 and 5.6, the following order in terms of influence of main parameter effects is fracture conductivity (C), permeability (E),

fracture height (A), fracture half-length (B), reservoir pressure (F), and cluster spacing (D); while at late time of production (30 years), as shown in Figures 5.5 and 5.7, the order of influence becomes permeability (E), fracture conductivity (C), fracture half-length (B), fracture height (A), reservoir pressure (F), and cluster spacing (D). This illustrates that fracture conductivity is significantly more important than permeability at the early time of production, while permeability will become more important than fracture conductivity at the late time of production.

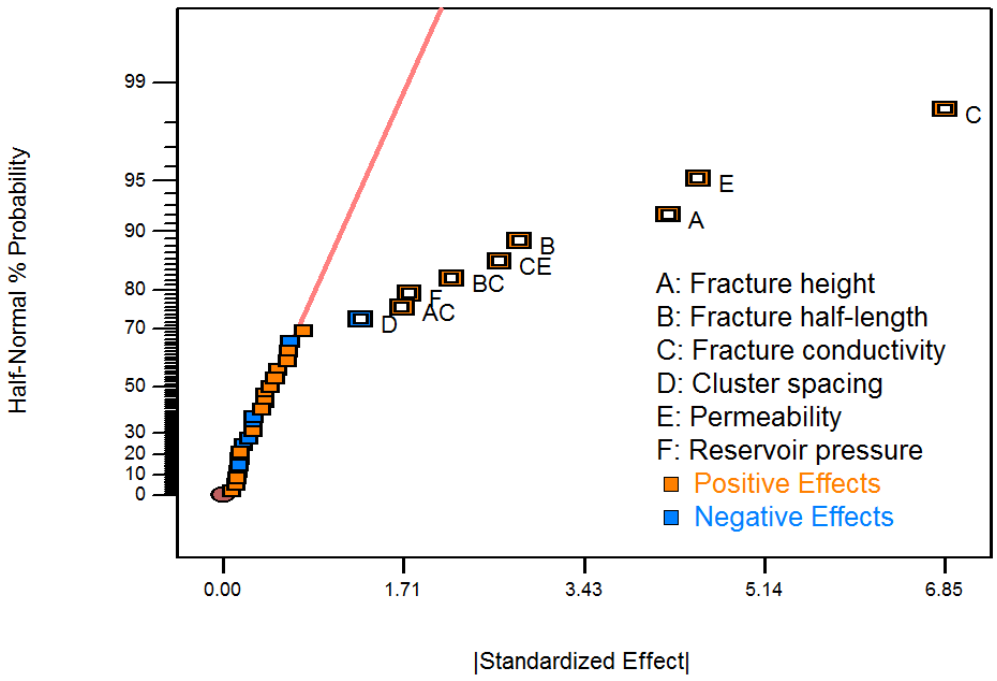

Figure 5.4: The half normal plot at 5 years of gas production.

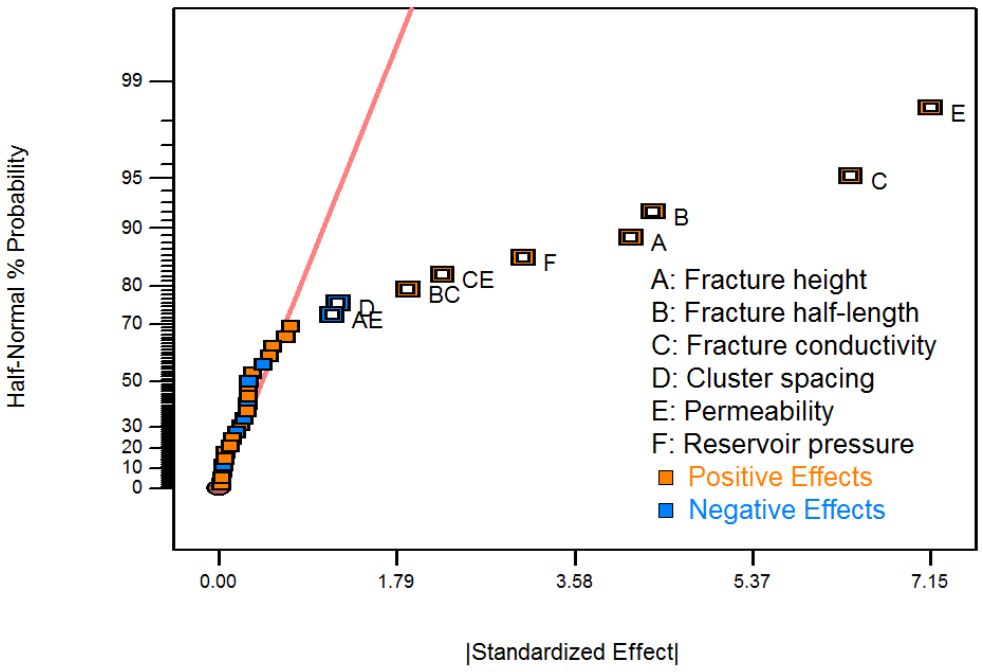

Figure 5.5: The half normal plot at 30 years of gas production.

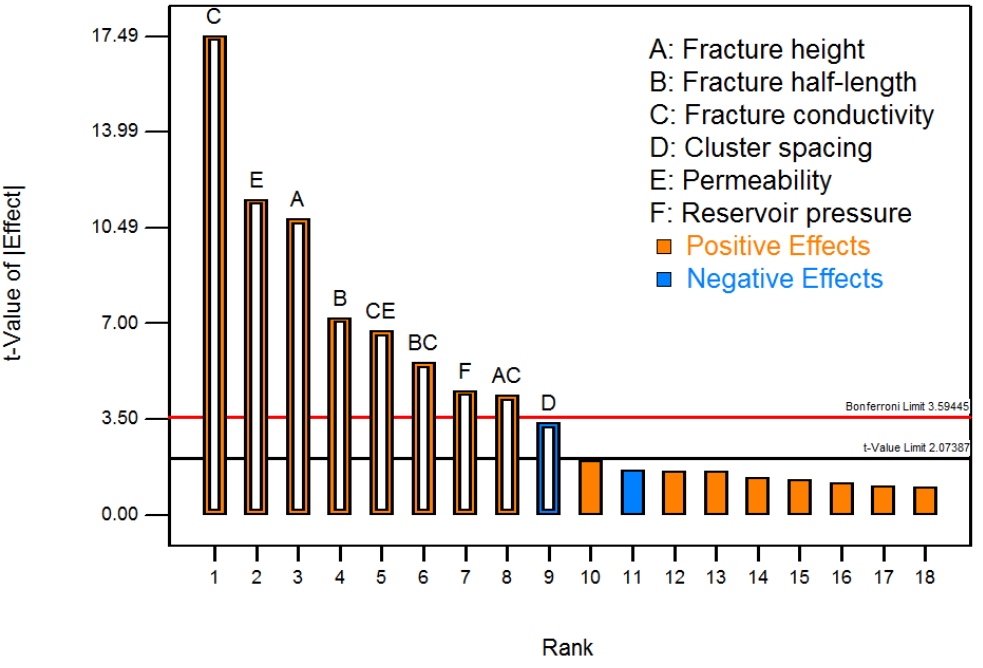

Figure 5.6: Pareto chart of important parameters at 5 years of gas production.

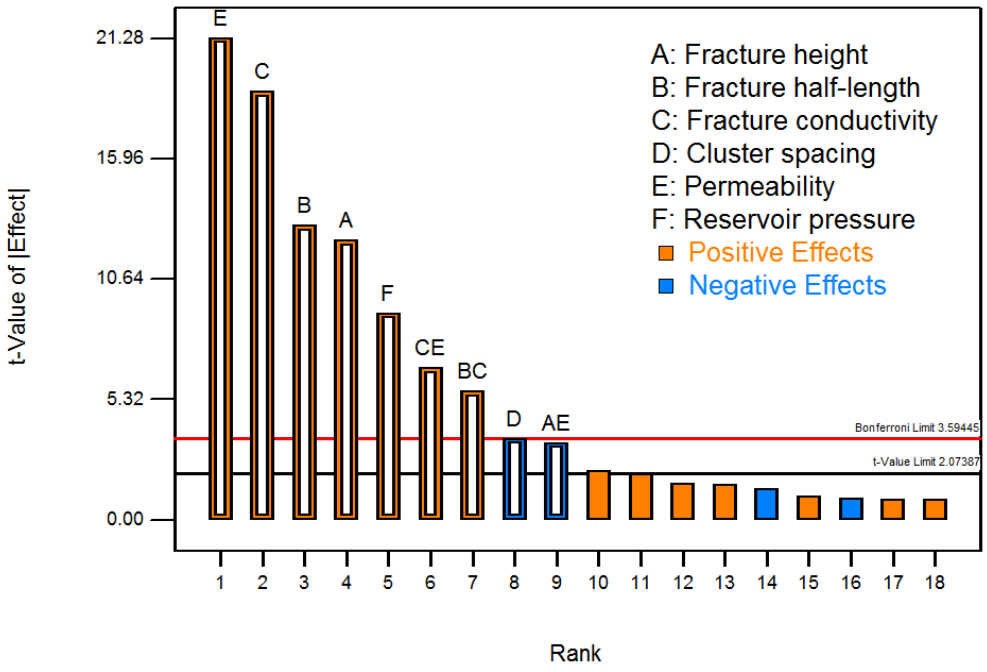

Figure 5.7: Pareto chart of important parameters at 30 years of gas production.

The significant and insignificant model parameters were also determined by the ANOVA table, as shown in Tables 5.4 and 5.5. A parameter having value of "Prob > F" (Probability of a large F-value) less than 0.1 is called a significant model term. F means F-value in the ANOVA table, which is defined as the ratio of model mean square to the appropriate error mean square (Anderson and Whitcomb, 2007). Parameters not presented in Tables 5.4 and 5.5 are insignificant model terms. More details about the definitions of the terms in the ANOVA table can be found in the package of Design-Expert (Stat-Ease Incorporated, 2014).

Source	Sum of squares	Degree of freedom	Mean square	F-value	P-value
Model	898.36	9	99.82	81.29	< 0.0001
A	142.81	1	142.81	116.31	< 0.0001
B	63.21	1	63.21	51.48	< 0.0001
C	375.57	1	375.57	305.88	< 0.0001
D	13.65	1	13.65	11.12	0.0030
E	162.48	1	162.48	132.33	< 0.0001
F	25.00	1	25.00	20.36	0.0002
AC	23.06	1	23.06	18.78	0.0003
BC	37.61	1	37.61	30.63	< 0.0001
CE	54.97	1	54.97	44.77	< 0.0001
Residual	27.01	22	1.23		
Cor. Total	925.37	31			

Table 5.4: ANOVA table for 5 years of gas production.

Source	Sum of squares	Degree of freedom	Mean square	F-value	P-value
Model	1188.05	9	132.01	145.91	< 0.0001
A	137.38	1	137.38	151.86	< 0.0001
B	152.42	1	152.42	168.48	< 0.0001
C	322.66	1	322.66	356.65	< 0.0001
D	11.51	1	11.51	12.73	0.0017
E	409.48	1	409.48	452.63	< 0.0001
F	74.94	1	74.94	82.84	< 0.0001
AE	10.35	1	10.35	11.44	0.0027
BC	28.88	1	28.88	31.92	< 0.0001
CE	40.43	1	40.43	44.69	< 0.0001
Residual	19.90	22	0.90		
Cor. Total	1207.95	31			

Table 5.5: ANOVA table for 30 years of gas production.

The detailed influences of all parameters on the well performance at a short-term period (5 years) and a long-term period (30 years) are shown in Figure 5.8. It can be observed that impacts of some parameters on gas recovery decrease with time, including fracture conductivity (C), fracture height (A), and cluster spacing (D); while effects of some parameters increase with time, including permeability (E), fracture half-length (B), and reservoir pressure (F). The interactions between various parameters are defined as CE, BC, AC, and AE. As shown, the interaction parameter CE is more important that the other interaction parameters. The rank of important parameters can provide critical insights into performing history matching with field production data.

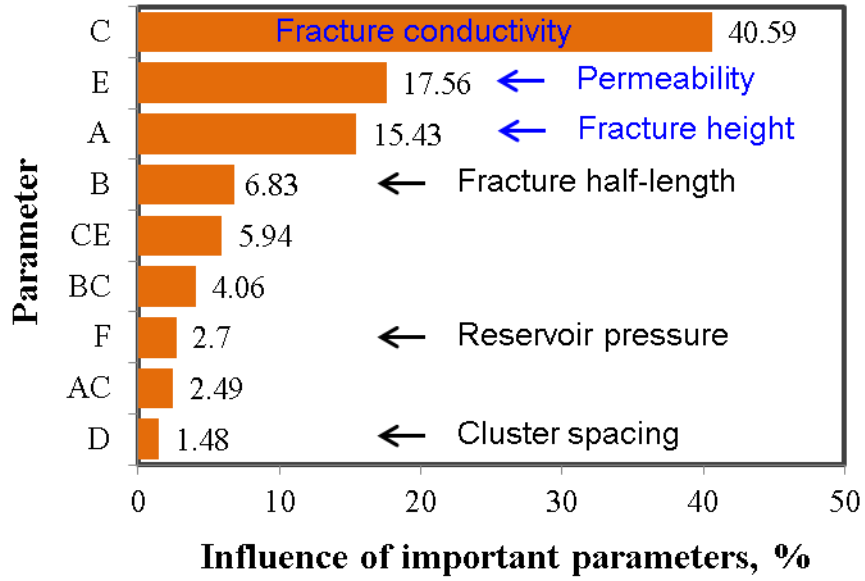

(a)

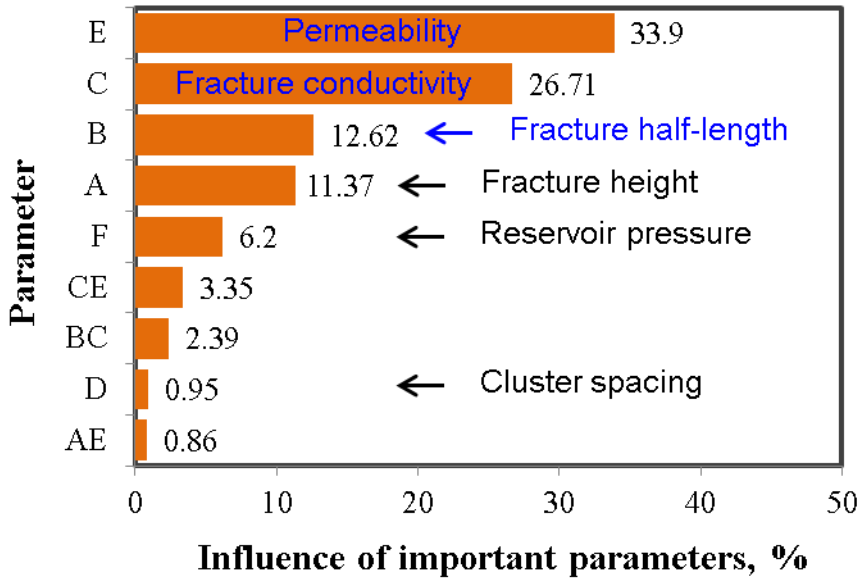

(b)

Figure 5.8: Rank of the influences of uncertainty parameters on well performance. (a) At a short-term of production (5 years). (b) At a long-term production (30 years).

5.2 HISTORY MATCHING AND PRODUCTION FORECASTING

One well, denoted as Well 1, from the Marcellus shale reservoir was selected to perform history matching and production forecasting. The production data was provided by Chief Oil and Gas LLC. The primary purpose of history matching is to better understand the fracture properties such as fracture half-length, fracture height, and fracture conductivity. The reservoir has two different shale layers with high TOC. Porosity of top layer is 9%, and porosity of bottom layer is around 13.8%. Thickness of top layer is 94 ft, and thickness of bottom layer is 43 ft. This well was drilled in the bottom layer and completed using a lateral length of 2,605 ft, 10 fracturing stages, four perforation clusters per stage, and the cluster spacing is 52.2 ft. Almost 180 days of production data were available to perform history matching and evaluate the well performance.

We set up a basic 3D reservoir model with dimensions of 3,105 ft × 1,000 ft × 137 ft, which corresponds to length, width, and thickness, respectively, as shown in Figure 5.9. As shown in this model, hydraulic fractures are assumed to completely penetrate the bottom layer and some part of top layer. Table 5.6 summarizes the detailed reservoir and fracture properties of the well required for simulation. Flowing bottom hole pressure in Figure 5.10 is used to constrain the simulation and gas flow rate and cumulative gas production are the history-matching variables. Based on the sensitivity analysis, the top four key parameters such as fracture height, fracture conductivity, fracture half-length, and permeability were tuned to perform history matching.

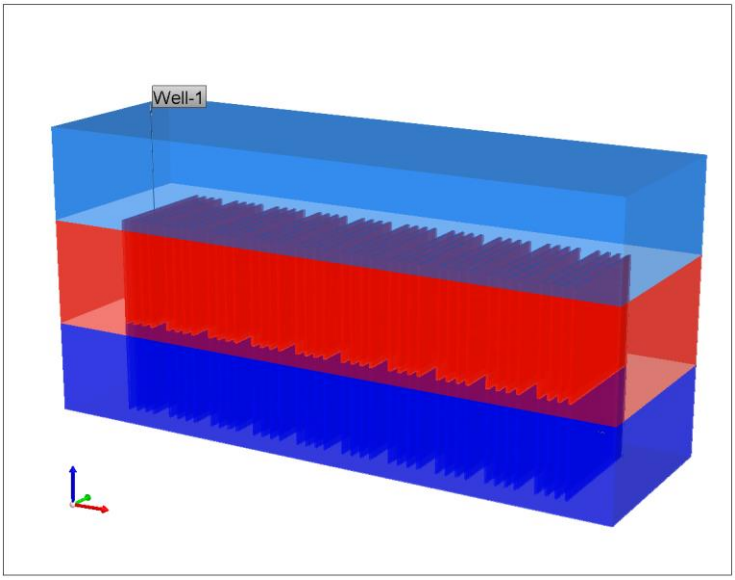

Figure 5.9: A basic 3D reservoir model for the Well 1.

Parameter	Value	Unit
Initial reservoir pressure	4,300	psi
Reservoir temperature	130	^{o}F
Reservoir permeability	800	nD
Reservoir porosity (top layer)	9%	
Reservoir porosity (bottom layer)	13.8%	
Reservoir thickness (top layer)	94	ft
Reservoir thickness (bottom layer)	43	ft
Initial water saturation	10%	
Total compressibility	3×10^{-6}	psi^{-1}
Horizontal well length	2,605	ft
Number of stages	10	
Cluster spacing	52.2	ft
Total number of fractures	40	
Gas specific gravity	0.58	

Table 5.6: Reservoir and fracture parameters for the Well 1 in Marcellus shale.

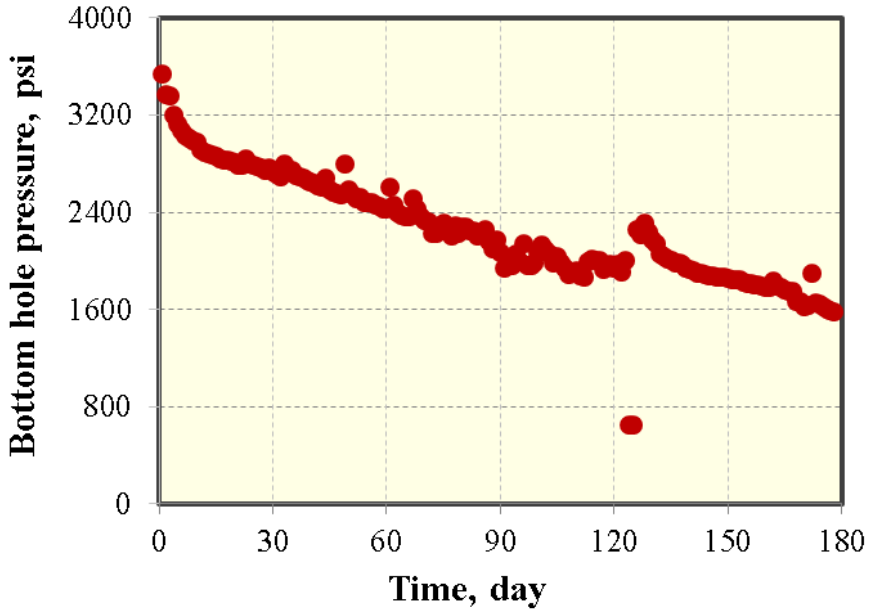

Figure 5.10: Flowing bottom hole pressure of the Well 1.

The history matching results for gas flow rate and cumulative gas production are shown in Figure 5.11, illustrating that a good match between simulation results and field data is obtained with fracture conductivity of 5 md-ft, fracture height of 93 ft, fracture half-length of 330 ft, and permeability of 800 nD. It should be noted that history matching is not unique and the match obtained in this study is only one possible solution. The pressure distribution at end of field production is shown in Figure 5.12, clearly showing the effective drainage volume of this well.

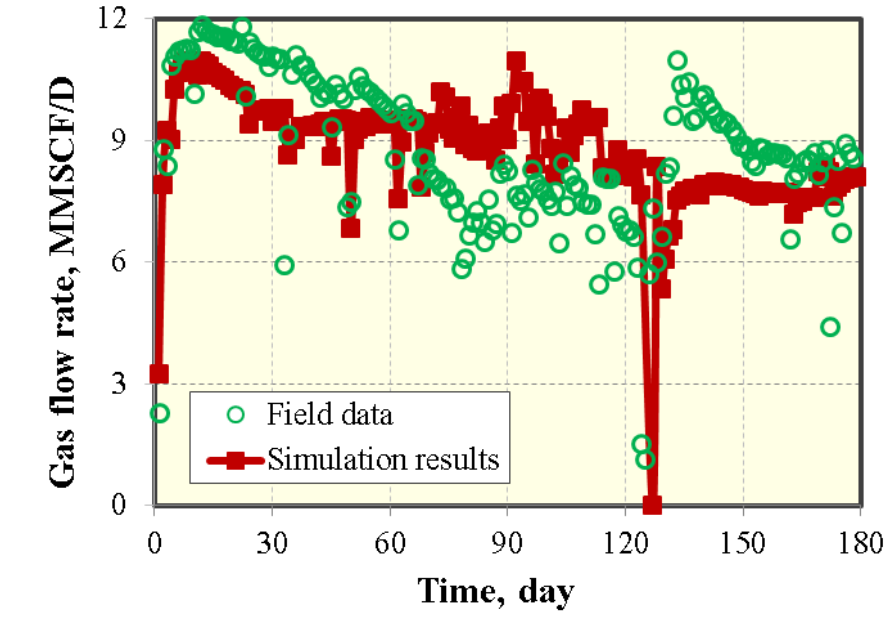

(a)

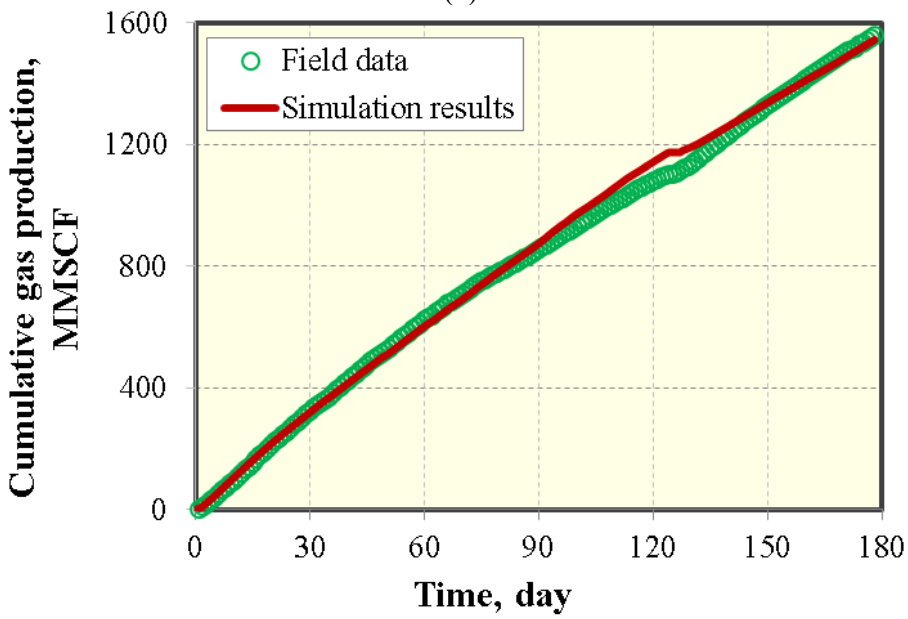

(b)

Figure 5.11: History matching results. (a) Gas flow rate. (b) Cumulative gas production.

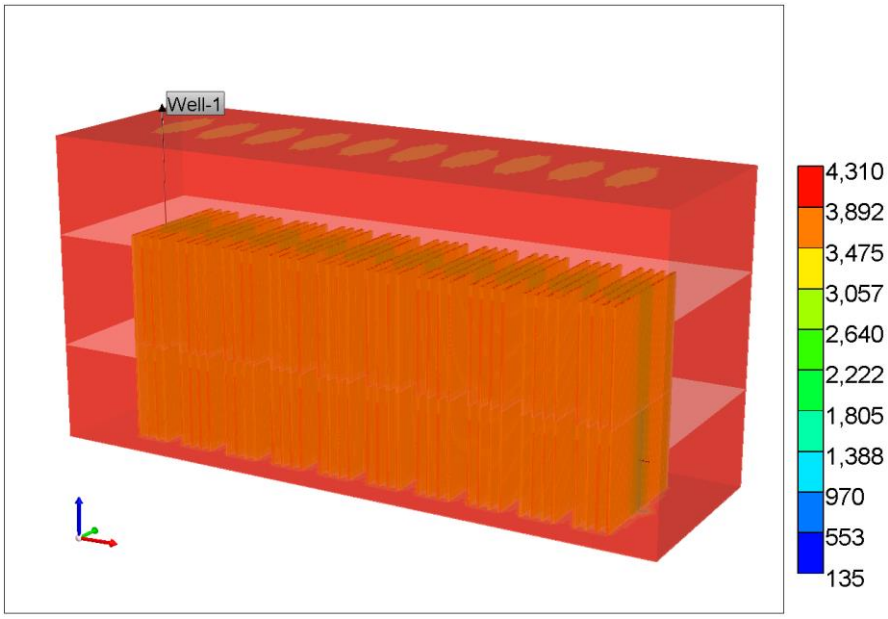

Figure 5.12: Pressure distribution at end of field production (pressure unit: psi).

Incorporating the history match period, we performed a production forecasting for 30 years. After history matching period, bottom hole pressure of 100 psi remained constant until 30 years of production. Figure 5.13 shows the gas recovery at 30 years of production. It can be seen that the estimated ultimate recovery at 30 years is quantified as 11.12 BCF for this well. The pressure distribution at 30 years of production is shown in Figure 5.14, clearly illustrating the effective drainage volume of this well.

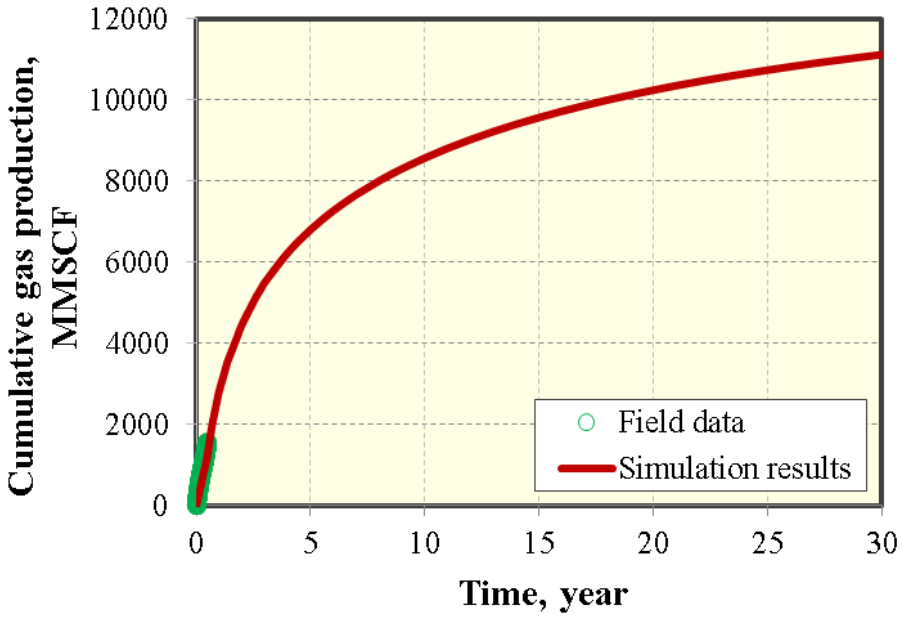

Figure 5.13: Production forecasting for a 30-year period incorporating the history match period.

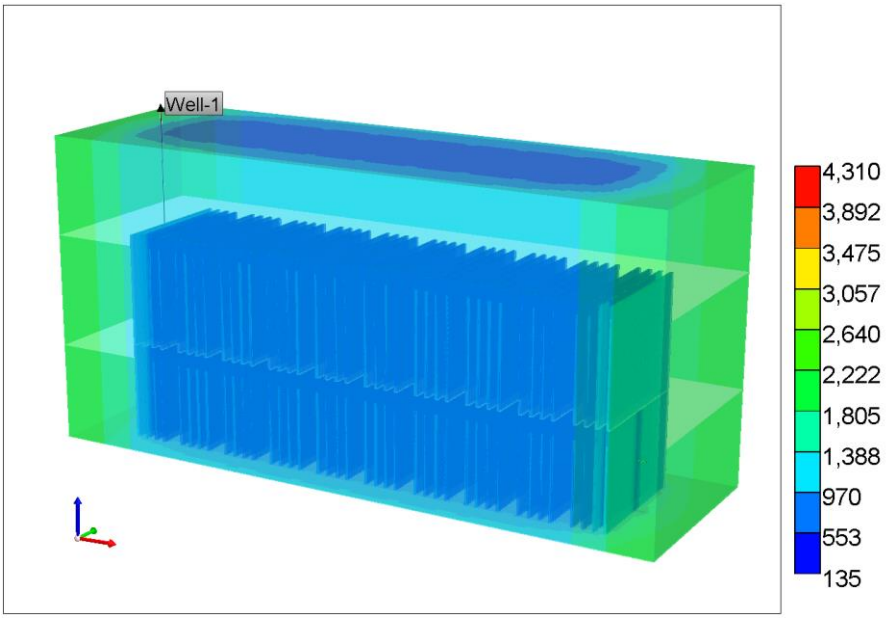

Figure 5.14: Pressure distribution after 30 years of production (pressure unit: psi).

5.3 FRACTURE TREATMENT COST

In order to perform economic optimization, the fracture treatment cost is an important part and it is determined based on the field data from Marcellus shale in this section. The fracturing treatments cost is mainly divided into well drilling cost and completion cost. In this study, hydraulic fracture treatment data from four wells in Marcellus shale in combination with performing history matching with field production data are used to determine the fracture treatment cost. In general, the average well drilling cost is around $2.5 MM (MM refers to one million in this study). The completion cost of single hydraulic fracture is strongly related to the volume of injected fluid and the amount of pumped proppants.

5.3.1 Reservoir and operation parameters

Table 5.7 summarizes the detailed reservoir properties and operation parameters of the four wells in Marcellus shale, which were provided by Chief Oil and Gas LLC. Four different hydraulic fracture treatment designs with various numbers of perforation clusters and injected amount of proppants per stage were investigated for these four wells as follows:

1. Fracture design 1: 5 clusters per stage with 554,660 lbs per stage;
2. Fracture design 2: 4 clusters per stage with 381,444 lbs per stage;
3. Fracture design 3: 4 clusters per stage with 436,156 lbs per stage;
4. Fracture design 4: 3 clusters per stage with 439,989 lbs per stage.

First, we set up a basic 3D numerical reservoir model including multiple hydraulic fractures to perform history matching. The reservoir model includes two layers with different thickness and porosity for each layer, as shown in Table 5.7. The horizontal well was drilled in the bottom layer. Fracture is assumed to completely penetrate the bottom layer and some part of the top layer, as shown in Figure 5.15. For

each well, flowing bottom hole pressure (BHP) is used to constrain the simulation and gas flow rate and cumulate gas production are the history-matching variables. A bi-wing fracture model is selected to perform history matching. Fracture half-length, fracture conductivity, fracture height, and reservoir permeability were the main tuning parameters to obtain a good history match. Gas desorption measurement data, as shown in Figure 3.4(a), is used to consider the gas desorption effect in the model.

Parameter	Well 1	Well 2	Well 3	Well 4
True vertical depth, ft	7,050	7,549	7,120	7,354
Reservoir temperature, ^{o}F	130	130	130	130
Reservoir pressure, psi	4,500	4,960	4,300	4,300
Porosity (top layer)	0.0857	0.08	0.09	0.09
Porosity (bottom layer)	0.134	0.13	0.138	0.138
Thickness (top layer), ft	90	88	94	94
Thickness (bottom layer), ft	40	51	43	43
Well length, ft	5,017	4,046	2,853	1,904
Stage spacing, ft	426	254	259	272
Number of stage	12	16	11	7
Number of cluster	60	63	44	21
Cluster spacing, ft	80	53	52	68
Fracture design	2	3	4	5
Total sand, lbs	6,655,920	6,007,757	4,797,713	3,079,918
Total liquid, bbls	142,007	146,360	89,581	53,814
Sand per cluster, lbs	110,932	95,361	109,039	146,663
Gas specific gravity	0.58	0.58	0.58	0.58

Table 5.7: Reservoir and operation parameters for four horizontal wells in Marcellus shale.

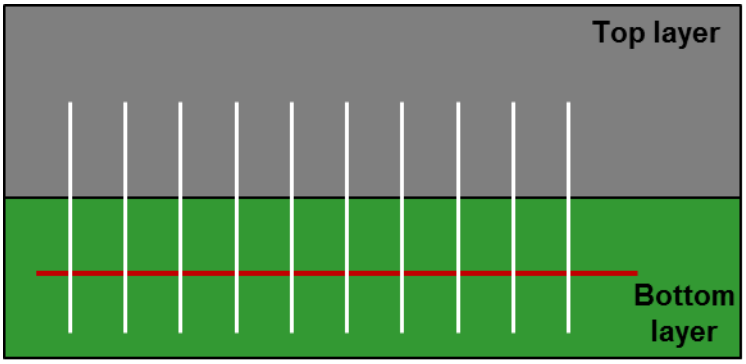

Figure 5.15: Two layers with multiple hydraulic fractures and the horizontal well located in the bottom layer.

5.3.2 History matching

Figure 5.16 shows the flowing BHP with different production time for these four horizontal wells. Comparisons between field production data and simulate results for gas flow rate and cumulative gas production are shown in Figures 5.17 and 5.18, respectively. As shown, a good agreement for each well was obtained. Figure 5.19 presents the pressure distribution of four wells at end of field production period, clearly illustrating the drainage area of each well.

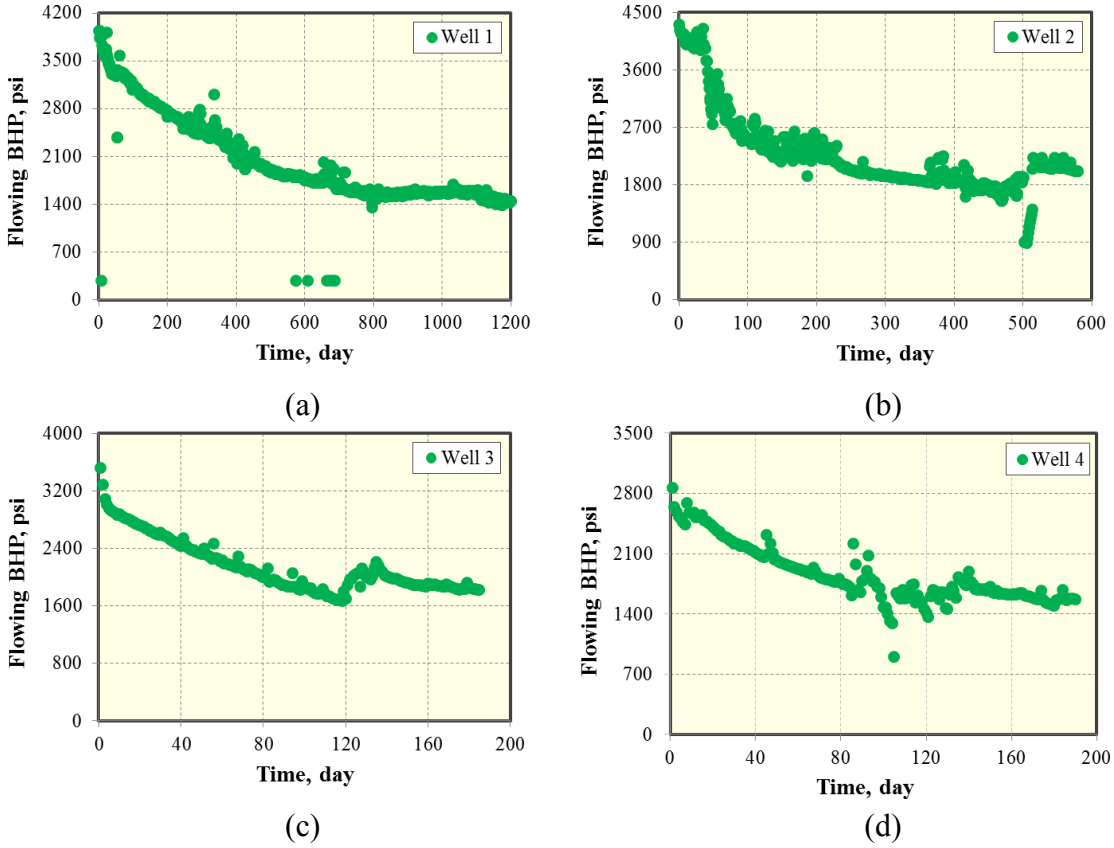

Figure 5.16: Flowing bottom hole pressure of four wells in Marcellus shale. (a) Well 1. (b) Well 2. (c) Well 3. (d) Well 4.

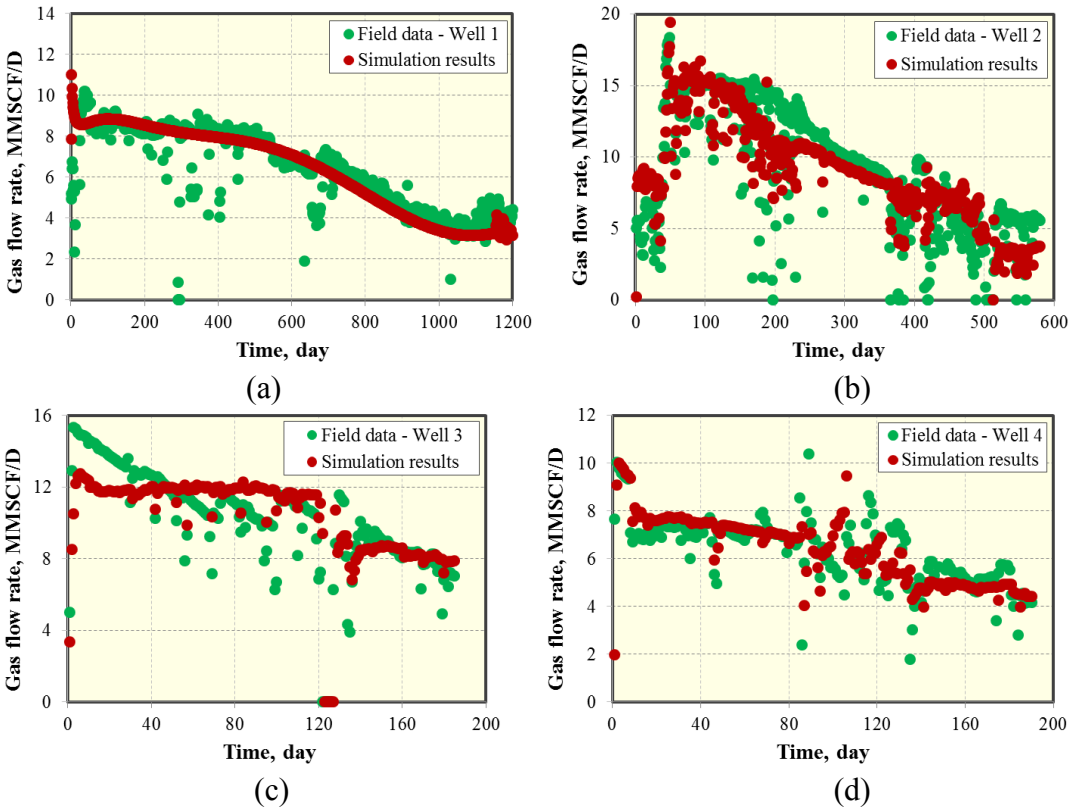

Figure 5.17: History matching results for gas flow rate of four wells in Marcellus shale. (a) Well 1. (b) Well 2. (c) Well 3. (d) Well 4.

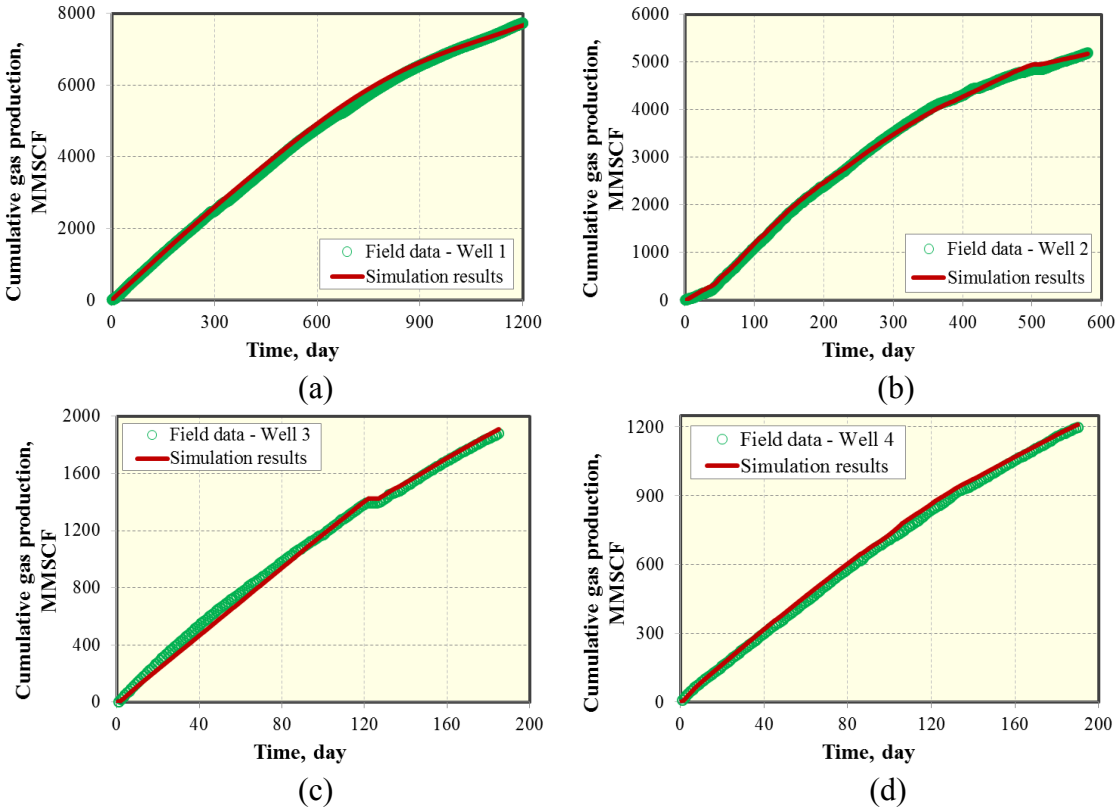

Figure 5.18: History matching results for cumulative gas production of four wells in Marcellus shale. (a) Well 1. (b) Well 2. (c) Well 3. (d) Well 4.

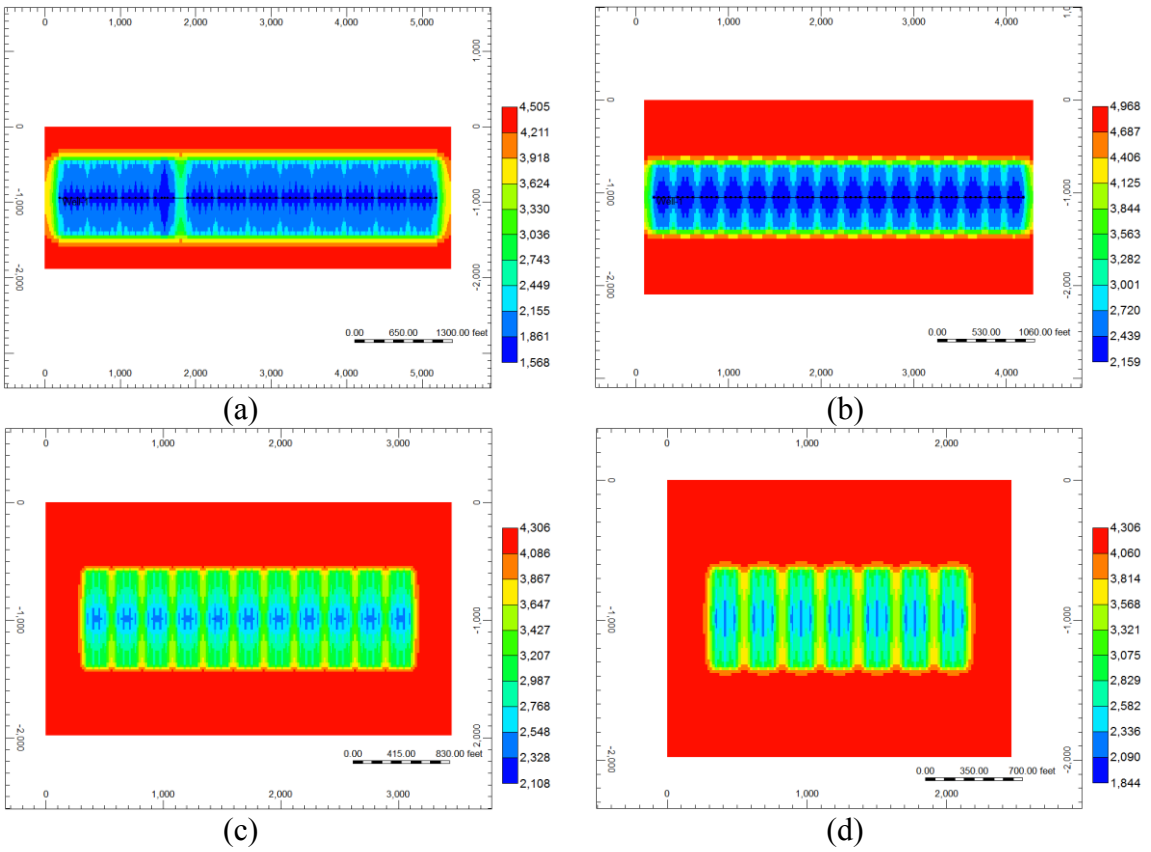

Figure 5.19: Pressure distribution of four wells at end of different production times in Marcellus shale, respectively (pressure unit: psi). (a) Well 1. (b) Well 2. (c) Well 3. (d) Well 4.

Based on a good history match result, the key fracture properties and reservoir permeability were quantified (see Table 5.8). As shown, the range for fracture conductivity is 3-6 md-ft, for fracture half-length is 350-495 ft, and for fracture height is 80-111 ft. Reservoir permeability is 800 nD.

Parameter	Well 1	Well 2	Well 3	Well 4
Fracture conductivity, md-ft	5	3	4.5	6
Fracture half-length, ft	495	350	410	410
Fracture height, ft	80	111	98	96
Reservoir permeability, nD	800	800	800	800

Table 5.8: History matching results of fracture properties and reservoir permeability for four wells in Marcellus shale.

In order to determine the infinite fracture conductivity in the reservoir models for these wells, the effect of fracture conductivity with a range from 1 md-ft to 1,000 md-ft on gas recovery of Well 3 at a 30-year period was studied and the simulation results are shown in Figure 5.20. The flowing BHP of 200 psi is used in the simulation. It can be seen that there is a very small difference of gas recovery between fracture conductivity of 100 md-ft and 1,000 md-ft, illustrating that 100 md-ft is very close to the infinite fracture conductivity. Hence, the current fracture treatment design for fracture conductivity based on the history matching results is far away from the infinite fracture conductivity.

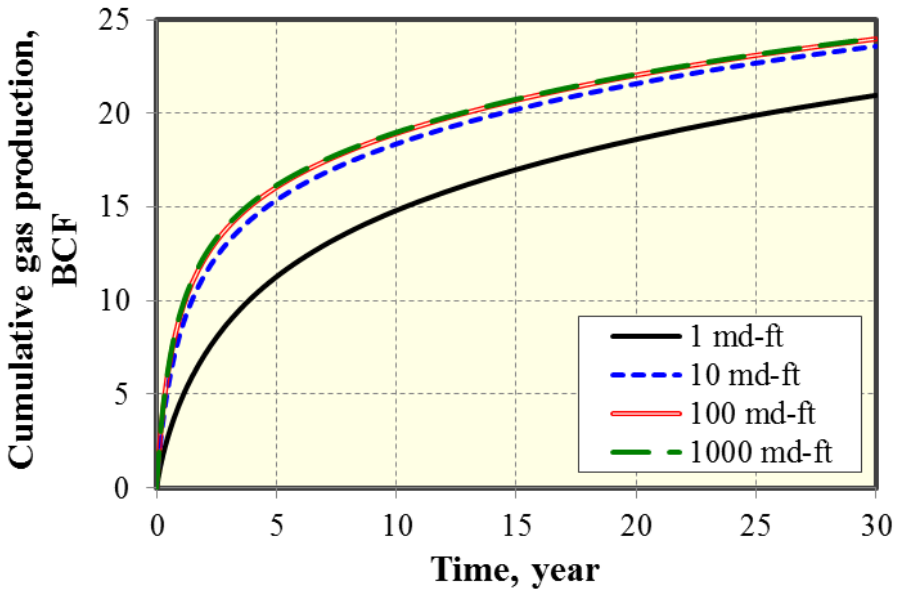

Figure 5.20: Effect of fracture conductivity on gas recovery of Well 3.

5.3.3 Cost of single hydraulic fracture

Based on the history matching results, the relationship between proppant amount pumped per cluster and fracture conductivity and the relationship between fluid injected per cluster and single fracture area is shown in Figures 5.21 and 5.22, respectively. Single fracture area is defined as fracture length times fracture height in this work.

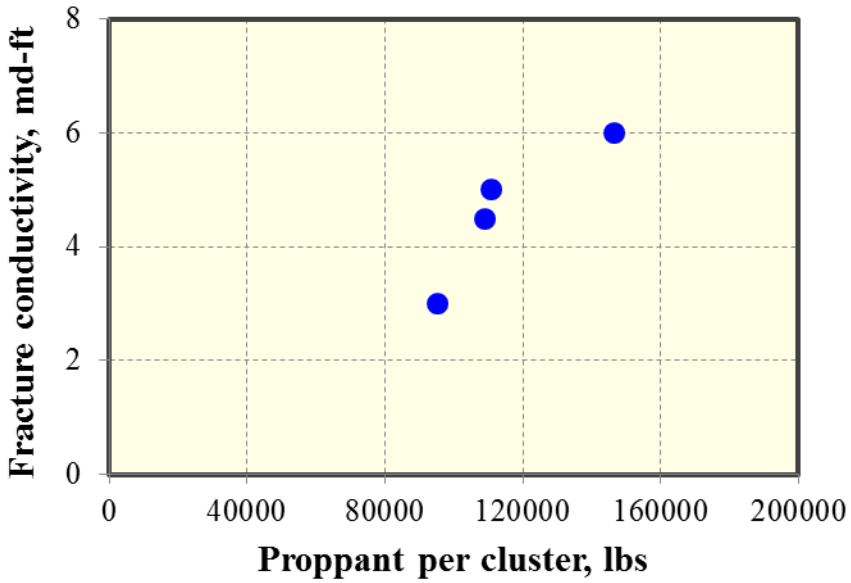

Figure 5.21: Relationship between proppant amount pumped per cluster and fracture conductivity based on history matching results for four wells.

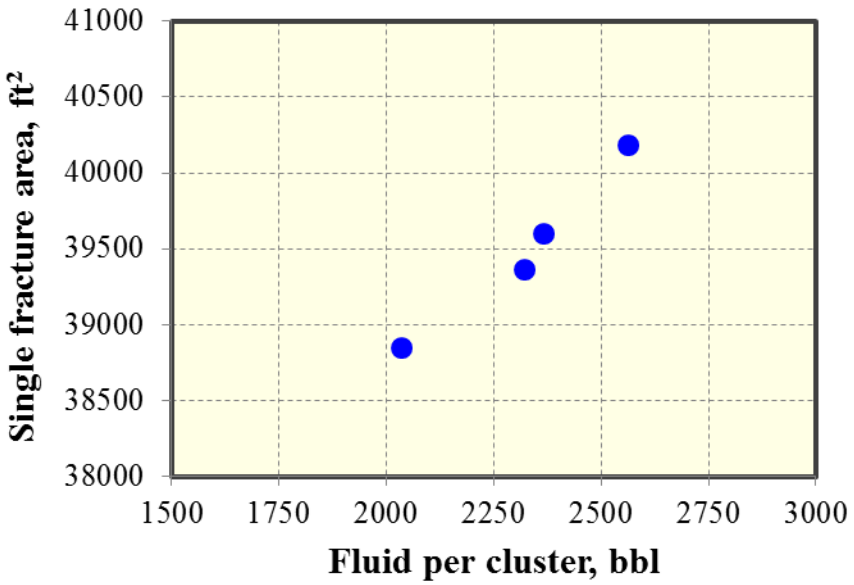

Figure 5.22: Relationship between fluid injected per cluster and single fracture area based on history matching results for four wells.

The cost of single hydraulic fracture corresponding to proppants pumped and fluid injected is shown in Figures 5.23 and 5.24, respectively. Also, through fitting these values, the expressions were obtained as follows:

For fracture cost related to proppants pumped:

$$y = 4393.63 \times e^{2.097x},\ R^2 = 99\%, \tag{5.1}$$

where y is fracture cost and x is $\log_{10}$ (fracture conductivity).

For fracture cost related to fluid injected:

$$y = 8 \times 10^{-18} \times e^{10.72x},\ R^2 = 99\%, \tag{5.2}$$

where y is fracture cost and x is $\log_{10}$ (fracture area).

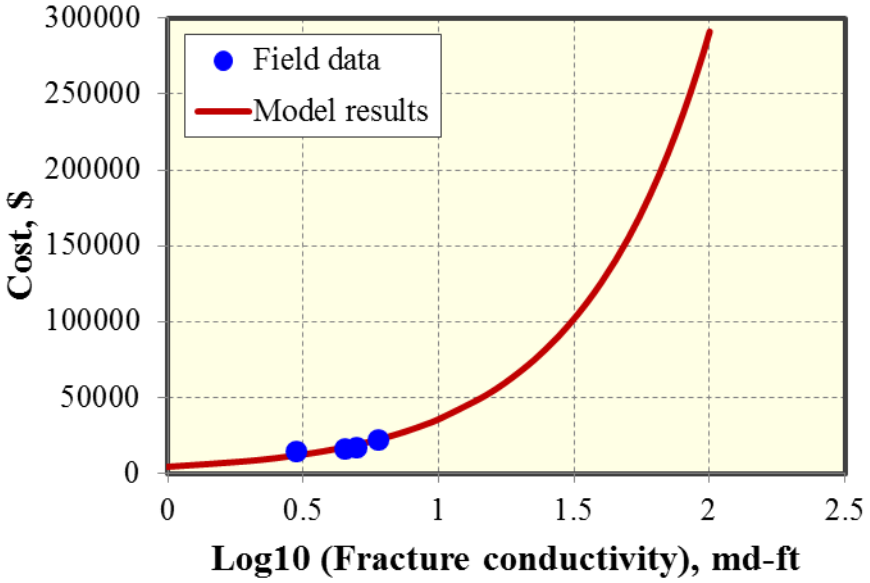

Figure 5.23: Cost of single fracture corresponding to proppants pumped for four wells.

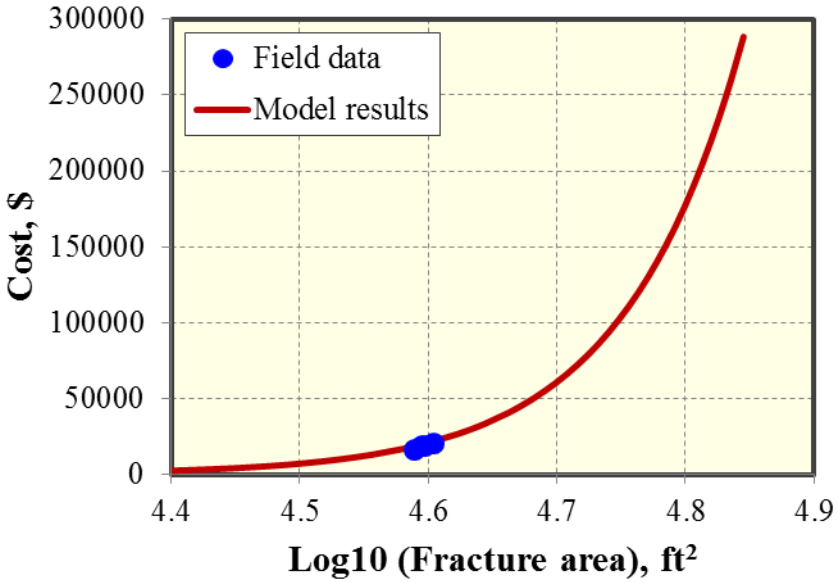

Figure 5.24: Cost of single fracture corresponding to fluid injected for four wells.

5.3.4 Economic evaluation of four fracture designs

In order to evaluate the economics of these four different fracture treatment designs, we set up a new 3D numerical reservoir model including multiple hydraulic fractures with a constant well length of 4,500 ft. The reservoir also has two layers: the bottom layer is fixed at 43 ft and the top layer is fixed 92 ft. The total thickness is 135 ft. Hydraulic fractures are assumed to completely penetrate the bottom layer and some part of the top layer, as shown in Figure 5.25. Fracture properties such as fracture spacing, fracture height, fracture half-length, and fracture conductivity are the same as the history matching results for each well. The other parameters used for simulation are listed in Table 5.9.

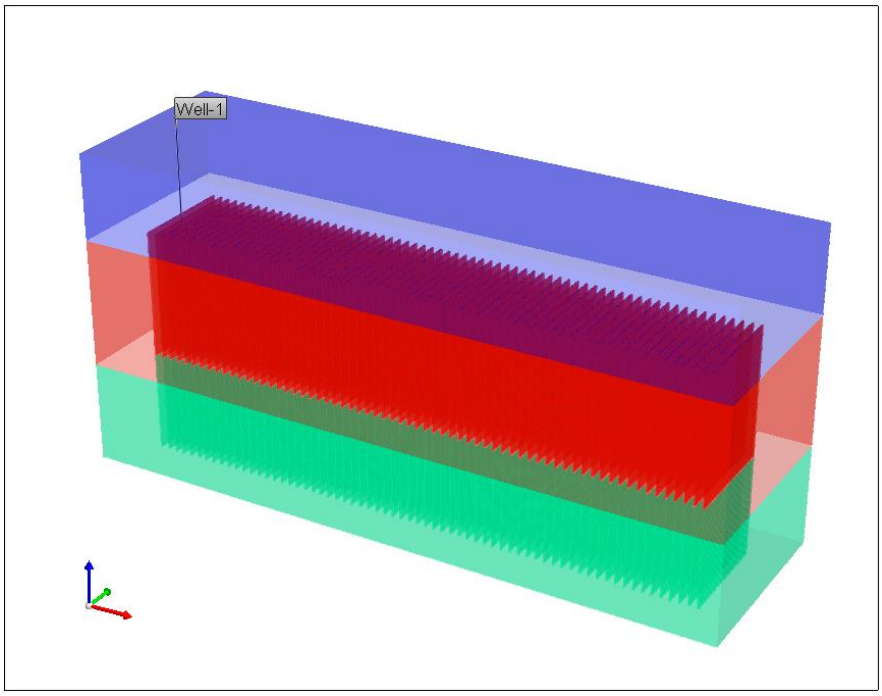

Figure 5.25: A basic reservoir model with two layers for economic evaluation of four different fracture designs in Marcellus shale.

Parameter	Value
Reservoir pressure, psi	4,400
Porosity (Bottom layer)	13%
Porosity (Top layer)	9%
Reservoir permeability, nD	800
Total compressibility, psi^{-1}	3×10^{-6}
Temperature, ^{o}F	130
Flowing BHP, psi	200
Initial gas saturation	90%
Gas specific gravity	0.58
Produciton time, year	30

Table 5.9: Parameters used simulation to perform economic evaluation of four different fracture designs in Marcellus shale.

Figure 5.26 compares the cumulative gas production for four wells with different fracture designs. As shown, the rank of gas recovery at 30 years of production is Well 1, Well 3, Well 4, and Well 2, respectively.

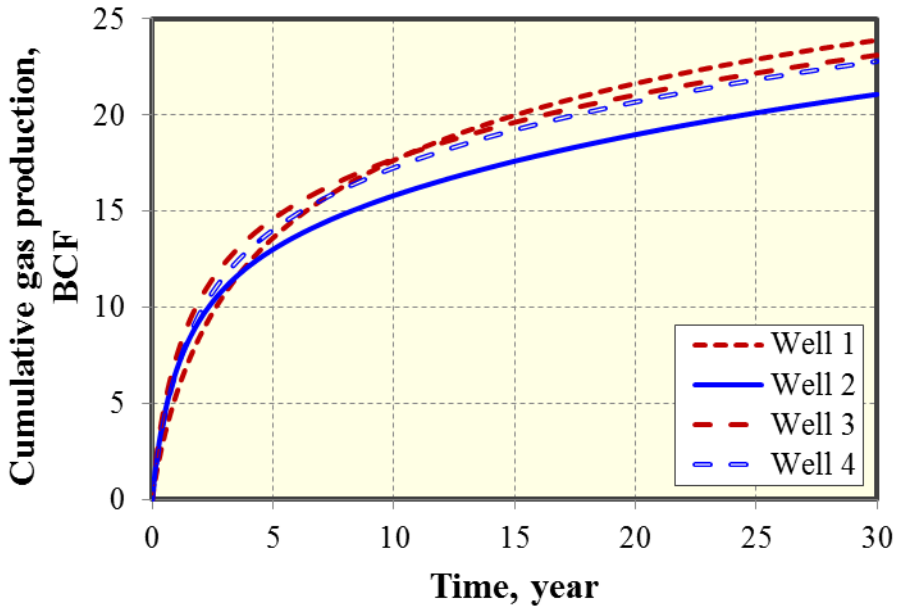

Figure 5.26: Comparison of cumulative gas production for four wells with different fracture designs.

The NPVs of four wells are calculated by assuming the gas price of $3.5/MSCF, the interest rate of 10%, and the royalty tax of 12.5%, as shown in Figure 5.27. It can be seen that the rank of NPV is Well 3, Well 1, Well 4, and Well 2, respectively. Hence, the fracture design 3 with 4 clusters per stage and 436,156 lbs of proppants per stage for Well 3 is the best design among these four different designs in Marcellus shale.

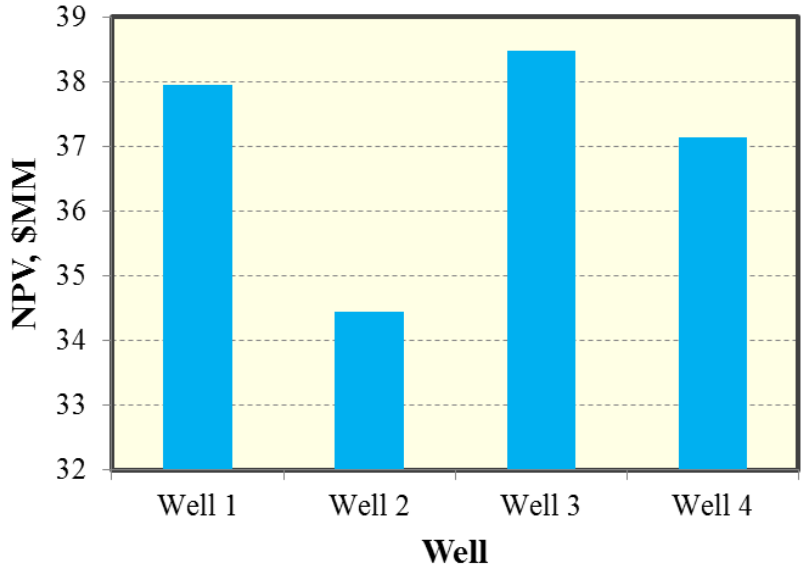

Figure 5.27: Comparison of NPV for four wells with different fracture designs.

5.4 ECONOMIC OPTIMIZATION

After the sensitivity analysis using the framework, the response surface of NPV based on the four design variables such as fracture height (A), fracture half-length (B), fracture conductivity (C), and cluster spacing (D) was built. The range for each parameter is the same as that in Table 5.1. The reservoir permeability is assumed to be 800 nD and the average reservoir pressure is assumed to be 4,500 psi. According to four variables in this study, 25 simulation cases were generated based on the approach of D-Optimal design, which was originated from the optimal design theory (Kiefer and Wolfowitz, 1959), as shown in Table 5.10. More details about the approach of D-optimal design can be found elsewhere (Myers et al., 2008). Similarly with sensitivity study, the ISPUR is used to generate 25 cases automatically and efficiently.

Run	A	B	C	D
1	135	390	47	40
2	82	380	9	70
3	40	500	100	40
4	40	300	100	50
5	40	400	1	40
6	135	500	100	90
7	99	420	100	60
8	62	310	67	80
9	135	300	100	40
10	40	300	1	90
11	121	300	100	90
12	40	500	39	70
13	40	300	1	90
14	135	300	1	60
15	135	500	1	40
16	96	500	50	50
17	135	300	1	60
18	85	300	38	40
19	54	400	61	50
20	135	400	35	90
21	40	450	100	90
22	89	500	1	90
23	40	500	100	40
24	40	450	100	90
25	135	500	100	90

Table 5.10: 25 simulation cases based on D-Optimal design.

After numerical simulation of each case, cumulative gas production was obtained and shown in Figure 5.28. It clearly shows that the cumulative gas production at 30 years of gas production has a large uncertainty. This means that further optimization is needed.

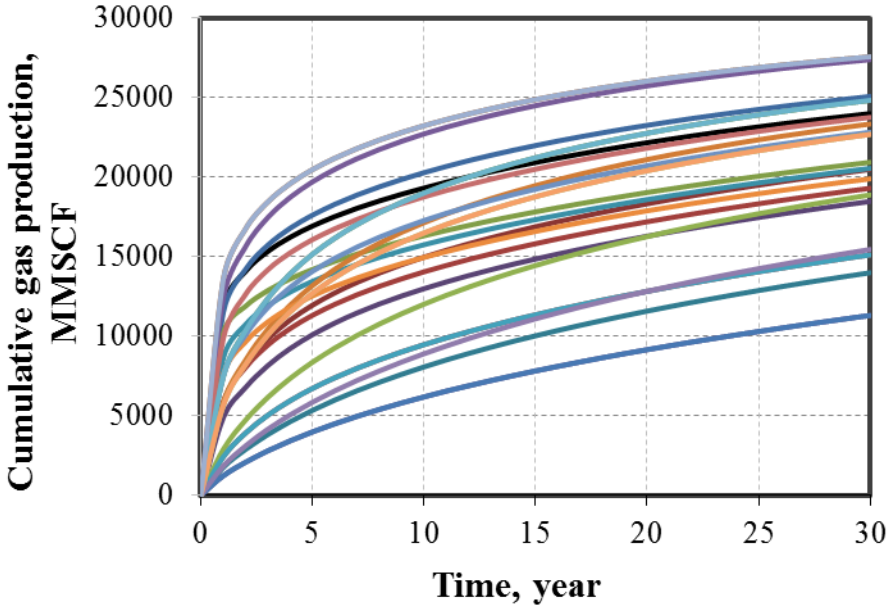

Figure 5.28: Cumulative gas production of 25 simulation cases for a 30-year period.

Once the cumulative gas production of 25 cases was obtained, the economic Excel spreadsheet is used to calculate the corresponding NPVs based on the price of natural gas of $3.5/MSCF, interest rate of 10%, and Royalty tax of 12.5%. The fracture cost related to single fracture conductivity and area, as shown in Figures 5.23 and 5.24, respectively, is used. The single well drilling cost is around $2.5 MM in this case study. Figure 5.29 presents NPVs of 25 simulation cases at 30 years of production.

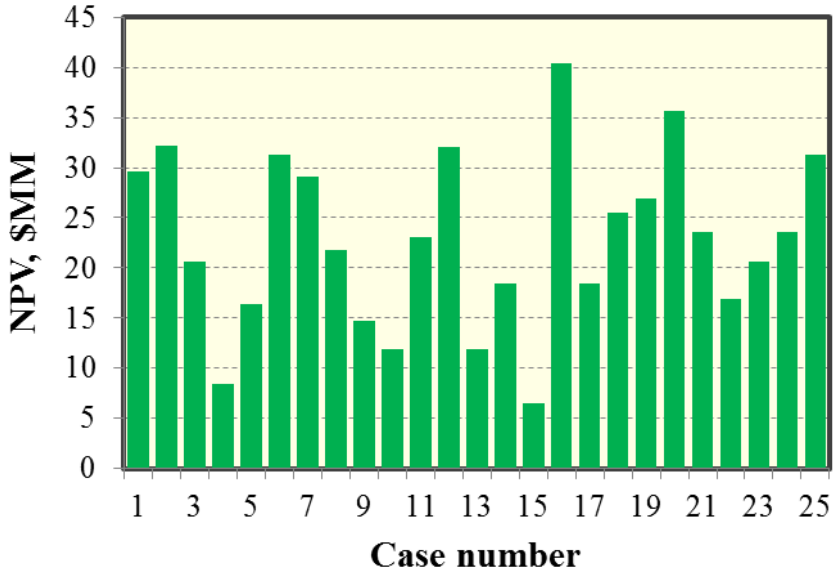

Figure 5.29: NPVs of 25 cases at 30 years of gas production with the gas price of $3.5/MSCF.

Once NPVs of 25 simulation cases were obtained, the Design-Expert software package is used to build the NPV response surface model. To select the appropriate model, the statistical approach is used to determine which polynomial fits the equation among linear model, two-factor interaction model (2FI), quadratic model, and cubic model, as shown in Table 5.11. The criterion for selecting the appropriate model is choosing the highest polynomial model, where the additional terms are significant and the model is not aliased. Although the cubic model is the highest polynomial model, it is not selected because it is aliased. Aliasing means some effects are confounded with each other, which is a result of reducing the number of experimental runs (Zhang, 2005). When it occurs, several groups of effects are combined into one group and the most significant effect in the group is used to represent the effect of the group. Essentially, it is important that the model is not aliased. In addition, other criteria are to select the model that has the maximum "Adjusted R-Squared" and "Predicted R-Squared". Thus, the fully

quadratic model is selected to build the NPV response surface in the subsequent optimization process.

Source	Std. Dev.	R-Squared	Adjusted R-Squared	Predicted R-Squared	Press	
Linear	0.19	0.21	0.052	-0.37	1.27	
2FI	0.19	0.47	0.088	-2.20	2.96	
Quadratic	0.050	0.97	0.936	0.62	0.35	Suggested
Cubic	0.00	1.00	1.00			Aliased

Table 5.11: Statistical approach to select the RSM model with gas price of $3.5/MSCF.

The equation fitted to the NPV response surface with the actual factors is presented below:

$$
\begin{aligned}
&Log_{10}(NPV) = \\
&-1.0544 + 0.01609 \times A + 7.9739 \times 10^{-3} \times B - 9.4093 \times 10^{-4} \times C + 5.6403 \times 10^{-3} \times D \\
&-2.0868 \times 10^{-5} \times AB + 2.5452 \times 10^{-5} \times AC + 2.7032 \times 10^{-5} \times AD + 2.1057 \times 10^{-5} \times BC \\
&+6.4429 \times 10^{-6} \times BD + 1.1089 \times 10^{-5} \times CD - 5.6609 \times 10^{-5} \times A^2 - 8.8926 \times 10^{-6} \times B^2 \\
&-9.2179 \times 10^{-5} \times C^2 - 6.7692 \times 10^{-5} \times D^2,
\end{aligned}
\tag{5.1}
$$

where A is fracture height, B is fracture half-length, C is fracture conductivity, and D is cluster spacing.

The normal plot of residuals, reflecting the distribution of the residuals, is shown in Figure 5.30. All the points in the "Normal Plot of Residuals" fall on the straight line, meaning the residuals are normally distributed. Figure 5.31 shows the plot of "Predicted vs. Actual", illustrating whether the generated equation of NPV response surface accurately predicts the actual NPV values. It can be seen that generated NPV response surface models provide such reliable predicted values of NPV, as compared with the

actual values of NPV. This means that the generated NPV response surface model is reliable.

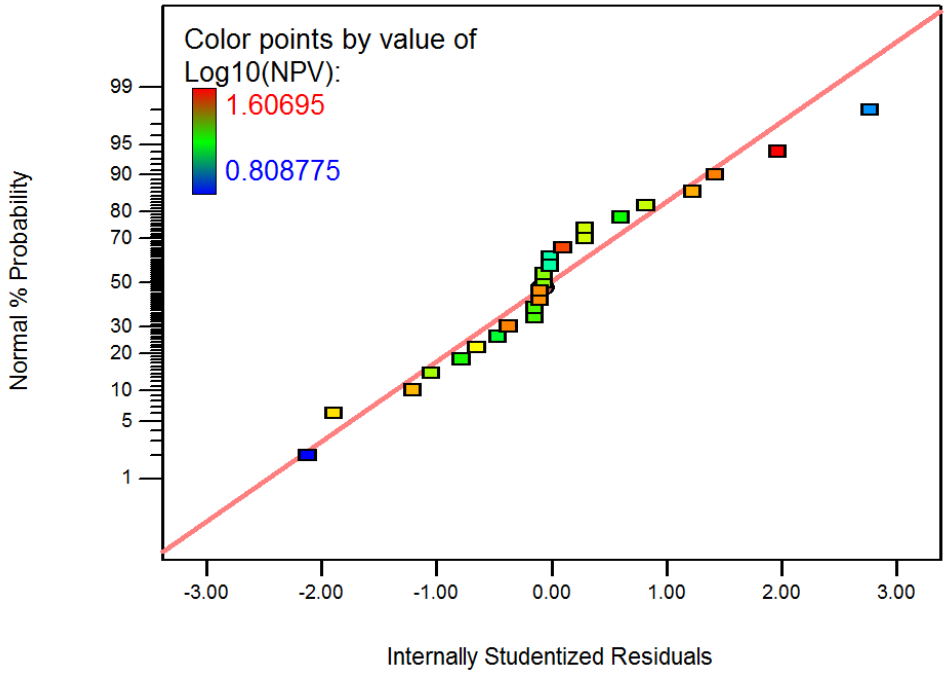

Figure 5.30: Normal plot of residuals at gas price of $3.5/MSCF.

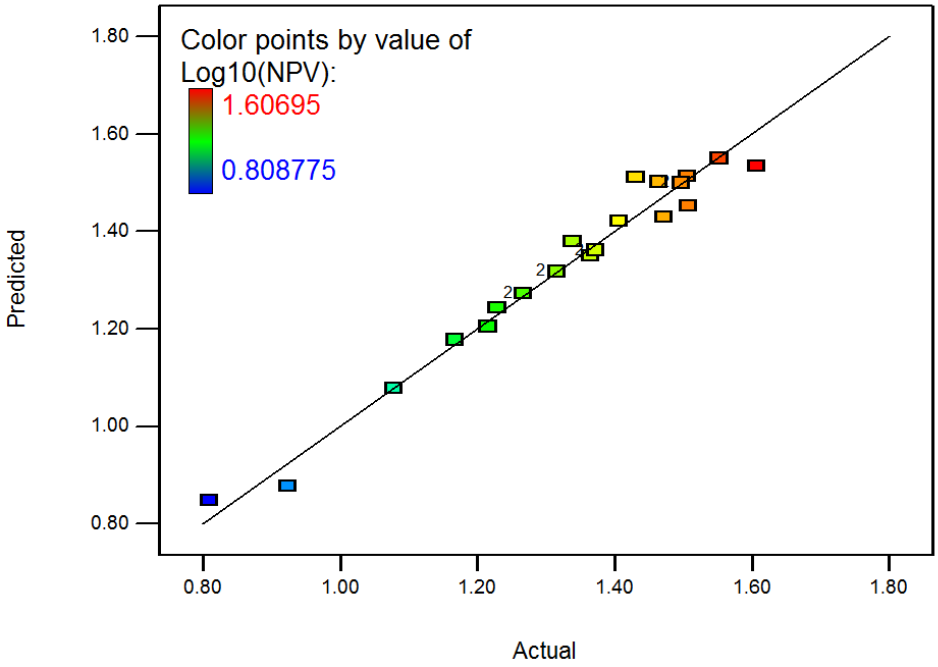

Figure 5.31: Predicted NPV versus the actual NPV plot at gas price of $3.5/MSCF.

Figure 5.32 shows the 3D surface of NPV at varied values of fracture conductivity and fracture height with gas price of $3.5/MSCF. It shows that there is an optimal fracture design related to fracture conductivity and fracture height. Therefore, this methodology can provide some insights into optimization of fracturing treatment design to obtain the maximum economic viability of the field.

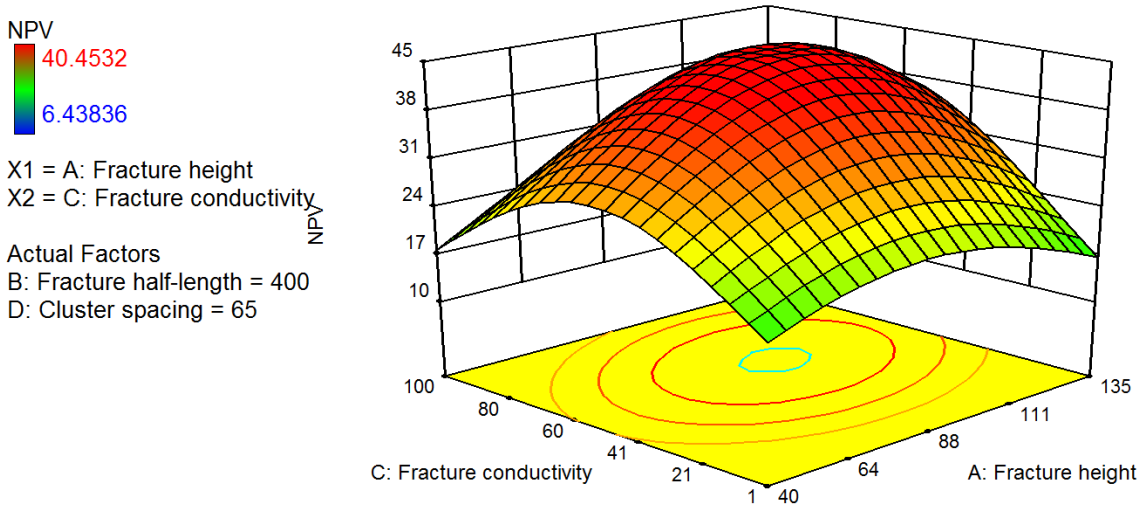

Figure 5.32: 3D surface of NPV at varied values of fracture conductivity and fracture height.

The objective function of NPV will be maximized by selecting the best combinations with uncertain parameters through the method of RSM. The best scenario is obtained based on the range of parameters investigated in this study for the Marcellus shale. The best case with the highest NPV value of $49.25 MM corresponding to fracture height of 90 ft, fracture half-length of 460 ft, fracture conductivity of 62 md-ft, and cluster spacing of 80 ft, as shown in Figure 5.33. Figure 5.34 shows gas flow rate and cumulative gas production at 30 years of production. Figure 5.35 presents pressure distribution for the best case at 30 years of gas production, illustrating the drainage volume clearly.

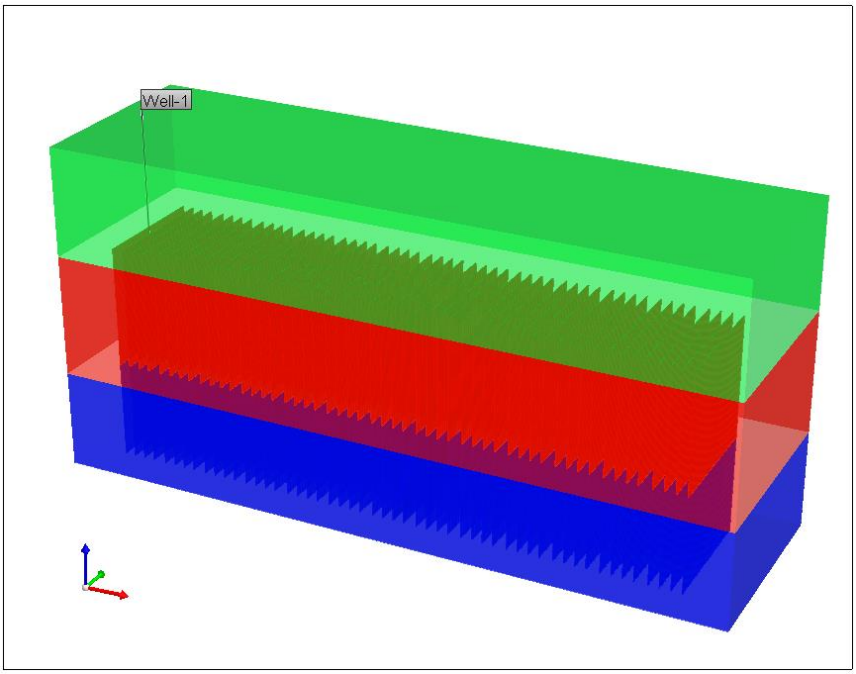

Figure 5.33: The best case with fracture height of 90 ft, fracture half-length of 460 ft, fracture conductivity of 62 md-ft, and cluster spacing of 80 ft for the Marcellus Shale.

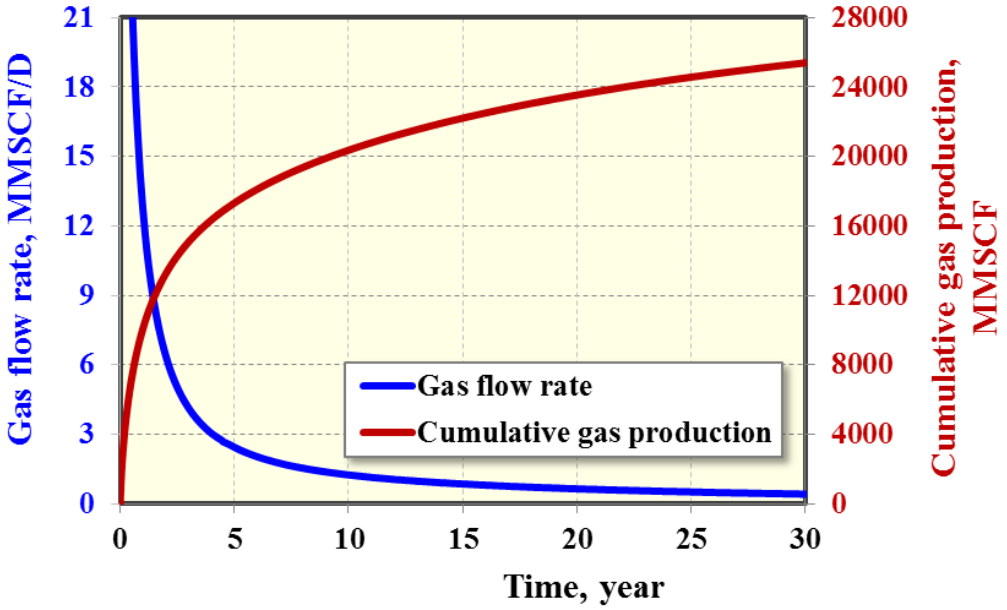

Figure 5.34: Cumulative gas production and gas flow rate of the best case.

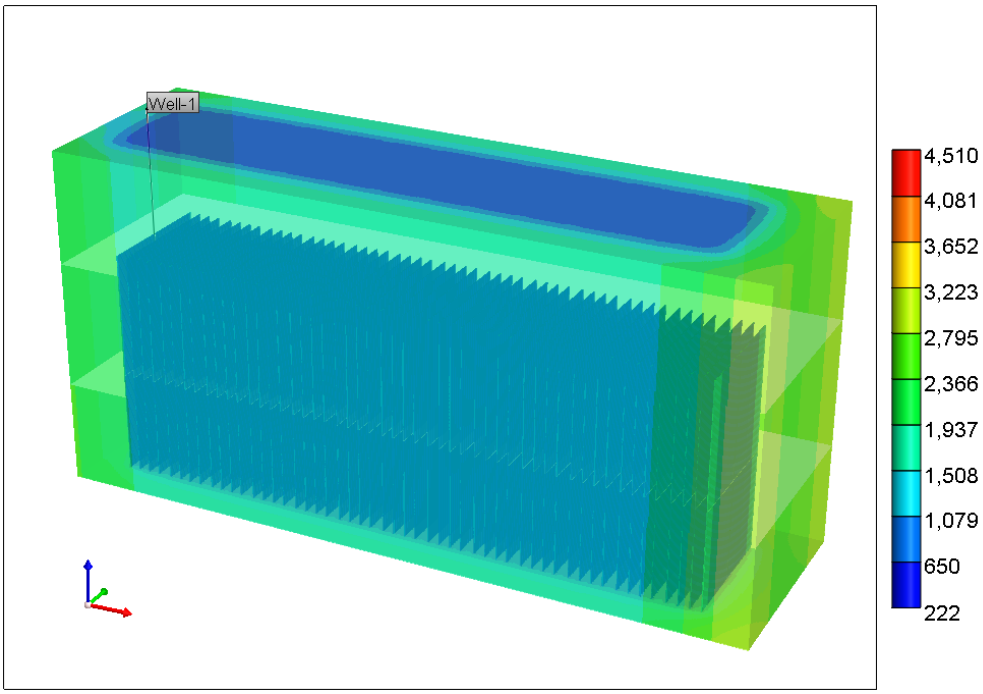

Figure 5.35: Pressure distribution at 30 years of production for the best case (pressure unit: psi).

5.5 CONCLUSIONS

We applied the framework developed in Chapter 4 to perform sensitivity study, history matching, and economic optimization for the Marcellus shale. The following conclusions can be drawn from this study:

(1) At early time of production (5 years), fracture conductivity is the most significant, followed by permeability, fracture height, fracture half-length, reservoir pressure, and cluster spacing; while at late time of production (30 years), permeability is the most important, followed by fracture conductivity, fracture half-length, fracture height, reservoir pressure, and cluster spacing.

(2) Based on the sensitivity analysis, a well from Marcellus shale was analyzed efficiently and the estimated ultimate recovery was determined as 11.12 BCF.

(3) The best case for the Marcellus shale was obtained as fracture height of 90 ft, fracture half-length of 460 ft, fracture conductivity of 62 md-ft, and cluster spacing of 80 ft for gas price of $3.5/MSCF, based on the range of parameters investigated in this study.

CHAPTER 6: Optimization of Fracture Treatment Design for Tight Oil Reservoirs

The framework developed in Chapter 4 is also used to quantify the high uncertainties and perform optimization of multiple well placement for the development of Bakken tight oil formation. For single horizontal well, six uncertain parameters including fracture spacing, fracture half-length, fracture conductivity, permeability, porosity, and initial water saturation were investigated, and each parameter was given a reasonable range based on typical reservoir and fracture properties from the Middle Bakken. We first used DOE to investigate the order of influence of each parameter and parameter interactions to determine which parameter significantly impacts the oil recovery. Based on sensitivity analysis, we performed history matching and production forecasting with one field production well. Based on the history matching results, the key fracture parameters such as fracture half-length, height, and conductivity were examined. Subsequently, based on the significant design variables of single well in combination of the variable of well number, we built the response surface model in terms of net present value to obtain the best economic scenario for multiple well placement. This work is valuable for guiding fracture design and completion optimization for multiple well placement in the Bakken tight oil reservoirs.

6.1 INTRODUCTION

Bakken formation is one of the largest tight oil developments in North America, which consists of Upper and Lower Bakken shales, Middle Bakken, Sanish and Three Forks, as shown in Figure 6.1. The Middle Bakken and Three Forks are two primary targets for the current field development. Recently, the United States Geological Survey (USGS) performed an assessment and reported that Middle Bakken has an estimated average oil resource of 3.65 billion barrels and Three Forks has an estimated average resource of 3.73 billion barrels (USGS, 2013).

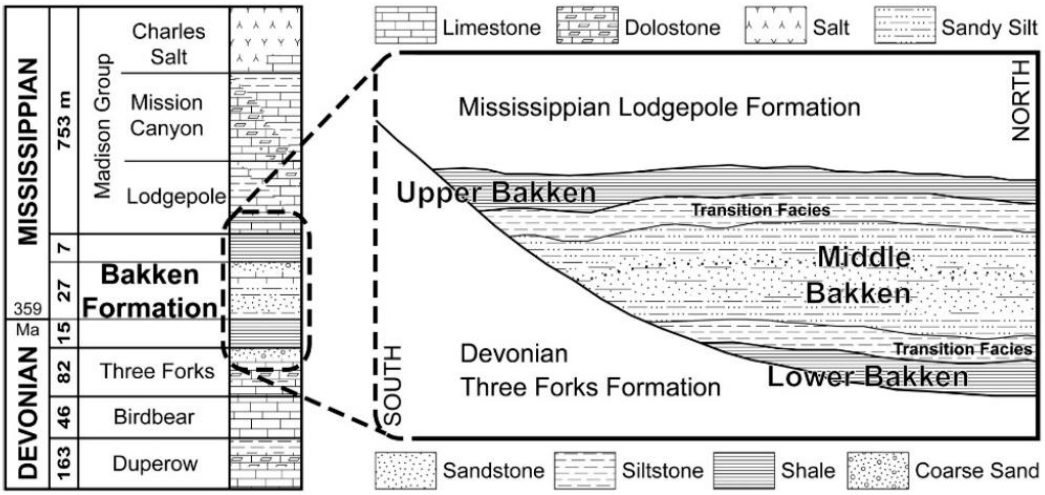

Figure 6.1: A cross section of the Bakken formation (West et al., 2013).

Numerous horizontal wells along with hydraulic fracturing are required to make the economic development of the Bakken formation. Multiple created hydraulic fractures can generate a large contact area between the wellbore and formation with low or ultra-low permeability. Fracture conductivity, representing the ability of propped fracture to transmit fluid flow, is defined as propped fracture permeability multiplied by propped fracture width in this study. It plays an important role in providing an adequate connection between the wellbore and the formation to transmit reservoir fluids. Also, it is

a key parameter for evaluation of post-fracture treatments and optimization of fracture design for new completion strategy. Most horizontal wells are drilled in the N-S orientation, which is the approximate direction of the minimum horizontal stress (Besler, 2007). The majority of wells are drilled in the depth between 10,500 ft and 11,000 ft true vertical depth (TVD) (Flowers et al., 2014). Lateral length in the Bakken in most cases has two scenarios, one is "short laterals" with approximately one mile long and spaced at 640 acres; the other is "long laterals" with approximately two miles long and spaced at 1280 acres (West et al., 2013). West et al. (2013) recommended the optimal stage spacing to be 325 ft with three clusters per single fracturing stage. An average of 30 perforation stages is used for each long lateral (Luo et al., 2011).

During hydraulic fracturing, a total of about 182,500 bbl of fluid and 2,555,000 lbs of proppant are pumped for each well in the Middle Bakken and 153,000 bbl of fluid and 2,454,000 lbs of proppant for each well in the Three Forks (Ganpule et al., 2013). The main goal of proppant is to keep the created hydraulic fractures open with enough fracture conductivity. There are many proppant types used in the Bakken formation, such as sand, ceramic, resin coated sand or their combinations (Flowers et al., 2014). Ceramic proppant can provide not only a higher fracture conductivity but also a greater longevity and durability than sand or resin-coated sand (Handren and Palisch, 2007; Rankin et al., 2010). Retaining high fracture conductivity over the lifetime of a well is critical for the economic development of the Bakken formation. However, it is very challenging to maintain such high fracture conductivity for a long-term period due to proppant embedment, proppant crushing, proppant fines generation and migration, proppant flowback, and proppant diagenesis, resulting in the loss of fracture conductivity (Pope et al., 2009; LaFollette and Carman, 2010; Fan et al., 2010). Also, non-Darcy flow and

multiphase flow in propped fractures will decrease fracture conductivity significantly (McDaniel et al., 2010).

In the Bakken formation, hydraulic fracturing is performed in the deeper depth with higher fracture closure pressure. The phenomenon of proppant embedment becomes an important issue in the loss of fracture conductivity. The deeper well depth leads to the pumped proppants being exposed to a high stress over 9,450 psi based on the fracture gradient of 0.90 psi/ft. The Bakken is over-pressured with pressure gradient up to 0.73 psi/ft in the central part of the Williston Basin (Meissner, 1978). Accordingly, if the initial reservoir pressure is around 7,600 psi, then the effective stress of 1,850 psi is generated on the proppants at the beginning of production. When the flowing bottom hole pressure declines to 1,000 psi, the effective stress will increase to about 8,450 psi. Propped fracture conductivity is a function of effective stress, and it decreases with the increasing effective stress. Additionally, mixing of various proppant sizes might reduce fracture conductivity due to proppants with small size invading and occupying pore space (McDaniel and Willingham, 1978; Schmidt et al., 2014). It is recognized in the industry that the actual fracture conductivity is often a small fraction of those measured by the American Petroleum Institute (API) conductivity test, and it is still less than the optimal fracture conductivity (McDaniel et al., 2010). Flowers et al. (2014) analyzed the field production data of 205 wells with production history of 325 days in the Bakken, and presented that the wells treated with proppant of ceramic only outperform the wells treated with proppant type of sand only by 40% and the wells treated with the mixture of ceramic and sand by 21%. Accordingly, the selection of proppant type and concentration to achieve high fracture conductivity for a long-term in the Bakken formation is still important to improve well productivity and profitability.

Similar with many shale gas reservoirs, there is a large uncertainty in reservoir and fracture properties in the Bakken formation. It was reported that porosity in the Middle Bakken is in the range of 4%-12%, and initial water saturation is 25%-60% (Cherian et al., 2013). The average porosity of the Middle Bakken is 6% and permeability is in the order of microdarcies (Nojabaei et al., 2013). Reservoir temperature is approximately 240 ^{o}F (Rankin et al., 2010). Average oil gravity is about 42 ^{o}API, indicating the crude oil is light with low viscosity. Nojabaei et al. (2013) presented that the range of gas oil ratio (GOR) is from 507 to 1,712 SCF/bbl and bubble point pressure varies from 1,617 to 3,403 psi. Cherian et al. (2013) reported that although fracture half-length in most cases in the Bakken exceeds 300 ft (300-900 ft), the proppants only transport 10-30% of that distance because of fracture height growth. They found that an equivalent fracture half-length is in the range of 100-200 ft and fracture conductivity ranges between 4-7 md-ft based on history matching results. The number of fractures in each stage plays a key role in controlling the fracture half-length and corresponding drainage area. It may have one fracture or multiple fractures in single perforation stage.

Although there are many attempts to optimize fracture design in the Bakken formation, the existence of high uncertainty in reservoir and fracture properties is still poorly understood. In addition, economic analysis is required for the optimal multiple well placement due to the high drilling and completion cost. In this study, we used the framework to first quantify the significant parameters and screen insignificant ones for single horizontal well. Six uncertain parameters including fracture spacing, fracture half-length, fracture conductivity, permeability, porosity, and initial water saturation were investigated, and each parameter was given a reasonable range based on the typical reservoir and fracture properties from the Middle Bakken. Then, based on the sensitivity analysis, we performed history matching with field production data from Middle Bakken.

Subsequently, we performed production forecasting to predict long-term oil recovery. Finally, we optimized fracture design in combination with maximizing net present value (NPV) for multiple well placement. This work is valuable for guiding fracture design and completion optimization for multiple well placement in the Bakken formation.

6.2 Numerical Modeling for Tight Oil Reservoirs

Reservoir simulation is an effective approach to simulate multiphase flow (gas-water-oil) in the Bakken formation, especially in the early stage of field developments. In this study, reservoir simulator of CMG-IMEX (a black-oil simulator) is used to model multiple hydraulic fractures and fluid flow in the Bakken tight oil reservoirs. For reservoir modeling including multiple fractures, local grid refinement (LGR) method is utilized to accurately model fluid flow from matrix to fractures.

For single horizontal well, we set up a basic 3D reservoir model with dimensions of 10,560 ft × 1,320 ft × 40 ft, which corresponds to length, width, and thickness, respectively. For multiple horizontal wells, the width of basic reservoir model is extended to 5,280 ft. A bi-wing fracture model is used in the basic reservoir model. The horizontal well length is set at 10,000 ft with 31 perforation stages. The number of effective fractures in each stage ranges from 1 to 4, as shown in Figure 6.2. Figure 6.2(a) assumes that there is only one effective fracture in each stage and the fractures are evenly spaced, so there are totally 31 effective hydraulic fractures along the horizontal well. Figure 6.2(b) assumes that there are four effective fractures in each stage; hence, there are totally 124 effective hydraulic fractures along the horizontal well. The stage spacing is 320 ft and the cluster spacing (the distance between two neighboring fractures) is 80 ft for the case with four fractures per stage.

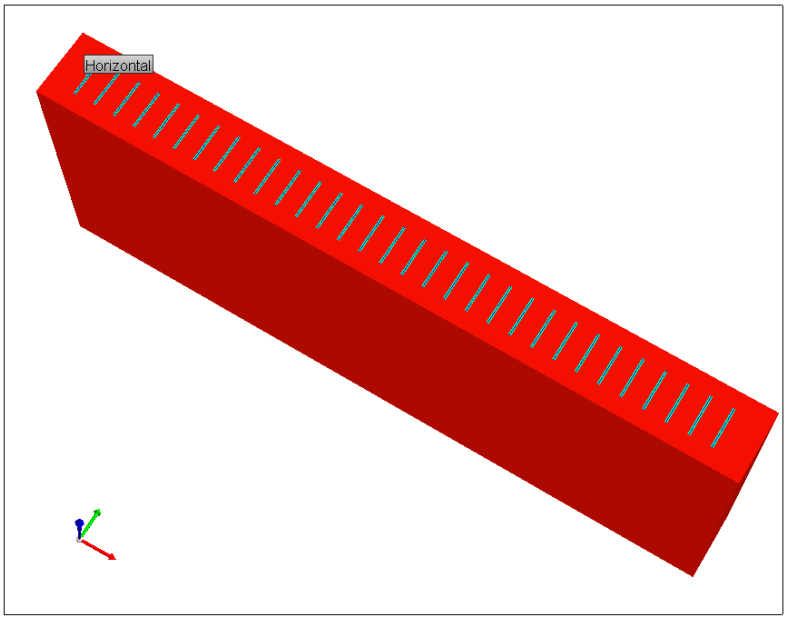

(a)

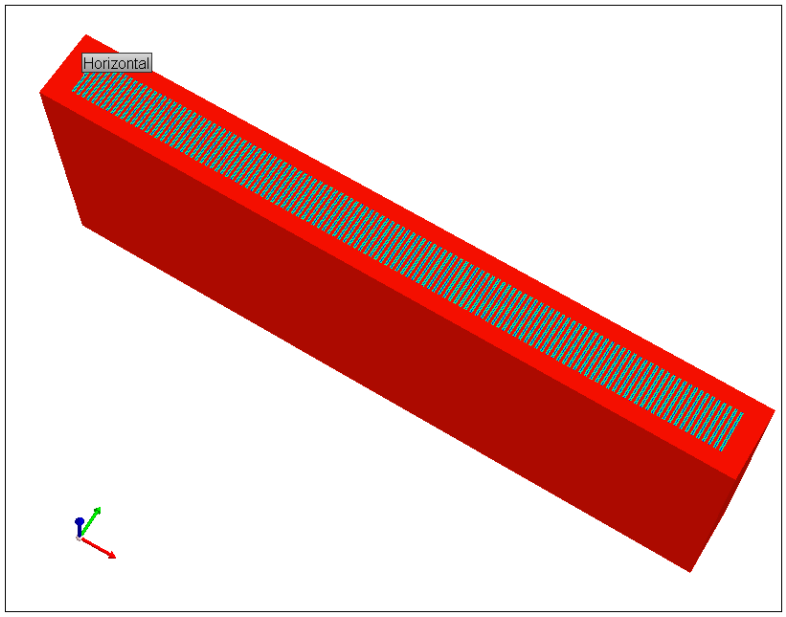

(b)

Figure 6.2: A basic 3D reservoir model including 31 fracturing stages for Bakken tight oil reservoir. (a) One effective fracture per stage. (b) Four effective fractures per stage.

The typical fluid and rock properties from the Middle Bakken are used for the subsequent simulation study, as listed in Table 6.1. Six uncertainty parameters were investigated including fracture spacing, fracture half-length, fracture conductivity, permeability, porosity, and water saturation. Each parameter was given a reasonable range with the actual maximum and minimum values or coded symbol of "+1" and "–1" based on the actual field data of the Bakken formation, as listed in Table 6.2. The reservoir is assumed to be homogeneous. Fracture height is equal to the reservoir thickness. A synthetic flowing bottom hole pressure curve is used to represent the real pressure drawdown, as illustrated in Figure 6.3.

Parameter	Value	Unit
Initial reservoir pressure	7,500	psi
Reservoir temperature	240	^{o}F
Total compressibility	1×10^{-6}	psi^{-1}
Horizontal well length	10,000	ft
Reservori thickness	40	ft
Gas specific gravity	0.92	
Bubble point	2,500	psi
Fracture spacing	80	ft
Fracture half-length	260	ft
Fracture conductivity	10	md-ft
Permeability	10	μD
Porosity	7%	
Water saturation	35%	

Table 6.1: Parameters used for simulations in the Middle Bakken.

Parameter	Coded symbol	Minimum (-1)	Maximum (+1)	Unit
Fracture spacing	A	80	320	ft
Fracture half-length	B	140	380	ft
Fracture conductivity	C	1	100	md-ft
Peremability	D	1	100	μD
Porosity	E	4%	10%	
Water saturation	F	25%	45%	

Table 6.2: Six uncertainty parameters investigated in this study for the Bakken formation.

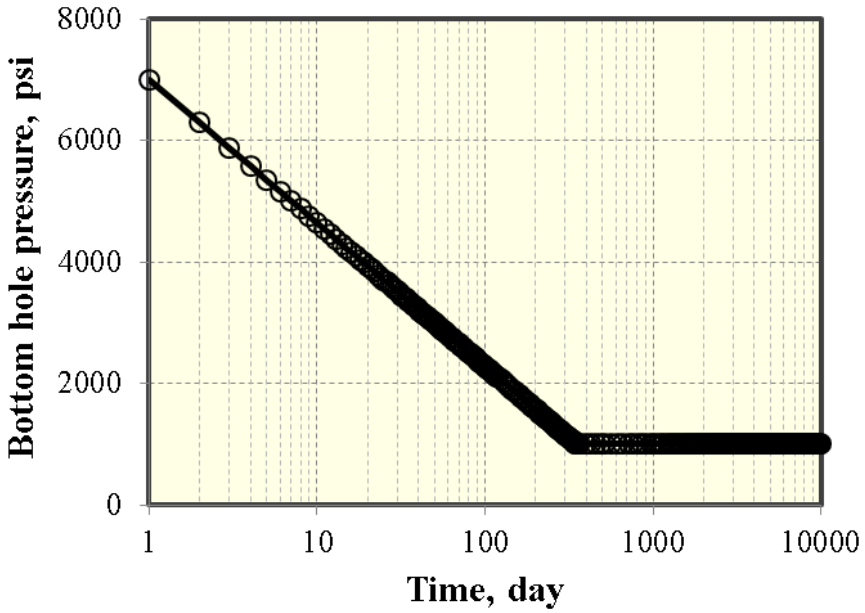

Figure 6.3: Flowing bottom hole pressure used for simulation of the Bakken formation.

The bottom hole pressure decreases from 7,000 psi to 1,000 psi at the early time of production (around 1 year), after that, it stabilizes until the end of production (30 years). The relative permeability curves, such as water-oil relative permeability and liquid-gas relative permeability (see Figure 6.4), are used in the numerical model.

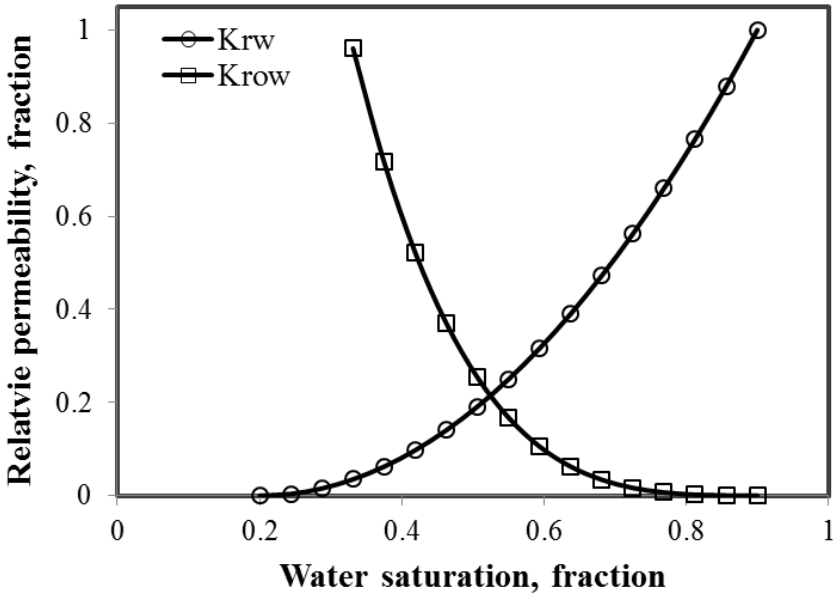

(a)

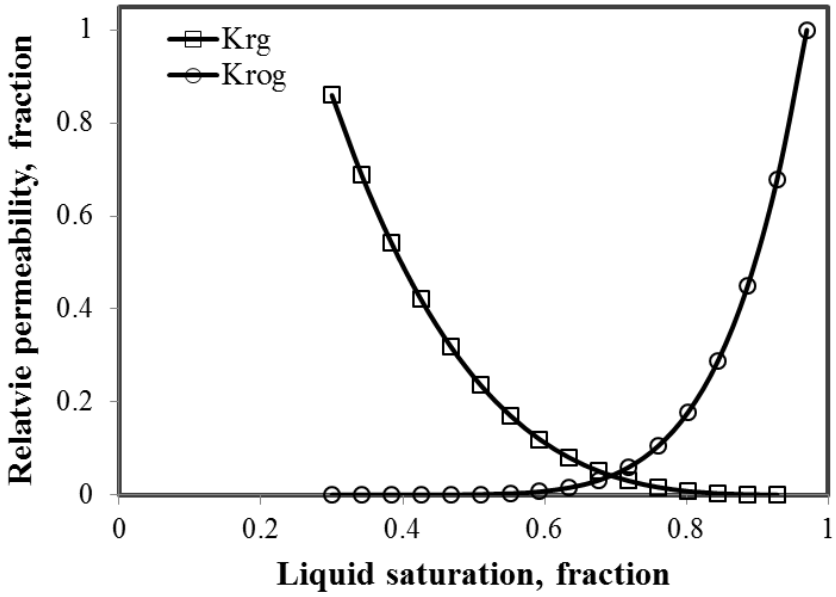

(b)

Figure 6.4: Relative permeability curves for the Middle Bakken tight oil reservoirs. (a) Water-oil relative permeability curve. (b) Liquid-gas relative permeability curve.

6.2.1 Effect of fracture conductivity

For the base case, effect of fracture conductivity on cumulative oil production is shown in Figure 6.5. The range fracture conductivity is from 0.1 md-ft to 100 md-ft. As shown, there is no big difference of cumulative oil production between 100 md-ft and 1,000 md-ft, illustrating that the fracture conductivity of 100 md-ft is very close to infinite fracture conductivity in this case study.

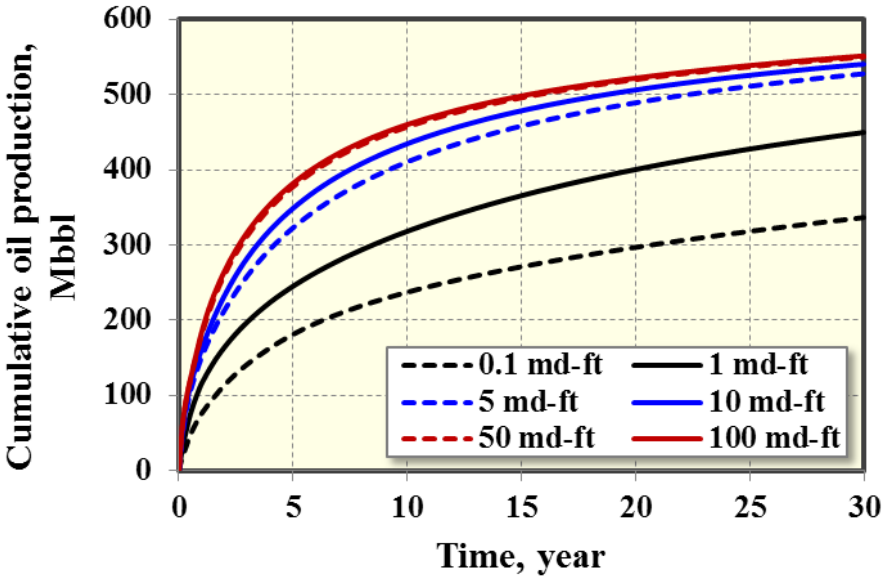

Figure 6.5: Effect of fracture conductivity on well performance in Bakken.

6.2.2 Effect of geomechanics

For the geomechanics effect, the stress-dependent fracture conductivity curve used in this case study is shown in Figure 6.6. As shown, the fracture conductivity corresponding to bottom hole pressure of 1,000 psi is about 22% of initial fracture conductivity corresponding to the initial reservoir pressure of 7,500 psi. Two initial fracture conductivities of 1 md-ft and 100 md-ft are used to evaluate the effect of geomechanics. Figure 6.7 shows the comparison of cumulative oil production with and

without the geomechanics effect. It can be seen that the initial fracture conductivity has a significant effect on the contribution of geomechanics to the decline rate of oil recovery. Cumulative oil production at 30 years of production decreases by around 13.6% and 0.8% for initial fracture conductivity of 1 md-ft and 100 md-ft, respectively. Hence, considering the geomechanics effect is important for completion optimization.

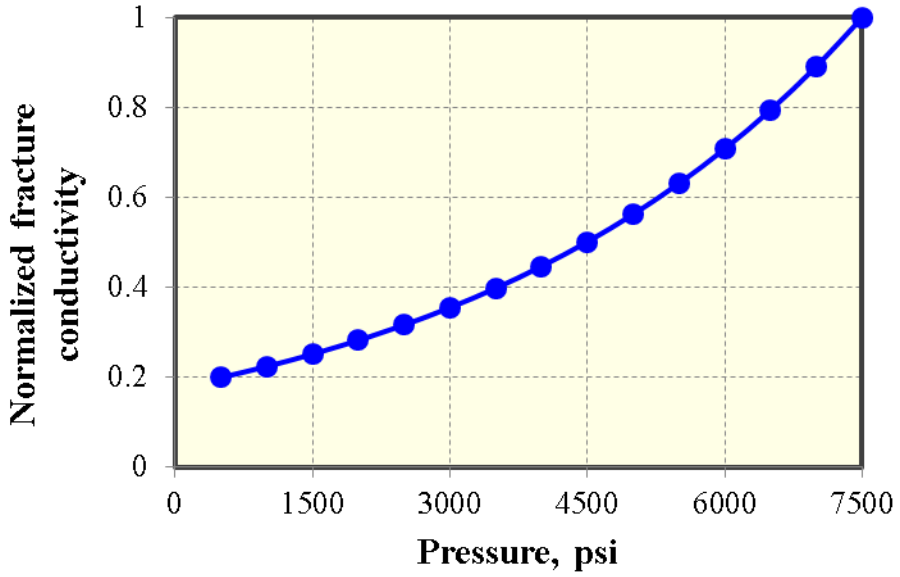

Figure 6.6: The stress-dependent fracture conductivity curve for the Middle Bakken.

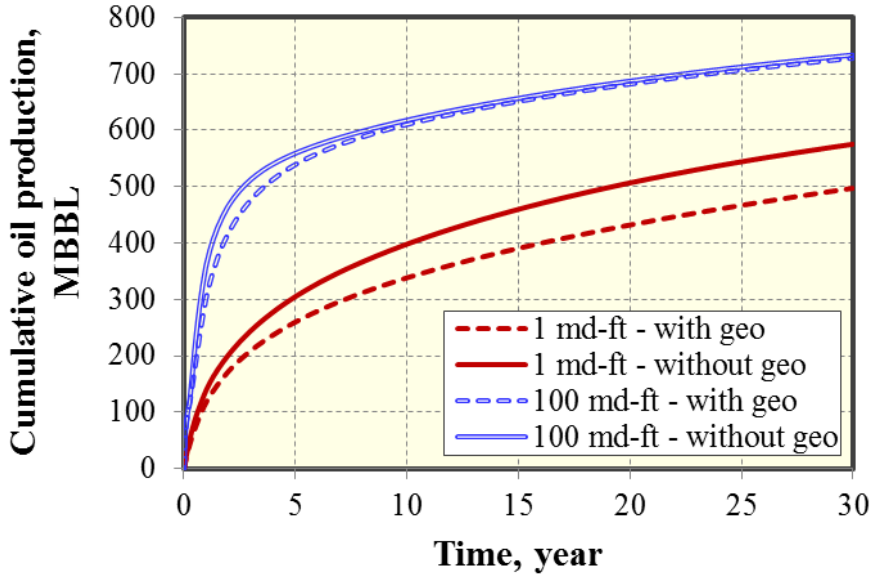

Figure 6.7: The comparison of well performance with and without the geomechanics effect for two scenarios.

6.3 SENSITIVITY STUDY

According to six parameters, 32 different simulation cases need to be prepared based on two-level fractional factorial design, as shown in Table 6.3. The ISPUR is used to generate 32 input files automatically and efficiently for reservoir simulator of CMG-IMEX. After performing numerical simulations for each case, cumulative oil production and oil recovery factor were obtained and shown in Figures 6.8 and 6.9, respectively. The figures clearly show that there is a wide range of cumulative oil production and oil recovery factor. The ranges for the cumulative oil production and oil recovery factor at a 30-year period are obtained as 91.6-1514.9 MBBL (10^3 BBL) and 4.3%-28.7%, respectively. The average cumulative oil production and oil recovery factor are 530.5 MBBL and 16.6%, respectively.

Run	A	B	C	D	E	F
1	80	140	1	100	0.10	0.25
2	80	140	100	100	0.10	0.45
3	80	380	100	100	0.04	0.45
4	80	140	1	100	0.04	0.45
5	320	380	100	100	0.04	0.25
6	320	380	1	100	0.10	0.25
7	80	140	1	1	0.10	0.45
8	320	380	1	100	0.04	0.45
9	80	380	1	100	0.04	0.25
10	80	380	1	1	0.10	0.25
11	80	140	1	1	0.04	0.25
12	320	380	100	100	0.10	0.45
13	320	380	100	1	0.04	0.45
14	320	140	1	1	0.04	0.45
15	320	380	1	1	0.10	0.45
16	80	380	1	1	0.04	0.45
17	80	380	100	1	0.04	0.25
18	80	380	1	100	0.10	0.45
19	80	140	100	100	0.04	0.25
20	320	140	100	100	0.04	0.45
21	320	140	1	1	0.10	0.25
22	320	380	100	1	0.10	0.25
23	80	140	100	1	0.10	0.25
24	80	380	100	100	0.10	0.25
25	80	140	100	1	0.04	0.45
26	80	380	100	1	0.10	0.45

Table 6.3 continued on next page

27	320	140	100	100	0.10	0.25
28	320	380	1	1	0.04	0.25
29	320	140	100	1	0.04	0.25
30	320	140	100	1	0.10	0.45
31	320	140	1	100	0.10	0.45
32	320	140	1	100	0.04	0.25

Table 6.3: 32 simulation cases based on half fractional factorial design for six parameters in the Middle Bakken.

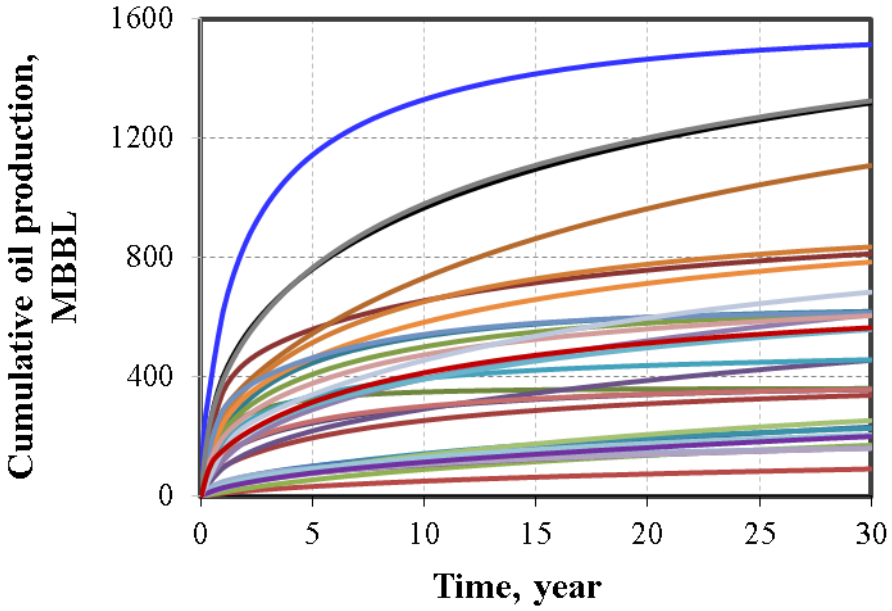

Figure 6.8: Cumulative oil production of 32 cases for the Middle Bakken.

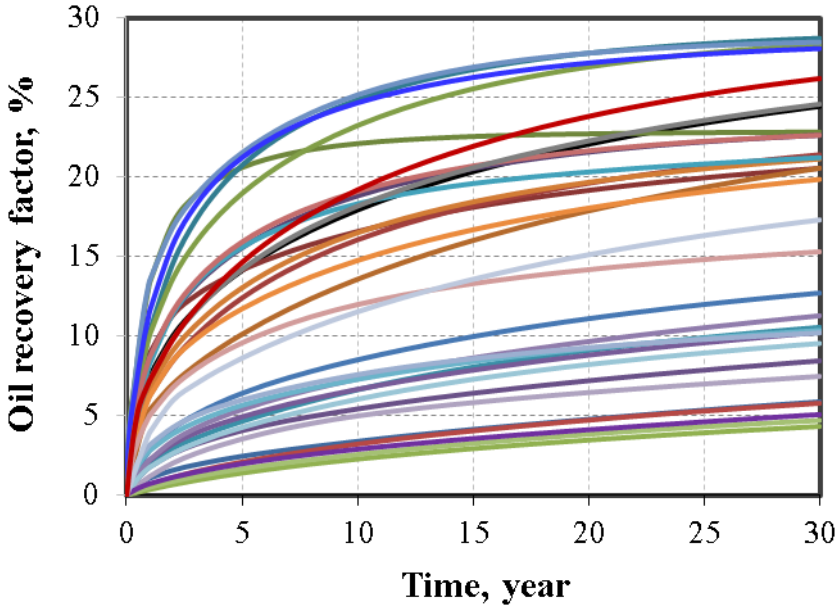

Figure 6.9: Oil recovery factor of 32 cases for the Middle Bakken.

Simulation results from Figure 6.8 are then used to construct the half-normal plot, Pareto chart, and the analysis-of-variance (ANOVA) table to identify the ranking of significant factors affecting cumulative oil production. The half-normal plot and the corresponding Pareto chart at different period of production for cumulative oil production are presented in Figures 6.10 through 6.13. Any parameters or two-parameter interaction highly deviating from the straight line are recognized as the parameters that affect the oil production significantly. At early time of production (5 years) as shown in Figures 6.10 and 6.12, the following order in terms of influence of main parameter effects is permeability (D), porosity (E), water saturation (F), fracture conductivity (C), fracture spacing (A), and fracture half-length (B); at late time of production (30 years) as shown in Figures 6.11 and 6.13, the order of influence of main parameters remains the same.

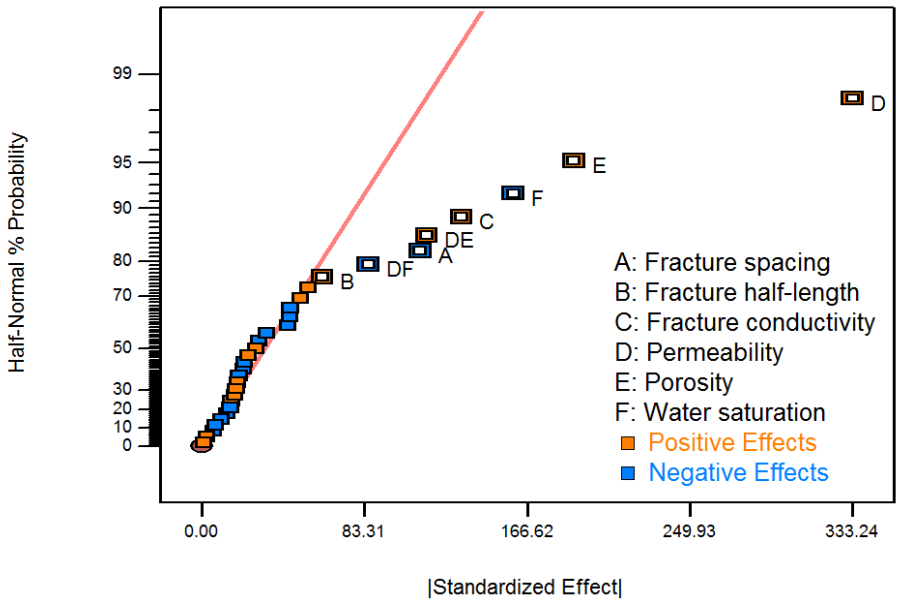

Figure 6.10: The half normal plot for cumulative oil production at 5 years of production.

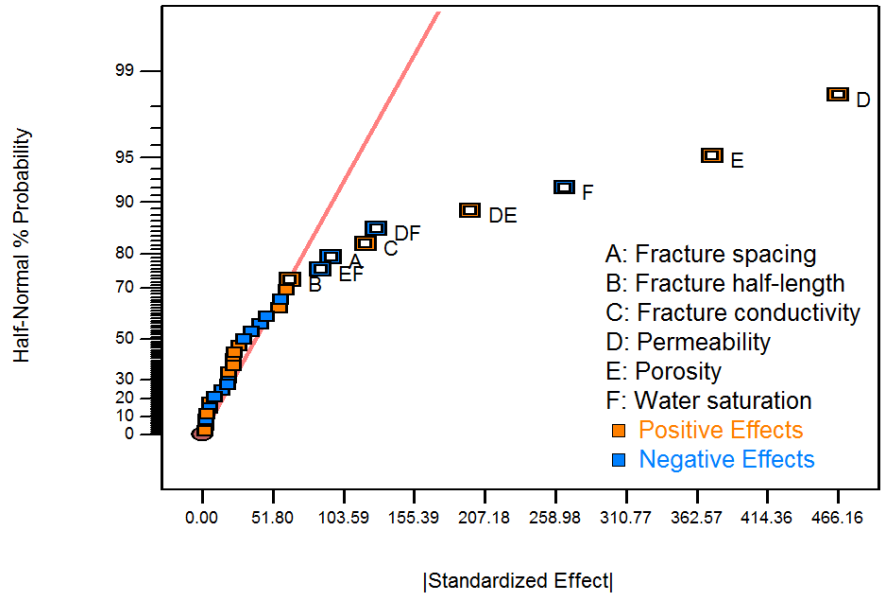

Figure 6.11: The half normal plot for cumulative oil production at 30 years of production.

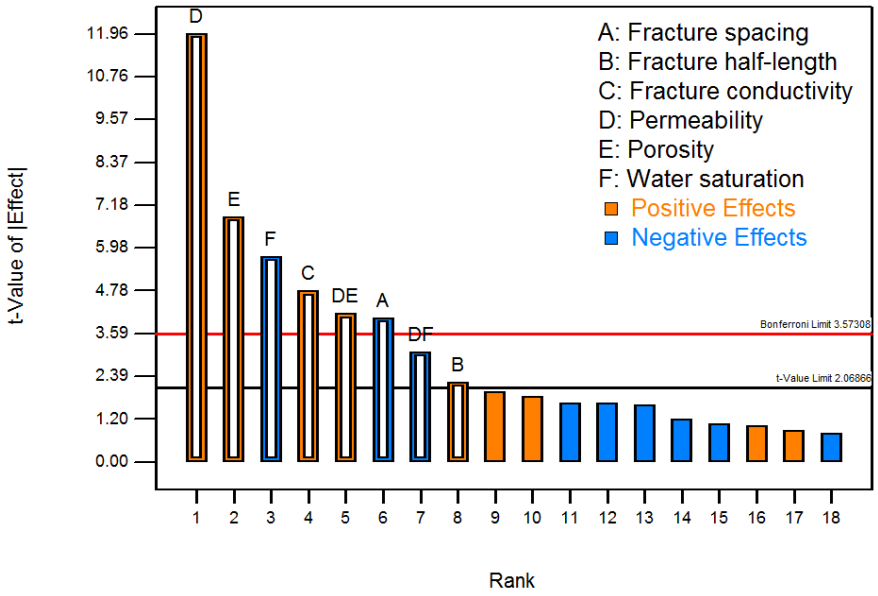

Figure 6.12: Pareto chart for cumulative oil production at 5 years of production.

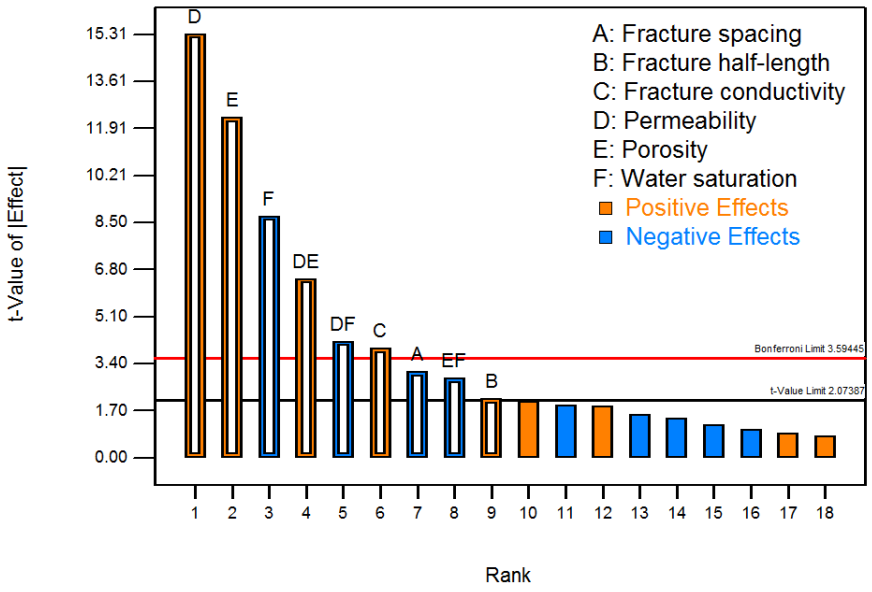

Figure 6.13: Pareto chart for cumulative oil production at 30 years of production.

The significant and insignificant model parameters are also determined by the ANOVA table, as shown in Tables 6.4 and 6.5. A parameter having value of "Prob > F"

(Probability of a large F-value) less than 0.1 is called a significant model term. Parameters not presented in Tables 6.4 and 6.5 are insignificant model terms.

Source	Sum of squares	Degree of freedom	Mean square	F-value	P-value
Model	1.818E+006	8	2.272E+005	36.58	< 0.0001
A	1.001E+005	1	1.001E+005	16.11	0.0005
B	30455.12	1	30455.12	4.90	0.0370
C	1.412E+005	1	1.412E+005	22.72	< 0.0001
D	8.884E+005	1	8.884E+005	143.01	< 0.0001
E	2.904E+005	1	2.904E+005	46.74	< 0.0001
F	2.033E+005	1	2.033E+005	32.73	< 0.0001
DE	1.059E+005	1	1.059E+005	17.05	0.0004
DF	58055.28	1	58055.28	9.35	0.0056
Residual	1.429E+005	23	6212.16		
Cor. Total	1.961E+006	31			

Table 6.4: ANOVA table for 5 years of cumulative oil production.

Source	Sum of squares	Degree of freedom	Mean square	F-value	P-value
Model	4.138E+006	9	4.598E+005	61.99	< 0.0001
A	70998.54	1	70998.54	9.57	0.0053
B	33108.08	1	33108.08	4.46	0.0462
C	1.148E+005	1	1.148E+005	15.48	0.0007
D	1.738E+006	1	1.738E+006	234.36	< 0.0001
E	1.118E+006	1	1.118E+006	150.72	< 0.0001
F	5.642E+005	1	5.642E+005	76.06	< 0.0001
DE	3.087E+005	1	3.087E+005	41.62	< 0.0001
DF	1.300E+005	1	1.300E+005	17.53	0.0004
EF	60005.14	1	60005.14	8.09	0.0094
Residual	1.632E+005	22	7417.67		
Cor. Total	4.301E+006	31			

Table 6.5: ANOVA table for 30 years of cumulative oil production.

The detailed influences of all parameters on the well performance in a short-term period (5 years) and a long-term period (30 years) are shown in Figure 6.14. It can be observed that impacts of some parameters on cumulative oil production decrease with time, including permeability (D), fracture conductivity (C), fracture spacing (A), and fracture half-length (B); while effects of some parameters increase with time, including porosity (E) and water saturation (F). The interactions between various parameters are defined as DE, DF, and EF. As it can be seen, the interaction parameter DE (interaction of permeability and porosity) is more important that the other interaction parameters. The rank of important parameters can provide critical insights into performing history matching with field production data in a short-term period.

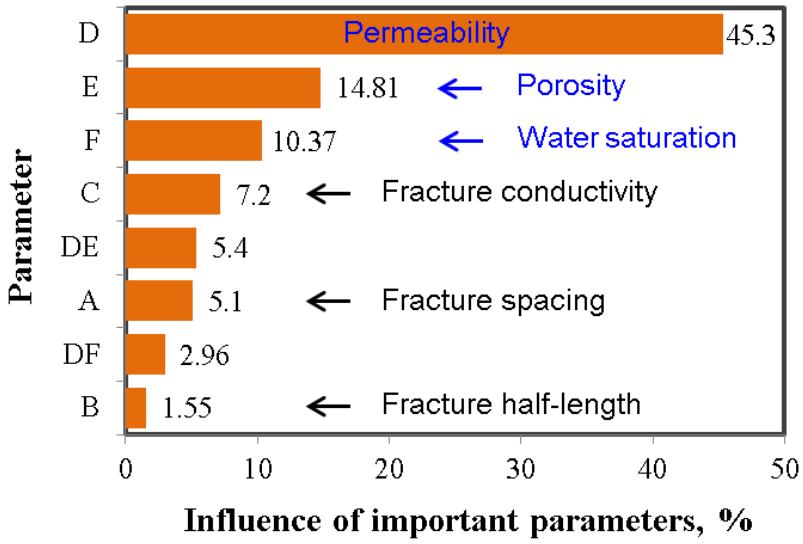

(a)

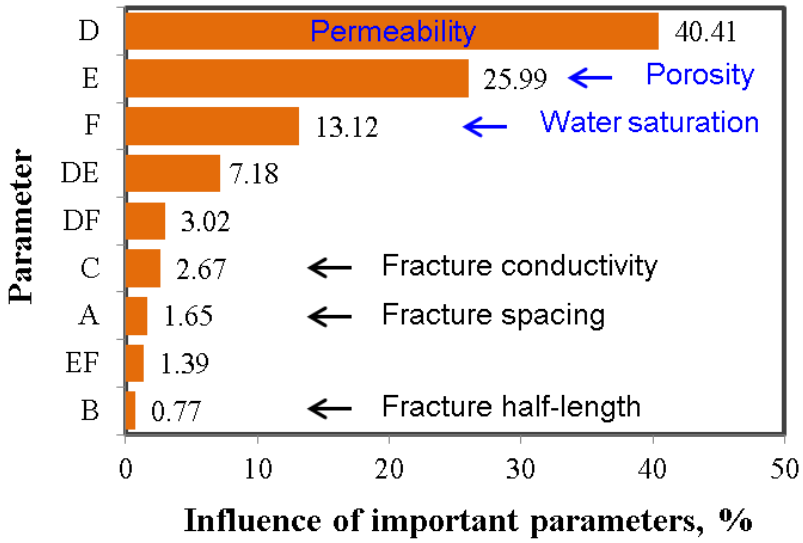

(b)

Figure 6.14: Rank of the influences of uncertainty parameters on cumulative oil production. (a) A short-term of production (5 years). (b) A long-term production (30 years).

6.4 History Matching and Production Forecasting

In this study, the field production data of a hydraulically fractured horizontal well from the Middle Bakken in North Dakota is used to perform history matching and

production forecasting (Kurtoglu and Kazemi, 2012). In this field case study, the horizontal well was stimulated with fifteen hydraulic fracturing stages. In the model, it is assumed that there are four effective fractures per single stage, so there are totally sixty hydraulic fractures along the horizontal well. The fracture width is set at 0.001 ft. An area of about 326 acres was simulated by setting up a basic 3D reservoir model using reservoir simulator of CMG-IMEX with dimensions of 10,500 ft × 2,640 ft × 50 ft, which corresponds to length, width, and thickness, respectively. The other detailed reservoir and fracture properties about this well are listed in Table 6.6. During history matching, bottom hole pressure measured from the field is used for a constraint input, as shown in red line in Figure 6.15. Oil and gas flow rate are the targets for history matching. Permeability, initial water saturation, fracture conductivity, and fracture half-length are mainly tuned to obtain a good match.

Parameter	Value	Unit
Initial reservoir pressure	7,800	psi
Reservoir temperature	245	^{o}F
Total compressibility	1×10^{-6}	psi^{-1}
Horizontal well length	8,828	ft
Reservoir thickness	50	ft
Gas specific gravity	0.92	
Bubble point	2,500	psi
Oil viscosity	0.32	cp
Fracture spacing	118	ft
Number of fracture	60	
Porosity	5.6%	

Table 6.6: Parameters used for history matching in the Middle Bakken.

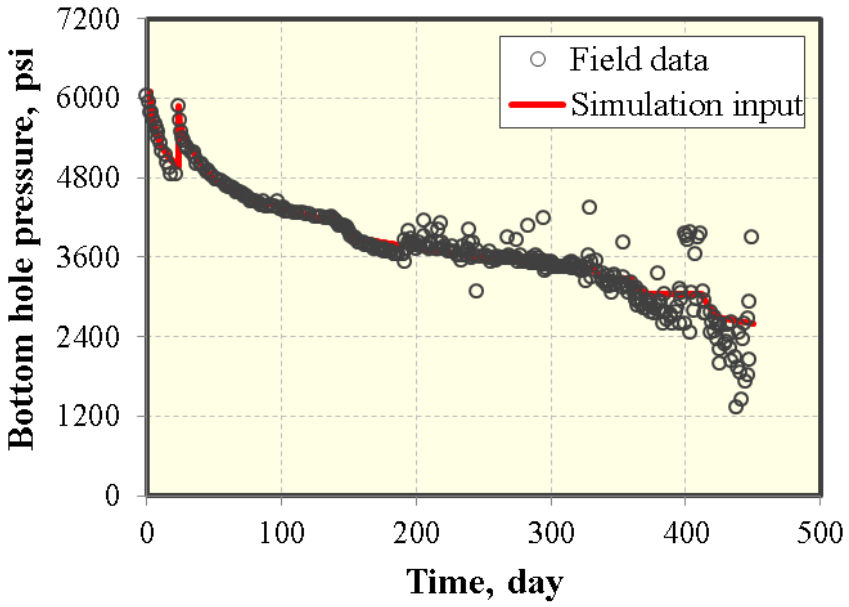

Figure 6.15: Bottom hole pressure used as a constraint input for history matching.

The history matching results for oil and gas flow rate are shown in Figures 6.16 and 6.17, respectively. As shown, a reasonable match between the numerical simulation results and the actual field data is obtained for oil and gas flow rate, respectively. Based on a good history matching result, we obtained matrix permeability of 5 μD, fracture half-length of 215 ft, fracture conductivity of 50 md-ft, and initial water saturation of 41%. Figure 6.18 presents the pressure distribution in 2D view at 1.2 years of field production. It can be seen that the effective drainage area is clearly illustrated in the horizontal fractured Bakken well.

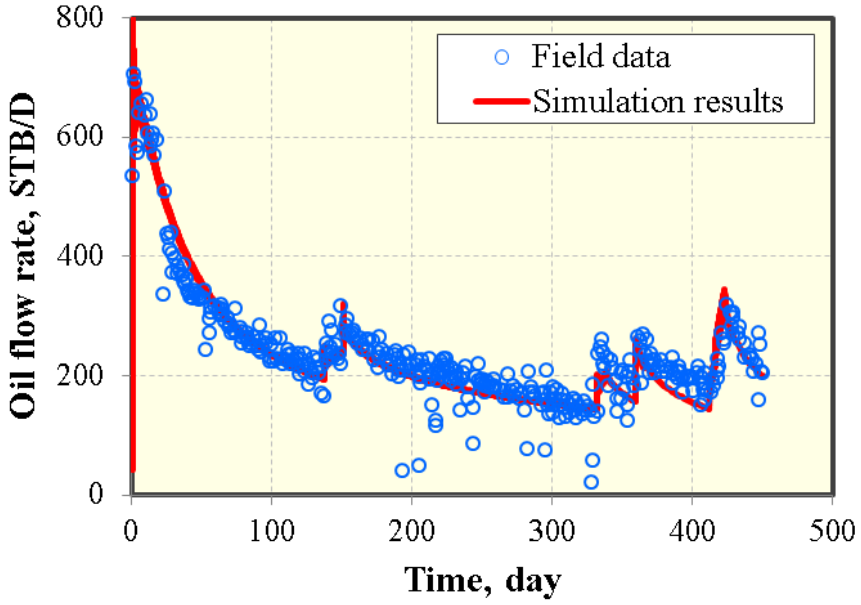

Figure 6.16: History matching for oil flow rate in the Middle Bakken.

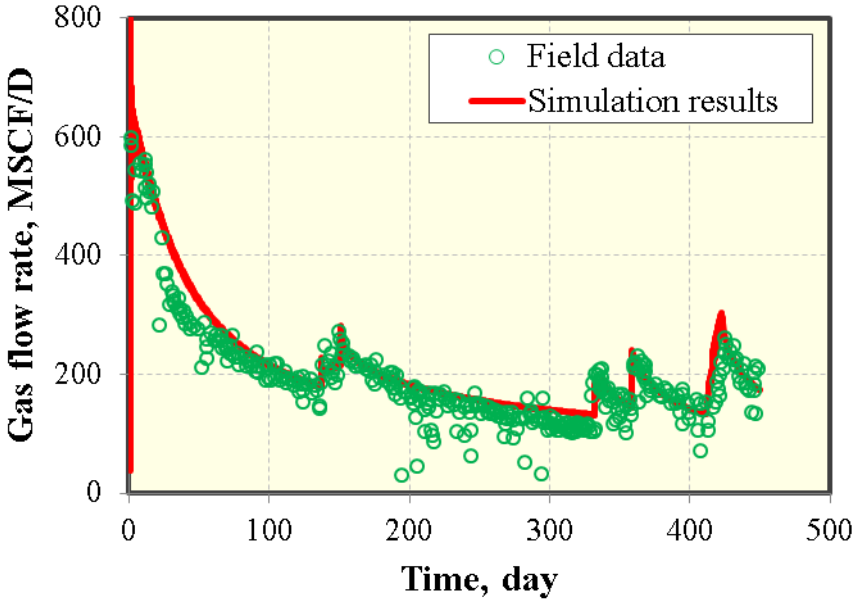

Figure 6.17: History matching for gas flow rate in the Middle Bakken.

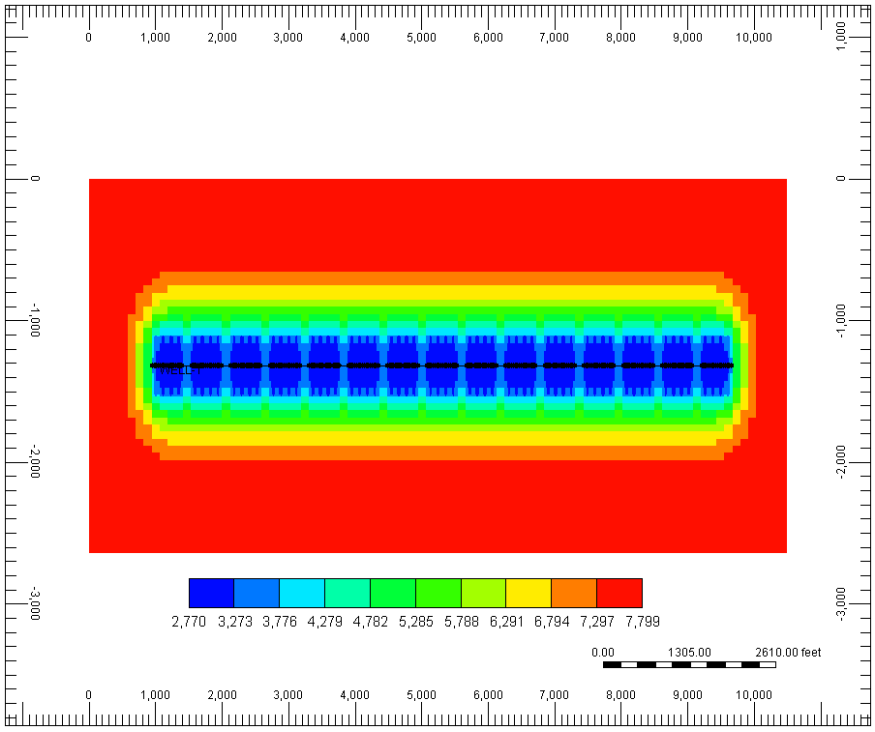

Figure 6.18: Pressure distribution at end of field production (pressure unit: psi).

Incorporating the history match period, we performed a production forecasting for 30 years. After history matching period, bottom hole pressure of 1,000 psi remains constant until 30 years of production. Cumulative oil production and oil recovery factor are shown in Figures 6.19 and 6.20, respectively. It can be seen that the cumulative oil production and oil recovery factor at 30 years of production are determined as 627 MBBL and 11%, respectively.

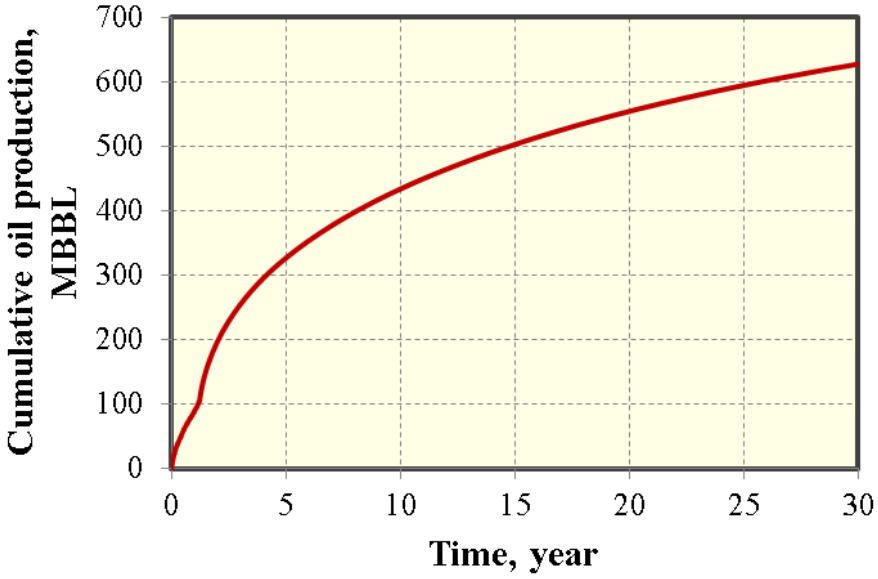

Figure 6.19: Production forecasting for cumulative oil production at a 30-year period.

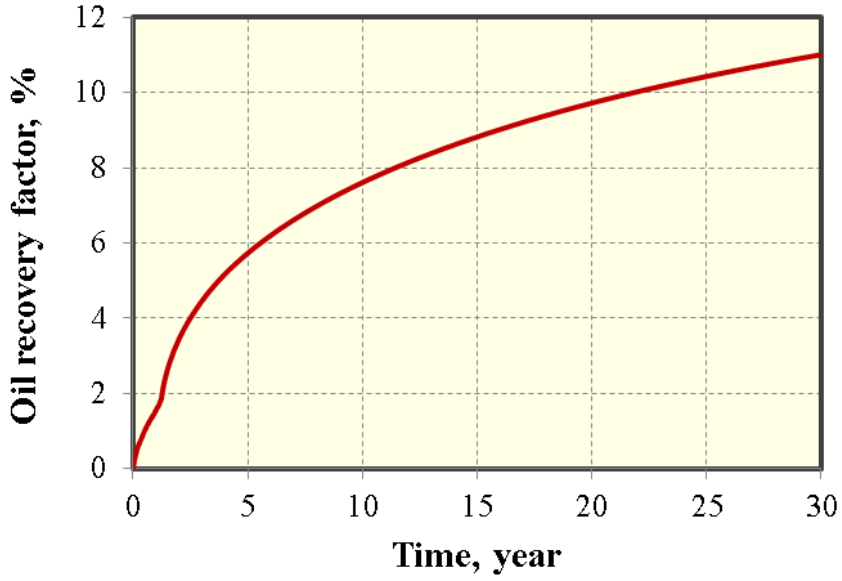

Figure 6.20: Production forecasting for oil recover factor at a 30-year period.

6.5 ECONOMIC OPTIMIZATION OF MULTIPLE WELL PLACEMENT

After the sensitivity analysis, the response surface of NPV based on the key design variables was built to optimize multiple well placement in the Bakken formation. Totally, there are four uncertain parameters, as shown in Table 6.7. Fracture height is assumed to be equal to reservoir thickness. The matrix permeability was fixed at 5 μD based on history matching results. The other reservoir and fracture properties are the same as that as shown in Table 6.1. The well number in the model ranges from 4 to 8. According to four variables in this study, 25 simulation cases were generated based on the approach of D-Optimal design, as shown in Table 6.8. Similarly with sensitivity study, the ISPUR of the framework is used to generate 25 cases automatically and efficiently.

Parameter	Coded symbol	Minimum (-1)	Maximum (+1)	Unit
Fracture spacing	A	80	320	ft
Fracture half-length	B	140	380	ft
Fracture conductivity	C	1	100	md-ft
Well number	B	4	8	

Table 6.7: Four uncertainty parameters investigated in this study for the Bakken formation.

Run	A	B	C	D
1	320	300	1	4
2	80	140	68	4
3	320	140	100	8
4	320	380	100	4
5	80	380	1	6
6	80	140	55	8
7	160	140	100	6
8	160	380	46	4
9	160	140	100	6
10	160	220	1	8
11	320	140	100	8
12	320	140	85	4
13	160	380	38	8
14	320	380	1	8
15	320	380	100	4
16	320	140	1	7
17	80	140	55	8
18	80	380	100	8
19	80	380	100	8
20	80	300	100	4
21	80	300	57	6
22	80	300	8	4
23	320	140	16	4
24	80	140	1	4
25	320	300	65	7

Table 6.8: 25 simulation cases based on D-Optimal design.

After numerical simulation of each case, cumulative oil production was obtained and shown in Figure 6.21. It clearly shows that the cumulative oil production at 30 years of production has a large uncertainty. This means that further optimization is required.

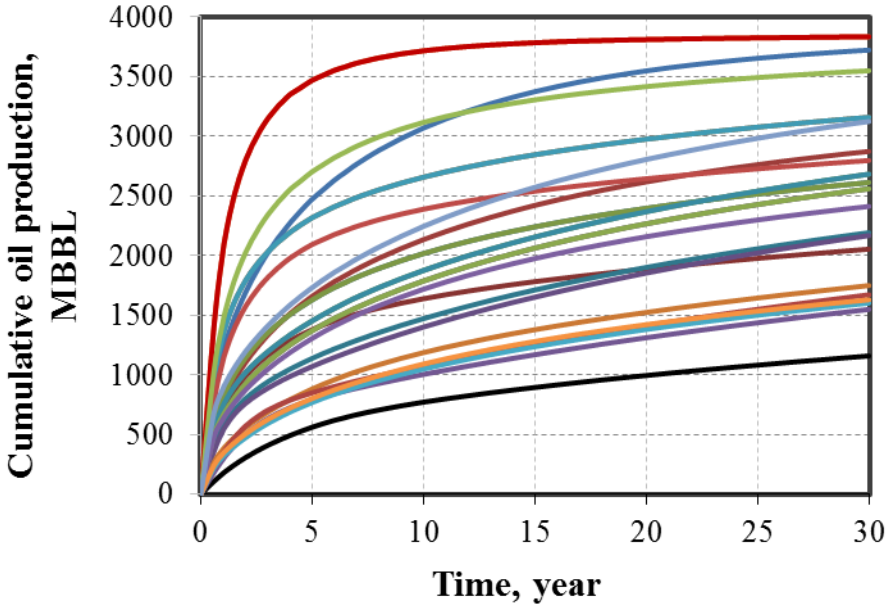

Figure 6.21: Cumulative oil production of 25 cases for a 30-year period.

Once the cumulative oil production of 25 cases was obtained, the economic EXCEL spreadsheet is used to calculate the corresponding NPVs based on the price of oil of $90/BBL, interest rate of 10%, and royalty tax of 12.5%. The fracturing treatments cost includes two parts: drilling cost and completion cost, as shown in Figure 6.22. It can be seen that the current total drilling and completion cost of Hess Corporation is about $8.4 MM. In this study, the well drilling cost of $5.0 MM is assumed. The completion cost related to fracture area and fracture conductivity, as shown in Figures 4.12 and 4.13, is used in this study. Figure 6.23 presents NPVs of 25 simulation cases at 30 years of production.

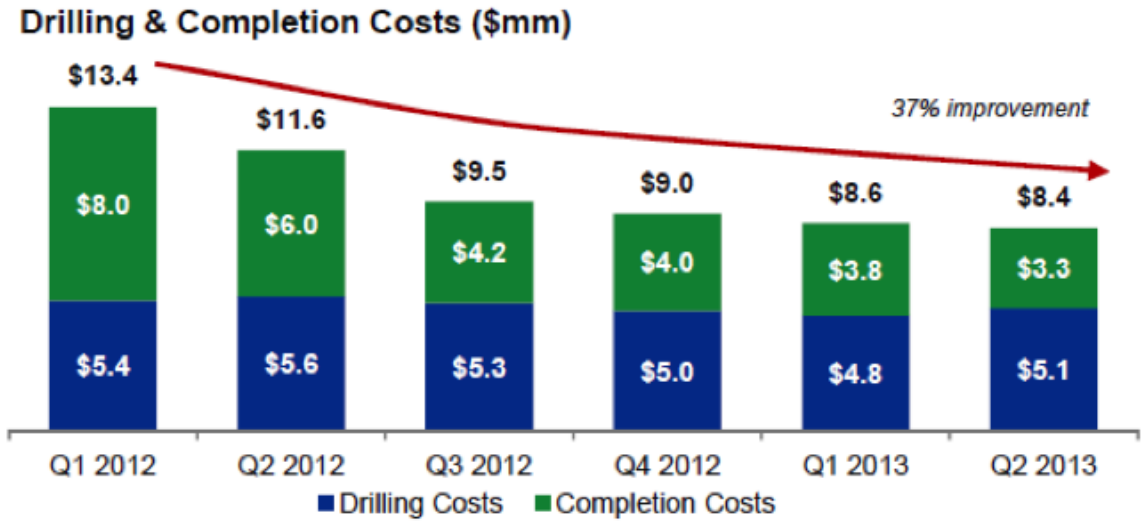

Figure 6.22: Drilling and completion costs of Hess Corporation in the Bakken formation (after Drillinginfo, 2013).

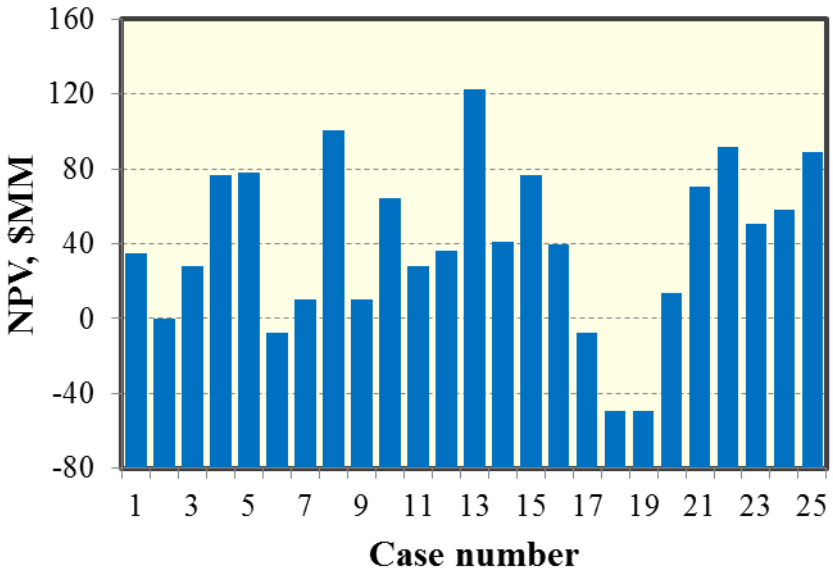

Figure 6.23: NPVs of 25 cases at 30 years of oil production with the oil price of $90/BBL.

Once NPVs of 25 simulation cases were obtained, the Design-Expert Software package is used to build the NPV response surface model. To select the appropriate

model, the statistical approach is used to determine which polynomial fits the equation among linear model, two-factor interaction model (2FI), quadratic model, and cubic model, as shown in Tables 6.9. The criterion for selecting the appropriate model is choosing the highest polynomial model, where the additional terms are significant and the model is not aliased. In addition, other criteria are to select the model that has the maximum "Adjusted R-Squared" and "Predicted R-Squared". Thus, the fully quadratic model is selected to build the NPV response surface in the subsequent optimization process.

Source	Std. Dev.	R-Squared	Adjusted R-Squared	Predicted R-Squared	Press	
Linear	36.33	0.43	0.32	0.104	41724	
2FI	29.53	0.74	0.74	0.088	42470	
Quadratic	15.25	0.95	0.95	0.439	26115	Suggested
Cubic	0.00	1.00	1.00			Aliased

Table 6.9: Statistical approach to select the RSM model with oil price of $90/BBL.

The equation fitted to the NPV response surface with the actual factors is presented below:

$$\begin{aligned} NPV = & \\ & -132.77 + 0.79205 \times A + 0.55511 \times B - 0.053947 \times C + 31.36357 \times D \\ & -3.25027 \times 10^{-4} \times AB + 4.94319 \times 10^{-3} \times AC + 0.047027 \times AD + 1.37909 \times 10^{-3} \times BC \\ & -1.54091 \times 10^{-3} \times BD - 0.048211 \times CD - 2.72371 \times 10^{-3} \times A^2 - 7.80724 \times 10^{-4} \times B^2 \\ & -0.013985 \times C^2 - 3.54896 \times D^2, \end{aligned} \quad (6.1)$$

where A is fracture spacing, B is fracture half-length, C is fracture conductivity, and D is well number.

The normal plot of residuals, reflecting the distribution of the residuals, is shown in Figure 6.24. All the points in the "Normal Plot of Residuals" fall on the straight line, meaning the residuals are normally distributed. Figure 6.25 shows the plot of "Predicted vs. Actual", illustrating whether the generated equation of NPV response surface accurately predicts the actual NPV values. It can be seen that generated NPV response surface models provide such reliable predicted values of NPV, as compared with the actual values of NPV. This means that the generated NPV response surface model is reliable.

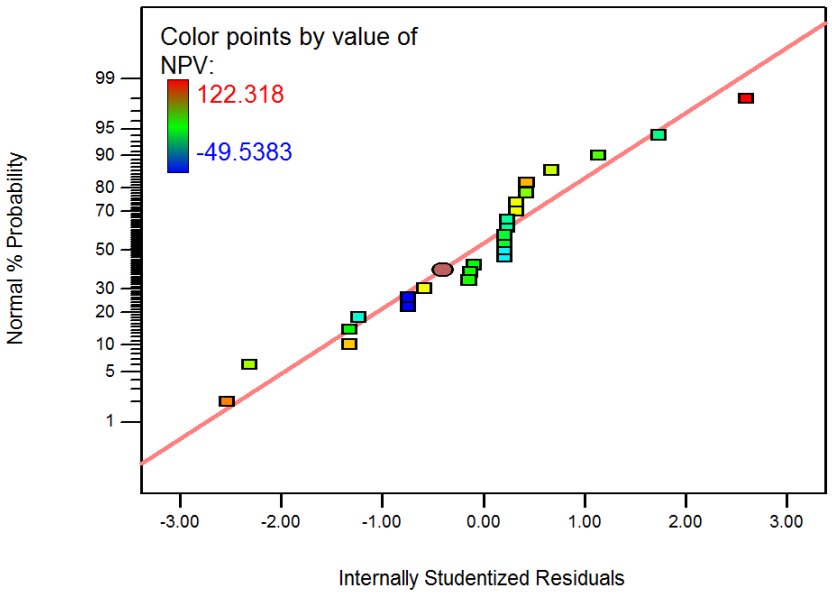

Figure 6.24: Normal plot of residuals at oil price of $90/BBL.

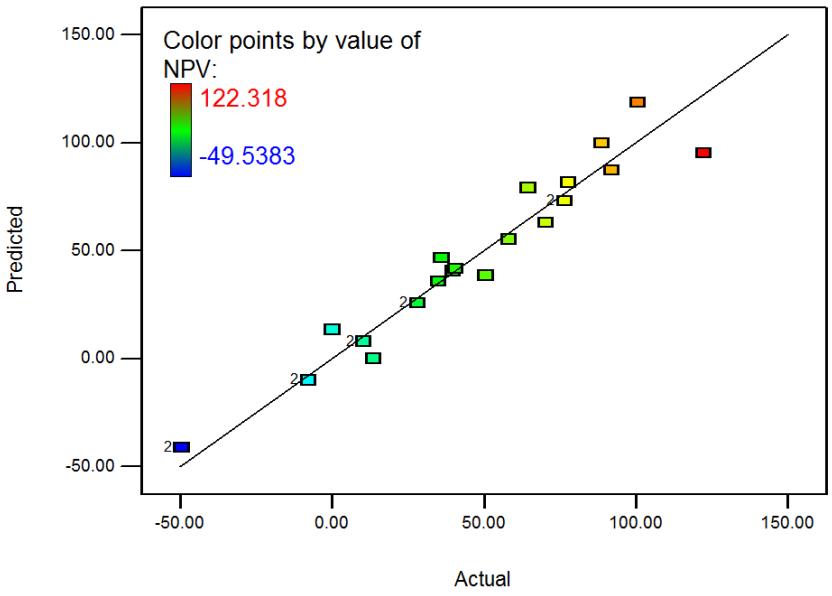

Figure 6.25: Predicted NPV versus the actual NPV plot at oil price of $90/BBL.

Figure 6.26 shows the 3D surface of NPV at varied values of fracture conductivity and fracture spacing. It shows that there is an optimal fracture design related to fracture conductivity and fracture spacing. Therefore, this methodology can provide some insights into optimization of fracturing treatment design to obtain the maximum economic viability of the field

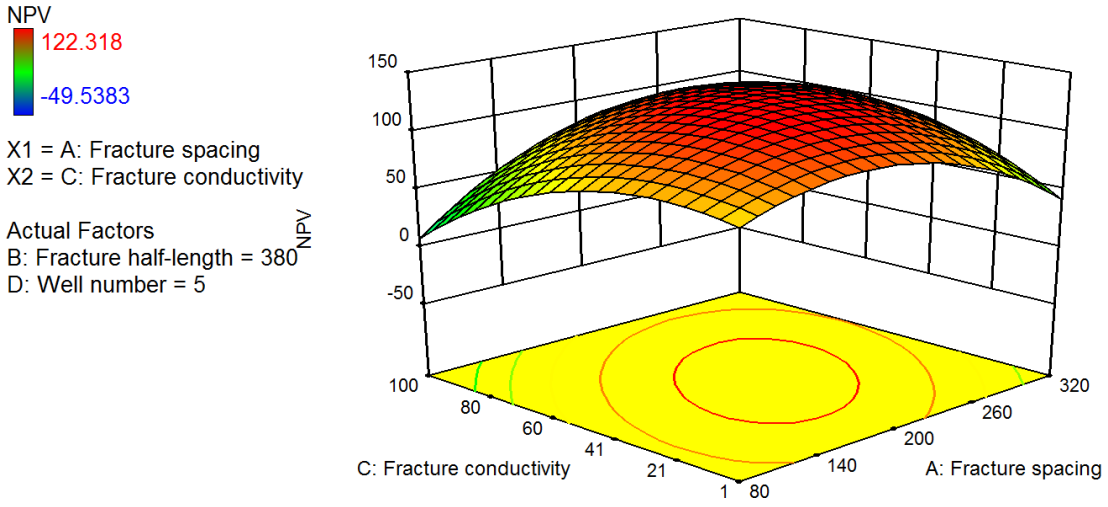

Figure 6.26: 3D surface of NPV at varied values of fracture conductivity and fracture spacing.

The objective function of NPV will be maximized by selecting the best combinations with uncertain parameters through the method of RSM. The best case is obtained based on the range of parameters investigated in this study for the Bakken formation, as listed in Table 6.7. The best case with the highest NPV value of \$124.77 MM (10^6) corresponding to fracture spacing of 160 ft, fracture half-length of 340 ft, fracture conductivity of 35 md-ft, and well number of 5, as shown in Figures 6.27 and 6.28.

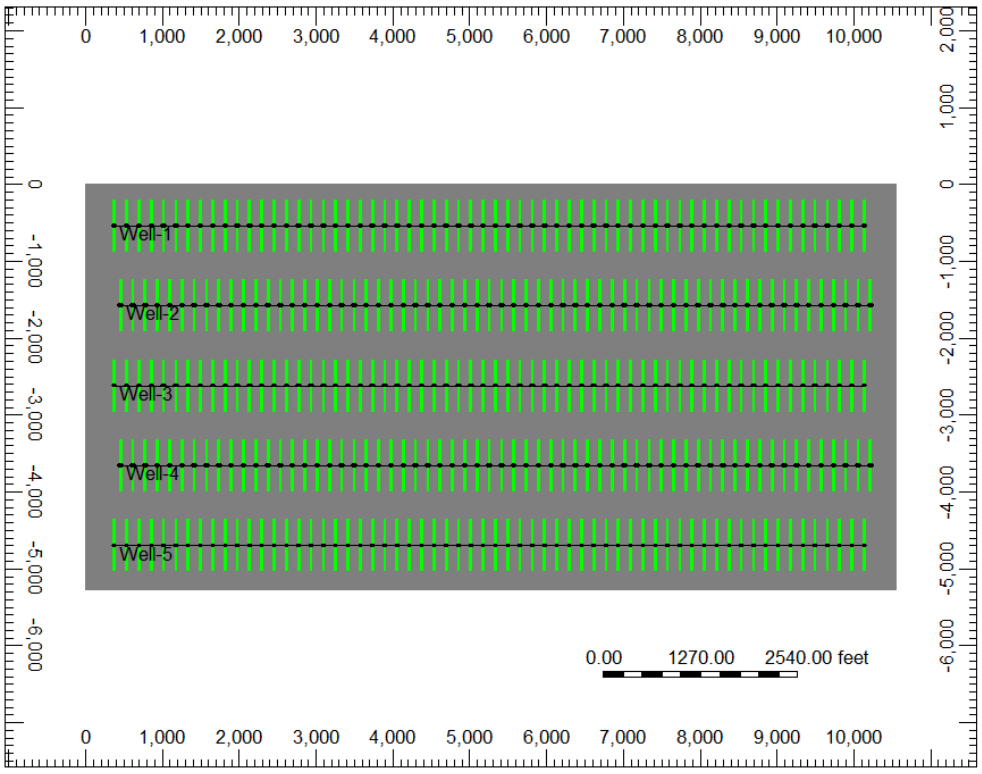

Figure 6.27: The best case in 2-dimension with fracture spacing of 160 ft, fracture half-length of 340 ft, fracture conductivity of 35 md-ft, and well number of 5 for the Middle Bakken.

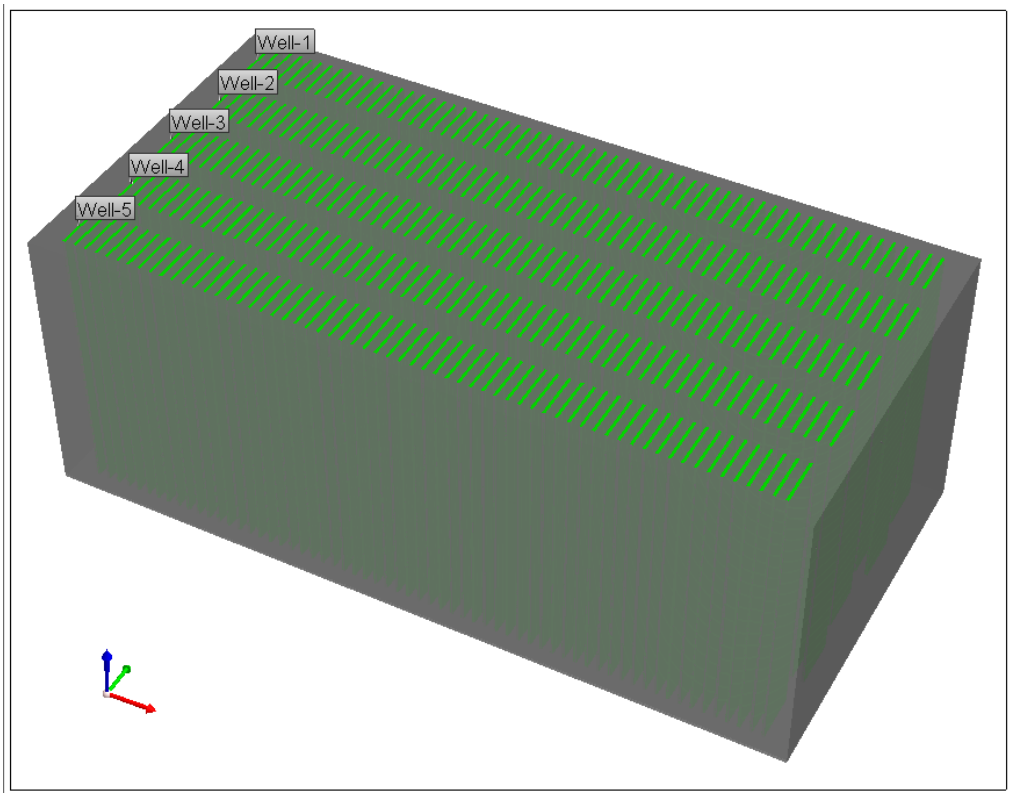

Figure 6.28: The best case in 3-dimension with fracture spacing of 160 ft, fracture half-length of 340 ft, fracture conductivity of 35 md-ft, and well number of 5 for the Middle Bakken.

Cumulative oil production and oil recovery factor are shown in Figures 6.29 and 6.30, respectively. It can be seen that the cumulative oil production and oil recovery factor at 30 years of production are determined as 3,101 MBBL and 23.7%, respectively.

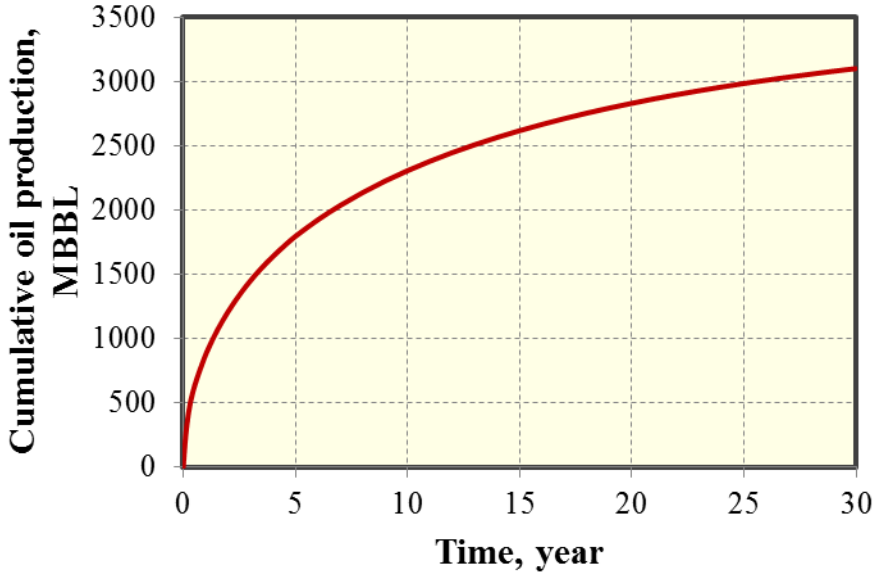

Figure 6.29: Production forecasting for cumulative oil production at a 30-year period.

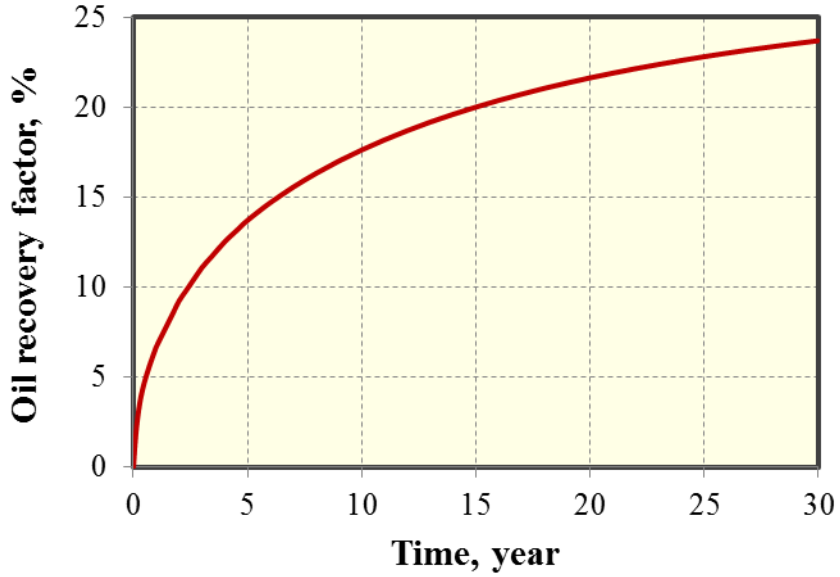

Figure 6.30: Production forecasting for oil recover factor at a 30-year period.

Figures 6.31 and 6.32 present pressure distribution for the best case at one month and 30 years of oil production, respectively, illustrating the drainage volume clearly.

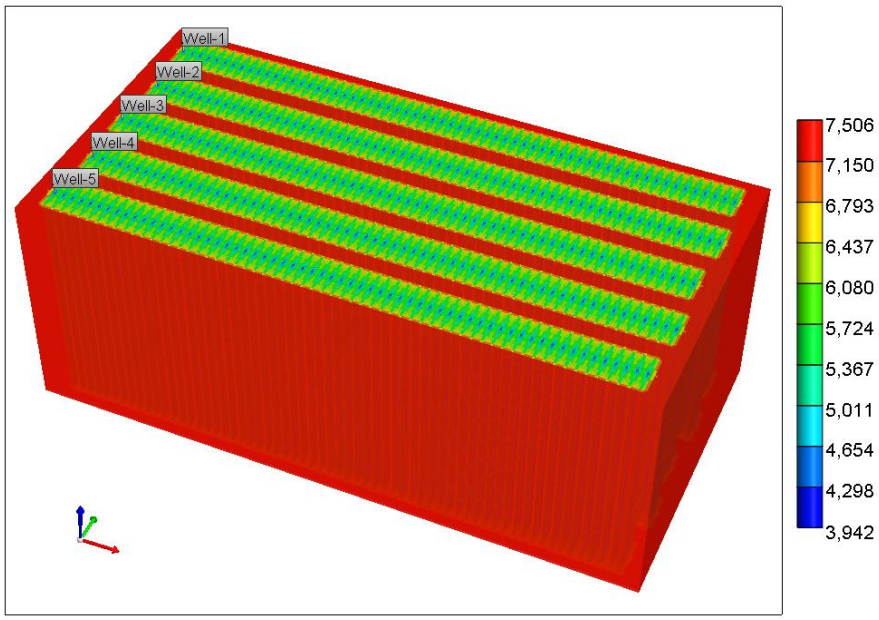

Figure 6.31: Pressure distribution at one month of production for the best case (pressure unit: psi).

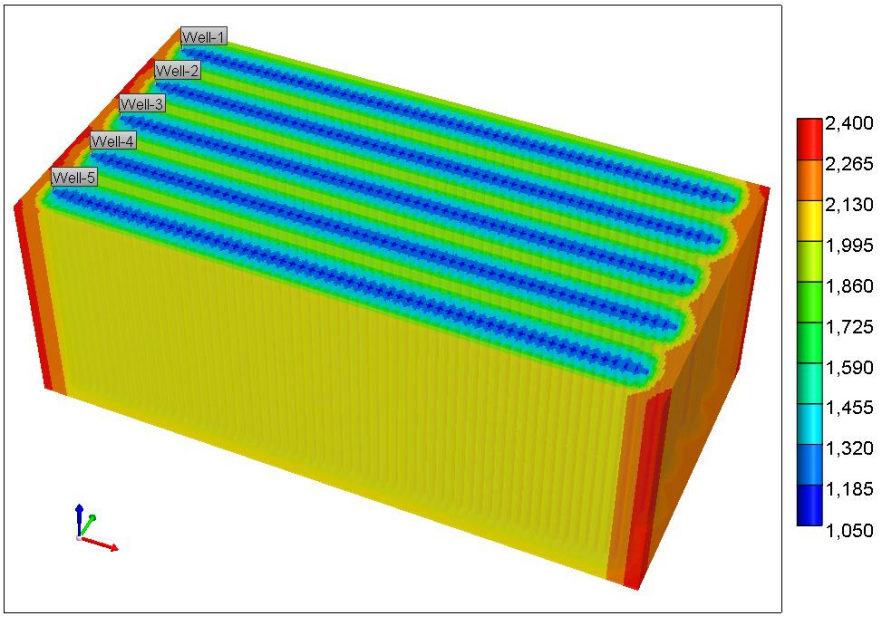

Figure 6.32: Pressure distribution at 30 years of production for the best case (pressure unit: psi).

6.6 CONCLUSIONS

We applied the framework developed in Chapter 4 to optimize multiple well placement in the Middle Bakken tight oil reservoir. The following conclusions can be drawn from this study:

(1) Both at a short-term of production (5 years) and long-term production (30 years), the influence order of main parameters for single well simulation is the same: permeability, porosity, water saturation, fracture conductivity, fracture spacing, and fracture half-length; while the effect of fracture half-length is less important in this case study.

(2) Based on the sensitivity analysis, a field well from Middle Bakken is analyzed and cumulative oil production and oil recovery factor at 30 years of production are determined as 627 MBBL and 11%, respectively.

(3) The best case for optimization of multiple well placement in the Middle Bakken is obtained as fracture spacing of 160 ft, fracture half-length of 340 ft, fracture conductivity of 35 md-ft, and well number of 5.

CHAPTER 7: Simulation of CO_2 Injection for Enhanced Oil Recovery in Tight Oil Reservoirs

The combination of horizontal drilling and multi-stage hydraulic fracturing has boosted the oil production from tight oil reservoirs. However, the primary oil recovery factor is very low due to the extremely tight formation, resulting in substantial volumes of oil still remaining in place. Hence, it is important to investigate the potential of applying enhanced oil recovery methods to increase oil recovery in the Bakken formation. Although carbon dioxide (CO_2) is widely used in conventional reservoirs to improve oil recovery, it is a new subject and not well understood in unconventional oil reservoirs such as the Bakken formation. In this study, we built a numerical model to simulate CO_2 injection for enhanced oil recovery using a huff-n-puff process with typical reservoir and fracture properties from the Bakken formation. Effects of CO_2 molecular diffusion, number of cycle, fracture half-length, permeability and reservoir heterogeneity on the well performance of CO_2 huff-n-puff were examined in detail. The results show that the CO_2 diffusion plays a significant role in improving oil recovery from tight oil reservoirs, which cannot be neglected in the reservoir simulation model. Additionally, the tight oil formation with lower permeability, longer fracture half-length, and more heterogeneity is more favorable for the CO_2 huff-n-puff process. This work can provide a good understanding of the physical mechanisms and key parameters affecting the effectiveness of CO_2 injection for enhanced oil recovery in the Bakken formation.

7.1 INTRODUCTION

The Bakken formation with multiple oil-bearing layers is one of major productive tight oil reservoirs in North America (West et al., 2013), where Middle Bakken and Three Forks are the two primary layers for oil production since they have the best reservoir qualities such as porosity and oil saturation (Iwere et al., 2012). It has been reported that the Middle Bakken has an estimated average oil resource of 3.65 billion barrels and Three Forks has an estimated average resource of 3.73 billion barrels (United States Geological Survey, 2013). Horizontal drilling and multi-stage hydraulic fracturing are the two key enabling technologies to make tight oil production commercial from the Bakken formation with low or ultra-low permeability. The key dominant mechanisms for the primary recovery are depressurization and solution gas drive. Although with the advanced technologies, most estimates for primary oil recovery factor remain very low due to tight nature of the Bakken formation (Cherian et al., 2012; Hoffman, 2012). Hence, there are still substantial volumes of oil remaining in the reservoir, resulting in a strong motivation of applying enhanced oil recovery (EOR) methods to improve oil recovery in tight oil reservoirs. It has been reported that a minor improvement in oil recovery factor such as 1% could yield 1.6 to 9 billion barrels of additional oil (Hawthorne et al., 2013). The 1% additional oil recovery factor could bring revenue of $128 to $720 billion with an assumption of crude oil price of $80 per barrel. Accordingly, it is important to investigate the potential of applying enhanced oil recovery methods to improve long-term oil productivity in the Bakken formation.

Although water flooding has been widely used in conventional oil reservoirs, it is challenging to be applied in unconventional oil reservoirs with low permeability because of low injectivity, poor sweep efficiency with fracture networks, and clay swelling problems. Nevertheless, it is believed that gas injection is more suitable due to lower

viscosity and larger injectivity than water injection. Additionally, the depth of the Bakken formation (average of 10,000 ft) and high oil saturation are beneficial to gas injection (Iwere et al., 2012). Most gases used for injection include carbon dioxide (CO_2), nitrogen (N_2), natural gas or the mixture of them. Among these gases, CO_2 has received much more attention for enhanced oil recovery in the Bakken formation (Kurtoglu et al., 2013; Song and Yang. 2013; Adekunle and Hoffman, 2014). CO_2 has a considerably lower minimum miscibility pressure (MMP) than that of the other gases such as N_2 and CH_4 (Stalkup, 1987; Holm, 1987). The so-called MMP refers to the lowest pressure required to recover about 95% of the contacted oil at a given temperature, which highly depends on the reservoir temperature and crude oil composition (Holm, 1986, 1987). A high percentage of intermediate hydrocarbons (especially C_5-through-C_{12}) have a significantly larger impact on the MMP (Holm, 1987; Orr Jr and Silva, 1987).

CO_2 injection is one of the most effective methods for enhanced oil recovery in conventional oil reservoirs, which has been well understood (Jarrell et al., 2002; Kong et al., 2015). The main mechanisms generally include oil swelling, oil viscosity reduction, oil density increasing, highly soluble in water, vaporization and extraction of crude oil, exerting an acid effect on rock (Holm and Josendal, 1974). CO_2-EOR process is generally classified as miscible or immiscible. For achieving a miscible oil-recovery process, the reservoir pressure is necessary to be maintained above the MMP. CO_2 and trapped oil will become completely miscible and CO_2 will extract light and intermediate hydrocarbons from the oil phase, and the interfacial tension will become zero and capillary pressure disappears, resulting in the oil phase and CO_2 phase, which contains some extracted hydrocarbon components, flow together more easily through the porous media (Taber and Martin, 1983; Lambert et al., 1996; Martin and Taber, 1992). Fai-Yengo et al. (2014) presented that the effect of capillary pressure has negligible effect on

oil recovery in the Bakken formation. The extraction of hydrocarbons is highly dependent on the density of the CO_2, and the CO_2 will extract more and heavier hydrocarbons with the increasing CO_2 density (Holm and Josendal, 1982; Orr Jr et al., 1983; Sigmund et al., 1984). The CO_2 density varies from 0.1 to 0.8 g/cm^3 at pressure from 1,000 to 4,000 psi when the temperature is above its critical temperature of 87.9 ^oF (Holm and Josendal, 1982). Holm and Josendal (1982) found that sufficient hydrocarbon extraction occurs when the CO_2 density is about 0.42 g/cm^3, which is close to the CO_2 critical density of 0.468 g/cm^3. In practice, CO_2 injection is typically a multiple contact process since it is hard for the injected gas to be miscible with the in-situ oil at the beginning, especially for the light and medium oil reservoirs (Wang et al., 2010). In the Bakken formation, the average reservoir pressure is between 7,500 psi and 8,000 psi and reservoir temperature is about 240 ^oF (Kurtoglu et al., 2014). Under these conditions, the injected CO_2 is actually at super critical condition. The density of the super critical CO_2 is more like liquid, but the viscosity is like gas. Thus, the miscible process generally improves the oil recovery more effectively than that of immiscible process when injection pressure is below the MMP (Lambert et al., 1996).

Although CO_2-EOR in conventional reservoirs has been well understood, it is still a new subject in unconventional oil reservoirs such as the Bakken formation with low permeability and multiple hydraulic fractures. Hawthorne et al. (2013) proposed five conceptual steps for CO_2 injection in the Bakken formation: (1) CO_2 flows into and through the fractures, (2) unfractured rock matrix is exposed to CO_2 at fracture surfaces, (3) CO_2 permeates the rock driven by pressure, carrying some hydrocarbon inward; however, the oil is also swelling and extruding some oil out of the pores, (4) oil migrates to the bulk CO_2 in the fractures via swelling and reduced viscosity, and (5) as the CO_2 pressure gradient gets smaller, oil production is slowly driven by concentration gradient

diffusion from pores into the bulk CO_2 in the fractures. Also, they demonstrated that CO_2 is effective to improve oil recovery based on CO_2-exposure experiments with some rock samples from the Bakken formation. The main mechanisms for gas-EOR in naturally fractured reservoirs include viscous forces, gravity drainage, and molecular diffusion (Hoteit, 2013). However, in tight oil reservoirs with low permeability, the viscous forces and gravity drainage become less important while molecular diffusion will be dominant (Hoteit and Firoozabadi, 2006). Although there are many attempts to evaluate CO_2 injection in the tight oil reservoirs (Wang et al., 2010; Ren et al., 2011; Shoaib and Hoffman, 2009; Sheng, 2015; Chen et al., 2014), the effect of CO_2 molecule diffusion on well performance of the CO_2 injection is still poorly understood. Furthermore, the impacts of key reservoir and fracture properties such as permeability, fracture half-length, and reservoir heterogeneity on the effectiveness of CO_2-EOR have not been evaluated quantitatively. Accordingly, a detailed study of investigation of the key parameters affecting the CO_2-EOR in the Bakken formation is necessary.

This study was mainly focused on numerical simulation of the CO_2 injection as a huff-n-puff process, which consists of three stages such as CO_2 injection, CO_2 soaking, and production, as shown in Figure 7.1 (Yu et al., 2014f), since it is more effective than CO_2 flooding, which will take longer time for pressure propagation from the injection well to production well (Chen et al., 2014). The numerical reservoir simulation approach is used to model the CO_2 huff-n-puff process with typical reservoir and fracture properties from the Bakken formation. Effect of CO_2 molecular diffusion on the effectiveness of CO_2 injection was discussed in detail. Furthermore, a comprehensive sensitivity study was performed to investigate the effects of number of cycle, fracture half-length, permeability and reservoir heterogeneity on the well performance of CO_2 huff-n-puff. This work can provide a better understanding of the effectiveness of CO_2

huff-n-puff process in the Bakken formation, which can be easily extended to evaluate CO_2 injection in the other tight oil reservoirs in North America such as Eagle Ford shale in the Western Gulf Basin and Permian Basin in West Texas.

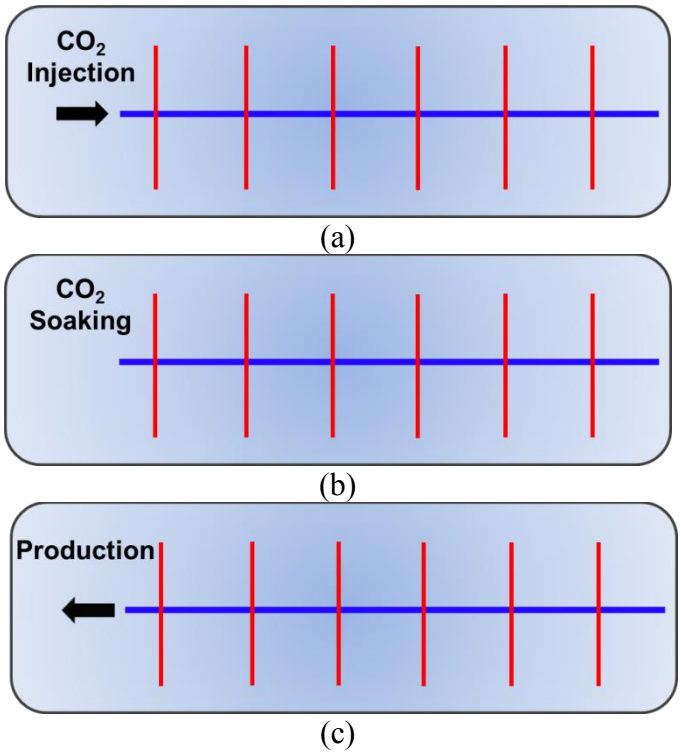

Figure 7.1: The CO_2 huff-n-puff process in a horizontal well with multiple fractures. (a) Stage 1: CO_2 injection. (b) Stage 2: CO_2 soaking. (c) Stage 3: production.

7.2 METHODOLOGY

7.2.1 Reservoir simulation model

The governing equation that describes the total mass balance for component *i* in the oil and gas phases is expressed by the continuity equation below, including accumulation term of component *i* in rock and fluid phases as well as convection, dispersion and molecular diffusion terms of component *i* in phase ℓ (oil and gas phases) (Lashgari, 2014).

$$\frac{\partial}{\partial t}\left((1-\phi)\rho_s w_{is} + \phi\sum_{\ell=1}^{N_p}\rho_\ell S_\ell w_{i\ell}\right)$$
$$+\vec{\nabla}\cdot\left(\sum_{\ell=1}^{N_p}\rho_\ell w_{i\ell} u_\ell - \phi\rho_\ell S_\ell \overline{\overline{K}}_{i\ell}\nabla w_{i\ell}\right) - r_i = 0 \qquad i = 1,...,N_c, \tag{7.1}$$

where ϕ is matrix porosity, ρ_s is matrix density, ρ_ℓ is density of phase ℓ, S_ℓ is saturation of phase ℓ, r_i is mass rate injection or production as source or sink term, N_p is number of phase, N_c is number of component, w_{is} is mass fraction of component i that precipitates on the matrix rock per unit volume, $w_{i\ell}$ is mass fraction of component i in the phase per unit volume, u_ℓ is Darcy's flow velocity, which is defined as

$$\bar{u}_\ell = -\frac{\overline{\overline{k}}}{\mu_\ell}\left(\bar{\nabla}p_\ell - \rho_\ell \bar{g}\right), \tag{7.2}$$

where $\overline{\overline{k}}$ is the formation permeability tensor, $k_{r\ell}$ is the relative permeability of phase ℓ, p_ℓ is pressure of phase ℓ and μ_ℓ is viscosity of phase ℓ, $\overline{\overline{K}}_{i\ell}$ is the dispersivity coefficient of component i in the phase ℓ, which is defined as

$$\overline{\overline{K}}_{i\ell} = \frac{\overline{\overline{D}}_{i\ell}}{\tau} + \frac{\bar{\alpha}_\ell |\bar{u}_\ell|}{\phi S_\ell}, \tag{7.3}$$

where $\bar{\alpha}_\ell$ is the dispersivity coefficient of fluid ℓ in the longitudinal direction and two transverse directions, τ is tortuosity of the matrix, $\overline{\overline{D}}_{i\ell}$ is the diffusion coefficient of component i in phase ℓ. The Sigmund correlation (Sigmund, 1976) is often used to calculate the oil and gas diffusion coefficients (unit is cm^2/s) since it is valid for both oil and gas phases (Nghiem et al., 2000). The binary diffusion coefficient between component i and j is calculated by (Sigmund, 1976; Nghiem et al., 2000)

$$D_{ij} = \frac{\rho_\ell^0 D_{ij}^0}{\rho_\ell}\cdot\left(0.99589 + 0.096016\rho_{\ell r} - 0.22035\rho_{\ell r}^{\ 2} + 0.032874\rho_{\ell r}^{\ 3}\right), \tag{7.4}$$

where $\rho_\ell^0 D_{ij}^0$ is the zero pressure limit of the product of density and diffusivity, which can be calculated by

$$\rho_\ell^0 D_{ij}^0 = \frac{0.0018583 T^{1/2}}{\sigma_{ij}^2 \Omega_{ij} R} \left(\frac{1}{M_i} + \frac{1}{M_j} \right)^{1/2}, \tag{7.5}$$

$\rho_{\ell r}$ is the reduced density, which can be calculated from the following form:

$$\rho_{\ell r} = \rho_\ell \cdot \left(\frac{\sum_{i=1}^{n_c} y_{i\ell} v_{ci}^{5/3}}{\sum_{i=1}^{n_c} y_{i\ell} v_{ci}^{2/3}} \right), \tag{7.6}$$

where M_i is molecular weight of component i, R is universal gas constant, T is absolute temperature (K), v_{ci} is critical volume of component i, $y_{i\ell}$ is mole fraction of component i in phase ℓ, n_c is number of hydrocarbon components, σ_{ij} is the collision diameter (Å), and Ω_{ij} is the collision integral of the Lennard-Jones potential (dimensionless). The diffusion of component i in the mixture is defined as

$$D_{i\ell} = \frac{1 - y_{i\ell}}{\sum_{j \neq i} \frac{y_{i\ell}}{D_{ij}}}. \tag{7.7}$$

Equation 7.7 is used to calculate the amount of molecular diffusivity for Eq. 7.3. The collision diameter (σ_{ij}) and the collision integral of the Lennard-Jones potential (Ω_{ij}) can be calculated based on the component critical properties as follows (Nghiem et al., 2000; Reid et al., 1977):

$$\sigma_i = \left(2.3551 - 0.087\omega_i\right) \cdot \left(\frac{T_{ci}}{p_{ci}} \right)^{1/3}, \tag{7.8}$$

$$\varepsilon_i = k_B \left(0.7915 + 0.1963\omega_i\right) \cdot T_{ci}, \tag{7.9}$$

$$\sigma_{ij} = \frac{\sigma_i + \sigma_j}{2}, \tag{7.10}$$

$$\varepsilon_{ij} = \sqrt{\varepsilon_i \varepsilon_j}, \tag{7.11}$$

$$T_{ij}^* = \frac{k_B T}{\varepsilon_{ij}}, \tag{7.12}$$

$$\Omega_{ij} = \frac{1.06036}{(T_{ij}^*)^{-0.15610}} + \frac{0.19300}{\exp(-0.47635 T_{ij}^*)} + \frac{1.03587}{\exp(-1.52996 T_{ij}^*)} + \frac{1.76474}{\exp(-3.89411 T_{ij}^*)}, \tag{7.13}$$

where ω is acentric factor, p_c is critical pressure (atm), T_c is critical temperature (K), ε is the characteristic Lennard-Jones energy (ergs), and k_B is the Boltzmann's constant (1.3805×10^{-16} ergs/K).

The system of partial differential equation (PDE) of Eq. 7.1 represents a reservoir simulation model. In this study, CMG-GEM (CMG-GEM, 2012), which is a numerical reservoir simulator, is used to solve the Eqs. 7.1-7.7.

7.2.2 Reservoir model including multiple hydraulic fractures

In our simulation model, a local grid refinement (LGR) with logarithmic cell spacing is utilized to model multiple hydraulic fractures explicitly. The fracture width is set at a small value (0.01 ft) but a large permeability. A no-flow boundary condition is used. This approach has been extensively used to model transient gas flow in hydraulically fractured shale gas reservoirs.

7.3 FLUID CHARACTERIZATION OF BAKKEN

Typical fluid properties of the Bakken formation are used to simulate the CO_2 injection for enhanced oil recovery. The average oil gravity of the Bakken formation is around 42 ^{o}API, indicating that the crude oil is light. Nojabaei et al. (2013) reported that the range for gas oil ratio (GOR) is from 507 to 1,712 SCF/bbl and bubble point pressure varies from 1,617 to 3,403 psi based on the field production data from different location in the Bakken formation. Kurtoglu et al. (2014) conducted laboratory measurements of oil properties of eight fluid samples from the Middle Bakken and Three Forks, and presented that the bubble point is 1,389-2,674 psi, oil formation factor is 1.34-1.68 RB/STB, oil viscosity is 0.184-0.4883 cp, and GOR is 455-1,062 psi. In this study, the crude oil of the Bakken is carefully divided into seven different pseudo components, i.e., CO_2, N_2, CH_4, C_2-C_4, C_5-C_7, C_8-C_9, C_{10+}, and their corresponding molar fractions are

0.02%, 0.04%, 25%, 22%, 20%, 13%, and 19.94%, respectively. In addition, these components are convenient to investigate different gas injection (CO_2, N_2, CH_4, or mixture) in the future study. The key oil properties are calculated based on these components using CMG-WinProp (CMG-WinProp, 2012): oil gravity is 42 ^{o}API, GOR is 1,000 SCF/bbl, bubble point is 2,000 psi, oil formation factor is 1.6, which are within the reasonable range of typical values for the Bakken formation. The MMP is calculated as 3,334 psi, which has a great match with the measured data of 3,300 psi by Kurtoglu et al. (2014) using a rising-bubble apparatus (RBA). The other input data required for the Peng-Robinson equation-of-state (EOS) are listed in Table 7.1. The binary coefficient used for flash calculation is listed in Table 7.2.

Component	Molar fraction	Critical pressure (atm)	Critical temperature (K)	Critical volume (L/mol)	Molar weight (g/gmol)	Acentric factor	Parachor coefficient
CO_2	0.0002	72.80	304.20	0.0940	44.01	0.2250	78.0
N_2	0.0004	33.50	126.20	0.0895	28.01	0.0400	41.0
CH_4	0.25	45.40	190.60	0.0990	16.04	0.0080	77.0
C_2-C_4	0.22	42.54	363.30	0.1970	42.82	0.1432	145.2
C_5-C_7	0.20	33.76	511.56	0.3338	83.74	0.2474	250.0
C_8-C_9	0.13	30.91	579.34	0.4062	105.91	0.2861	306.0
C_{10+}	0.1994	21.58	788.74	0.9208	200.00	0.6869	686.3

Table 7.1: Compositional data for the Peng-Robinson EOS in the Bakken formation.

Component	CO_2	N_2	CH_4	C_2-C_4	C_5-C_7	C_8-C_9	C_{10+}
CO_2	0	-0.0200	0.1030	0.1327	0.1413	0.1500	0.1500
N_2	-0.0200	0	0.0130	0.0784	0.1113	0.1200	0.1200
CH_4	0.1030	0.0310	0	0.0078	0.0242	0.0324	0.0779
C_2-C_4	0.1327	0.0784	0.0078	0	0.0046	0.0087	0.0384
C_5-C_7	0.1413	0.1113	0.0242	0.0046	0	0.0006	0.0169
C_8-C_9	0.1500	0.1200	0.0324	0.0087	0.0006	0	0.0111
C_{10+}	0.1500	0.1200	0.0779	0.0384	0.0169	0.0111	0

Table 7.2: Binary interaction parameters for oil components from the Bakken formation.

7.4 RESULTS AND DISCUSSION

7.4.1 Base case

For the base case, we set up a basic reservoir model with four effective hydraulic fractures within one stage because of the expensive computational time for the entire well with multiple fractures, as shown in Figure 7.2. The dimensions for this segment are 340 ft × 1,300 ft × 40 ft, which corresponds to length, width, and thickness, respectively. The grid block size is set to 20 ft × 20 ft × 40 ft in *x*, *y*, *z* directions, respectively. Fracture half-length is 210 ft, fracture height is 40 ft, fracture conductivity is 50 md-ft, fracture width is 0.001 ft, and fracture spacing is 80 ft. The LGR for each grid with fracture is set as 7×1×1 to reduce the numerical dispersion effect. The air permeability of the Middle Bakken is on the order of microdarcies (Nojabaei et al., 2013). Water saturation ranges between 25% and 50% in the Middle Bakken (Cherian et al., 2012). In this study, matrix permeability of 10 μD and initial water saturation of 25% are used. Table 7.3 summarizes all the parameters used for simulation study based on the typical values of the Middle Bakken. The relative permeability curves, as shown in Figure 6.4, are used. The reservoir

is assumed to be homogeneous and the fractures are with stress-independent porosity and permeability. Flowing BHP of 1,000 psi is used for simulation constraint.

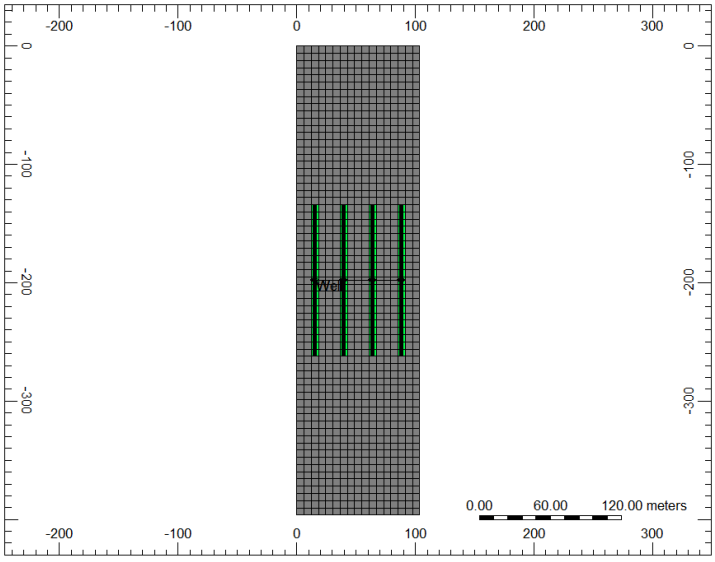

Figure 7.2: A basic 3D model with four effective hydraulic fractures within one stage.

Parameter	Value	Unit
Initial reservoir pressure	8,000	psi
Reservoir temperature	240	^{o}F
Initial water saturation	0.25	
Total compressibility	1×10^{-6}	psi^{-1}
Matrix permeability	10	μD
Matrix porosity	0.07	
Stage spacing	340	ft
Fracture conductivity	50	md-ft
Fracture half-length	210	ft
Fracture height	40	ft

Table 7.3: Basic reservoir and fracture properties from Middle Bakken for simulation study of CO_2 huff-n-puff process.

The CO_2 diffusion coefficient in oil and gas phases can be determined based on the published laboratory measurements (Grogan et al., 1988; Renner, 1988). Grogan et al. (1988) conducted experimental measurements of the CO_2 diffusion coefficients in pentane, decane, and hexadecane at temperature of 77 ^oF and pressure up to 870 psi and presented that the CO_2 diffusion coefficients are in the range of 1.80×10^{-5} cm^2/s-7.59×10^{-5} cm^2/s. Renner (1988) measured the CO_2 diffusion coefficients in decane at temperature of 100 ^oF and pressure up to 850 psi and reported that the CO_2 diffusion coefficients range from 1.97×10^{-5} cm^2/s to 12.6×10^{-5} cm^2/s. It is worth noting that the CO_2 diffusion coefficients in oil phase at reservoir condition are 5-10 times higher than those measured at ambient conditions (Denoyelle and Bardon, 1983). More importantly, the diffusion coefficient for the super critical CO_2 is 10-100 times of that for liquid (Kumar and Mittal, 1999). Thus, the range of CO_2 diffusion coefficient of 0.0001-0.01 cm^2/s is selected and investigated in this study. For the base case, CO_2 diffusion coefficient in both oil phase and gas phase is assumed to be 0.001 cm^2/s and the diffusion coefficient of the other components is assumed to be zero. For the CO_2 huff-n-puff process, initially the horizontal well produces for three years, and then it is converted to a CO_2 injector with constraints of the maximum injection rate of 500 MSCF/day and the maximum bottom hole pressure of 8,000 psi. After one year of CO_2 injection, the well is shut-in and soaking for three months. Finally, the well is put back into production. This is defined as one cycle of CO_2 huff-n-puff process. After one year of production of this cycle, another cycle of CO_2 huff-n-puff continues. The total production period of the well is 30 years. In order to compare the well performance of the base case with CO_2 injection and CO_2 diffusion, the case without CO_2 injection is simulated, which means that the well is only under shut in corresponding to the well is under CO_2 injection and soaking for the case

with CO_2 injection, and another case with CO_2 injection while without considering CO_2 diffusion effect is also simulated.

Figure 7.3 compares the oil recovery factor with and without CO_2 injection and CO_2 diffusion and only with primary production. As shown, the oil recovery factor at 30 years of production for the case with CO_2 injection and diffusion is the highest. Also, the oil recovery factor is almost the same for the case without CO_2 injection and the case only with primary production. In addition, the recovery factor of the case with CO_2 injection while without CO_2 diffusion is the lowest, illustration that CO_2 diffusion plays an important role in simulating CO_2 injection for enhanced oil recovery. Figures 7.4 and 7.5 compare CO_2 gas mole fraction distribution for the CO_2 injection cases with and without considering CO_2 diffusion. As shown, without CO_2 diffusion, most CO_2 molecules are mainly concentrated around hydraulic fractures due to the low permeability of shale matrix; however, with CO_2 diffusion, the CO_2 molecules can diffuse into the shale matrix to mix with the oil phase, leading to a higher oil recovery. Thus, the CO_2 diffusion term should be considered in order to accurately model CO_2 injection for enhanced oil recovery in reservoir simulation model. Without considering CO_2 diffusion term, large amount of CO_2 will backflow to the surface after the end of soaking time and impede oil production, as shown in Figure 7.6. The results show that about 88% of CO_2 injected is produced back at the end of production period without considering CO_2 diffusivity, while 69% of CO_2 injected is produced back with considering CO_2 diffusivity. For the base case, the oil recovery factor is increased by 2.90%, 1.93%, and 1.40% through CO_2 injection when compared to the case without CO_2 injection at 10, 20, and 30 years of production, respectively.

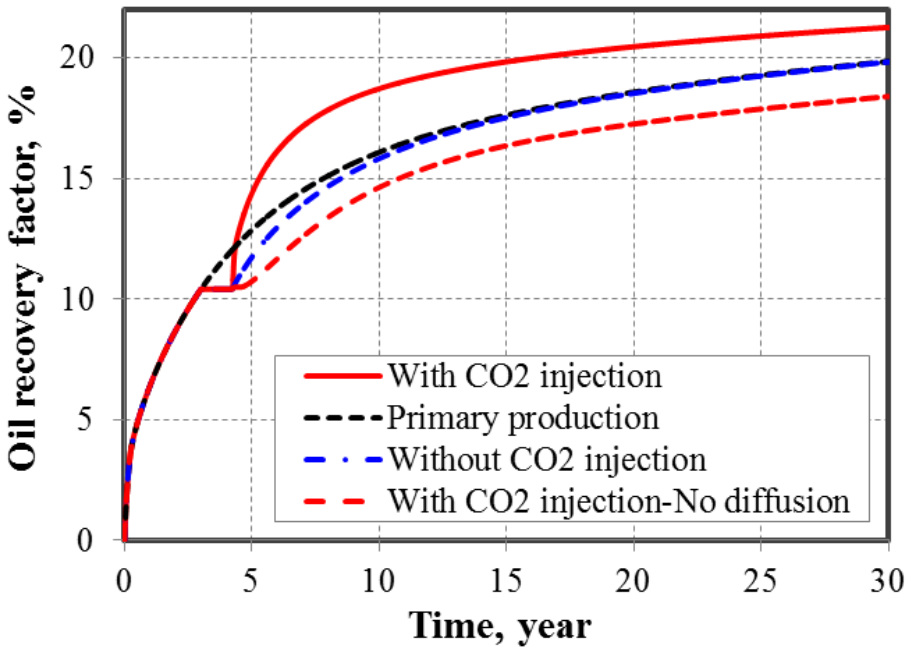

Figure 7.3: Comparison of oil recovery factor with and without CO_2 injection and CO_2 diffusion and only with primary production.

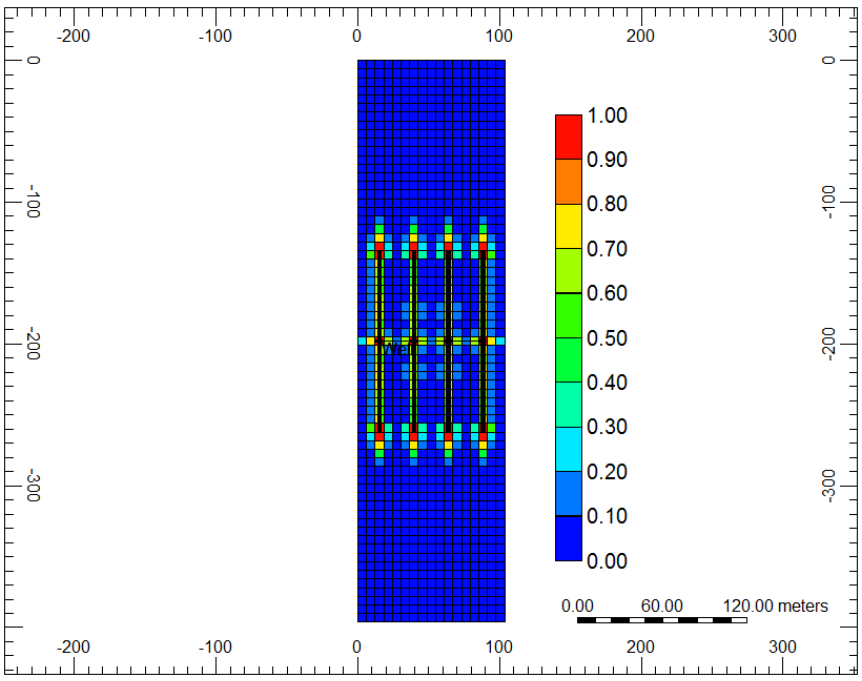

Figure 7.4: CO_2 gas mole fraction distribution without considering CO_2 diffusion.

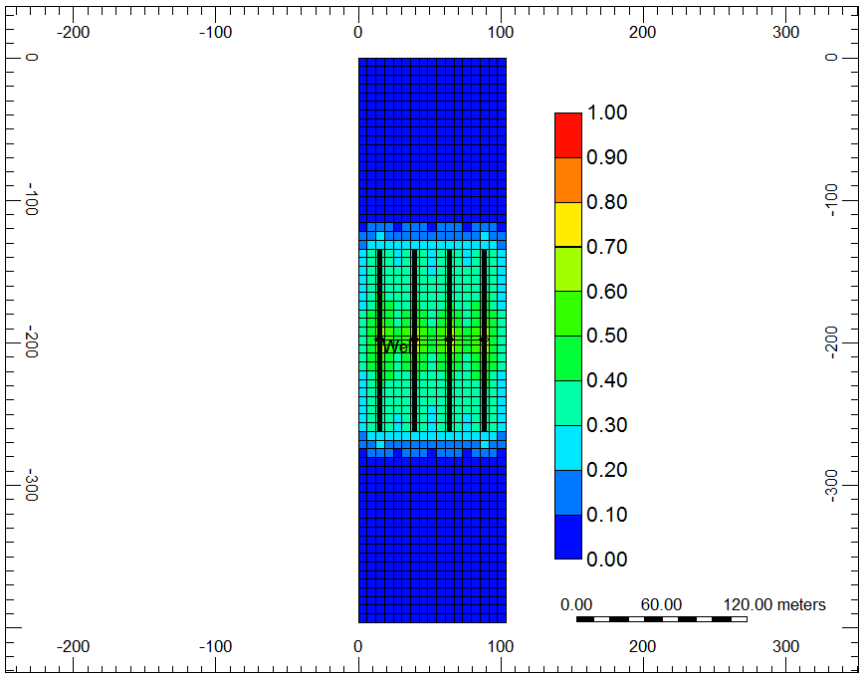

Figure 7.5: CO_2 gas mole fraction distribution with considering CO_2 diffusion.

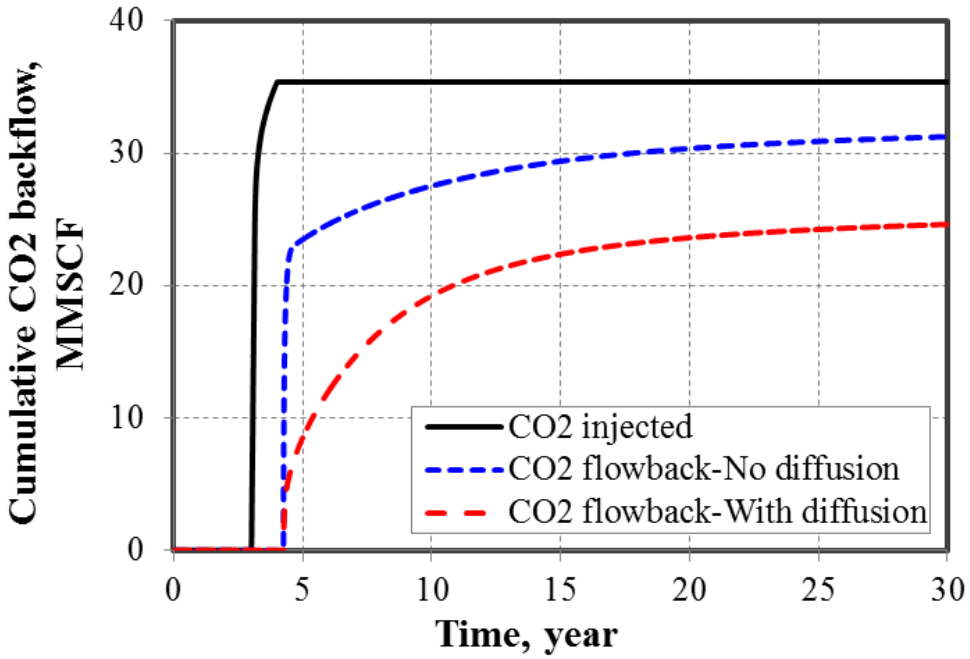

Figure 7.6: Comparison of total volume of CO_2 injected and volume of CO_2 backflow to the surface with and without considering CO_2 diffusion.

7.4.2 Effect of CO_2 diffusion coefficient

The effect of CO_2 diffusion coefficient for the comparison of well performance with and without CO_2 injection is shown in Figure 7.7, while keeping the other parameters same as those in the base case. The case without CO_2 injection represents the primary production. As shown, the incremental oil recovery factor at 30 years of production is 0.10%, 1.40%, and 3.25% corresponding to the CO_2 diffusion coefficient of 0.0001 cm^2/s, 0.001 cm^2/s, and 0.01 cm^2/s, respectively, illustrating that the CO_2 diffusion plays an important role in improving oil recovery during the process of CO_2 huff-n-puff.

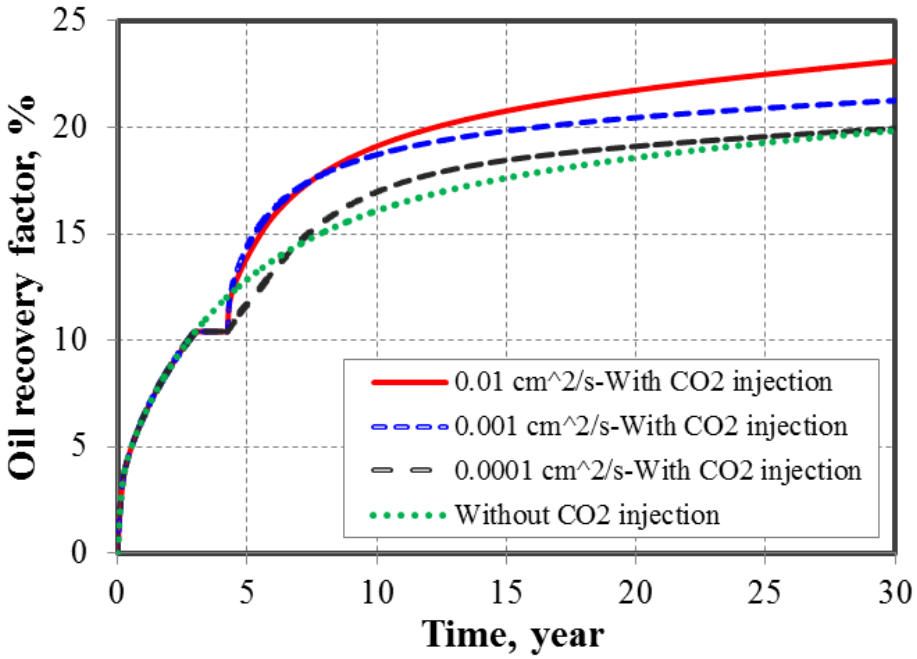

Figure 7.7: Effect of CO_2 diffusion coefficient on comparison of oil recovery factor with and without CO_2 injection.

7.4.3 Effect of number of cycle

Figure 7.8 shows the impact of number of cycle of CO_2 huff-n-puff on the comparison of well performance with and without CO_2 injection, while keeping the other parameters same as those in the base case. It can be seen that oil recovery factor increases

with an increase in the number of cycle and the incremental oil recovery factor at 30 years of production is 1.40%, 2.12%, and 2.43% corresponding to the number of cycle of 1, 2, and 3, respectively.

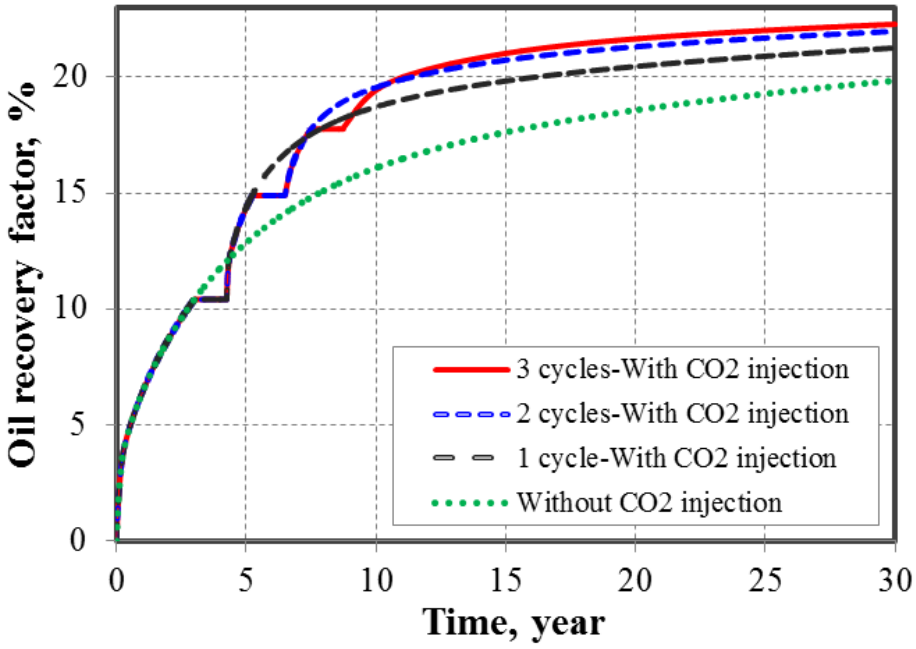

Figure 7.8: Effect of number of cycle on comparison of oil recovery factor with and without CO_2 injection.

7.4.4 Effect of fracture half-length

In practice, fracture half-length is uncertain, which is hard to characterize exactly. The typical range of 110 ft to 310 ft is investigated. Figure 7.9 presents the impact of fracture half-length on the comparison of well performance with and without CO_2 injection, while keeping the other parameters same as those in the base case. It can be observed that the incremental oil recovery factor at 30 years of production is -0.13%, 1.40%, and 2.79% for the fracture half-length of 110 ft, 210 ft and 310 ft, respectively, illustrating that longer fracture half-length is more favorable for the CO_2 huff-n-puff

process. This is because longer fracture has more contact area with the reservoir, resulting in CO_2 diffusing in larger portion of the reservoir and leading to a higher recovery factor.

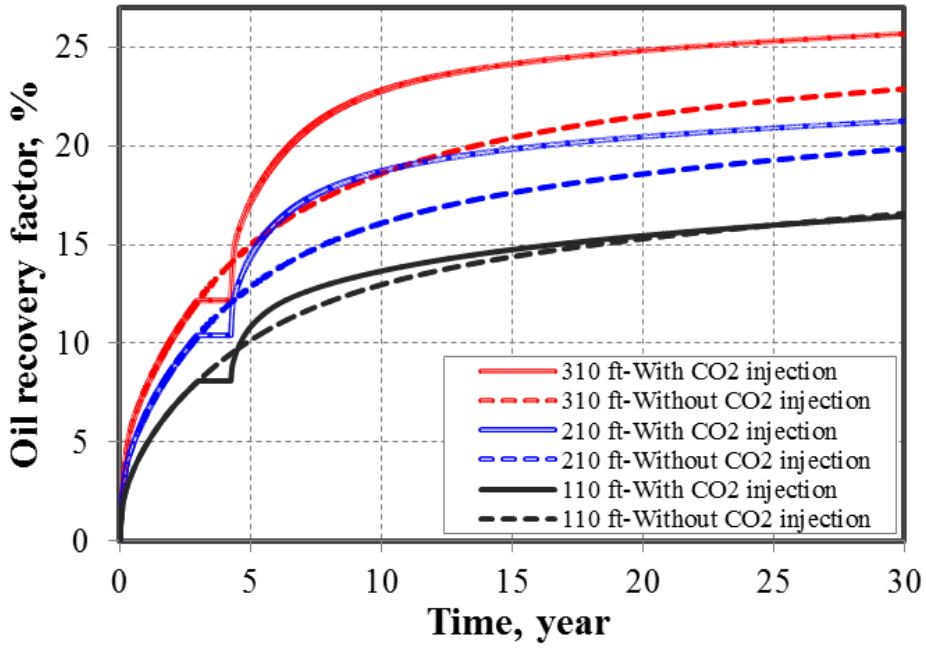

Figure 7.9: Effect of fracture half-length on comparison of oil recovery factor with and without CO_2 injection.

7.4.5 Effect of reservoir permeability

The typical reservoir permeability range of 0.001 md (1 μD) to 0.1 md (100 μD) is considered. Figure 7.10 shows the effect of reservoir permeability on the comparison of well performance with and without CO_2 injection, while keeping the other parameters same as those in the base case. It can be seen that the incremental oil recovery factor at 30 years of production is 2.35%, 1.40%, and -0.70% for the permeability of 0.001 md, 0.01md and 0.1 md, respectively, illustrating that lower permeability is more beneficial for the CO_2 huff-n-puff process. This is because the reservoir with lower permeability at

the end of primary production has larger residual oil saturation and the diffusion mechanism is more dominant than the convection mechanism compared to the larger permeability.

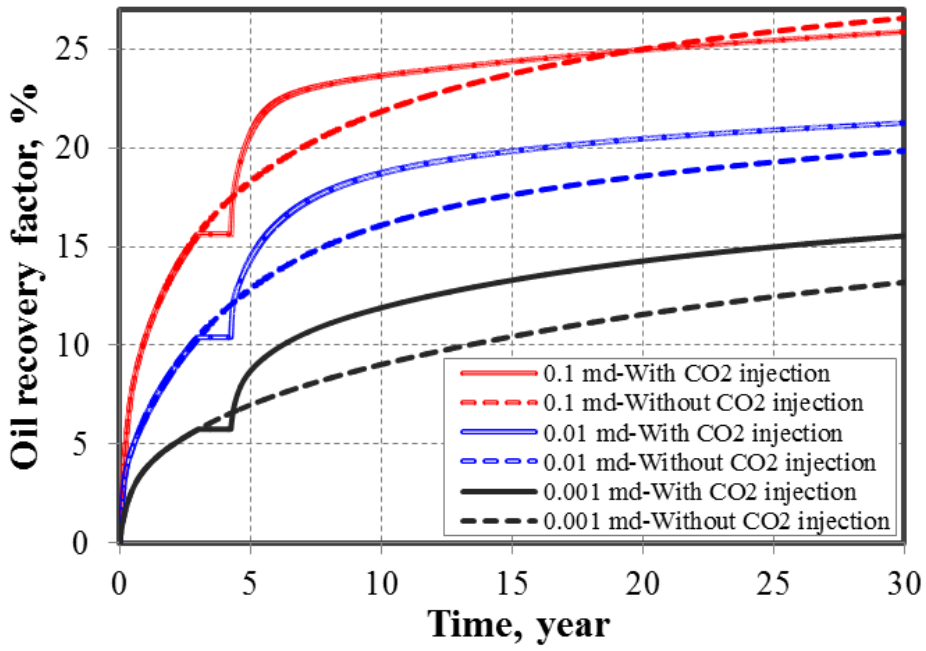

Figure 7.10: Effect of reservoir permeability on comparison of oil recovery factor with and without CO_2 injection.

7.4.6 Effect of reservoir heterogeneity

In order to evaluate the reservoir heterogeneity effect, we used the geostatistical approach to generate stochastically multiple realizations of the permeability. The stochastic method uses and honors the mean and variances of observed static data in the presence of correlation lengths, which represent anisotropy of model in different dimensions and provide a relationship between data in space. This approach can give a better representation of the natural variability of the property. It is also a useful tool to quantify the uncertainty in the reservoir description. In order to generate heterogeneity,

the spherical variogram type is used. We set up the correlation length of 1,000 ft and 170 ft in the X and Y direction, respectively. The nugget effect is used to generate discontinuity between data in reservoir. Larger nugget value causes more discontinuity and more heterogeneity. In this work, three different nugget values such as 0.0001, 0.2, and 0.7 are used to represent the minimum heterogeneity, the medium heterogeneity, and the maximum heterogeneity, respectively, as shown in Figure 7.11. The average permeability of these three cases remains the same as the base case of 0.01 md. The other parameters are the same as the base case.

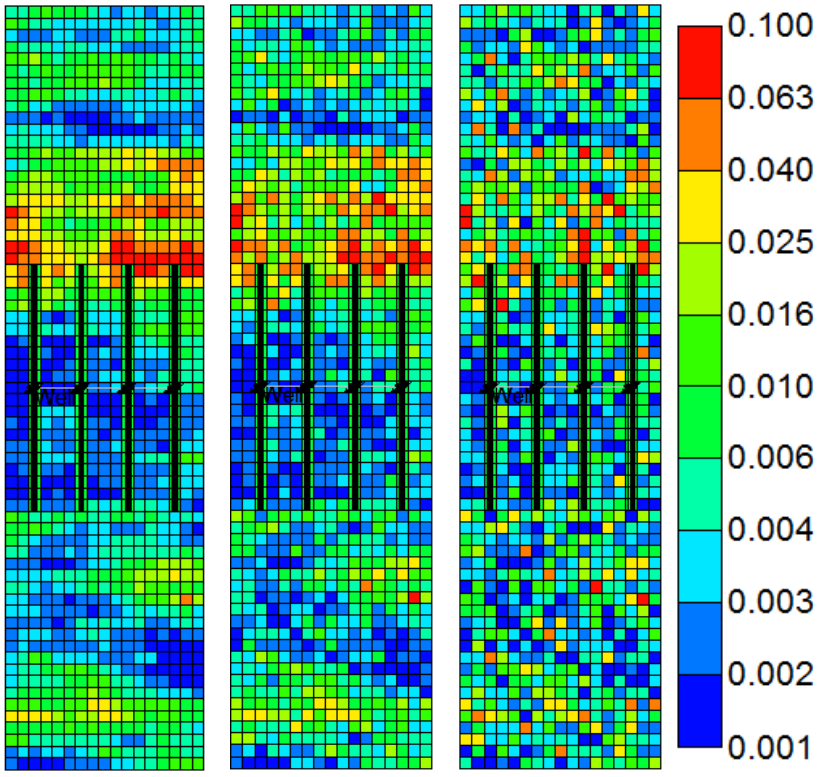

Figure 7.11: Three cases of reservoir heterogeneity. (a) The minimum heterogeneity. (b) The medium heterogeneity. (c) The maximum heterogeneity.

Comparison of oil recovery factor with and without CO_2 injection for the homogeneous and heterogeneous cases is shown in Figure 7.12. As shown, the incremental oil recovery factor at 30 years of production is 1.96%, 1.97%, and 2.02% for the minimum heterogeneity, the medium heterogeneity, and the maximum heterogeneity, respectively, which are larger than the homogeneous case (the base case) of 1.40%, illustrating that the more heterogeneous reservoir is more beneficial for the CO_2 huff-n-puff process in tight oil reservoirs. The reason is that the more heterogeneous reservoir has larger portion of lower permeability and higher residual oil saturation, resulting in the CO_2 diffusion process to be more pronounced.

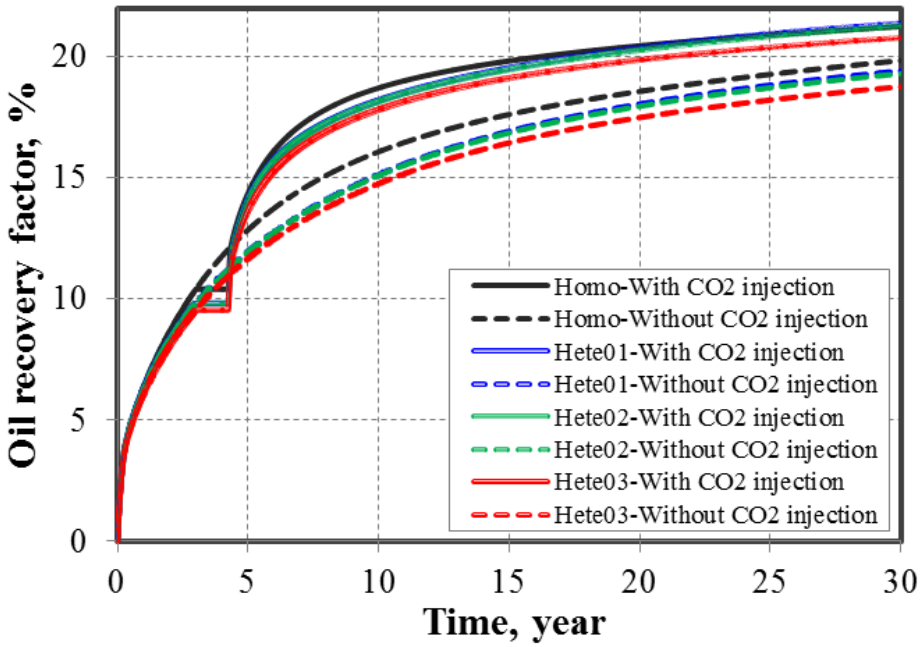

Figure 7.12: Effect of reservoir heterogeneity on comparison of oil recovery factor with and without CO_2 injection (Hete01: minimum heterogeneity, Hete02: medium heterogeneity, Hete03: maximum heterogeneity).

7.5 CONCLUSIONS

We performed a series of simulations for the CO_2 huff-n-puff process for enhanced oil recovery in the Bakken formation. The following conclusions can be drawn from this work:

(1) CO_2 molecular diffusivity is a significant factor in reservoir simulation model to capture the real physics mechanism during CO_2 injection into the tight oil reservoirs.

(2) Oil recovery factor increases with the increasing number of cycle of CO_2 huff-n-puff, and the incremental oil recovery factor at a 30-year period is 2.43% corresponding to three cycles in this case study.

(3) Lower permeability, longer fracture half-length, and more heterogeneity are much favorable for the CO_2 huff-n-puff process.

(4) The CO_2 diffusion mechanism is more pronounced than the convention mechanism for the reservoir with lower permeability during the CO_2 huff-n-puff process.

CHAPTER 8: Summary, Conclusions and Future Work

This chapter first summarizes the key points of the semi-analytical model, the framework for shale gas and tight oil reservoirs, and modeling of CO_2 injection for enhanced oil recovery in tight oil reservoirs. Then, the specific conclusions of this dissertation are presented. Finally, recommendations for future work are given.

8.1 SUMMARY

An efficient semi-analytical model was developed by discretizing hydraulic fractures into several segments to simulate shale gas and tight oil production. The key summaries for the semi-analytical model are as follows:

1. The model combines an analytical solution for the diffusivity equation for gas or oil flow in shale and a numerical solution for gas or oil flow in fractures.
2. The model can simulate shale gas and tight oil production from not only ideal rectangular hydraulic fractures with constant fracture width, but also realistic non-planar hydraulic fractures with varying fracture width.
3. The model is efficient because no gird is required.
4. For shale gas simulation, the diffusivity equation of conventional gas reservoirs was modified and implemented in the semi-analytical model by considering the important transport mechanisms including gas slippage, gas diffusion, and gas desorption.
5. For gas desorption effect, two models are considered in the semi-analytical model: Langmuir isotherm and BET isotherm.
6. For gas flow in hydraulic fractures, non-Darcy flow effect was considered.
7. Both finite fracture conductivity and infinite fracture conductivity can be simulated.
8. The Newton-Raphson iterative method is used to solve the final non-linear system of equations for shale gas simulation using the semi-analytical model.
9. The superposition principle in space and time is used to take into account the effects of all fracture segments and previous production time.
10. Two simulation constraints were allowed in the model: constant bottom hole pressure and constant flow rate.

11. Different flow regimes based on the model for simulation well performance from non-planar hydraulic fractures can be studied.
12. The model can provide a direct link between the fracture propagation model and field production performance analysis.

An integrated reservoir simulation framework was developed to perform sensitivity studies, history matching, and economic optimization for the development of shale gas and tight oil reservoirs. Also, an integrated simulation platform for unconventional resources (ISPUR) was developed and implemented in the framework. The key summaries for the framework are as follows:

1. The framework can be used to optimize fracture treatment design for both single well and multiple wells by reducing the number of simulation studies needed under conditions of large uncertainty in shale gas and tight oil reservoirs.
2. The ISPUR integrated three numerical reservoir simulators (CMG, ECLISPE, and UTCOMP), the semi-analytical model, an economic model, Design of Experiment (DOE), and Response Surface Methodology (RSM) with a global optimization search engine.
3. The DOE is used to perform sensitivity studies to quantify the rank of important single parameter and two-parameter interaction and screen non-significant parameters.
4. The rank of important parameters can provide guidance to perform history matching with field production data more efficiently.
5. The RSM is used to perform optimization with maximizing the net present value (NPV) to determine the best production scenario.

6. The ISPUR can produce input files for different reservoir simulators required by the DOE and RSE more easily and more efficiently.
7. Four hydraulic fracture geometries can be simulated: bi-wing fractures, orthogonal fracture networks, unstructured fracture networks, and non-planar fractures.
8. Three stress-dependent fracture conductivity curves for stiff shale, medium shale, and soft shale were implemented in the framework.
9. The framework is efficient and practical to guide hydraulic fracture treatment design in the field.

A numerical reservoir simulation model was built to simulate CO_2 injection using a huff-n-puff process with typical reservoir and fracture properties from the Bakken formation. The key summaries for the model are as follows:

1. Effect of CO_2 molecular diffusion is considered.
2. The key reservoir and fracture parameters affecting the CO_2 huff-n-puff process were quantified.
3. The model can be easily extended to compare CO_2 flooding scenario and CO_2 huff-n-puff scenario in multiple horizontal wells.

8.2 CONCLUSIONS

We used the semi-analytical model to perform a series of simulation studies for both shale gas and tight oil reservoirs. In addition, for the first time, we combined the realistic multiple non-planar hydraulic fractures generated from complex fracture propagation model and the semi-analytical model to analyze a field well performance from Marcellus shale. The key conclusions are as follows:

1. Good matches between the semi-analytical model and the numerical model were obtained for simulation of shale gas and tight oil production from single rectangular fracture, multiple rectangular fractures, and single planar fracture with varying width.
2. Under the condition of finite fracture conductivity and the assumptions of total fracture length and area between rectangular fractures and non-planar fractures, there is no big difference between them at early time of production, however, a big difference occurs at later time of production since the drainage area of non-planar fractures is larger than that of rectangular fractures. Hence, modeling of production from multiple non-planar fractures generated from the fracture propagation model is important.
3. Based on one field well analysis from Marcellus shale in this case study, the contribution of flow mechanisms of gas slippage, gas diffusion, and gas desorption to gas recovery at 30 years of production compared to that without considering them is 13%, 17%, and 22%, respectively. Hence, modeling the important gas flow mechanisms in shale gas reservoirs is significant.
4. Under the condition of lower fracture conductivity, the flux distribution of fracture segments between the rectangular fracture geometry and the planar fracture geometry with varying width is different. The difference between them decreases with the increasing fracture conductivity and becomes negligible at the infinite fracture conductivity.
5. Single curving non-planar fracture makes well performance less than that of single planar fracture with varying width under the condition of the same fracture length because of the fracture width restriction near the wellbore.

6. Transient flow regime analysis is different between single curving non-planar fracture and single planar fracture. It might be used to identify whether or not there is a severe fracture width restriction around the wellbore.

We evaluated several core measurements for methane adsorption from some area in Marcellus shale and found the gas adsorption behavior does not obey the Langmuir isotherm but obey the BET isotherm. To the best of our knowledge, such behavior has not been presented in the literature for shale gas reservoirs to behave like multilayer adsorption. Also, we compared the gas recovery by considering different models of Langmuir and BET. The key conclusions are as follows:

1. For the gas desorption behavior obeying the BET isotherm, the adsorbed gas has similar contribution to gas recovery with the free gas at both low and high reservoir pressure.
2. The range of specific surface area based on the BET isotherm for the area investigated in Marcellus shale was obtained as 3.38-14.16 m^2/g.
3. For a field well from Marcellus shale, the gas desorption effect with the Langmuir isotherm contributed to 1.1%-4.7% of gas recovery at early time of production (190 days), and 4.3%-15.1% of gas recovery at 30 years of production. However, the gas desorption effect with the BET isotherm contributed to 6.3%-26% of gas recovery at early time of production (190 days), and 8.1%-36.5% of gas recovery at 30 years of production.

We used the framework to optimize fracture treatment design for a single well development in Marcellus shale and multiple well placement in Bakken tight oil reservoirs. In addition, the fracturing cost was determined based on four wells in Marcellus shale. The key conclusions are as follows:

1. For Marcellus shale, six uncertain parameters were investigated and the rank of important parameters were quantified: at early time of production (5 years), fracture conductivity is the most significant, followed by permeability, fracture height, fracture half-length, reservoir pressure, and cluster spacing; while at late time of production (30 years), permeability becomes the most important, followed by fracture conductivity, fracture half-length, fracture height, reservoir pressure, and cluster spacing.
2. Based on the sensitivity analysis, we performed history matching for a well in Marcellus shale more efficiently with fracture conductivity of 5 md-ft, fracture height of 93 ft, fracture half-length of 330 ft, and permeability of 800 nD. Also, we performed production forecasting and quantified the estimated ultimate recovery of this well at 30 years is 11.12 BCF.
3. Through economic analysis of four different fracture designs in Marcellus shale, the fracture design with 4 clusters per stage and 436,156 lbs of proppants per stage is the best design.
4. The best economic production scenario for Marcellus shale investigated in this study is determined with the gas price of $3.5/MSCF: fracture height of 90 ft, fracture half-length of 460 ft, fracture conductivity of 62 md-ft, and cluster spacing of 80 ft.
5. For the Bakken formation, six uncertain parameters were also investigated for the single well and the rank of important parameters were the same regardless of short-term and long-term production: permeability is the most significant, followed by porosity, water saturation, fracture conductivity, and fracture spacing; while the fracture half-length is less important in this case study.

6. Based on the sensitivity analysis, we performed history matching for one field well from the Bakken formation more efficiently with permeability of 5 μD, initial water saturation of 41%, fracture conductivity of 50 md-ft, and fracture half-length of 215 ft. Also, we performed production forecasting and quantified the cumulative oil production and oil recovery factor at 30 years of production are 627 MBBL and 11%, respectively.
7. Finally, the best economic production scenario for multiple well placement in the Middle Bakken investigated in this study is determined with the oil price of $90/BBL: fracture spacing of 160 ft, fracture half-length of 340 ft, fracture conductivity of 35 md-ft, and well number of 5.

We build a numerical reservoir model to simulate CO_2 injection using a huff-n-puff process for enhanced oil recovery in the Bakken formation by considering the effect of CO_2 molecular diffusion. The key conclusions are as follows:

1. CO_2 molecular diffusion is an important physical mechanism during CO_2 injection into tight oil reservoirs and should be included in the numerical model.
2. For the base case with one cycle of CO_2 huff-n-puff, the oil recovery factor was increased by 2.90%, 1.93%, and 1.40% with CO_2 injection compared with the case without CO_2 injection at 10, 20, and 30 years of production, respectively.
3. Larger CO_2 molecular diffusivity coefficient, more number of cycle of CO_2 huff-n-puff, lower permeability, longer fracture half-length, and more heterogeneity are much favorable for the CO_2 huff-n-puff process.

8.3 FUTURE WORK

For the semi-analytical model development, the following future research should be considered:

1. Extension of the semi-analytical model to simulate production from complex fracture networks in multiple horizontal wells.
2. Extension of the semi-analytical model to simulate well interference through connection of hydraulic fractures between two horizontal wells.
3. Extension of the semi-analytical model to simulate the process of re-fracturing.
4. Using the semi-analytical model to perform transient flow regime analysis for multiple non-planar hydraulic fractures.
5. Coupling the semi-analytical model with the fracture propagation model to optimize hydraulic fracture treatment design and minimize the stress shadow effects in combination with economic analysis.

For the integrated reservoir simulation framework, the following future research should be considered:

1. Extension of the framework to perform history matching and production forecasting automatically.
2. Extension of the framework to optimize the process of re-fracturing.
3. Extension of the framework to investigate the effects of natural fractures and heterogeneity on well performance.
4. Application of the framework to the other shale gas reservoirs and tight oil formation.

For the numerical model of CO_2 injection for enhanced oil recovery in tight oil reservoirs, the following future research should be considered:

1. Investigation of the comparison between continuous CO_2 flooding and CO_2 huff-n-puff scenarios in tight oil reservoirs.
2. Investigation of different types of gas injection for enhanced oil recovery in tight oil reservoirs (i.e., N_2, CH_4, or lean gas).
3. Economic optimization of gas injection for enhanced oil recovery in tight oil reservoirs.
4. Investigation the effects of natural fractures, oil properties, and multiple wells on gas injection for enhanced oil recovery in tight oil reservoirs.

References

Adekunle, O., Hoffman, B. T. 2014. Minimum miscibility pressure studies in the Bakken. Paper SPE 169077, SPE Improved Oil Recovery Symposium, Tulsa, Oklahoma, 12-16 April.

Albo, S. E., Broadbelt, L. J., and Snurr, R. Q. 2006, Multiscale modeling of transport and residence times in nanostructured membranes. *AIChE Journal*, 52(11): 3679-3687.

Al-Husseiny, R., Ramey Jr, H. J., and Crawford, P. B. 1966. The flow of gases through porous media. *Journal of Petroleum Technology*, 18(5): 624-636.

Alramahi, B., and Sundberg, M. I. 2012. Proppant embedment and conductivity of hydraulic fractures in shales. Paper ARMA 12-291, The 46th US Rock Mechanics/Geomechanics Symposium, Chicago, Illinois, USA, 24-27 June.

Ambrose, R. J., Hartman, R. C., Diaz-Campos, M., Akkutlu, I. Y., and Sondergeld, C. H. 2010. New pore-scale considerations for shale gas in place calculations. SPE 131772, SPE Unconventional Gas Conference, Pittsburgh, Pennsylvania, USA, 23-25 February.

Anderson, M. J., and Whitcomb P. J. 2007. DOE simplified: practical tools for effective experimentation. 2nd Edition, New York, Productivity Press.

Aybar, U., Yu, W., Wshkalak, M. O., and Sepehrnoori, K. 2015. Evaluation of production losses from unconventional shale reservoirs. *Journal of Natural Gas Science and Engineering*, 23: 509-516.

Bagherian, B., Sarmadivaleh, M., Ghalambor, A., Nabipour, A., Rasouli, V., and Mahmoudi, M. 2010. Optimization of multiple-fractured horizontal tight gas well. Paper SPE 127899, SPE International Symposium and Exhibition on Formation Damage Control, Lafayette, Louisiana, USA, 10-12 February.

Bellman, R. E. 1961. A brief introduction to theta functions. New York, Holt, Reinhart, and Winston.

Besler, M. R., Steele, J. W., Egan, T., and Wagner, J. 2007. Improving well productivity and profitability in the Bakken-a summary of our experiences drilling, stimulating, and operating horizontal wells. Paper SPE 110679, SPE Annual Technical Conference and Exhibition, Anaheim, California, USA, 11-14 November.

Bhattacharya, S., and Nikolaou, M. 2011. Optimal fracture spacing and stimulation design for horizontal wells in unconventional gas reservoirs. Paper SPE 147622, SPE Annual Technical Conference and Exhibition, Denver, Colorado, USA, 30 October-2 November.

Bird, G. A. 1994. Molecular gas dynamics and the direct simulation of gas flows. Oxford, UK, Oxford University Press.

Bird, R. B., Stewart, W. E., and Lightfoot, E. N. 2007. Transport phenomena. New York, John Wiley & Sons, Inc.

Blasingame, T. A., and Poe Jr, B. D. 1993. Semianalytic solutions for a well with a single finite-conductivity vertical fracture. Paper SPE 26424, SPE Annual Technical Conference and Exhibition, Houston, Texas, USA, 3-6 October.

Bourdet, D. P., Whittle, T. M., Douglas, A. A., and Pirard, Y. M. 1983. A new set of type curves simplifies well test analysis. *World Oil*, 95-106, Houston, Gulf Publishing Co.

Bowker, K. A. 2008. Barnett shale and other unconventional gas play. HAPL technical workshop.

Britt, L. K., and Smith, M. B. 2009. Horizontal well completion, stimulation optimization, and risk mitigation. Paper SPE 125526, SPE Eastern Regional Meeting, Charleston, West Virginia, USA, September 23-25.

Brunauer, S., Emmett, P. H., and Teller, E. 1938, Adsorption of gases in multimolecular layers. *Journal of the American Chemical Society*, 60: 309-319.

Cavalcante Filho, J. S. A., Shakiba, M., Moinfar, A., Sepehrnoori, K. 2015. Implementation of a preprocessor for embedded discrete fracture modeling in an IMPEC compositional reservoir simulator. Paper SPE 173289, SPE Reservoir Simulation Symposium, Houston, Texas, USA, 23-25 February.

Carlson, E. S., and Mercer, J. C. 1991. Devonian shale gas production: mechanisms and simple models. *Journal of Petroleum Technology*, 43(4): 476-482.

Carman, P. C. 1956. Flow of gases through porous media. New York, Academic Press Inc.

Chen, C. C., and Raghavan, R. 1997. A multiply-fractured horizontal well in a rectangular drainage region. *SPE Journal*, 2(4): 455-465.

Chen, C., Balhoff, M., and Mohanty, K. K. 2014. Effect of reservoir heterogeneity on primary recovery and CO_2 huff 'n' puff recovery in shale-oil reservoirs. SPE Reservoir Evaluation and Engineering, 17(3): 404-413.

Cherian, B. V., Nichols, C. M., Panjaitan, M. L., Krishnamurthy, J. K., Sitchler, J. 2013. Asset development drivers in the Bakken and Three Forks. Paper SPE 163855, SPE Hydraulic Fracturing Technology Conference, The Woodlands, Texas, USA, 4-6 February.

Cherian, B. V., Stacey, E. S., Lewis, R., Iwere, F. O., Heim, R. N., and Higgins, S. M. 2012. Evaluating horizontal well completion effectiveness in a field development

program. Paper SPE 152177, SPE Hydraulic Fracturing Technology Conference, The Woodlands, Texas, USA, 6-8 February.

Cinco-Ley, H. and Samaniego, V. F. 1981. Transient-pressure analysis for fractured wells. *SPE Journal*, 33(9): 1749-1766.

Cipolla, C. L., and Wallace, J. 2014. Stimulated reservoir volume: a misapplied concept? Paper SPE 168596, SPE Hydraulic Fracturing Technology Conference, The Woodlands, Texas, USA, 4-6 February.

Cipolla, C. L., Fitzpatrick, T., Williams, M. J., and Ganguly, U. K. 2011. Seismic-to-simulation for unconventional reservoir development. Paper SPE 146876, SPE Reservoir Characterisation and Simulation Conference and Exhibition, Abu Dhabi, UAE, 9-11 October.

Cipolla, C. L., Mack, M., and Maxwell, S. 2010. Reducing exploration and appraisal risk in low permeability reservoirs using microseismic fracture mapping - part 2. Paper SPE 138103, SPE Latin American and Caribbean Petroleum Engineering Conference, Lima, Peru, 1-3 December.

Cipolla, C. L., Maxwell, S., and Mack, M. 2012. Engineering guide to the application of microseismic interpretations. Paper SPE 152165, SPE Hydraulic Fracturing Technology Conference, The Woodlands, Texas, USA, 6-8 February.

Cipolla, C. L., Warpinski, N. R., Mayerhofer, M. J., and Lolon, E. P. 2008. The relationship between fracture complexity, reservoir properties, and fracture treatment design. Paper SPE 115769, SPE Annual Technical Conference and Exhibition, Denver, Colorado, USA, 21-24 September.

Civan, F., Rai, C. S., Sondergeld, C. H. 2010. Shale-gas permeability and diffusivity inferred by improved formulation of relevant retention and transport mechanisms. *Transport in Porous Media*, 86(3): 925-944.

Clarkson, C. R., and Haghshenas, B. 2013, Modeling of supercritical fluid adsorption on organic-rich shales and coal. SPE 164532, SPE Unconventional Resources Conference, The Woodlands, Texas, USA, 10-12 April.

CMG-GEM. 2012. GEM User's Guide, Computer Modeling Group Ltd.

CMG-IMEX. 2012. IMEX User's Guide. Computer Modeling Group Ltd.

CMG-WinProp. 2012. WinProp User's Guide, Computer Modeling Group Ltd.

Computer Modeling Group Ltd. 2012. CMG reservoir simulator. http://www.cmgl.ca/.

Crank, J. 1975. The mathematics of diffusion. Clarendon Press, Oxford.

Cui, X., Bustin, A. M. M., and Bustin, R. M. 2009. Measurements of gas permeability and diffusivity of tight reservoir rocks: different approaches and their applications. *Geofluids*, 9(3): 208-223.

Dake, L. P. 1978. Fundamentals of reservoir engineering. Elsevier Science Publishing Company.

Damsleth, E., Hage, A., and Volden, R. 1992. Maximum information at minimum cost: a north sea field development study with an experimental design. *Journal of Petroleum Technology*, 44:1350-1356.

Daniels, J., Waters, G., LeCalvez, J., Lassek, J., and Bentley, D. 2007. Contacting more of the Barnett shale through an integration of real-time microseismic monitoring, petrophysics, and hydraulic fracture design. Paper SPE 110562, SPE Annual Technical Conference and Exhibition, Anaheim, California, USA, 11-14 November.

Darin, S. R., and Huitt, J. L. 1960. Effect of a partial monolayer of propping agent on fracture flow capacity. *AIME-Petroleum Transactions*, 219: 31-37.

Dejean, J. P., and Blanc, G. 1999. Managing uncertainties on production predictions using integrated statistical methods. Paper SPE 56696, SPE Annual Technical Conference and Exhibition Proceedings, Houston, Texas, USA, 3-6 October.

Denoyelle, L., and Bardon, C. 1983. Influence of diffusion on enhanced oil recovery by CO_2 injection. International Symposium on CO_2 Enhanced Oil Recovery, Budapest, Hungary, 8-11 March.

Drillinginfo. 2013. 5 top Bakken shale producers-what's their secret? http://info. drillinginfo.com/5-top-bakken-shale/.

Dullien, F. A. L. 1979. Porous media, fluid transport and pore structure. New York, Academic Press.

Ertekin, T., King, G. R., and Schwerer, F. C. 1986. Dynamic gas slippage: a unique dual-mechanism approach to the flow of gas in tight formations. *SPE Formation Evaluation*, 1(1): 43-52.

Evans, R. D., and Civan, F. 1994, Characterization of non-Darcy multiphase flow in petroleum bearing formations. Report, U.S. DOE Contract No. DE-AC22-90BC14659, School of Petroleum and Geological Engineering, University of Oklahoma.

Fai-Yengo, V., Rahnema, H., and Alfi, M. 2014. Impact of light component stripping during CO_2 injection in Bakken formation. Paper URTeC 1922932, Unconventional Resources Technology Conference, Denver, Colorado, USA, 25-27 August.

Fan, L., Thompson, J. W., Robinson, J. R. 2010. Understanding gas production mechanism and effectiveness of well stimulation in the Haynesville shale through reservoir simulation. Paper SPE 136696, Canadian Unconventional Resources and International Petroleum Conference, Calgary, Canada, 19-21 October.

Fisher, M. K., Davidson, B. M., Goodwin, A. K., Fielder, E. O., Buckler, W. S., Steinberger, N. P. 2002. Integrating fracture mapping technologies to optimize stimulations in the Barnett shale. Paper SPE 77411, SPE Annual Technical Conference and Exhibition, San Antonio, Texas, 29 September-2 October.

Fisher, M. K., Heinze, J. R., Harris, C. D., Davidson, B. M., Wright, C. A., and Dunn, K. P. 2004. Optimizing horizontal completion techniques in the Barnett shale using microseismic fracture mapping. Paper SPE 90051, SPE Annual Technical Conference and Exhibition, Houston, Texas, USA, 26-29 September.

Flowers, J. R., Guetta, D. R., Stephenson, C. J., Jeremie, P., and d'Arco, N. 2014. A statistical study of proppant type vs. well performance in the Bakken central basin. Paper SPE 168618, SPE Hydraulic Fracturing Technology Conference, The Woodlands, Texas, USA, 4-6 February.

Freeman, C. M., Moridis, G. J., Michael, G. E., and Blasingame, T. A. 2012. Measurement, modeling, and diagnostics of flowing gas composition changes in shale gas wells. Paper SPE 153391, SPE Latin American and Caribbean Petroleum Engineering Conference, Mexico City, Mexico, 16-18 April.

Ganpule, S., Cherian, B., Gonzales, V., Hudgens, P., Aguirre, P. R., Mata, D., Olarte, D. P., Yunuskhojayev, A., and Moore, W. R. 2013. Impact of well completion on the uncertainty in technically recoverable resource estimation in Bakken and Three Forks. Paper SPE 167131, SPE Unconventional Resource Conference, Calgary, Canada, 5-7 November.

Gao, C., Lee, J. W., Spivey, J. P., and Semmelbeck, M. E. 1994. Modeling multilayer gas reservoirs including sorption effects. Paper SPE 29173, SPE Eastern Regional Conference and Exhibition, Charleston, West Virginia, USA, 8-10 November.

Gorucu, S. E., and Ertekin, T. 2011. Optimization of the design of transverse hydraulic fractures in horizontal wells placed in dual porosity tight gas reservoirs. Paper SPE 142040, SPE Middle East Unconventional Gas Conference and Exhibition, Muscat, Oman, 31 January-2 February.

Gringarten A. C., Ramey Jr., H. J., and Raghavan, R. 1975. Applied pressure analysis for fractured wells. *Journal of Petroleum Technology*, 27(7): 887-892.

Gringarten, A. C., and Rameny, H. J. Jr. 1973. The use of source and Green's functions in solving unsteady-flow problems in reservoirs. *SPE Journal*, 13(5): 285-296.

Gringarten, A. C., Ramey, H. J. Jr., and Raghavan, R. 1972. Unsteady-state pressure distribution created by a well with a single infinite-conductivity vertical fracture. *SPE Journal*, 14(4): 347-360.

Grogan, A. T., Pinczewski, V. W., Ruskauff, G. J., and Orr Jr, F. M. 1988. Diffusion of CO_2 at reservoir conditions: models and measurements. *SPE Reservoir Engineering*, 3(1): 93-102.

Gu, M., Dao, E., and Mohanty, K. K. 2015. Investigation of ultra-light weight proppant application in shale fracturing. *Fuel*, 150: 191-201.

Gu, M., and Mohanty, K. K. 2014. Effect of foam quality on effectiveness of hydraulic fracturing in shales. *International Journal of Rock Mechanics and Mining Sciences*, 70: 273-285.

Gu, M., Kulkarni, P., Rafiee, M., Ivarrud, E., and Mohanty, K. K. 2014. Understanding the optimum fracture conductivity for naturally fractured shale and tight reservoirs. Paper SPE 171648, SPE/CSUR Unconventional Resources Conference, Calgary, Canada, 30 September-2 October.

Guppy, K. H., Cinco-Ley, H., Ramey, H. J. Jr., Samaniego-V, F. 1982. Non-Darcy flow in wells with finite conductivity vertical fractures. *SPE Journal*, 22(5): 681-698.

Handren, P., and Palisch, T. 2007. Successful hybrid slickwater fracture design evolution-an east Texas cotton valley taylor case history. Paper SPE 110451, SPE Annual Technical Conference and Exhibition, Anaheim, California, USA, 11-14 November.

Hawthorne, S. B., Gorecki, C. D., Sorensen, J. A., Steadman, E. N., Harju, J. A., and Melzer, S. 2013. Hydrocarbon mobilization mechanisms from upper, middle, and lower Bakken reservoir rocks exposed to CO_2. Paper SPE 167200, SPE Unconventional Resources Conference, Calgary, Canada, 5-7 November.

Heidemann, R. A., Jeje, A. A., and Mohtadi, F. 1984. An introduction to the properties of fluids and solids. Calgary, Canada, University of Calgary Press.

Hoffman, B. T. 2012. Comparison of various gases for enhanced recovery from shale oil reservoirs. Paper SPE 154329, SPE Improved Oil Recovery Symposium, Tulsa, Oklahoma, USA, 14-18 April.

Holm, L. W. 1986. Miscibility and miscible displacement. *Journal of Petroleum Technology*, 38(8): 817-818.

Holm, L. W. 1987. Evolution of the carbon dioxide flooding processes. *Journal of Petroleum Technology*, 39(11): 1337-1342.

Holm, L. W., and Josendal, V. A. 1974. Mechanisms of oil displacement by carbon dioxide. *Journal of Petroleum Technology*, 26(12): 1427-1438.

Holm, L. W., and Josendal, V. A. 1982. Effect of oil composition on miscible-type displacement by carbon dioxide. *SPE Journal*, 22(1): 87-98.

Hoteit, H. 2013. Modeling diffusion and gas-oil mass transfer in fractured reservoirs. *Journal of Petroleum Science and Engineering*, 105: 1-17.

Hoteit, H., and Firoozabadi, A. 2006. Compositional modeling by the combined discontinuous Galerkin and mixed method. *SPE Journal*, 11(1): 19-34.

Iwere, F. O., Heim, R. N., and Cherian, B. V. 2012. Numerical simulation of enhanced oil recovery in the middle Bakken and upper Three Forks tight oil reservoirs of the Williston basin. Paper SPE 154937, SPE Americas Unconventional Resources Conference, Pittsburgh, Pennsylvania, USA, 5-7 June.

Jarrell, P. M., Fox, C. E., Stein, M. H., and Webb, S. L. 2002. Practical aspects of CO_2 flooding. SPE monograph, Volume 22, Henry L. Doherty Series, Richardson, Texas, USA.

Javadpour, F., Fisher, D., and Unsworth, M. 2007. Nanoscale gas flow in shale gas sediments. *Journal of Canadian Petroleum Technology*, 46(10): 55-61.

Kang, S. M., Fathi, E., Ambrose, R. J., Akkutlu, I. Y., and Sigal, R. F. 2011. Carbon dioxide storage capacity of organic-rich shales. *SPE Journal*, 16: 842-855.

Khan, W. A., Rehman, S. A., Akram, A. H., and Ahmad, A. 2011. Factors affecting production behavior in tight gas reservoirs. Paper SPE 149045, SPE/DGS Saudi Arabia Section Technical Symposium and Exhibition, Al-Khobar, Saudi Arabia, 15-18 May.

Kiefer, J., and Wolfowitz, J. 1959. Optimum designs in regression problems. *The Annals of Mathematical Statistics*, 30(2): 271-294.

Kong, X., Delshad, M., Wheeler, M. F. 2015. A numerical study of benefits of adding polymer to WAG processes for a pilot case. Paper SPE 173230, SPE Reservoir Simulation Symposium, Houston, Texas, USA, 23-25 February.

Kuila U., and Prasad, M. 2013. Specific surface area and pore-size distribution in clays and shales. *Geophysical Prospecting*, 61: 341-362.

Kumar, P., and Mittal, K. L. (eds.) 1999. Handbook of microemulsion science and technology. New York, Marcel Dekker.

Kurtoglu, B., and Kazemi, H. 2012. Evaluation of Bakken performance using coreflooding, well testing, and reservoir simulation. Paper SPE 155655, SPE Annual Technical Conference and Exhibition, San Antonio, Texas, USA, 8-10 October.

Kurtoglu, B., Kazemi, H., Rosen, R., Michelson, W., and Kosanke, T. 2014. A rock and fluid study of middle Bakken formation: key to enhanced oil recovery. Paper SPE 171668, SPE Unconventional Resources Conference, Calgary, Canada, 30 September-2 October 2.

Kurtoglu, B., Sorensen, J. A., Braunberger, J., Smith, S., and Kazemi, H. 2013. Geologic characterization of a Bakken reservoir for potential CO_2 EOR. Paper SPE 168915, Unconventional Resources Technology Conference, Denver, Colorado, USA, 12-14 August.

LaFollette R. F., and Carman, P. S. 2010. Proppant diagenesis: results so far. Paper SPE 131782, SPE Unconventional Gas Conference, Pittsburgh, Pennsylvania, USA, 23-25 February.

Lambert, M. R., Marino, S. D., Anthony, T. L., Calvin, M. W., Gutierrez, S., and Smith, D. P. 1996. Implementing CO_2 floods: no more delays! Paper SPE 35187, Permian Basin Oil and Gas Recovery Conference, Midland, Texas, USA, 27-29 March.

Lane, H. S., Watson, A. T., and Lancaster, D. E. 1989. Identifying and estimating desorption from Devonian shale gas production data. SPE 19794, SPE Annual Technical Conference and Exhibition, San Antonio, Texas, USA, 8-11 October.

Langmuir, I. 1918. The adsorption of gases on plane surfaces of glass, mica and platinum. *Journal of the American Chemical Society*, 40: 1403-1461.

Lashgari, H. R. 2014. Development of a four-phase thermal-chemical reservoir simulator for heavy oil. PhD dissertation, The University of Texas at Austin.

Leahy-Dios, A., Das, M., Agarwal, A., and Kaminsky, R. 2011. Modeling of transport phenomena and multicomponent sorption for shale gas and coalbed methane in an unstructured grid simulator. SPE 147352, SPE Annual Technical Conference and Exhibition, Denver, Colorado, USA, 30 October-2 November.

Li, L., and Lee, S. H. 2008. Efficient field-scale simulation of black oil in a naturally fractured reservoir through discrete fracture networks and homogenized media. *SPE Reservoir Evaluation and Engineering*, 11(4): 750-758.

Lu, X., Li, F., and Watson, A. T. 1995, Adsorption measurements in Devonian shales. *Fuel*, 74(4): 599-603.

Luo, S., Wolff, M., Ciosek, J., Rasdi, F., Neal, L., Arulampalam, R., Willis, S. 2011. Probabilistic reservoir simulation workflow for unconventional resource play: Bakken case study. Paper SPE 142896, SPE EUROPEC/EAGE Annual Conference and Exhibition, Vienna, Austria, 23-26 May.

Mahmoud, M. 2014. Development of a new correlation of gas compressibility factor (Z-factor) for high pressure gas reservoirs. *Journal of Energy Resources Technology*, 136: 1-11.

Marongiu-Porcu, M., Wang, X., and Economides, M. J. 2009. Delineation of application: physical and economic optimization of fractured gas wells. Paper SPE 120114, SPE Production and Operations Symposium, Oklahoma City, Oklahoma, USA, 4-8 April.

Martin, F. D., and Taber, J. J. 1992. Carbon dioxide flooding. *Journal of Petroleum Technology*, 44(4): 396-400.

Martin, J. P., Hill, D. G., Lombardi, T. E., and Nyahay, R. 2010, A primer on New York's gas shales. http://offices.colgate.edu/bselleck/AppBasin/GasshaleMartin.pdf.

Matthew, C. S., and Russell, D. G. 1967. Pressure buildup and flow tests in wells. AIME Monograph, Volume 1, SPE-AIME, New York.

Maxwell, S. C., Urbancic, T. I., Steinsberger, N. P., Zinno, R. 2002. Microseismic imaging of hydraulic fracture complexity in the Barnett shale. Paper SPE 77440, SPE Annual Technical Conference and Exhibition, San Antonio, Texas, USA, 29 September-2 October.

Maxwell, S. C., Weng, X., Kresse, O., and Rutledge, J. 2013. Modeling microseismic hydraulic fracture deformation. Paper SPE 166312, SPE Annual Technical Conference and Exhibition, New Orleans, Louisiana, USA, 30 September-2 October.

Mayerhofer, M. J., Lolon, E. P., Warpinski, N. R., Cipolla, C. L., Walser, D., and Rightmire, C. M. 2008. What is stimulated reservoir volume (SRV)? Paper SPE 119890, SPE Shale Gas Production Conference, Fort Worth, Texas, 16-18 November.

McDaniel, G. A., Abbott, J., Mueller, F. A., Mueller, F., Mokhtar, A., Pavlova, S., Nevvonen, O., Parias, T., and Alary, J. A. 2010, Changing the shape of fracturing: new proppant improves fracture conductivity. Paper SPE 135360, SPE Annual Technical Conference and Exhibition, Florence, Italy, 19-22 September.

McDaniel, R. R., and Willingham, J. R. 1978. The effects of various proppants and proppant mixtures on fracture permeability. Paper SPE 7573, The 53rd Annual Fall Technical Conference and Exhibition, Houston, Texas, USA, 1-3 October.

McDuff, R. E., Ellis, R. A. 1979. Determining diffusion coefficients in marine sediments: a laboratory study of the validity of resistivity techniques. *American Journal of Science*, 279: 666-675.

Meissner, F. F. 1978. Petroleum geology of the Bakken formation, Williston basin, North Dakota and Montana. In Estelle, D. and Miller, R. eds, The economic geology of the Williston Basin, 1978 Williston Basin Symposium, Billings, Montana, Montana Geological Society, 207-230.

Meyer, B. R., Bazan, L. W., Jacot, R. H., and Lattibeaudiere, M. G. 2010. Optimization of multiple transverse hydraulic fractures in horizontal wellbores. Paper SPE 131732, SPE Unconventional Gas Conference, Pittsburgh, Pennsylvania, USA, 23-25 February.

Mirzaei, M., and Cipolla, C. L. 2012. A workflow for modeling and simulation of hydraulic fractures in unconventional gas reservoirs. Paper SPE 153022, SPE Middle East Unconventional Gas Conference and Exhibition, Abu Dhabi, UAE, 23-25 January.

Moinfar, A. 2013. Development of an efficient embedded discrete fracture model for 3D compositional reservoir simulation in fractured reservoirs. PhD dissertation, The University of Texas at Austin.

Moinfar, A., Varavei, A., Sepehrnoori, K., and Johns, R. T. 2013. Development of a coupled dual continuum and discrete fracture model for the simulation of unconventional reservoirs. Paper SPE 163647, SPE Reservoir Simulation Symposium, The Woodlands, Texas, USA, 18-20 February.

Myers, R. H., Montgomery, D. C., and Anderson-Cook, C. 2008. Response surface methodology: process and product optimization using designed experiments, 3rd Edition, New York, John Wiley and Sons.

Nghiem, L. X., Kohse, B. F., and Sammon, P. H. 2000. Compositional simulation of the vapex process. Paper PETSOC 2000-034, Canadian International Petroleum Conference, Calgary, Canada, 4-8 June.

Nikiforuk, A. 2011. Fracking contamination 'will get worse': Albert expert. http://thetyee.ca/News/2011/12/19/Fracking-Contamination/.

Nojabaei, B., Johns, R. T., and Chu, L. 2013. Effect of capillary pressure on phase behavior in tight rocks and shales. SPE Reservoir Evaluation and Engineering, 16(3): 281-289.

Olorode, O. M., Freeman, C. M., Moridis, G. J., and Blasingame, T. A. 2013. High-resolution numerical modeling of complex and irregular fracture patterns in shale-gas reservoirs and tight gas reservoirs. *SPE Reservoir Evaluation and Engineering*, 16(4): 1-13.

Olson, J. E. 1995. Fracturing from highly deviated and horizontal wells: numerical analysis of non-planar fracture propagation. Paper SPE 29573, Low Permeability Reservoirs Symposium, Denver, Colorado, USA, 19-22 March.

Olson, J. E., and Wu, K. 2012. Sequential vs. simultaneous multizone fracturing in horizontal wells: insights from a non-planar, multifrac numerical model. Paper SPE 152602, SPE Hydraulic Fracturing Technology Conference, The Woodlands, Texas, USA, 6-8 February.

Orr Jr, F. M., and Silva, M. K. 1987. Effect of oil composition on minimum miscibility pressure-part 2: correlation. *SPE Reservoir Engineering*, 2(4): 479-491.

Orr Jr, F. M., Silva, M. K., and Lien, C. L. 1983. Equilibrium phase compositions of CO_2/crude oil mixtures-part 2: comparison of continuous multiple-contact and slim-tube displacement tests. *SPE Journal*, 23(2): 281-291.

Patzek, T. W., Male, F., and Marder, M. 2013. Gas production in the Barnett shale obeys a simple scaling theory. *PNAS*, 110(49): 19731-19736.

Peng, C. Y., and Gupta, R. 2003. Experimental design in determining modeling: assessing significant uncertainties. Paper SPE 80537, SPE Asia Pacific Oil and Gas Conference and Exhibition, Jakarta, Indonesia, 9-11 Sepetember.

Pope, C., Benton, T., and Palisch, T. 2009. Haynesville shale-one operator's approach to well completions in this evolving play. Paper SPE 125079, SPE Annual Technical Conference and Exhibition, New Orleans, Louisiana, USA, 4-7 October.

Rankin, R., Thibodeau, M., Vincent, M. C., and Palisch, T. T. 2010. Improved production and profitability achieved with superior completions in horizontal wells: a Bakken/Three Forks case history. Paper SPE 134595, SPE Annual Technical Conference and Exhibition, Florence, Italy, 19-22 September.

Reid, R. C., Frautsnitz, J. M., and Sherwood, T. K. 1977. The properties of gases and liquids. 3rd Edition, New York, McGraw-Hill.

Ren, B., Xu, Y., Niu, B., Ren, S., Li, X., Guo, P., Song, X. 2011. Laboratory assessment and field pilot of near miscible CO_2 injection for IOR and storage in a tight oil reservoir of ShengLi oilfield China. Paper SPE 144108, SPE Enhanced Oil Recovery Conference, Kuala Lumpur, Malaysia, 19-21 July.

Renner, T. A. 1988. Measurement and correlation of diffusion coefficients for CO_2 and rich-gas applications. *SPE Reservoir Engineering*, 3(2): 517-523.

Rezaveisia, M., Javadpourb, F., and Sepehrnoori, K. 2014. Modeling chromatographic separation of produced gas in shale wells. *International Journal of Coal Geology*, 121: 110-122.

Rouquerol, J., Rouquerol, F., and Sing, K. S. W. 1999. Adsorption by powers and porous solids: principles, methodology and applications. London, Academic Press.

Rubin, B. 2010. Accurate simulation of non-Darcy flow in stimulated fractured shale reservoirs. Paper SPE 132093, SPE Western Regional Meeting, Anaheim, California, USA, 27-29 May.

Sakhaee-Pour, A., and Bryant, S. L. 2012. Gas permeability of shale. *SPE Reservoir Evaluation and Engineering*, 15(4): 401-409.

Schlumberger. 2012. ECLIPSE reservoir engineering software. http://www.software.slb.com/products/domains/Pages/reservoir-engineering.aspx.

Schmidt, D., Rankin, P. E. R., Williams, B., Palisch, T., and Kullman, J. 2014. Performance of mixed proppant sizes. Paper SPE 168629, SPE Hydraulic Fracturing Technology Conference, The Woodlands, Texas, 4-6 February.

Schmoker, J. W. 1980. Organic content of Devonian shale in western Appalachian basin. *AAPG Bulletin*, 64(12): 2156-2165.

Shakiba, M. 2014. Modeling and simulation of fluid flow in naturally and hydraulically fractured reservoirs using embedded discrete fracture model (EDFM). Master thesis, The University of Texas at Austin.

Sheng, J. J. 2015. Enhanced oil recovery in shale reservoirs by gas injection. *Journal of Natural Gas Science and Engineering*, 22: 252-259.

Shi, J., Zhang, L., Li, Y., Yu, W., He, X., Liu, N., Wang, T. 2013. Diffusion and flow mechanisms of shale gas through matrix pores and gas production forecasting. Paper SPE 167226, SPE Unconventional Resources Conference, Calgary, Alberta, Canada, 5-7 November.

Shoaib, S., and Hoffman, B. T. 2009. CO_2 flooding the Elm Coulee field. Paper SPE 123176, SPE Rocky Mountain Petroleum Technology Conference, Denver, Colorado, 14-16 April.

Sigmund, P. M. 1976. Prediction of molecular diffusion at reservoir conditions. Part II-estimating the effects of molecular diffusion and convective mixing in multicomponent systems. *Journal of Canadian Petroleum Technology*, 15(3): 53-62.

Sigmund, P. M., Kerr, W., and MacPherson, R. E. 1984. A laboratory and computer model evaluation of immiscible CO_2 flooding in a low-temperature reservoir. Paper SPE 12703, SPE Enhanced Oil Recovery Symposium, Tulsa, Oklahoma, 15-18 April.

Silin, D., and Kneafsey, T. 2012. Shale gas: nanometer-scale observations and well modeling. *Journal of Canadian Petroleum Technology*, 51(6): 464-475.

Sing, K. S. W., Everett, D. H., Haul, R. A. W., Moscou, L., Pierotti, R. A., Rouquerol, J., and Siemieniewska, T. 1985. Reporting physisorption data for gas/solid systems with special reference to the Determination of surface area and porosity (Recommendations 1984). *Pure and Applied Chemistry*, 57(4): 603-619.

Smith, D. M., and Williams, F. L. 1984. Diffusional effects in the recovery of methane from coalbeds. *SPE Journal*, 24(5): 529-535.

Sneddon, I. N. 1951. Fourier transforms. New York, McGraw-Hill.

Solar, C., Blanco, A. G., Vallone, A., and Sapag K. 2010. Adsorption of methane in porous materials as the basis for the storage of natural gas. In Natural Gas, P. Potocnik. Rijeka, Crootia: Sciyo. http://www.intechopen.com/books/natural-gas.

Song, C., and Yang, D. 2013. Performance evaluation of CO_2 huff-n-puff processes in tight oil formations. Paper SPE 167217, SPE Unconventional Resources Conference, Alberta, Canada, 5-7 November.

Stalkup, F. I. 1987. Displacement behavior of the condensing/vaporizing gas drive process. Paper SPE 16715, SPE Annual Technical Conference and Exhibition, Dallas, Texas, USA, 27-30 September.

Stat-Ease, Inc. 2011. Design-Expert® 8 User's Guide.

Taber, J. J., and Martin, F. D. 1983. Technical screening guides for the enhanced recovery of oil. Paper SPE 12069, SPE Annual Technical Conference and Exhibition, San Francisco, California, USA, 5-8 October.

Tavassoli, S., Yu, W., Javadpour, F., and Sepehrnoori, K. 2013a. Well screen and optimum refracturing time: a Barnett shale well. *Journal of Petroleum Engineering*, Article ID 817293.

Tavassoli, S., Yu, W., Javadpour, F., and Sepehrnoori, K. 2013b. Selection of candidate horizontal wells and determination of the optimal time of refracturing in Barnett shale (Johnson county). Paper SPE 167137, SPE Unconventional Resources Conference, Calgary, Alberta, Canada, 5-7 November.

Terracina, J. M., Turner, J. M., Collins, D. H., and Spillars, S. E. 2010. Proppant selection and its effect on the results of fracturing treatments performed in shale formations. Paper SPE 135502, SPE Annual Technical Conference and Exhibition, Florence, Italy, 19-22 September.

Thambynayagam, R. M. K. 2011. The diffusion handbook: applied solutions for engineers. New York, McGraw-Hill Professional.

U.S. Department of Energy (DOE). 2013. Modern shale gas development in the United States: an update, http://www.netl.doe.gov/File%20Library/Research/Oil-Gas/shale-gas-primer -update-2013.pdf.

U.S. Energy Information Administration (EIA). 2011. Review of emerging resources: U.S. shale gas and shale oil plays, http://www.eia.gov/analysis/studies/usshalegas/pdf/usshaleplays.pdf.

U.S. Energy Information Administration (EIA). 2014b. Drilling productivity report, http://www.eia.gov/petroleum/drilling/#tabs-summary-1.

U.S. Energy Information Administration. 2012. Global shale gas basins. http://blog.thomsonreuters.com/index.php/global-shale-gas-basins-graphic-of-the-day.

U.S. Energy Information Administration. 2013a. Technically recoverable shale oil and shale gas resources: an assessment of 137 shale formations in 41 countries outside the United States. http://www.eia.gov/analysis/studies/worldshalegas/.

U.S. Energy Information Administration. 2013b. Early release overview. http://www.eia.gov/forecasts/aeo/er/pdf/0383er%282013%29.pdf.

U.S. Energy Information Administration. 2014a. Annual energy outlook. http://www.eia.gov/forecasts/aeo/mt_naturalgas.cfm.

U.S. Energy Information Administration. 2015. Shale gas and tight oil are commercially produced in just four countries. http://www.eia.gov/todayinenergy/detail.cfm?id=19991.

United States Geological Survey (USGS). 2013. USGS releases new oil and gas assessment for Bakken and Three Forks formations. USGS Webpost, http://www.usgs.gov/blogs/features/usgs_top_story/usgs-releases-new-oil-and-gas-assessment-for-bakken-and-three-forks-formations/.

UTCOMP. 2014. The University of Texas at Austin.

Wang, X., Luo, P., Er, V., and Huang, S. 2010. Assessment of CO_2 flooding potential for Bakken formation, Saskatchewan. Paper SPE 137728, Canadian Unconventional Resources and International Petroleum Conference, Calgary, Canada, 19-21 October.

Warpinski, N. R., Kramm, R. C., Heinze, J. R., Waltman, C. K. 2005. Comparison of single and dual-array microseismic mapping techniques in the Barnett shale. Paper SPE 95568, SPE Annual Technical Conference and Exhibition, Dallas, Texas, USA, 9-12 October.

Weng X. 2014. Modeling of complex hydraulic fractures in naturally fractured formation. *Journal of Unconventional Oil Gas Resources*, 9: 114-135.

Weng, X., Kresse, O., Cohen, C., Wu, R., and Gu, H. 2011. Modeling of hydraulic-fracture-network propagation in a naturally fractured formation. *SPE Production and Operation*, 26(4): 368-380.

West, D. R. M., Harkrider, J., Besler, M. R., Barham, M., and Mahrer, K. D. 2013. Optimized production in the Bakken shale: south Antelope case study. Paper SPE 167168, SPE Unconventional Resources Conference, Calgary, Canada, 5-7 November.

Williams, H., Khatri, D., Keese, R., Roy-Delage, L., Roye, J., Leach, D., Rottler, P., Procherie, O., and Rodriguez, J. 2011. Flexible, expanding cement system (FECS) successfully provides zonal isolation across Marcellus shale gas trends. Paper SPE 149440, Canadian Unconventional Resources Conference, Calgary, Alberta, Canada, 15-17 November.

Witherspoon, P., Wang, J., Iwai, K., and Gale, J. 1980. Validity of cubic law for fluid flow in a deformable rock fracture. *Water Resources Research*, 16(6): 1016-1024.

Wu, K. 2014. Numerical modeling of complex hydraulic fracture development in unconventional reservoirs. PhD dissertation, The University of Texas at Austin.

Wu, K., and Olson, J. E. 2013. Investigation of the impact of fracture spacing and fluid properties for interfering simultaneously or sequentially generated hydraulic fractures. *SPE Production and Operation*, 28(4): 427-436.

Wu, K., and Olson, J. E. 2014a. Simultaneous multi-frac treatments: fully coupled fluid flow and fracture mechanics for horizontal wells. SPE Journal, preprint.

Wu, K., and Olson, J. E. 2014b. Mechanics analysis of interaction between hydraulic and natural fractures in shale reservoirs. Paper SPE-2014-1922946, SPE/AAPG/SEG

Unconventional Resources Technology Conference, Denver, Colorado, USA, 25-27 August.

Wu, K., Li, X., Wang, C., Chen, Z., and Yu, W. 2015a. A model for gas transport in microfractures of shale and tight gas reservoirs. *AIChE Journal*, in press.

Wu, K., Li, X., Wang, C., Yu, W., and Chen, Z. 2015b. Model for surface diffusion of adsorbed gas in nanopores of shale gas reservoirs. *Industrial and Engineering Chemistry Research*, 54: 3225-3236.

Wu, K., Li, X., Wang, C., Yu, W., Guo, C., Ji, D., Ren, G., and Chen, Z. 2014. Apparent permeability for gas flow in shale reservoirs coupling effects of gas diffusion and desorption. Paper SPE-2014-1921039, SPE/AAPG/SEG Unconventional Resources Technology Conference, Denver, Colorado, USA, 25-27 August.

Wu, R., Kresse. O., Weng, X., Cohen, C., and Gu, H. 2012. Modeling of interaction of hydraulic fractures in complex fracture networks. Paper SPE 152052, SPE Hydraulic Fracturing Technology Conference, The Woodlands, Texas, USA, 6-8 February.

Xu, G., and Wong, S. W. 2013. Interaction of multiple non-planar hydraulic fractures in horizontal wells. Paper IPTC 17043, International Petroleum Technology Conference, Beijing, China, 26-28 March.

Xu, W., Thiercelin, M., Ganguly, U., Weng, X., Gu, H., Onda, H., Sun, J., and Calvez, J. L. 2010. Wiremesh: a novel shale fracturing simulator. Paper SPE 132218, International Oil and Gas Conference and Exhibition, Beijing, China, 8-10 June.

Yu, W., Al-Shalabi, E. W., and Sepehrnoori, K. 2014b. A sensitivity study of potential CO_2 injection for enhanced gas recovery in Barnett shale reservoirs. Paper SPE 169012, SPE Unconventional Resources Conference, The Woodlands, Texas, USA, 1-3 April.

Yu, W., and Sepehrnoori, K. 2013a. Optimization of multiple hydraulically fractured horizontal wells in unconventional gas reservoirs. Paper SPE 164509, SPE Production and Operation Symposium, Oklahoma, Oklahoma, USA, 23-26 March.

Yu, W., and Sepehrnoori, K. 2013b. Numerical evaluation of the impact of geomechanics on well performance in shale gas reservoirs. Paper ARMA 13-555, 47th US Rock Mechanics/Geomechanics Symposium, San Francisco, California, USA, 23-26 June.

Yu, W., and Sepehrnoori, K. 2013c. Simulation of proppant distribution effect on well performance in shale gas reservoirs. Paper SPE 167225, SPE Unconventional Resources Conference, Calgary, Alberta, Canada, 5-7 November.

Yu, W., and Sepehrnoori, K. 2014a. Sensitivity study and history matching and economic optimization for Marcellus shale. Paper SPE-2014-1923491, SPE/AAPG/SEG

Unconventional Resources Technology Conference, Denver, Colorado, USA, 25-27 August.

Yu, W., and Sepehrnoori, K. 2014b. An efficient reservoir simulation approach to design and optimize unconventional gas production. *Journal of Canadian Petroleum Technology*, 53: 109-121.

Yu, W., and Sepehrnoori, K. 2014c. Simulation of gas desorption and geomechanics effects for unconventional gas reservoirs. *Fuel*, 116: 455-464.

Yu, W., and Sepehrnoori, K. 2014d. Optimization of well spacing for Bakken tight oil reservoirs. Paper SPE-2014-1922108, SPE/AAPG/SEG Unconventional Resources Technology Conference, Denver, Colorado, USA, 25-27 August.

Yu, W., Gao, B., and Sepehrnoori, K. 2014c. Numerical study of the impact of complex fracture patterns on well performance in shale gas reservoirs. *Journal of Petroleum Science Research*, 3: 83-89.

Yu, W., Huang, S., Wu, K., Sepehrnoori, K., and Zhou, W. 2014a. Development of a semi-analytical model for simulation of gas production in shale gas reservoirs. Paper SPE-2014-1922945, SPE/AAPG/SEG Unconventional Resources Technology Conference, Denver, Colorado, USA, 25-27 August.

Yu, W., Lashgari, H., and Sepehrnoori, K. 2014f. Simulation study of CO_2 huff-n-puff process in Bakken tight oil reservoirs. Paper SPE 169575, SPE Western North American and Rocky Mountain Joint Regional Meeting, Denver, Colorado, USA, 16-18 April.

Yu, W., Luo Z. Y., Javadpour, F., Varavei, A., and Sepehrnoori, K. 2014d. Sensitivity analysis of hydraulic fracture geometry in shale gas reservoirs. *Journal of Petroleum Science and Engineering*, 113: 1-7.

Yu, W., Sepehrnoori, K., and Patzek, T. W. 2014e. Evaluation of gas adsorption in Marcellus shale. Paper SPE 170801, SPE Annual Technical Conference an Exhibition, Amsterdam, The Netherlands, 27-29 October.

Yu, W., Varavei, A., and Sepehrnoori, K. 2015b. Optimization of shale gas production using design of experiment and response surface methodology. *Energy Sources, Part A: Recovery, Utilization, and Environmental Effects*, 37(8): 906-918.

Yu, W., Zhang, T., Du, S., and Sepehrnoori, K. 2015a. Numerical study of the effect of uneven proppant distribution between multiple fractures on shale gas well performance. *Fuel*, 142: 189-198.

Zhang, J. 2005. IRSS: an integrated reservoir simulation system. PhD dissertation, The University of Texas at Austin.

Zhang, j., Delshad, M., and Sepehrnoori, K. 2007. Development of a framework for optimization of reservoir simulation studies. *Journal of Petroleum Science and Engineering*, 59:135-146.

Zhang, X., Du, C., Deimbacher, F., Crick, M., and Harikesavanallur, A. 2009. Sensitivity studies of horizontal wells with hydraulic fractures in shale gas reservoirs. Paper IPTC 13338, International Petroleum Technology Conference, Doha, Qatar, 7-9 December.

Zhou, W., Banerjee, R., Poe, B., Spath, J., and Thambynayagam, M. 2013. Semianalytical production simulation of complex hydraulic-fracture networks, *SPE Journal*, 19(1): 6-18.